UNIVERSITY OF LJUBLJANA
FACULTY OF MATHEMATICS AND PHYSICS

Matevž Tadel

Electron track reconstruction in the ATLAS experiment

Doctoral Thesis

Supervisor: prof. dr. Marko Mikuž
Co-supervisor: prof. dr. Allan Clark

Ljubljana, 2001

Abstract

Before entering the hardware production phase of a HEP experiment, the detector elements that have been chosen during the planning process need to be thoroughly tested. At the LHC, silicon detectors will operate in a high-rate environment which requires low-noise electronics with a shaping time of 25 ns. A prototype silicon-strip half-module equipped with the analogue read-out chip SCTA128-HC was put in a 200 GeV pion beam. An analysis of the collected data is presented. The tested module was found to conform to the SCT-modules specification for the ATLAS experiment.

Electron reconstruction in the ATLAS detector is compromised by the large amount of material in the tracking volume, which leads to frequent emissions of hard bremsstrahlung photons. This affects the measurement of the transverse projections of track parameters in the inner detector as well as the measurement of energy and azimuthal angle in the EM calorimeter for $p_T < 20\,\mathrm{GeV}$. Reconstruction and electron identification efficiencies are both degraded. A detailed analysis of bremsstrahlung effects has been performed and it is shown that a first-order treatment is unsatisfactory. An algorithm for efficient and robust electron reconstruction has been developed which placed a strong emphasis on bremsstrahlung detection and recuperation so as to provide the best possible track parameters from the ID reconstruction. The algorithm was benchmarked against simulated data: single electrons, electrons in jets and electrons in the presence of high-luminosity pile-up.

The $\mathrm{B}^0 \to \mathrm{J}/\Psi \to ee$ and $\mathrm{Z} \to ee$ processes, crucial for EM calorimeter calibration, as well as the potential Higgs discovery via $\mathrm{H} \to \mathrm{ZZ}^{(\star)} \to 4e$ (for m_{H}=130, 150, 180, 200 GeV), were studied using the developed electron reconstruction algorithm. Typically, a 10% improvement of reconstruction efficiency has been achieved for these channels with respect to the results quoted in the ATLAS *Physics Performance TDR*. At low and intermediate electron p_T values, the experimental parameter resolution has likewise been improved with a better understanding and handling of the bremsstrahlung effects.

PACS:	07.05.Kf	Data analysis: algorithms and implementation
	14.80.Bn	Standard-model Higgs bosons
	29.40.Gx	Tracking and position-sensitive detectors

Contents

Preface

As we go deeper and deeper into the smallness of space, mysterious entities are encountered. They do not speak and yet they pose more questions than they provide answers to. One asks these questions in terms of *high–energy physics* (HEP), being either theoretical or experimental in nature. We believe that quantum mechanics (or a physical theory expressed with a mathematical model of higher complexity) governs the domain we are probing. There, the inherent problem of quantum measurement is waiting for us: 'How can a quantum process manifest itself on a classical level?' One can not explain the results of a measurement without an underlying theory and the theory itself is meaningless without an experiment that has the power of falsifying it. The dialectical game has been pushed to a scale of 100 GeV where physics is currently explained with the *Standard Model of elementary particles and their interactions* (SM). Its mathematical formulation is a majestic symphony of non-euclidian geometry, group theory and functional analysis. That's how far we have come from the simple differential formulation of Newton's laws of mechanics. Likewise, we have travelled far from the objects that constitute the world that we live in. We have plunged down, towards the atoms of the world, leaving behind us many levels that are still not completely understood from first principles. By going further and further away from the world of human experience, our senses have become inadequate instruments and the basic concepts of physics have swollen with new meanings needed to incorporate them in different contexts. Nevertheless, there is a certain rationale in pushing experiments and human thoughts up to higher energies. Surprisingly, it is cosmology that makes the best use of the data harvested in HEP experiments. It is a generally accepted scientific fact that our universe is expanding (witness red shifts of light coming from distant galaxies). Therefore there was a time when it was much smaller, having a correspondingly higher energy density. Cosmic microwave background radiation is a relic from the time when the average energy density dropped below the level needed to keep electrons off the scattered nuclei. Neutral atoms were formed, the universe became transparent and photons were caught in the vastness of space. Extrapolation backwards from this time is made in accordance with observations of how matter behaves in high-energy collisions. Furthermore, twisting things around, as the universe had to come from somewhere, there must be a mechanism in nature that makes universes possible. By going to higher energies, we're getting closer to the realm in which our universe was created. It might be that we are still far from that point. However, without trying, without reaching out for what is feasible, we would still be hunting mammoths. I'm not saying we are better off the way we are ... but I'm confident that, after embarking on the route of scientific exploration, it would be a great mistake to stop. For the fruits of scientific research have shifted society far out of the equilibrium position with the surrounding nature and it is my belief that science is the only power in human hands that can, if pursued wisely, regain us the lost balance.

⋆ ⋆ ⋆

The work presented here was done at the *European Organization for Nuclear Research* (CERN) in the framework of the ATLAS collaboration which is building a general-purpose detector at the Large Hadron Collider (LHC). The main goal of the ATLAS experiment is to search for the Higgs boson (a particle predicted by the SM) and to chart the territory up to, and beyond, 1 TeV in cms energy. As the theory, the instrumentation used to probe the new realms and to verify predictions of the theory has likewise grown in its complexity. HEP experiments in general are craving for the investment of knowledge into the construction of detector elements, into analysis techniques, electronics and computing. For example, the ATLAS experiment will, including the preparation time, and experimental operation, devour more than 10 000 physicist-years of human effort.

The thesis, as a whole, presents most of my work for the ATLAS collaboration, performed during the four years of my engagement. One should understand that ATLAS will begin its operation in the year 2006 and that it is currently in its early experiment-building phase. While the ATLAS physics aims were the determinant of all the goals set in the process, the results can only form a skeleton on which the flesh of real data will attach to form the body of physical results.

My first task, after joining the collaboration and being genuinely puzzled for about half a year, was the performance benchmarking of different pattern recognition programs on simulated single particle events. Through this work I gradually understood parts of the detector, came to grips with their functioning and expected response. I plunged into the depths of detector description and the simulation tools which are used for obtaining the response of the detector to simulated events. Somehow I got involved with electron reconstruction and it suddenly became my main commitment. It soon became apparent that the knowledge of electron behaviour in the ATLAS detector is more sketchy than believed and that bremsstrahlung recuperation is implemented using inadequate algorithms. At that time I was already working with Alan Poppleton, the author of `iPatRec`, a software package for track finding and reconstruction in the ATLAS inner tracker. Under his careful guidance a detailed study of bremsstrahlung effects was performed and the guidelines for an adequate electron reconstruction algorithm were prepared.

Then my battle started. I implemented a very elaborate algorithm, trying to take into account every possible case. It turned out to be rather slow and not to bring as much improvement as anticipated. The words of the guru, Alan Poppleton, saved me once again. He proposed to make the algorithm as simple as possible, pick out the obvious cases and then worry about the rest later. Only at this point did I truly grasp the conclusions that could be extracted from the results of the detailed analysis of bremsstrahlung: there will be some events in ATLAS, for which there is nothing in human power that can be done to reconstruct them properly. After that, my work was easier and much more fruitful.

In spring 1999 I joined a group pursuing the research and development of silicon-strip detectors and a custom-made analogue read-out electronics to be used in the LHC environment. My work was to help in the preparation for a beam-test of a prototype module and, in particular, in the reconstruction of the harvested data. In one sentence, I was analysing the module's response to a passing particle. Before that, I regarded data just as something that you read from a disk or generate on the fly so that your algorithms have something to operate upon. Although I was aware of the fact that there will come a day when the data on disk will be the recorded, experimental data, I saw the transition from a physics event, occurring in the detector, to a series of zeros and ones on the disk, as a taking of a photograph. I couldn't be more wrong ... but the mistake taught me that what is *seen* by the detector is not entirely the same as what *happens* in it. And the results obtained for a silicon-strip module will eventually help us to work out this difference on the scale of the ATLAS detector.

After that I returned to the electron reconstruction. There were many things that needed to be checked and the algorithm itself had to be carefully optimised and benchmarked. After dealing with single particles, the time came to test it on a simulation of the physical events that will be of interest for ATLAS. This was the first time that I had to deal with programs, referred to as *event generators*. The basic idea is simple. You say to it: "Having a pp beam at 14 TeV cms energy, generate for me an event where a Higgs boson decays into two Z's and further into four electrons." And it returns a list of particles that fly out of the interaction zone. Looks simple ... and again it isn't. Already the first stage, the Higgs production, is tricky. At 14 TeV the protons are a colourful collage of quarks and gluons, their momentum distributions described theoretically by the proton's structure functions. Different sub-processes compete to be chosen for generation and each of them has different kinematics. After that, the final state has to be generated, with higher-order corrections included in the process. What is really tricky, is how to weight the phase-space so that when you pick a few thousand events, they will form a good representation of the real process. If you ever wondered why some theorists calculate higher order corrections for processes that don't have a slightest chance of ever being measured independently, here is a part of the answer: so they can be used in elaborate event generators that will mix this specific process with others and let it contribute to inclusive cross-sections of complete events that can be observed.

Acknowledgments

As already mentioned, Alan Poppleton played a central role in my understanding of the ATLAS experiment in general and problems associated with the track reconstruction in particular. But what made our cooperation really fruitful, was his willingness to learn from my work and to consult me as an equal when he encountered his own problems. Moreover, the manuscript, as well as my knowledge of the English language, benefitted immensely from his detailed inspection. I am grateful to him more than mere words can describe.

I would like to express gratitude to my supervisors, Marko Mikuž and Allan Clark, who had helped me choose my field of interest, as well as supported and guided my work.

Many thanks to members of the *Solid State Detector Development* group at CERN and *ATLAS group of the Jožef Stefan Institute.* In particular, Vladimir Cindro, Gregor Kramberger and Julio Lozano–Bahilo helped me solve and understand many problems I encountered in the silicon-detector lore.

A short overview

This section is an expanded abstract of material covered in each chapter. The first chapter consists of introductory material merged from various sources so as to provide a complete context for further expositions. Contents of chapters 2 to 4 is what I consider to be, at least in part, an original contribution to the ATLAS experiment and HEP community. Things that have found themselves in the appendix are more technical in nature and they might be of some interest to people solving similar problems.

Ch.1 Context begins with a historical motivation for the LHC project together with its technical specifications and physical processes expected to occur. A discussion of a development and life cycle of a large scale HEP experiment follows, trying to persuade the reader that this is a great scientific and technological undertaking requiring a joint effort of a large group of specialists.

An overview of the ATLAS spectrometer is done in a view of detector components, physics studies and electronic/computing requirements. In preparation for a later discussion the *inner detector* (ID) and *electro-magnetic calorimeter* (ECAL) are described in more detail. In the same spirit a role of electrons in the ATLAS physics is presented.

Ch.2 Beam test of a prototype SCT module sets out by summarizing the role and requirements for the silicon micro-strip detectors in ATLAS. The SCTA128HC read-out chip, the one mounted on the detectors put in the test-beam, is presented. The experimental set-up is described together with the alignment and resolution of the beam telescope. The path leading from raw data, as read off the detector, to reconstructed hits is traversed and the methods used for the determination of a cluster position are discussed. Then the results are presented in terms of efficiency, noise occupancy, resolution, reconstructed cluster properties and charge distribution.

Ch.3 Electron track reconstruction presents the core of my work. Technical difficulties connected with the electron tracking are explained and a detailed study of electron energy losses by bremsstrahlung in the ATLAS detector is presented. Based on these results an algorithm for electron reconstruction, named `ieElRec`, was constructed. Its environment, internal logic and input/output quantities are scrutinized so as to enable a user to understand and make use of the algorithm.

To quantify the results and make the algorithm useful for higher-level analyses in a variety of conditions, a detailed analysis of the results obtained from `ieElRec` on single electrons in transverse energy range form $p_T = 1.5$ to $60\,\mathrm{GeV}$ is presented. Furthermore, pion rejection capabilities of `ieElRec` are addressed and impact of jets and a high-luminosity pile-up on the electron reconstruction are discussed.

Ch.4 Applications of the electron reconstruction algorithm documents analyses of three physical process that will be of interest for ATLAS physics : $\mathrm{B}^0 \to \mathrm{J}/\Psi \to ee$, $\mathrm{Z}^0 \to ee$ and $\mathrm{H} \to \mathrm{ZZ}^{(\star)} \to 4e$. A strong emphasis is put on the quality of reconstruction of electron tracks and derived quantities. Nevertheless, all analyses are carried out till the final results, namely the invariant masses of the decaying particles, are obtained and the corresponding precision of the ATLAS detector studied.

Chapter 1

Context

1.1 The LHC project

The Large Hadron Collider (LHC) project is CERN's move towards the accelerators of the next generation and is a natural successor to previous particle accelerators. There is little sense in talking about an accelerator without some indication of the physics that is accessible using it and there is not much point in talking physics without being able to measure anything ... without having a detector in the case of an accelerator.

1.1.1 Historical motivation

The first ideas for the LHC appeared in the early 1980's. These were the times after the discovery of the W and Z bosons by the UA1 and UA2 collaborations at CERN which gave new wind to physicists sailing the sea of the Standard Model. The large electron-positron collider (LEP) was being built together with the four experiments that were to become the messengers of its glory. LEP was seen as the machine to provide high precision measurements of the Standard Model in the electro-weak sector.

A major problem with the electron accelerators is the huge energy loss due to synchrotron radiation (proportional to γ^4) which makes them true energy suckers also during continuous beam operation. An alternative obvious choice is to use proton–antiproton collider ... but at high energies the collisions are between partons and therefore we only use some fraction of proton's energy in a single reaction. Going up in energy hits back with the cross-section dependency on the cms energy which is roughly proportional to $1/Q^2$ so one must also increase the luminosity. By going to a higher luminosity one encounters two problems. The first is that one needs high incoming currents of particles and massive production of anti-protons is technologically difficult. It is more reasonable to make two parallel beam-pipes with specially designed dipole magnets. The second problem is that the high density of charged particles in a bunch makes it a nightmare to keep them together without significant losses.

Nevertheless, it was already obvious that machines with a higher energy and higher luminosity would be needed to make one step further ... to get to the gist of spontaneous symmetry breaking (the Higgs boson hunt) and to produce b and t quarks in the abundance needed for spectroscopy. Super-symmetric and string theories were lurking in the theoretical mist pointing to energies in the TeV region. In astrophysics dark matter was haunting the souls seeking their comfort in the cosmological models giving rise to ideas of new states of matter (like lepto-quarks, excited leptons and quark-gluon plasma). Fermilab was building the Tevatron proton–antiproton collider and plans for the SSC were slowly emerging. All of these things were putting imagination on fire and in 1990 there was a LHC Workshop held at Aachen organized by the European Committee for Future Accelerators [1]. The basic building blocks of the project were presented: physics for different modes of LHC operation, the basic parameters of detectors that could be used in the LHC environment and data acquisition services needed (electronics and software tools). In 1992 the LHC committee was established at CERN and in 1993 'Letters of Intent' to build a detector at the LHC were submitted by the ALICE, ATLAS and CMS collaborations followed by the LHC–b collaboration in 1994.

1.1.2 Technical details

The primary operation of the LHC will be in *pp* collisions at 14 TeV cms energy with a luminosity starting at $\sim 3 \cdot 10^{33}$ in the first year, increasing to $\sim 10^{34}\,\mathrm{cm}^{-2}\,\mathrm{s}^{-1}$ for the rest of the operation. Studies of heavy ion collisions with Pb-Pb beams accelerated up to 1250 TeV (2.76 TeV/u) are also planned. As main physics goals of the ATLAS and cms collaborations require the *p*-*p* mode, all numbers will be quoted for this regime.

The LHC will be filled from the Super Proton Synchrotron (SPS) with 450 GeV bunches consisting of 1.1×10^{11} protons (see Fig.1.1 for a schematic view). Acceleration to 7 TeV will take 4.3 minutes during which the magnetic field in the dipole bending magnets will increase from 0.535 T to 8.33 T. Luminosity is designed to be maintained at a usable level for 10 hours. The energy loss via synchrotron radiation will be 3.8 kW which poses a technical difficulty for cryogenics (the beam-pipe, the RF cavities and the bending magnets will be held at a temperature of 1.4 K). The bunch spacing will be 7.48 m (or 24.95 ns). A single bunch will have a length of 8.4 cm (or 0.28 ns) and a fractional energy spread of $0.105 \cdot 10^{-3}$.

1.2 Life cycle of an HEP experiment and the importance of beam tests

In high energy physics one deals with particles of various energies, lifetimes, decay modes and the properties of interaction with matter. From a theoretical point of view one attempts to understand the interaction process in terms of a physical model. But to 'see' the process one needs to detect the final state particles and to perform some sort of measurement in order to assign them momentum and energy as well as to identify them.

When a new HEP experiment is being planned, the physical goals are set first. The beam particle-type and energy are usually known in advance, so the production mechanisms and final-state kinematics for the processes of interest can be established. The sought-for precision of measurements is the first source of requirements for the precision of the detector. For each candidate channel, a similar reasoning is followed to identify the processes that result in the same (or at least indistinguishable) signature in the detector as the studied process; these processes are called *background*. Here extreme caution is paid to assure a statistically significant signal over background ratio, since the production cross-sections of the background processes can be orders of magnitude above the cross-section for the process of interest. From the required background rejection factors, the second set of requirements for the detector precision is determined. Based on the requirements and available resources,

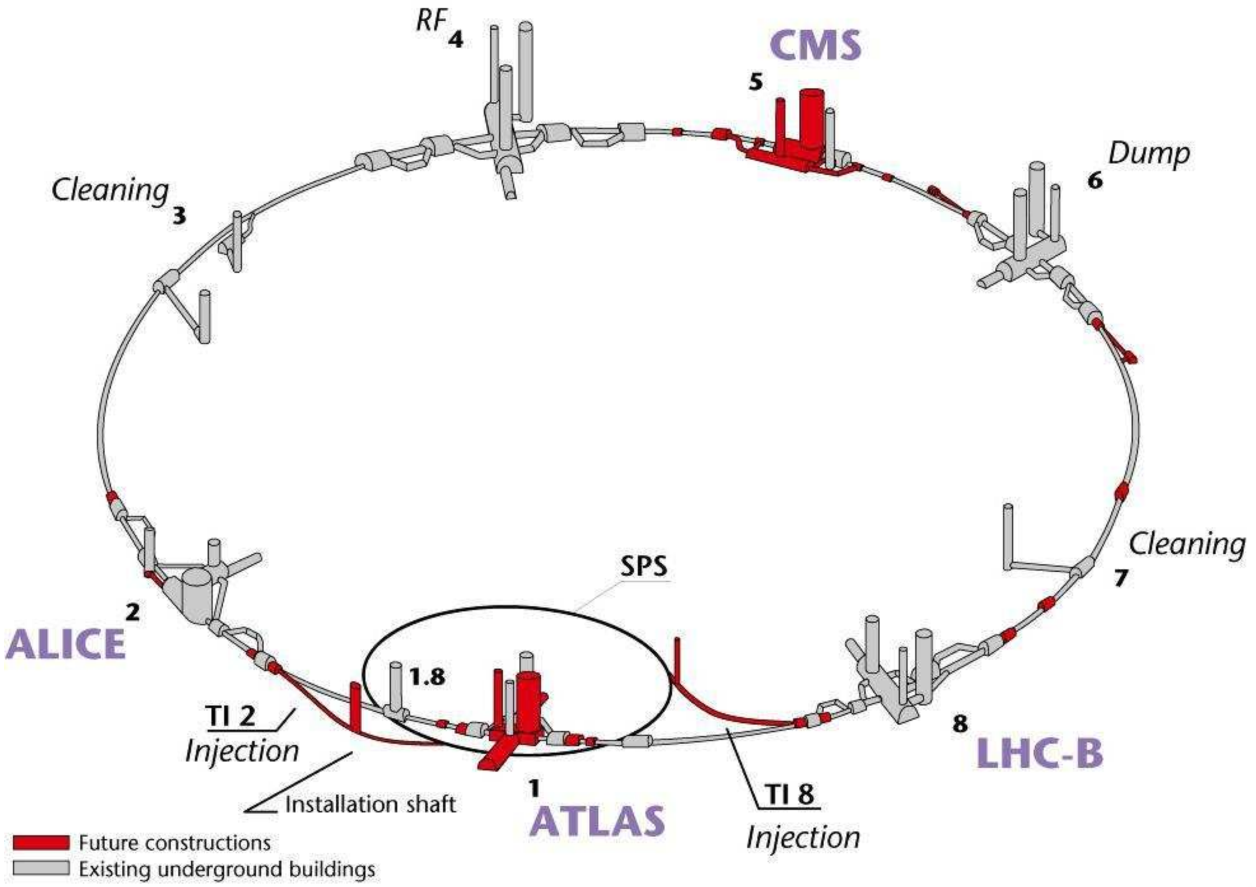

Figure 1.1: Schematic view of the LHC accelerator.

the detector elements are chosen. Furthermore, the sub-detector specifications are deduced from the detector physics requirements.

As HEP experiments probe deep into the quantum structure of nature, the interaction of particles with a sensitive material is of probabilistic nature (or statistical if one prefers this formulation). The detectors used are often constrained by a large number of requirements, some of them entirely earthly in origin (cost is one of the most painful ones), which makes the optimisation of a given detector a delicate process. That's why we need to put the detectors at different stages of development into a test beam: to see the detector and related electronic response in a near real-life situation. Results help us evaluate the device, give us development guidelines and in later stages provide a means for testing prototypes before entering into mass production. Another important use of the beam test data is to provide the detector simulation tools with ample sources of cross-checks and calibrations. Without that we could never be certain that our simulations are really describing the animal we're building.

In a large scale HEP experiment test beam analyses are used during pre-production stage using the prototypes of detector elements. To go into slightly more detail, the evolution of an experiment can be roughly apportioned to four phases taking into account the manpower (in terms of educational structure and quantity) and infrastructure involved.

The early planning phase begins with a handful of people becoming aware of a technical possibility to probe into a more or less uncharted territory of physics. Questions asked are 'Can we do it?' and 'How can we do it?' and the answers are in a somewhat sketchy form. Problems are addressed to a certain depth but not in every possible detail. However the goals are well defined and the areas where surprises or difficulties are expected are pointed out.

The experiment planning phase leads from a 'Letter of Intent' to a 'Technical Proposal'. A detailed study of the main physics being addressed is made from the theoretical point of view and several detector geometries are simulated to find the best solution for a set of often antipodal demands. This is where the base of the experiment's pyramid of scientific force begins to form: institutes (or groups) with previous experience join the experiment to provide solutions for the sub-detectors which are expected to form the detector. Also, estimates are made on requirements for electronics and CPU power.

The experiment preparation and building phase is where everything must be studied down to the smallest detail. Three goals must be satisfied:

- A detailed specification and preparation of the technical support needed by the experiment is required. This includes engineering of the experimental area, services, DAQ systems and computational infrastructure.
- A final choice of detector elements must be made. They must be tested and proven to work in experimental conditions with given requirements from the physics programme and DAQ capabilities. A detailed simulations of the detector's geometry and response is prepared and cross-checked with beam test data obtained from prototypes of sub-detectors.
- Analysis programs must be prepared in order to test the detector acceptance for relevant processes with Monte-Carlo simulations and give feedback to detector engineering.

The results of all this work are presented in the experiment's *Technical Design Report* (TDR). It gives a detailed account of every part of the detector, its performance and its mode of operation.

Experiment building is the actual work of constructing the experiment. In time aspect it largely overlaps with the preparation since decision making and selection process for specifications of subsystems goes from coarse description to fine tuning. This way parts of the system can be built before the final specifications are agreed upon.

The experimental operation begins with data collection. In the commissioning phase the detector's operation is scrutinized and its response optimised in respect to available parameters. Quality assessment is made and calibration of the detectors carried out. Analyses prepared at previous stages are fine tuned to the existing system ... the real physics begins.

1.3 ATLAS experiment and ATLAS detector

The ATLAS collaboration will build a general-purpose pp detector designed to exploit the full discovery potential of the LHC (see ATLAS Physics TDR [2], [3] and ATLAS Technical

Proposal [4]). The major focus of interest for ATLAS is the origin of mass at the electro-weak scale. Detector optimization is therefore guided by physics issues such as the sensitivity to the largest possible Higgs mass range. Other important goals are the searches for the heavy W and Z-like objects, for super-symmetric particles, for compositeness of the fundamental fermions, as well as the investigation of CP violation in B-decays, and detailed studies of the top quark. The ability to cope well with a broad variety of possible physics processes is expected to maximize the detector's potential for the discovery of new, unexpected, physics.

As the LHC physics depends crucially on the high luminosity, it is important to select processes with distinguishable, robust signatures that allow for high-precision measurements and an efficient background rejection. Processes with e and μ leptons as well as photons in the final state are a natural choice in the LHC environment. Furthermore, to allow for a missing transverse energy determination and for a hadronic jet energy measurement, a hermetic hadronic calorimetry is also vital. Since heavy-quark systems will be an important chapter of the LHC physics, a precise secondary vertex determination, full reconstruction of final states with relatively low-p_T particles (e.g., $J/\Psi \to l^+l^-$), low-p_T lepton first level trigger thresholds as well as second-level track triggering capability are all necessary requirements for the experiment. The variety of signatures is considered to be important in the high-rate environment of the LHC in order to achieve robust and redundant physics measurements with the ability of an internal cross-check.

All things considered, one can summarize the basic design considerations for ATLAS in the following points:

- very good electro-magnetic calorimetry for electron and photon identification and measurements, complemented by hermetic jet and missing E_T calorimetry;
- efficient tracking at high luminosity for lepton momentum measurements, for b-quark tagging, and for enhanced electron and photon identification, as well as for τ and heavy-flavour vertexing and a reconstruction capability of some B decay final states at lower luminosity;
- stand-alone, precision, muon momentum measurements up to the highest luminosity, and very low-p_T trigger capability at lower luminosity.

Secondary goals to maximize the physics reach and to optimize the exploration of the LHC give two additional points:

- large acceptance in η coverage;
- triggering and measurements of particles at low-p_T thresholds.

1.3.1 Structure of the detector

The overall detector concept of the ATLAS detector, dictated by the requirements listed above, is not far from the general detector layout of LEP experiments. Going outwards from the interaction point, the first large block one encounters, is the inner detector encompassed by a solenoidal magnetic field and followed by the electro-magnetic and hadronic calorimeters. On the outside of the detector there is the muon system equipped with an air-toroid magnet system for stand-alone momentum measurements. It defines the overall dimensions of the ATLAS detector: outer barrel chambers are at a radius of 11 m and the third layer

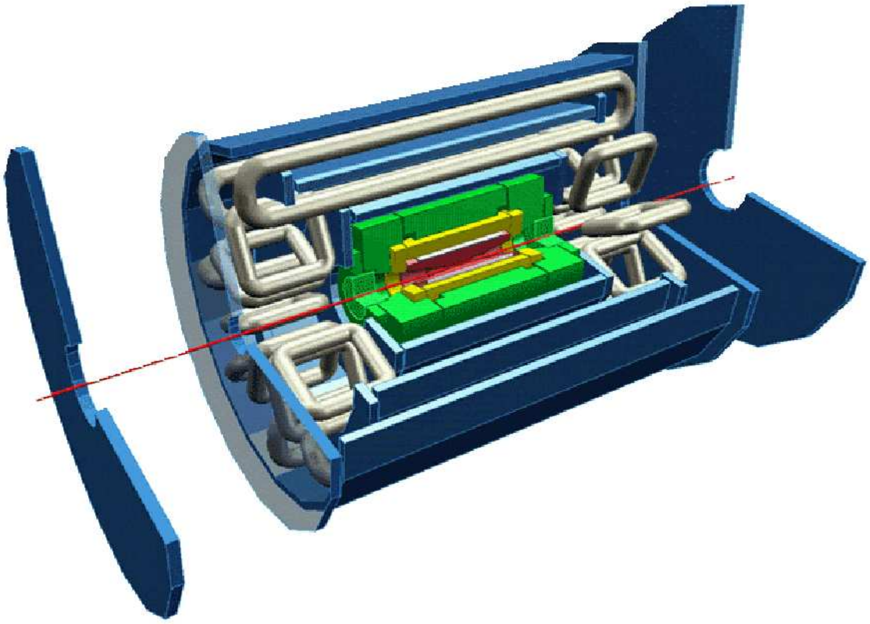

Figure 1.2: A schematic view of the ATLAS detector.

of the forward muon chambers is located ± 21 m from the interaction point. Fig:1.2 shows a schematic overview.

1.3.2 Inner detector

The Inner Detector (ID, also called inner tracker) is composed of three parts: the silicon pixel detectors, the silicon strip detectors (*SemiConductor Tracker* – SCT) and the transition radiation tracker (TRT). It combines the high-resolution detectors at inner radii with continuous tracking elements at outer radii. An overview of the inner tracker can be seen in Fig.1.3. Each of the above mentioned sub-detectors has a barrel region (up to $|\eta| \lesssim 1$) where detector layers are arranged on concentric cylinders around the beam axis, while in the forward region (or end-cap) detectors are mounted on disks perpendicular to the beam axis. This can be clearly seen in Fig.1.4 and will be explained in detail together with the separate detector parts. The full ID extends over $|\eta| \leq 2.5$.

The ID is enclosed within a super-conducting solenoid of 5.3 m length (to be compared to the ID's length 6.7 m) creating an axial magnetic field with a strength of 2 T. Since the coil is shorter than the tracking volume the field deviates significantly from uniformity ($B_z \sim 1$ T at the end of the coil and $B_z \sim 0.4$ T at the end of the tracker). This poses some technical difficulties for the pattern recognition algorithms.

The detailed requirements for the ID can be found in [5]:Ch:2.3. They include the geometrical specifications (η coverage, number of space-points per track), the measurement precision (p_T, vertex position), the pattern recognition efficiencies and physics requirements (e/γ identification, secondary vertex resolutions and b-tagging).

The Pixel Detector is designed to provide a very high-granularity, high-precision set of measurements as close to the interaction point as possible. There are three pixel barrels (at radii 47.5 mm, 105.5 mm and 137.5 mm) and four forward disks (with z coordinates

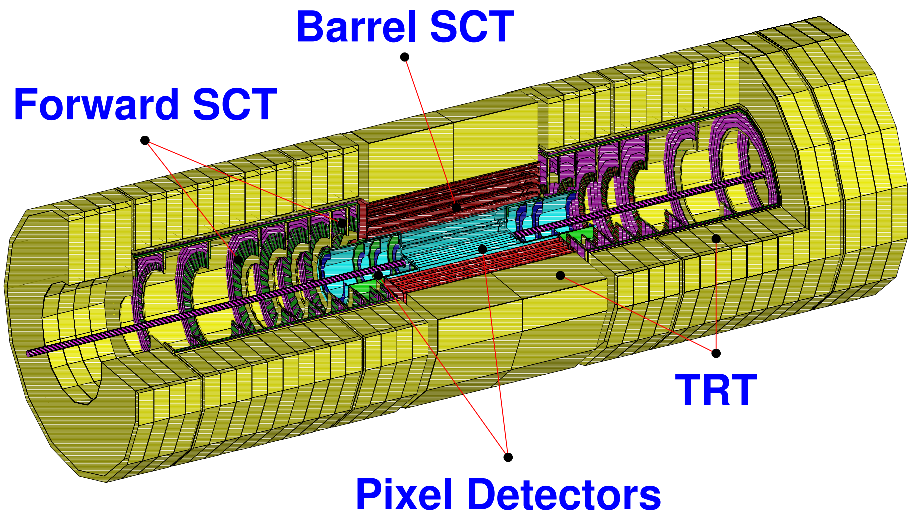

Figure 1.3: A look into the inner tracker.

of 490 mm, 608 mm, 759 mm and 1035 mm), giving at least three measurements of track intersection with a precision of $\delta R\varphi \times \delta z = 50\,\mu m \times 300\,\mu m$.

Its most important role is to provide the desired vertex resolution and enable one to find secondary vertices to be used for the b and τ–tagging. For a complete description see [6].

The Semiconductor Tracker is designed to provide four precision measurements per track in the intermediate radial range, contributing to the measurement of momentum, impact parameter and vertex position, as well as providing good pattern recognition as a result of the detector's high granularity and low occupancy. The barrel SCT has four layers at radii from 30 cm to 52 cm with active half-length of 74.5 cm. The layers are composed of modules consisting of two pairs of silicon micro-strip detectors glued back-to-back with a small stereo angle to obtain the z measurement. Each silicon detector has 768 active readout strips (80 μm pitch) and measures 12.8 cm in length (composed of two 6.4 cm detectors with bonded strips). The end-cap SCT has nine axial wheels positioned at z coordinates from 83.5 cm to 277.8 cm. Forward modules are very similar in design but use tapered strips with one set aligned radially. Technical details of the SCT are presented in [7]:Ch:11.

The TRT is the outermost part of the ID. It consists of 370,000 straws made of coated polyamide film. Their diameter is 4 mm and their length is in the range 40-150 cm (depending on the straw position). In the barrel region straws are parallel to the beam pipe and are mounted on rings. They are embedded in stacks of polypropylene/polyethylene fibre radiator which produces the transition radiation (TR). The end-cap straws are placed radially and regular foils are used for the TR production. Straws are filled with a mixture of 70% Xe + 20% CF_4 + 10%CO_2. Xe allows for detection of the transition radiation (by the use of a double threshold) and contributes significantly to the electron identification power of ATLAS. CF_4 increases the drift velocity and CO_2 is necessary to stabilize the operation. The TRT also contributes to the accuracy of the momentum measurement by providing (on average) 42 measurements in R-φ direction with a resolution of 170 μm per straw. You can also try your luck with [6]:Ch:12.

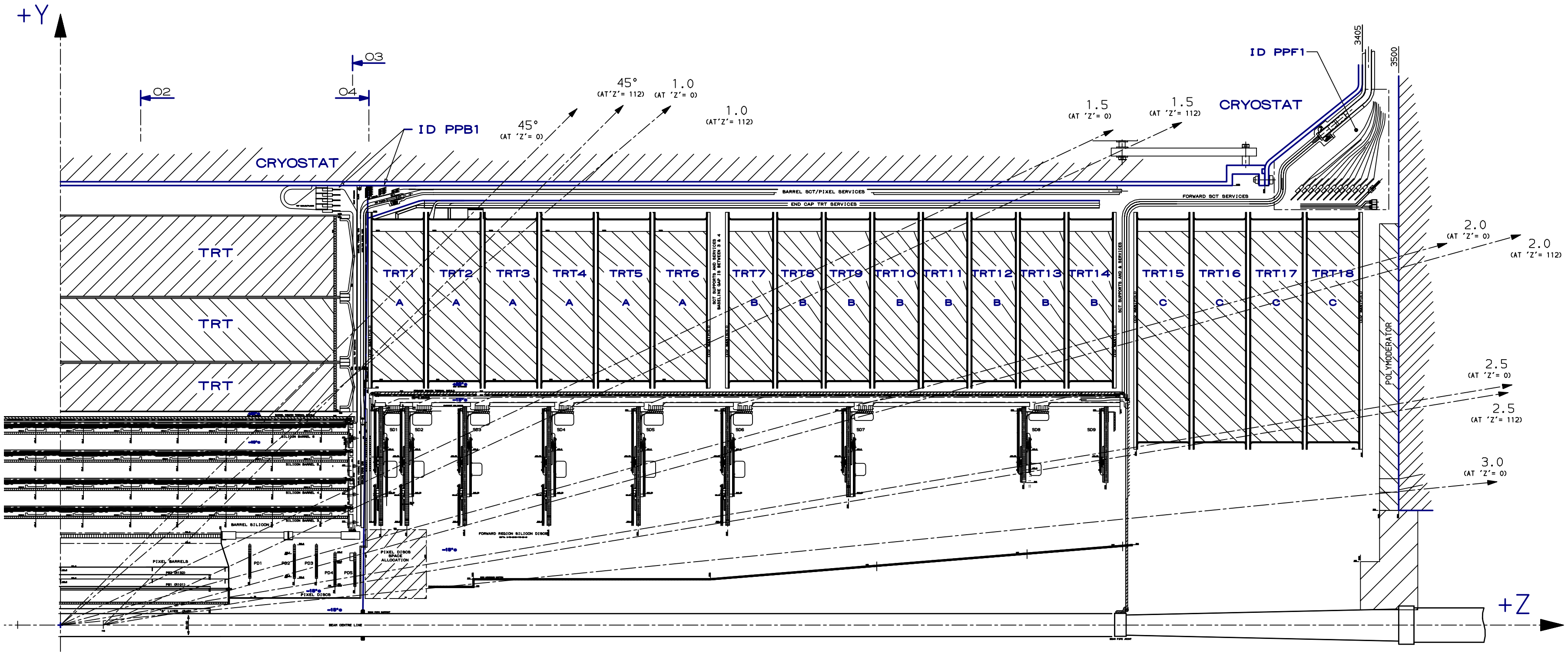

Figure 1.4: An engineering drawing of the ID (a 'Post TDR' layout).

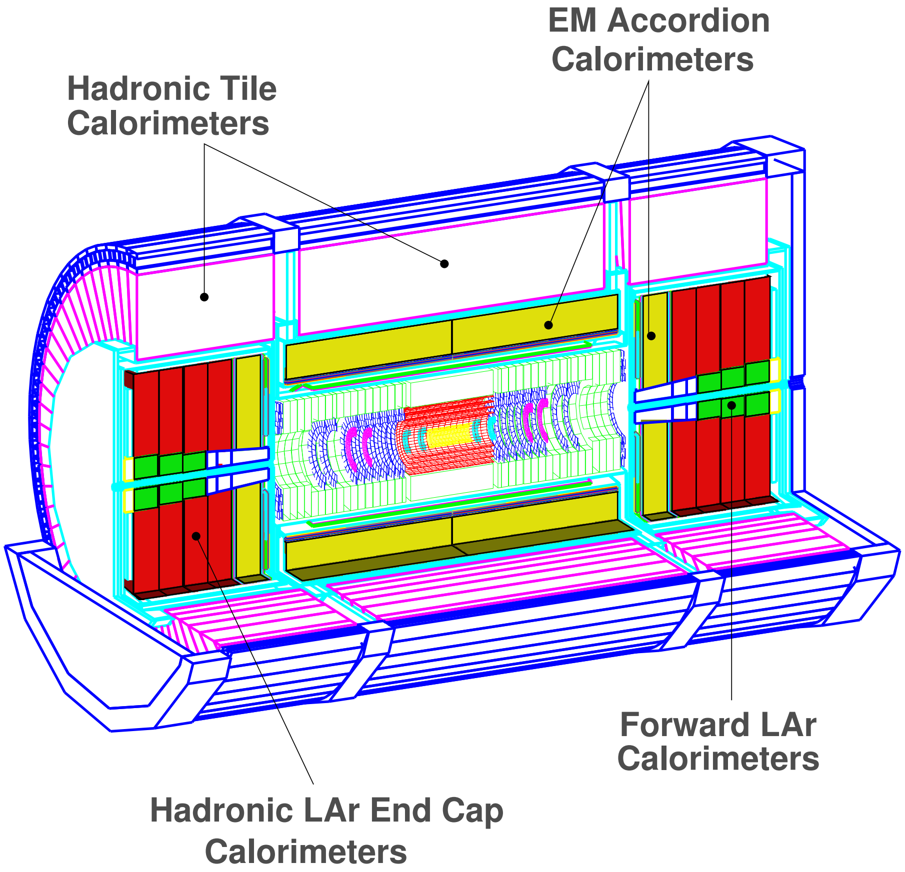

Figure 1.5: Overview of ATLAS calorimetry.

1.3.3 Calorimetry

At the LHC experiments calorimeters are of great importance as their intrinsic resolution improves with energy. The main calorimeter tasks at ATLAS are:

- an accurate measurement of the energy and position of electrons and photons;
- a measurement of the energy and direction of jets;
- a measurement of the missing transverse momentum;
- particle identification;
- event selection at the first trigger level.

The operational environment at the LHC poses several difficulties: the large center-of-mass collision energy implies the need for a good performance over an unprecedented range, extending from $< 1\,\mathrm{GeV}$ up to the TeV scale. At high luminosity a signal from the soft hadronic interactions will be piling-up, both in space and time. A fast detector response and fine granularity are therefore required to minimize its impact on physics performance. The position of the calorimeters in ATLAS is shown in Fig.1.5. A detailed description of the calorimeter's performance is available in [8].

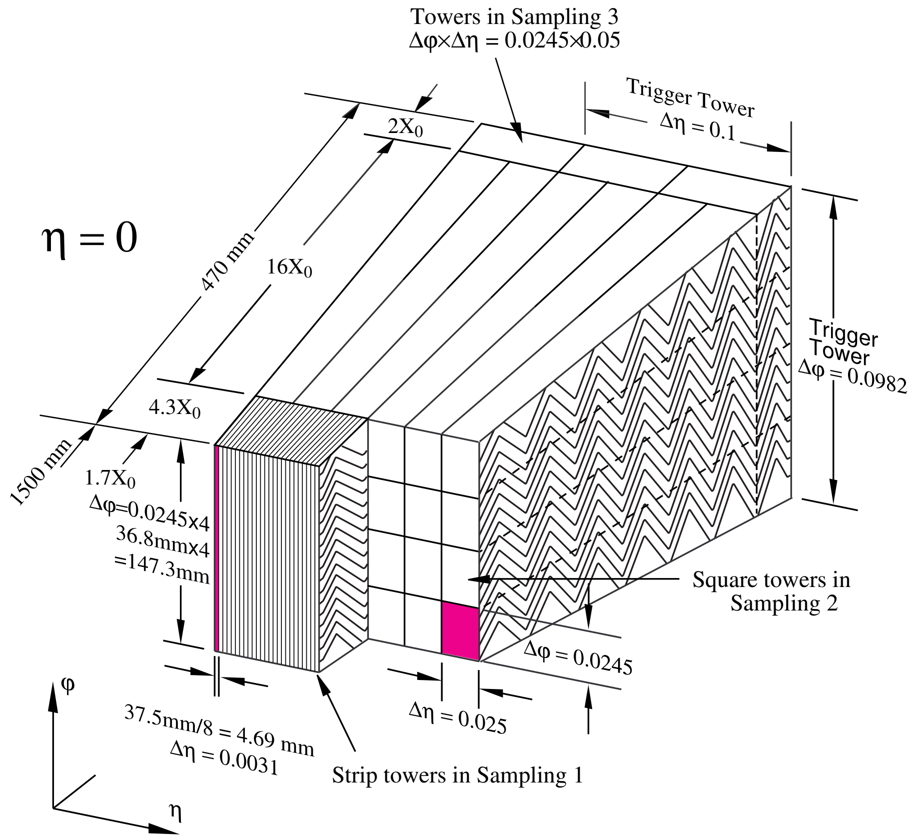

Figure 1.6: A sketch of the structure of the EM calorimeter.

EM calorimeter

The EM calorimeter is a lead-liquid-argon sandwich detector with accordion-shaped kapton electrodes and lead absorber plates over its full coverage. The lead thickness in the absorber plates has been chosen as a function of rapidity, so as to optimise the calorimeter performance in terms of energy resolution. It covers the rapidity region $|\eta| < 3.2$ with total thickness of > 24 radiation lengths (X_0) in the barrel ($|\eta| < 1.475$) and $\sim 26X_0$ in the end-cap ($1.375 < |\eta| < 3.2$). The energy resolution is $\delta E/E \sim 10\%/\sqrt{E(\,\mathrm{GeV})}$ with the constant term smaller than 1%. The linearity of response is better than 0.5% for energies up to 300 GeV. Measurement of shower direction has a resolution of $\sim 50\,\mathrm{mrad}/\sqrt{E(\,\mathrm{GeV})}$.

The EM calorimeter is divided into towers pointing away from the interaction point and has three longitudinal samplings (see Fig.1.6). In the region $|\eta| < 1.8$ a presampler is installed in front of the calorimeter to correct for the energy lost in the upstream material. It is a 1.1 cm thick (5 mm for $|\eta| > 1.5$) active LAr layer with a segmentation $(\Delta\eta \times \Delta\varphi) = (0.0025 \times 0.1)$. The first sampling is $6X_0$ thick (including dead material and presampler) and has a granularity of $(\Delta\eta \times \Delta\varphi) = (0.003 \times 0.1)$. This very high precision in η is needed for $\pi^0 : \gamma$ separation (π^0 decays almost exclusively as $\pi^0 \to \gamma\gamma$). The second sampling has square towers of size $(\Delta\eta \times \Delta\varphi) = (0.025 \times 0.025)$ and thickness of $16X_0$. The third sampling with thickness from 2 (central barrel) to 12 X_0 and a twice coarser granularity in η is reached only at transverse energies above 50 GeVand is also used for the prediction of leakage into the hadronic calorimeter. In the region of transition from the barrel to end-cap there is a crack in the active material ($1.4 < |\eta| < 1.6$). Scintillators are installed there to allow for

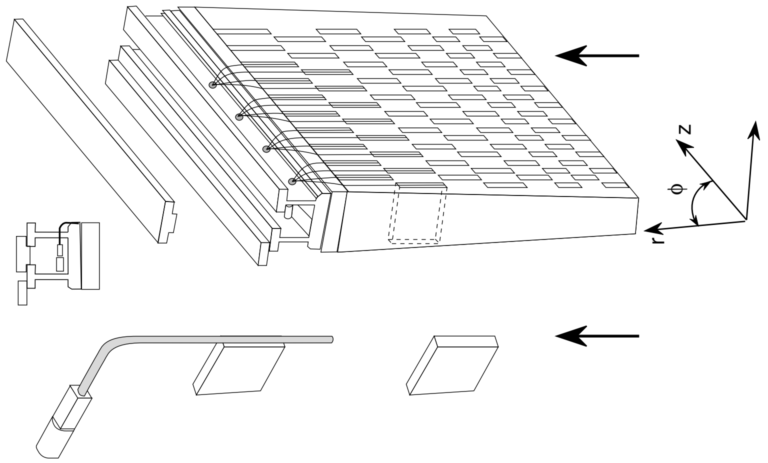

Figure 1.7: A module of the iron tile-scintillator.

the measurement of energy lost in this region. The details of this detector can be found in [9].

Hadronic calorimeter

The ATLAS hadronic calorimetry covers the range $|\eta| < 5$ using different techniques and devices as best suited for the different requirements and radiation environment. The main calorimeter task is the reconstruction of jets and the measurement of missing E_T. The designated energy resolution is $50\%/\sqrt{E} \oplus 3\%$ for $|\eta| < 3$ and $100\%/\sqrt{E} \oplus 10\%$ for $3 < |\eta| < 5$. The linearity of the energy measurement up to 4 TeV is within 2%.

In the barrel region ($|\eta| < 1.5$) iron tile-scintillators are used with an overall thickness of 11 interaction lengths (λ_l) and a granularity of $(\Delta\eta \times \Delta\varphi) = (0.1 \times 0.1)$. The schematic of the tile calorimeter module is shown in Fig.1.7.

In the end-cap and forward regions (see Fig.1.5) a similar technique as in the EM calorimeter (LAr accordion) is used because of the sensitivity of plastic scintillators to radiation damage. Copper is used instead of lead and the plates themselves are some ten times thicker. The granularity in this region is $(\Delta\eta \times \Delta\varphi) = (0.2 \times 0.2)$ and the overall thickness is $14\lambda_l$. For more information consult [10] and [9].

1.3.4 Muon system

High-momentum muons provide a clear and robust signature of physics at the LHC. To exploit this potential, the ATLAS collaboration has designed a high-resolution muon spectrometer with a stand-alone triggering and momentum measurement capability (see [11]).

The spectrometer covers the pseudorapidity range $|\eta| < 2.7$ with divisions into barrel and end-cap regions (Fig:1.8). The magnet system consists of three air-core superconducting toroids. The barrel toroid's length is 25 m with inner and outer bores located at a radius of 9.4 m and 20.1 m respectively. The two end-cap toroids are inserted in the barrel at each end. Their length is 5 m and the bore radii are 1.65 m and 10.7 m. Each toroid consists of eight flat coils assembled radially around the beam axis. Typical bending powers are 3 T m in the barrel and 6 T m in the end-cap.

Over most of the η coverage a precision measurement of the track coordinate in the principle bending plane is provided by three stations of monitored drift tubes (MDT). At large pseudorapidities and close to the interaction point cathode strip chambers (CSC) with higher granularity are used. Their response time is about 500 ns. The resolution of each measurement is 50 μm giving a momentum precision of $\Delta p/p = 10^{-4} \cdot p/[\,\mathrm{GeV}]$ for $p_T > 300\,\mathrm{GeV}$. At smaller momenta the resolution is limited to a few percent by multiple scattering in the inner parts of the detector.

The trigger chambers extend up to $|\eta| < 2.4$. Resistive plate chambers (RPC) are used in the barrel and thin gap chambers (TGC) are used in the end-cap region. Both have response times of about 5 ns. They serve for first level triggering, bunch crossing identification and provide measurement of the second coordinate in a direction orthogonal to the one measured in the precision chambers with a typical resolution of 5-10 mm. The p_T acceptance of the muon trigger extends down to $p_T \sim 5\,\mathrm{GeV}$ which is needed for physics studies, including CP violation in the b-quark sector.

1.4 ATLAS Trigger system and computing infrastructure

The collision rate at the LHC will be 40 MHz and the number of binary output channels from the ATLAS detector is approximately 10^7, giving a data-flow of approximately 4×10^{14}bit/s. This is far too much data to be effectively handled and stored. Besides, one doesn't want to study soft hadronic interactions but only the 'interesting' physics at and above the m_W scale, as well as some selected b-hadron events. The luminosity and the estimated pp cross-sections at 14 TeV are expected to yield about 100 such events per second. This gives 100 MB/s of output from the detector, which we believe can be managed by future data storage systems. For comparison, note that LEP experiments produced less than 1 MB/s.

1.4.1 Overview of the ATLAS trigger

The ATLAS trigger is divided into three levels (see Fig.1.9). Each of them performs some specialized functions and the number of events processed by each level becomes progressively smaller.

The Level 1 trigger bases its decisions solely on calorimeter and muon system information. In addition, the granularity used by the Level 1 is coarser than the full detector granularity. It reduces the event rate from 40 MHz to about 10-100 kHz.

The Level 2 trigger uses output from Level 1 to guide it toward the regions of interest (RoI), does unpacking of the ID tracking information and uses the full calorimeter granularity in these regions. By doing track reconstruction it then makes a decision based on the status of allowed trigger menus. This will be discussed in more detail in the following sections. The output rate from Level 2 is 0.1-1 kHz.

Events passing the Level 2 trigger enter the full-reconstruction phase or the Level 3 trigger where the standard offline software is used to build the events. This means using the full detector information and a current version of the reconstruction software. At the end the final decision is made: will the event be stored or not. If so, the event is stored together with the reconstruction information that tags the event with its particle content and can later be

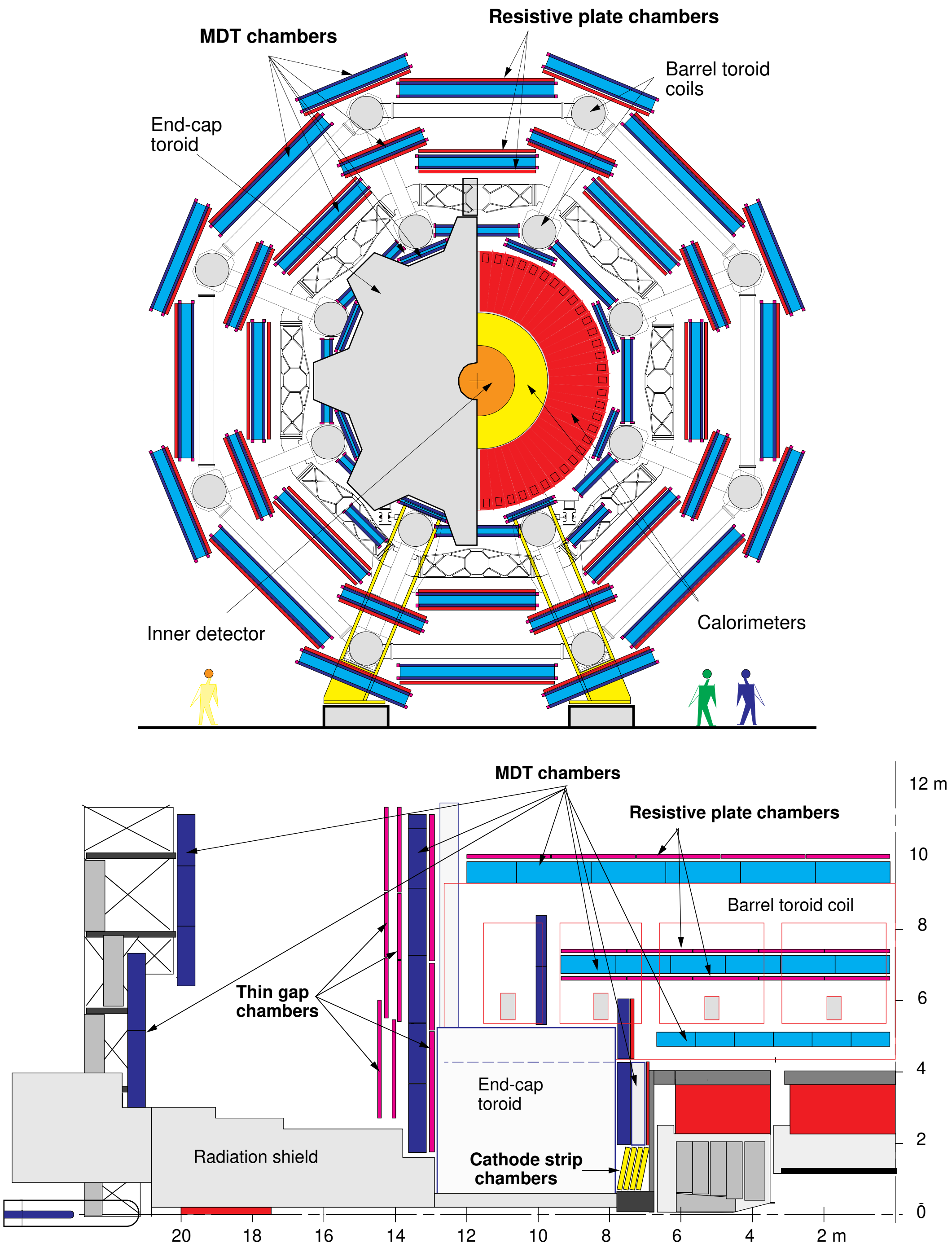

Figure 1.8: x-y (top) and r-φ (bottom) view of the ATLAS muon spectrometer.

used as a selection criteria for detailed analysis. The output rate from Level 3 is the wanted 10-100 Hz.

This last step can later be repeated with a more accurate version of the reconstruction software and new tags can be added to its record but the final selection has already been made.

First of all we have to decide what interests us. Which means that we must write down the physical processes, identify their detectable decay channels and find their signatures in the detector. Then we must study them in the context of the detector and surrounding physics, which will create the background.

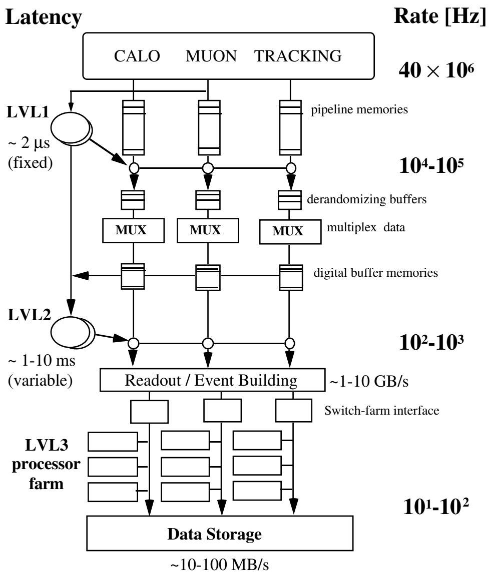

Figure 1.9: Overview of the 3-level ATLAS trigger.

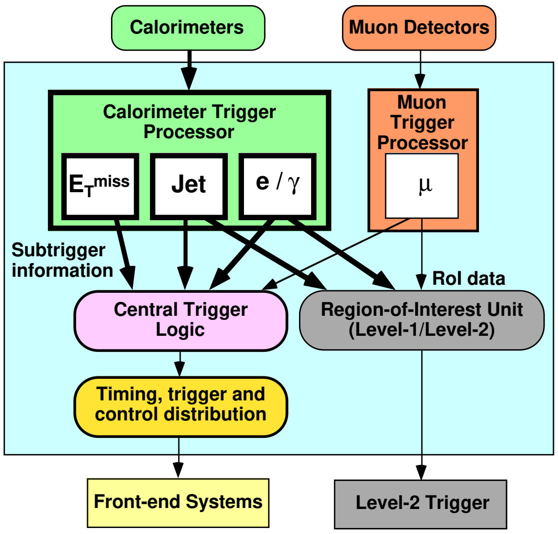

Figure 1.10: An overview of the Level 1 logic.

1.4.2 The Level 1 trigger

As the Level 1 trigger is the most critical part of the system its detailed study is the subject of a dedicated TDR ([12]). Only a brief sketch of its workings is presented here. Level 1 bases its decision on calorimeter and muon system data (see Fig.1.10 for an overview). Custom-made electronics processes the incoming information and generates a list of trigger objects. This list includes:

- information on multiplicity of e, γ above several thresholds
- information on multiplicity of jets above several thresholds
- information on multiplicity of μ above several thresholds

Trigger	Rate [kHz]
Single muon, $p_T > 6\,\mathrm{GeV}$	23
Single isolated EM cluster, $E_T > 20\,\mathrm{GeV}$	11
Two isolated EM clusters, $E_T > 15\,\mathrm{GeV}$	2
Single jet, $E_T > 180\,\mathrm{GeV}$	0.2
Three jets, $E_T > 75\,\mathrm{GeV}$	0.2
Four jets, $E_T > 55\,\mathrm{GeV}$	0.2
Jet, $E_T > 50\,\mathrm{GeV} \oplus$ missing $E_T > 50\,\mathrm{GeV}$	0.4
Tau, $E_T > 20\,\mathrm{GeV} \oplus$ missing $E_T > 30\,\mathrm{GeV}$	2
Other triggers	5
Total	~ 40

Table 1.1: An example of the Level 1 trigger objects and their expected rates for the low luminosity operation.

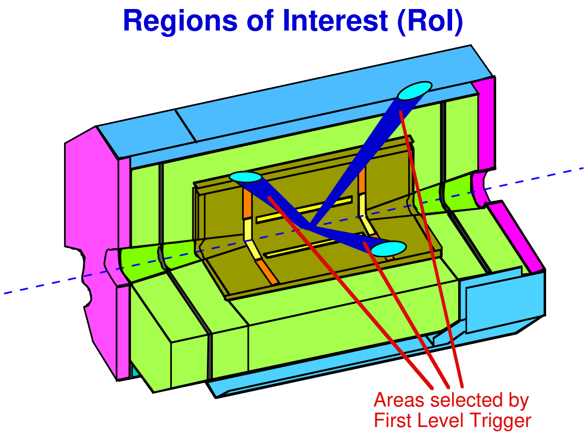

Figure 1.11: The typical regions of interest generated by the Level 1.5 trigger.

- information on $\not{E}_T$.

This list is then compared to the current Level 1 menu. An example of a Level 1 menu is shown in Tab:1.1. These are inclusive objects . . . an event can match more than one of them. When we have a match, the event is passed to an intermediate step (Level 1.5 trigger) to build RoIs for Level 2 (Fig.1.11). As you might expect, the RoI builder must be fully aware of the structure of the Level 2 menus in order to feed it with the appropriate search regions.

The processing time (or latency) is fixed to 2.5 μs and the input flow of data is 1500 Gbit/ s. Until now, read-out has been done only on some detector parts and only if the event passes the Level 1, will the full detector data be read out. This means that each piece of the detector (e.g., an SCT module or EM calorimeter block) must hold the results of the last 2.5 μs (last 100 events) stored in a pipeline in case the Level 2 trigger will request the full information to be available for any event.

1.4.3 The Level 2 trigger

As an event passes to Level 2 (Fig.1.12) the read out buffers (ROB) are filled from the detector. The input flow is 150 Gbit/ s. From the ROBs each RoI's data is sent over the

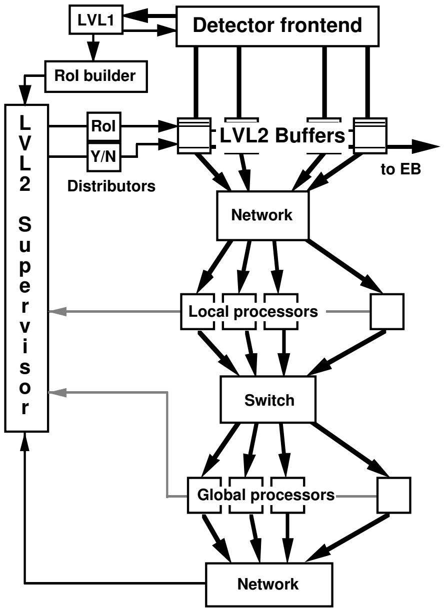

Figure 1.12: Architecture of the Level 2 trigger.

network to a set of local processors. Each of them reconstructs tracks in its RoI and passes the information generated to the global processors which collect data from all ROIs and make the final Level 2 decision. If it is negative, the event is simply flushed from the ROBs. If it is positive, the event is sent from the ROB's to the event builder (EB). The processing time of Level 2 is not fixed; on average it takes about 10 ms. The processors used here will be a farm of commercial platforms.

The data processed for each RoI by local processors at Level 2 includes:

- full ID information in the road given by the RoI,
- full granularity of EM and hadronic calorimeter information in a given RoI,
- muon system information for the RoI.

From this data we can obtain a good indication of particle type and energy that resulted in the acceptance of the event by the Level 2.

The global processors accumulate this information and match it to the Level 2 trigger menu (see Table 1.2). When a match is found, the Level 2 supervisor is notified to initiate event transfer to the EB together with the information built at the Level 2 stage. EB (or Level 2.5) collects this data and passes it to the Level 3.

1.4.4 The Level 3 trigger

The Level 3 is a farm of a multi-processor computing engines with full access to the EB and a permanent storage system. Its total input flow is 100–1000 MB/ s (100–1000 full events per second) and the average processing time is 1 s. The standard off-line detector reconstruction and track searching software is used to perform a full event reconstruction, as well as a detailed calculation of the missing transverse energy ($\not{E}_T$).

Additional selections decrease the output rate for one order of magnitude bringing us to an output flow of 10–100 MB/ s (10–100 events per second). The menus of the Level 3

Trigger	Rate [Hz]
Muon, $p_T > 40\,\mathrm{GeV}$	25
Isolated muon, $p_T > 20\,\mathrm{GeV}$	20
Two isolated muons, $p_T > 20\,\mathrm{GeV}$	5
Muon, $p_T > 20\,\mathrm{GeV} \oplus$ three jets, $p_T > 15\,\mathrm{GeV}$	50
Isolated muon, $p_T > 15\,\mathrm{GeV} \oplus$ isolated electron, $p_T > 15\,\mathrm{GeV}$	1
Two isolated muons, $p_T > 6\,\mathrm{GeV}$	10
Two isolated electrons, $p_T > 15\,\mathrm{GeV}$	8
Isolated muon, $p_T > 6\,\mathrm{GeV} \oplus$ two jets $p_T > 15\,\mathrm{GeV}$	200
Electron, $p_T > 80\,\mathrm{GeV}$	20
Isolated electron, $p_T > 20\,\mathrm{GeV}$	200
Isolated photon, $p_T > 40\,\mathrm{GeV}$	60
Two isolated photons, $p_T > 20\,\mathrm{GeV}$	5
Tau, $p_T > 150\,\mathrm{GeV}$	200
Two isolated taus, $p_T > 100\,\mathrm{GeV}$	5
Jet, $p_T > 500\,\mathrm{GeV}$	1
Two jets, $p_T > 400\,\mathrm{GeV}$	1
Two jets, $p_T > 100\,\mathrm{GeV} \oplus$ missing energy, $E_T > 100\,\mathrm{GeV}$	80
Four jets, $p_T > 100\,\mathrm{GeV}$	2
Jet, $p_T > 100\,\mathrm{GeV} \oplus$ three jets, $p_T > 15\,\mathrm{GeV}$	500
Four jets, $p_T > 50\,\mathrm{GeV}$	200
Missing energy, $E_T > 150\,\mathrm{GeV}$	30
Rate for Level 2 (without B-physics)	1 623

Table 1.2: An example of the Level 2 trigger menu for the low luminosity.

trigger are complex since they fully specify the selection criteria together with some cuts on sets of trigger objects. It also does a detailed calculation of the missing transverse energy ($\not{E}_T$).

When all is done and if the event passes the selection criteria, it's written to the permanent storage system. The trigger has finished its job.

1.4.5 Thou shalt compute

This is only half of the story. Another burden of the LHC experiments will be storing the data in an accessible format and providing computational infrastructure to carry out the physics analysis. In previous CERN experiments all the data gathered were stored, processed and eventually reprocessed at CERN. The computing environment for the LHC collaborations can be best characterized by the data production rate ($\sim 1\,\mathrm{PB/year}$) and expected number of simultaneous analyses (~ 500). CERN will not be in a position (and has already refused) to provide the infrastructure for all this ... so different strategies will have to be employed.

Fortunately LHC experiments are not the only clients for a large scale distributed computing. In past few years a new concept of meta-computing on a large scale has emerged, first from scientific communities and later also from industry (it has been named `Grid`). It is slightly unclear at present time how requirements for giga networks will be met in the future but due to a rapid expansion of the networking infrastructure one can expect them to be provided in a few coming years.

The plan of attack is to create several `regional centers` providing the CPU power for analysis and simulation, storage devices (in order of 100TB of permanent storage per year of running and approximately half of that amount of disk storage) and network bandwidth (1Mbps per active user and 100Mbps connection to CERN). For the successful management of these resources events and data must be efficiently tagged in order to provide access for analysis programs. Further description can be found in [13].

1.5 Role of electrons in the ATLAS physics programme

As with any species of detectable particle in any experiment, its role in a particular decay channel can be twofold. Firstly, it can be part of the decay products and the reconstruction efficiency and precision therefore directly influences the ability of measurements in the channel. Secondly, it can form a part of the background, the reconstruction of which can result in efficient background rejection.

In what follows an indication on the processes where electrons play a major role is given. A complete description of these processes can be found in 'ATLAS Detector and Physics performance TDR, volume II' [3].

1.5.1 Physics of the electro–weak gauge bosons

Gauge bosons and gauge boson pairs will be abundantly produced at the LHC. The large statistics and a high cms energy will allow several precision measurements to be carried out, which should improve significantly the precision achieved at present machines. Furthermore, their decay modes with electrons in the final state will be used to determine the mass scale of the EM calorimeter.

W mass

The W mass is one of the fundamental parameters of the Standard Model and is related to other parameters of the theory. Its uncertainty therefore influences other measurements by introducing errors on theoretical calculations.

The cross-section for the production of $pp \to \mathrm{W} + X;\ \mathrm{W} \to l\nu$ with $l = e, \mu$ is $\sigma(\mathrm{W}) \doteq 30\,\mathrm{nb}$ giving approximately 300 million events in one year of data taking at the low luminosity. Half of those are electron events.

The W mass measurement at hadron colliders is performed in the leptonic channels. Since the longitudinal momentum of the neutrino cannot be measured, the transverse mass m_T^{W} is used. Transverse momentum of the neutrino p_T^{ν} is obtained from the transverse momentum of the lepton p_T^{l} and that of the recoiling system u_T:

$$m_T^{\mathrm{W}} = \sqrt{2p_T^l p_T^\nu (1 - \cos\Delta\phi)}, \tag{1.1}$$

$$\vec{p}_T^{\,\nu} = -\vec{u}_T - \vec{p}_T^{\,l}, \tag{1.2}$$

where $\Delta\phi$ is the opening angle between the electron and the neutrino in the transverse plane.

The distribution of the m_T^{W} is sensitive to the W mass which can therefore be obtained by fitting experimental distribution to the Monte-Carlo samples generated with different values of m_{W}.

Gauge boson pair production

The non-abelian gauge-group structure of the electro-weak interactions predicts very specific couplings between the gauge bosons. They are referred to as Triple Gauge Couplings (TGC) and Quadruple Gauge Couplings (QGC). Any theory predicting physics beyond the SM can introduce deviations to these couplings. Precise measurements of the T/QGCs therefore provide not only a test of the SM but also a probe of a new physics in the gauge boson sector.

On ATLAS the TGCs will be observed in the leptonic decay modes of the Wγ and WZ production. In both cases electrons in the final state represent one half of the expected sample.

1.5.2 B–physics

ATLAS will perform most of the B physics at the low luminosity running while some of the studies can be pursued further also at the high luminosity operation (most of it limited by the b-layer lifetime). The mean value of the B hadron transverse momentum in observable channels is 16 GeV or more. The Level 1 trigger for B physics will be an inclusive muon trigger with $p_T \geq 6$ GeV and $|\eta| < 2.4$. At Level 2 ATLAS will further trigger on the leptonic J/Ψ decays and $B^0 \to \pi^+\pi^-$.

As the $J/\Psi \to ee$ decays will be one of the entry points into the B physics, the quality of the electron reconstruction algorithms directly influences the trigger rates. Further, it enters into the analysis of the CP violation studies where the angle β of the unitary triangle is measured via the $B_d^0 \to J/\Psi K_s^0$ channel. For B_s^0 the angle γ, the width difference $\Delta\Gamma_s$ and mixing parameter $x_s = \Delta m_s/\Gamma_s$ will be observed via $B_s^0 \to J/\Psi\phi$.

Another important use of the $J/\Psi \to ee$ decay channel, although more technical in nature, is the calibration of the EM calorimeter at low energies.

1.5.3 Heavy quarks and leptons

Top quark physics

With the predicted production cross-section of $\sigma(t\bar{t}) = 833$ pb, the LHC will produce 8 million $t\bar{t}$ pairs per year of running at the low luminosity. Accurate measurement of m_t will improve the errors on theoretical calculations as well as help to constrain the SM Higgs boson mass. In the SM top quarks decay almost exclusively as $t \to \mathrm{W}b$. In 65.5% of all the events both W bosons will decay via $\mathrm{W} \to jj$ or at least one W will decay via $\mathrm{W} \to \tau\nu$. These events are hard to extract cleanly from the large multi-jet background and are not considered in ATLAS plans for the top physics. Instead at least one W is required to decay leptonically to either an electron or a muon. An energetic lepton with a large $\not{E}_T$ provides a clean trigger signature and a large suppression of the multi-jet background.

Fourth generation quarks and leptons

The data from LEP and the Tevatron imply the existence of only three SM families with light neutrinos. Models with heavy neutrinos have been proposed and current experimental limits on the fourth generation quarks and leptons are $m_Q > 128$ GeV and $m_l > 80$ GeV. Fourth generation up-like quarks would predominantly decay via $u_4 \to \mathrm{W}b$ giving the same signature

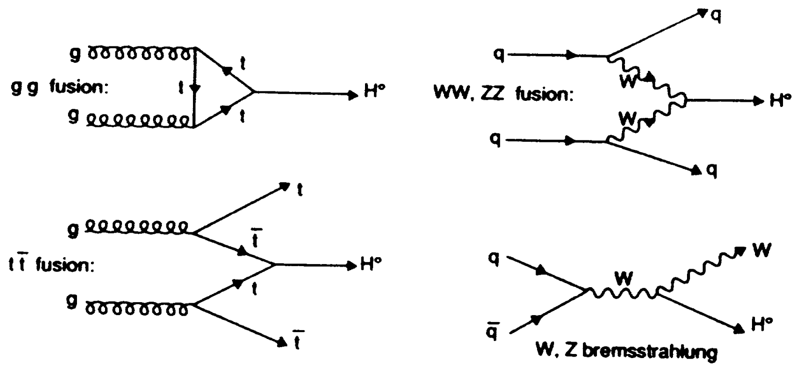

Figure 1.13: Feynmann diagrams representing major contributions to Higgs production cross–section in pp collisions.

as the top quark. Again, at least one of the Ws will be required to decay leptonically. For down-like quarks the dominant decay mode would be $d_4 \to tW$. For $pp \to d_4\bar{d}_4 \to t\bar{t}\mathrm{W}^+\mathrm{W}^- \to \mathrm{W}^+b\mathrm{W}^-\bar{b}\mathrm{W}^+\mathrm{W}^-$ at least one of the Ws is required to decay into leptons.

For heavy leptons $L \to N\mathrm{W}$ (N is the heavy neutrino) has been studied in some detail but it is not entirely clear whether this process could be separated from the background of single and pair productions of the W and Z bosons.

1.5.4 Standard Model Higgs boson searches

The experimental observation of one or several Higgs bosons will be fundamental to a better understanding of the electro-weak symmetry breaking. Its discovery and spectroscopy is one of the main physics goals of the ATLAS experiment. The detector is designed to observe it over a mass range from 80 GeV to 1 TeV in a variety of decay channels, the choice of which is given by the signal rates and signal to background ratios in various mass regions.

The main production channels of the Higgs boson at the LHC are shown in Fig.1.13. As associated Higgs production (H$t\bar{t}$, HW and HZ) is considered in all decay channels of interest and at least one lepton in final state is required by the trigger, efficient and accurate electron reconstruction is necessary for the analysis of the Higgs boson properties.

H $\to \gamma\gamma$

The decay mode H $\to \gamma\gamma$ is a rare decay mode, only observable over a limited Higgs boson mass range $80 < m_H < 150$ GeV. The biggest problem for an efficient reconstruction is resonant background from Z $\to ee$ decays which has a production cross-section roughly 25 000 times larger than the signal. To reduce this background below the 10% level, a rejection of ~ 500 per electron is required by the inner detector track reconstruction.

H $\to$ ZZ$^{(*)}$ and H $\to$ WW$^{(*)}$

H $\to$ ZZ* $\to 4l$ provides a clean signature in the Higgs boson mass range from 120 GeV to $2m_Z$. The branching ratio increases with m_H up to $m_H \sim 150$ GeV, where the H $\to$ WW channel begins to open up. Again, decay into leptons is favoured (WW$^{(*)}$ $\to l\nu l\nu$) due to the abundant jet background at the LHC. In WW$^{(*)}$ it is not possible to directly reconstruct the Higgs boson mass peak. Instead one has to rely on properties of the distribution of reconstructed transverse mass [14].

In the case of $m_H > 2m_Z$ and up to 700 GeV, $\mathrm{H} \to ZZ \to 4l$ is the most reliable channel for the discovery. For a larger m_H its width becomes the limiting factor as the observed rates drop significantly. Only in this case the decay channels with jets in final states are also considered.

The mass resolution in the decay channels including electrons is dominated by the EM calorimeter precision and therefore depends crucially on the calorimeter calibration.

Chapter 2

Beam Test of a Prototype SCT Module

As already pointed out in the previous chapter, beam tests form the backbone of the detector element evaluation process. This chapter documents one particular beam test carried out with a p^+ on n type silicon strip detector equipped with analogue read-out electronics. The true goal of the beam test was to test the analogue read-out chip SCTA128HC, as well as to perform a cross-check on the performance of the detector. The components under test and the experimental setup are described. Then the results of the analysis of the data collected in the beam test are presented.

2.1 Silicon strip detectors in ATLAS

The ATLAS SCT aims to operate reliably, according to the performance specifications, over a 10 year period of the high luminosity LHC operation. As the detectors will be exposed to fluencies 10-20 times higher than in past applications, a substantial development effort has been made to ensure adequate radiation resistance in the design. Additionally, the SCT's active area is $\sim 63\,\mathrm{m}^2$, more than 50 times that of any existing silicon vertex detector. It extends over 1 m in diameter and 6 m in length, again posing challenges to the detector services, cooling and precision mechanics techniques.

As the SCT is sub-detector of the ID, the physics requirements for the SCT can be projected from those for the ID by taking into account the pixel detector and TRT capabilities. The main points that can be extracted are:

- The required reconstruction efficiency requirement for isolated leptons of $p_T > 5\,\mathrm{GeV}$ to have an efficiency of 95% and a fake track rate $< 1\%$, imposes the need to reconstruct helices in 3D, especially since the TRT provides no r/z measurement. Thus we need at least six tracking layers providing full space point information, and a detector efficiency above 95% over the whole lifetime of the experiment to ensure good tracking and trigger efficiency. The upper limit on fake rate also determines the noise occupancy of the detector.

- The requirement that $\delta p_T/p_T < 0.3$ at $p_T = 500\,\mathrm{GeV}$ with a beam constraint imposes an r-φ measurement with a resolution of $\sim 20\,\mu\mathrm{m}$ at the SCT radius. The requirement to separate multiple vertices within a bunch crossing imposes an accuracy on the z

measurement of $< 1\,\mathrm{mm}$ in the SCT. For K^0 reconstruction this resolution should be even better.

- The requirement of a two–track resolution to be $< 200\,\mu\mathrm{m}$ at $r = 30\,\mathrm{cm}$, in order to minimize track losses in b-jets, also constrains the r-φ pitch.

- To minimise material effects preceding the calorimeter, the SCT and pixel layers must have a minimal radiation length. The design aim was to reach $< 0.2X_0$ preceding the TRT over a significant η range.

It would be a duplication of effort to go into all details of detector type and electronics selection. An overview of the studies performed can be found in [7]:Ch:11.

2.1.1 Detectors

A short overview of the current baseline solution is presented. It has already been changed with respect to the one presented in the TDR [5], namely the type of the detector has been changed from n^+ on n to p^+ on n, mainly to decrease cost of production.

The baseline detectors are of the p^+ on n variety, capacitively-coupled with polysilicon biasing. The detector thickness is $260\pm10\,\mu\mathrm{m}$ (inner barrel and inner wheel) and $285\pm15\,\mu\mathrm{m}$ otherwise. The barrel modules are 64 mm long and 63.6 mm wide. Forward modules have tapered strips and five slightly different designs are needed to optimally cover the desired space (variations in size with respect to the barrel module remain $< 20\%$). All detectors have a pitch of $80\,\mu\mathrm{m}$ (this is also the central value for the wedge detectors) and 768 read-out strips.

Modules are composed out of two detectors joined one after another, to give 128 mm in length. While this introduces some problems with alignment, the cost consideration has the final word (the detectors are optimised for production from 4" wafers). As each SCT layer must provide a space point per, two half-modules are glued together back-to-back with a 40mrad stereo angle. The complete module is installed with a 10° tilt angle for hermeticity and to compensate for the Lorentz angle.

The operational temperature of the detectors will be $< -7^\circ\,\mathrm{C}$. A low operating temperature is required to reduce the noise due to leakage current and minimise effects of radiation damage.

2.1.2 Read-out electronics

The SCT read-out electronics is responsible for supplying strip hit information to the second level trigger and the data acquisition system. The low signal yields of the silicon micro-strip detectors and the 25 ns shaping time necessitate that the front-end electronics be mounted directly at the silicon strip electrodes to ensure the low noise operation required. This dictates that the electronics must be of low mass and low power consumption. Of course, it must also survive the radiation environment at the LHC. The performance of the detectors combined with that of the electronics must meet the goals of the SCT specifications. A detailed discussion can be found in [7]:Sec:11.4. Here there are only the parameters that are directly connected with the beam test.

The efficiency of the read-out system must be above 99%. The combined efficiency of detector plus electronics must be 97% in order to meet the six space point requirement for the ID. **The noise** should not be larger than $1500e^-$. For silicon strip detectors with read-out electronics that has a short shaping time, the strip capacitance is the dominant source of noise. A typical equivalent noise charge of 600-800e^- (before irradiation) is a typical value for the detector choices considered by ATLAS. The upper limit on **noise occupancy** is set to 5×10^{-4}. This should be compared to an average occupancy of 0.6% during high luminosity operation and a 2-3% occupancy in b-jets.

With respect to the level 1 trigger additional requirements are imposed. The electronics should store the data for the maximum latency of the level 1 trigger (2.5 μs plus 0.5 μs for signal dispatching which corresponds to 120 bunch crossings). It should be able to operate with the average level 1 rate of 100 kHz. As this includes the read-out time, eight more memory locations are needed in the buffer to store selected events before they can be read-out.

While binary read-out is the present baseline, both analogue and binary versions of the read-out electronics are, being pursued. Various chip architectures have been designed and tested at different levels. Only few of them have made it to the final trial of being placed in the test beam, as part of a full prototype module.

2.1.3 SCTA128HC read-out chip

A detailed description of the SCTA128HC read-out chip and its performance has been published [15]. Here only a brief overview and a few details that particularly affect the measurements are presented.

The chip was designed to provide support for 128 read-out strips with capacitance from 0 to 25pF. Besides the control logic, the main components of the chip are the front-end amplifiers, the analogue data pipeline and the output multiplexer. The front-end block consists of a bipolar amplifier followed by a shaper providing a semi-Gaussian shaping ($CR-RC^2$) with a peaking time of 25 ns. The peak values are sampled at 40 MHz and stored in the 128-cell deep analogue buffer. Another 8-cell circular buffer is provided to store pointers to cells that were marked by the trigger. The time offset of the trigger signal can be set in internal clock units to allow for different trigger latencies. Upon receiving a trigger signal the data is sent out via a fast 40 MHz analogue multiplexer, which can also operate at a reduced rate of 20, 10 and 5 MHz.

The gain is linear for charges of up to 12fC (1fC $\sim 6240e^-$) with an average gain of 25.5 mV/ fC and a 2% error. As a reference point note that a minimum ionizing particle produces a charge of 3.5fC (most probable value, $\sim 21\,800e^-$) when passing through 280 μm of silicon. The pedestal variation from channel to channel is typically $\sim$ 25 mV, but this doesn't influence the measurements. More important is the variation along the pipeline (for a single channel), which has a rms variation of 1.2 mV or $300e^-$.

2.2 Experimental setup

The beam test was performed with 200 GeVpions at CERN in the X5 west area of the SPS (for a more detailed description of the beam infrastructure see [16]). The module was installed in the beam telescope of the RD42 group. Their readout system was modified to provide a common data output.

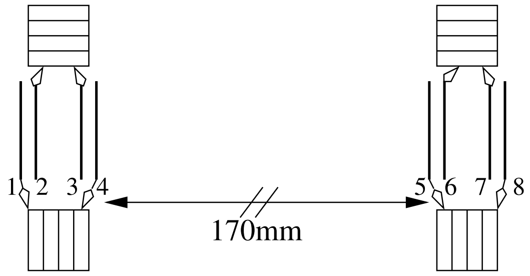

Figure 2.1: A schematic view of the beam telescope. Dashed boxes show orientations of telesope planes.

Plane ID	position	tilt	pitch	interpolation strips
1	$-95\,$mm	$0°$	$50\,\mu$m	2
2	$-93\,$mm	$90°$	$50\,\mu$m	2
3	$-87\,$mm	$90°$	$50\,\mu$m	2
4	$-85\,$mm	$0°$	$50\,\mu$m	2
5	$85\,$mm	$0°$	$50\,\mu$m	1
6	$87\,$mm	$90°$	$50\,\mu$m	1
7	$93\,$mm	$90°$	$50\,\mu$m	1
8	$95\,$mm	$0°$	$50\,\mu$m	1

Table 2.1: Beam telescope specifications

2.2.1 Beam telescope

The beam telescope used was composed of 8 single-sided silicon strip detectors installed over a distance of 19 cm. The dimensions of the detectors were $12.8\,\text{mm} \times 12.8\,\text{mm} \times 300\,\mu\text{m}$ and each had 256 read-out strips connected to the VIKING read-out hybrid. All telescope modules had interpolation strips (one half of the detectors had two and the other half a single one) which enable capacitive sharing between the read-out strips. Combined with a high signal to noise ratio of these devices this enables one to reliably reconstruct the intersection position using the *eta* method (discussed in Sec:2.4.2). A schematic view of the beam telescope is shown in Fig:2.1 and Tab:2.1 gives the important data. The typical cluster sizes and their signal to noise ratios are presented in Fig:2.2.

For our purposes the most important parameter of the telescope is its resolution at the point where our device under test is placed in the beam. The first step is to understand the intrinsic resolutions of the telescope modules. As the number of interpolation strips changes the module's resolution, one of each kind was excluded from the track fit (one at a time) and its resolution 'measured'. The residual distributions are shown in Fig:2.3. The obtained resolutions are $\sigma_{1-4} = 3.4\,\mu$m for the detectors with two interpolation strips and $\sigma_{5-8} = 7.8\,\mu$m for the detectors with a single one.

These numbers were used as the basis for a Monte-Carlo simulation which was tuned to give the same residuals on the planes 4 and 5 when their faked measurements were not used in the fit. Details of the procedure are given in App:A. In the same way the intrinsic spatial

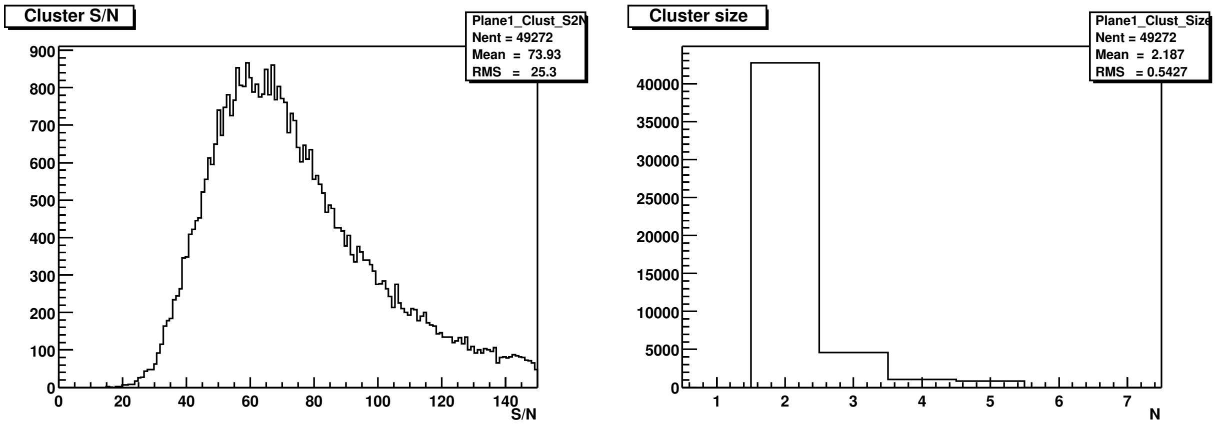

Figure 2.2: Left: the signal to noise ratio for the reconstructed clusters. Right: distribution of a cluster size.

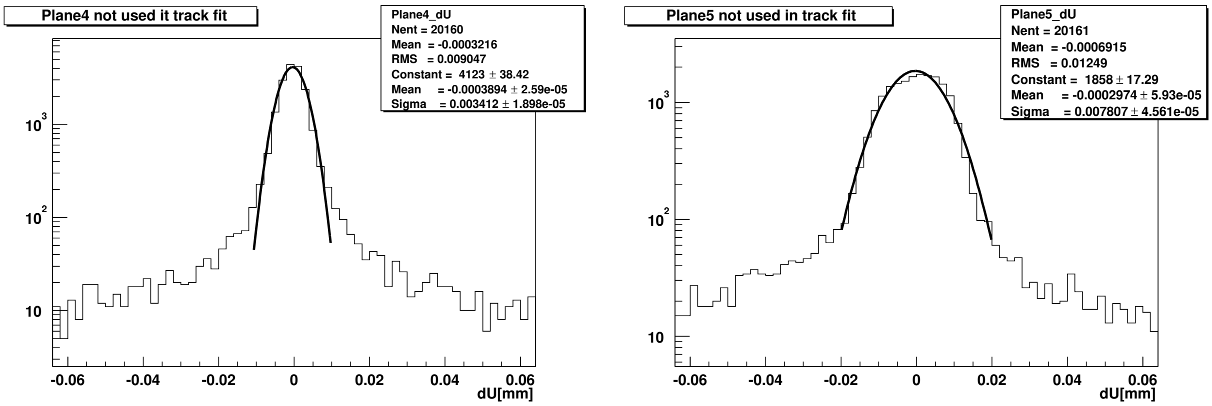

Figure 2.3: The residual distributions of the fourth and fifth telescope plane. For both plots only the plane in question was not used in the track fitting.

resolution of the tracker at plane $z = 0$ was 'measured'. See Fig:2.4. The standard deviation of this residual distribution is the precision of the tracker and *all subsequent resolutions are effectively convoluted with a Gaussian distribution of $\sigma = 2.5\,\mu$m.*

2.2.2 The device under test

The module under test was a standard barrel half-module composed of two p^+ on n AC coupled detectors with $80\,\mu$m pitch and thickness $280\,\mu$m. Their strip width was $25\,\mu$m and strip depth $4\,\mu$m. The two detectors were interconnected in the regions of the second and the fourth chip (strips 129-256 and 385-512) therefore enabling measurements on a 6 cm and 12 cm strip length simultaneously. Four SCTA128HC chips were connected to the strip range 1-512, but in fact only strips in the region 330-460 received hits from the beam. The detectors were operating at room temperature.

The baseline detector is optimised for a binary readout. For analogue readout the pitch would be larger, around $110\,\mu$m. The interpolation strips would also be added to the mask

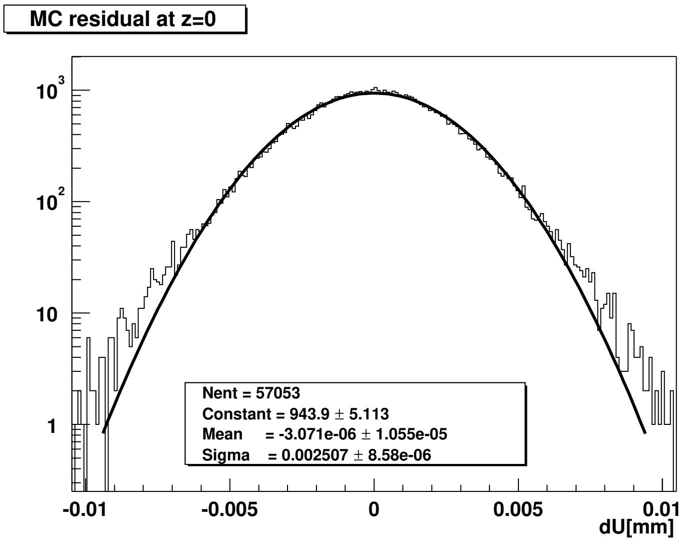

Figure 2.4: The intrinsic tracker residuals at $z = 0$.

of the detector to induce capacitive charge sharing between the read-out strips. Again it must be stressed that the main purpose of this beam test was to assess the quality of the analogue read-out system as well as to make a detailed assessment of detector's response under varying angles of incidence of incoming particles which enables a correct emulation of cluster sizes, noise and resolutions in the large scale simulations of the ATLAS detector.

2.3 Extraction of clusters from raw data

Information about the charge collected on a single strip is presented as a number of ADC counts in the channel representing the relevant strip. Alas, not all the voltage read off the strip electronics is due to amplification of the charge produced in the detector by the passing particle. The silicon detectors are diodes, under reverse bias, which means that in each measurement we necessarily pick up a contribution from the dark current. This contributes to the noise and pedestal. Secondly, internal structure of a read-out electronics (preamplifiers and ground level determination) brings in additional noise, pedestal and common mode pedestal variations. Common mode variations are reasonably defined for a region (or a zone) of a detector which is read-off by the same electronics (in our case: by the same chip).

All things considered, raw signal value on strip i for event n can be expressed as:

$$R_i^n = S_i^n + P_i^n + N_i^n + C_Z^n, \tag{2.1}$$

where R_i^n is the raw value, S_i^n signal, P_i^n pedestal, N_i^n noise and C_Z^n common mode shift for zone Z of which strip i is a member.

It is matter of convention (or even more of taste) how we define pedestal and noise. I choose to add the mean noise value into the pedestal so that noise represents the rms of pedestal variations around its mean value.

Of course the true values of S_i^n, P_i^n, N_i^n and C_Z^n are not known (and to be honest, R_i^n is only known up to the precision of AD conversion). We approximate them by using information from previous events. [1]

2.3.1 Pedestal, noise and common mode determination

The problem is that pedestal, noise and common mode variations are not constant in time. The estimator for pedestal and noise is calculated as a running average over the last $\mathcal{N}_p$ and $\mathcal{N}_n$ events respectively. Common mode variations are calculated on a per event basis.

But in the beginning of the run we know nothing about the pedestal nor noise. To get the estimators for the first event we therefore histogram the raw signals for the first $\mathcal{N}_p$ or $\mathcal{N}_n$ (whichever is greater) events on a per strip basis. Then we fit those distributions with a Gaussian curve and assign the mean value to $\widetilde{P_i^1}$ and the spread to $\widetilde{N_i^1}$.

Now assume that we know the estimators for event n and that we want to calculate the relevant quantities. A first approximation for the signal ($\dot{S_i^n}$) is just the pedestal estimator subtracted from the raw value:

$$\dot{S_i^n} = R_i^n - \widetilde{P_i^n}. \tag{2.2}$$

Next we select only strips with $\dot{S_i^n} < 3\widetilde{N_i^n}$ for common mode determination. Let $\mathcal{A}_Z$ represent a set of such indices for zone Z and calculate:

$$C_Z^n = \frac{\sum_{j\in\mathcal{A}_Z} \dot{S_j^n}}{|\mathcal{A}_Z|}. \tag{2.3}$$

Using this we come to a second and final approximation ($\ddot{S_i^n}$) for the signal:

$$\ddot{S_i^n} = \dot{S_i^n} - C_Z^n \qquad i \in \mathcal{M}_Z, \tag{2.4}$$

where $\mathcal{M}_Z$ is a set of all strips in zone Z. This is the value used for the cluster search and determination of the hit position. The only thing still needed is 'true' noise and pedestal for the calculation of estimators for the next event:

$$\left.\begin{array}{l} P_i^n = \widetilde{P_i^n} + \ddot{S_i^n} = R_i^n - C_Z^n \\ N_i^n = \ddot{S_i^n} \end{array}\right\} \quad i \in \mathcal{A}_Z \quad \text{for both eqs.} \tag{2.5}$$

Note that common mode correction is not followed by the pedestal estimator but is calculated on a per event basis. Taking into account also the common mode correction would require adding C_Z^n to P_i^n (which is equivalent to using R_i^n for P_i^n).

Now we can calculate the pedestal and noise estimators for the next event. Instead of keeping the old values and recalculating the average it is more practical to use a recursive digital filter (IIR).

$$\widetilde{P_i^{n+1}} = pP_i^n + (1-p)\widetilde{P_i^n} \qquad p = \frac{1}{\mathcal{N}_p} \tag{2.6}$$

$$\widetilde{N_i^{n+1}} = \sqrt{n\ddot{S_i^n}^2 + (1-n)\widetilde{N_i^n}^2} \qquad n = \frac{1}{\mathcal{N}_n} \tag{2.7}$$

Again only values for strips which are members of $\mathcal{A}_Z$ are updated. For other strips (which presumably collected some charge in this event) the estimators are kept unchanged for the next event.

[1] A tilde sign above quantities is used to mark them as estimators. Plain symbols are used for the quantities obtained for a particular event.

2.3.2 Clustering

After the signal is corrected for each strip, following the procedure as in Sec:2.3.1, a search is made for clusters of strips exceeding a predetermined signal-to-noise ratio. The definitions for quantities used in the cluster quality determination will be explained here and some practical problems will be addressed.

In the previous subsection we have described how signal S_i and noise N_i on strip i are obtained from the raw data. The event superscript n has been dropped, as it was only relevant for pedestal and noise updating. We will be mostly concerned about the signal to noise ratio of a strip i and of a cluster C of adjacent strips:

$$Q_i = \frac{S_i}{N_i} \tag{2.8}$$

$$Q_C = \sum_{i \in C} \frac{S_i}{N_i}. \tag{2.9}$$

The definition of Q_C is not entirely correct from a statistical point of view but this is the standard definition used in the literature.

A cluster is a contiguous set of strips that satisfies the following criteria:

1. The signal to noise ratio off all strips must be above the *clustering cut* Q^c: $Q_i \geq Q^c$. A typical value of Q^c is 3.

2. The strip with the highest signal to noise ratio (seed strip) is required to have the S/N ratio greater than the *seed cut* Q^s: $Q_{\text{seed}} \geq Q^s$. In our analysis the values of Q^s were in the range from 4 to 5.

3. The size of the cluster $\mathcal{N}_C$ must be within limits $\mathcal{N}^{min} \leq \mathcal{N}_C \leq \mathcal{N}^{max}$. If it is too small, the cluster is discarded. If it is too big, we start cutting on both sides, throwing out strips with worst Q_i until we hit the limit $\mathcal{N}^{max}$. The rationale behind this cut is that at a given angle of incidence the cluster size will be within well defined limits.

4. The sum of the signal collected in the cluster $S_C = \sum_{i \in C} S_i$ must lie within the range $S^{min} \leq S_C \leq S^{max}$. This prevents us from accepting clusters that are entirely due to noise or to read-out errors with a high ADC value.

The last step requirement is usually replaced by a cut on Q_C. In our case the presented method showed better results.

2.3.3 TDC information

In the ATLAS experiment (and at the LHC in general) bunch crossings will occur every 25 ns and the internal clock of the read-out chips will be set to make the measurement at the peak of signal collection. The experimental setup in the beam test did not conform to these requirements which means that events were recorded at random times, not only at the peak of signal collection. To correct for that, additional information was recorded with each event: the time difference from the beginning of the chip's internal clock cycle to the event trigger time with 125 ps resolution. We refer to this value by the name of the electronic circuit providing us with the measurement: *time to digit converter* (TDC). In the data-analysis, we therefore make a calibration run at the beginning to estimate appropriate cuts on the TDC value. See Fig:2.5 for example of the obtained $S_C(t_{\mathrm{TDC}})$ distribution and the cuts chosen. In a limited range this also shows the signal evolution in time.

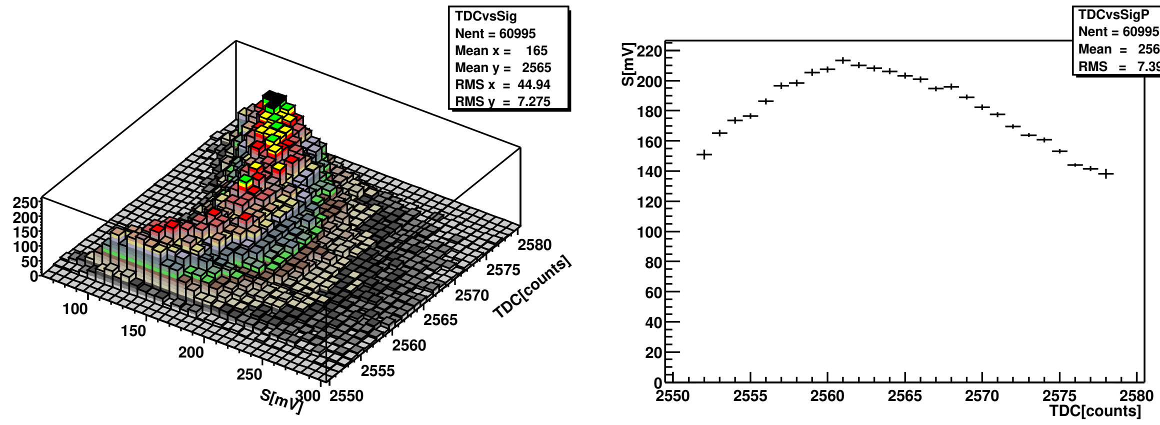

Figure 2.5: Two views of the $S_C(t_{\mathrm{TDC}})$ distribution. The selected cuts were $2559 \leq t_{\mathrm{TDC}} \leq 2566$.

2.4 Determination of cluster position

Having obtained a cluster one still has to determine the track intersection point. There are several possible methods and the relevant ones are presented in this section. Since our detector was being tested at different angles, the cluster size varied accordingly and different methods were used to handle each case. For an overview and a study of the spatial resolution of different position finding algorithms using Monte-Carlo techniques, see [17].

It is time to define a few abbreviations for strip indexes. Let s stand for the seed strip, l for the strip with the lowest index in the cluster and h for the strip with the highest one. Let P denote the pitch (strip to strip distance) of the detector.

In a way the position of the seed strip u_s is the first approximation of the intersection position. Each of the following methods will provide a correction δ_u to this value.

2.4.1 *Centre of gravity* method

This position correction is obtained by weighting the strip position by its signal and calculating the centre of gravity of the cluster.

$$\delta_u^{\mathrm{COG}} = \sum_{l \leq i \leq h} \frac{S_i}{S_C}(i-s)P \tag{2.10}$$

This is the simplest evaluation one can do and can be used as a reference point for evaluating the other methods.

2.4.2 *Eta* method

The eta method is based on the assumption of a 'flat' position distribution for incoming particles along the u coordinate. It only works for two–strip clusters under the assumption that in all cases with a given track intersection position between two strips, the charge will get distributed in the same way (but not linearly ... this reduces to the `CoG` method). One 'measures' the distribution of:

$$\eta = \frac{S_L}{S_L + S_R}, \tag{2.11}$$

where L is the 'left' or lower strip index and $R = L + 1$, that is the index of the next neighbouring strip. It can also be used for larger clusters, but then you need to take the seed strip and its neighbour with the highest signal and assign the L, R indexes correctly. This method was used for the telescope detectors where interpolation strips provide capacitive coupling to neighbouring read-out strips.

One then histograms this distribution ($dP/d\eta$) and transforms it to a cumulative one ($\mathcal{P}(\eta) = \int_0^\eta \frac{dP}{d\eta} d\eta$). Here the importance of the flat track distribution comes into the game: if $dP/du =$ const, then $P(\eta)$ gives a position correction in `pitch` units. If $\mathcal{P}(\eta) > 0.5$ this signals that strip R is in fact the seed and that the correction to the seed position should have a negative sign:

$$\delta_u^{\text{eta}} = P \cdot \begin{cases} \mathcal{P}(\eta) & \mathcal{P}(\eta) \leq 0.5 \\ \mathcal{P}(\eta) - 1 & \mathcal{P}(\eta) > 0.5 \end{cases} \tag{2.12}$$

2.4.3 ***Head–tail*** methods

For large clusters such as one obtains with inclined detectors the `eta` method is useless. In cases of a low signal to noise ratio, the `CoG` method is error prone due to noise fluctuations. This leads to the idea of using only strips at cluster boundaries for position correction (called head and tail) and to discard the information from the inner strips altogether. In a way it is a mixture of both previously discussed methods.

The first approximation is called the `digital head-tail` method, which discards the signal information and uses cluster's boundaries only:

$$\delta_u^{\text{DHT}} = \frac{(l - s) + (h - s)}{2} P. \tag{2.13}$$

To further improve it, we must know the average signal S_θ expected on a strip within the cluster. Let S_0^{MP} denote the *most probable* signal collected for a perpendicular track, W its width and P (pitch) its inter-strip distance (Fig:2.6). For an inclined track with incident angle θ its total signal is proportional to the length of track's path through the detector $L = W/\cos\theta$. On the other hand the length of a track under an inner strip equals $P/\sin\theta$. The term inner strip is only relevant when the incident angle of the track is larger than $\tan\theta \geq P/W$ ($\theta \geq 16°$ in our case), i.e., when the track is traversing more than one strip. The expected signal on a strip can then be written:

$$S_\theta = S_0^{\text{MP}} \cdot \begin{cases} \frac{1}{\cos\theta} & \tan\theta < P/W \\ \frac{P}{W\sin\theta} & \tan\theta \geq P/W \end{cases} \tag{2.14}$$

With this we can define the `analogue head-tail` method:

$$\delta_u^{\text{AHT}} = \Big(\frac{(l - s) + (h - s)}{2} + \frac{S_h - S_l}{2S_\theta}\Big) P. \tag{2.15}$$

Therefore we additionally correct the position by the ratio of the measured head/tail signal to the expected one.

Another option, in a way a more general and honest, is to estimate S_θ from the signal collected on the inner strips:

$$\widetilde{S}_\theta = \sum_{l<i<h} \frac{S_i}{h-l-1}. \tag{2.16}$$

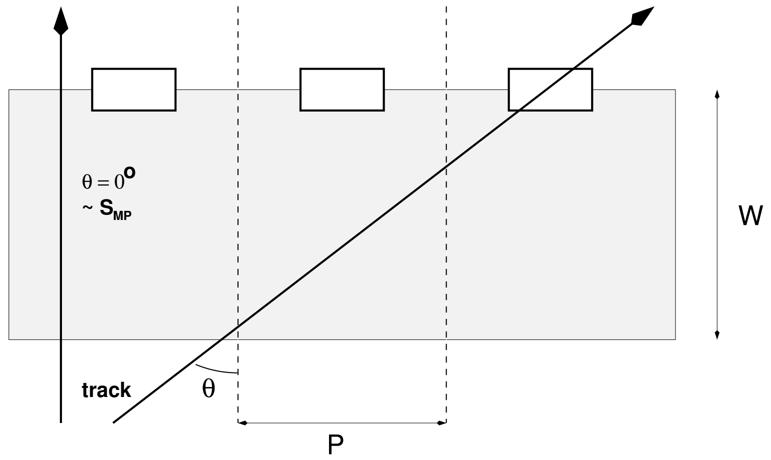

Figure 2.6: Schematic view of track passing through the detector.

2.5 Cluster analysis

Now we are in position to make an educated attack on the data collected in the beam test. A total of six data-sets were analysed, one for each of six different inclinations ranging from 0° to 50° in steps of 10°. For each of those sets we have to further differentiate the read-out channels connected to the 6 cm and 12 cm detectors. All data were collected with the same reverse bias voltage $U = 190\,\mathrm{V}$. The detectors were fully depleted, as the depletion voltage of the detector was measured to be $U_{FD} = 60V$.

For the detector under test, a special alignment procedure was adopted using simplex minimization crossed with the Metropolis algorithm. See Sec:1.3 for details.

2.5.1 Efficiency versus noise occupancy

The first thing one asks is how efficient is the detector. Here there is a bit of a problem: any cluster finding algorithm is subjected to certain cuts and by lowering our requirements for cluster quality one can easily make a detector 100% efficient. But this is not exactly the point here because by lowering the cuts one finds additional clusters that are entirely due to noise. This is quantified by `noise occupancy` which is the number of strips introduced by noise per number of all strips per event. The problem is that one wants the best efficiency with as few noise clusters as possible and that one generally can't have both. Finding out where we stand with our detector in this respect is the goal of this section.

The efficiency and occupancy were histogrammed versus a Q^c cut ranging from 0.25 to 30. The seed cut was set equal to the cluster cut so that no additional selection was

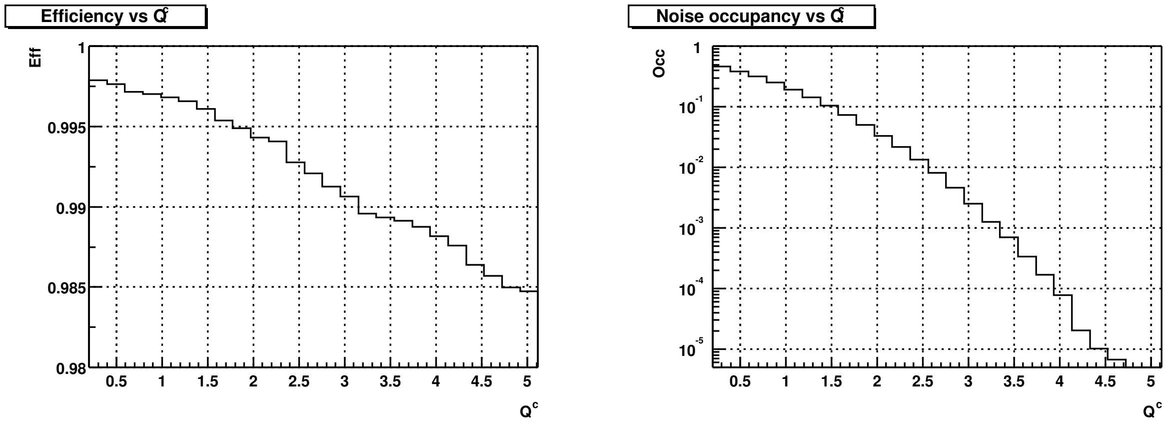

Figure 2.7: Example of efficiency and noise occupancy versus Q^c cut ($\theta = 0°$, 6cm strips).

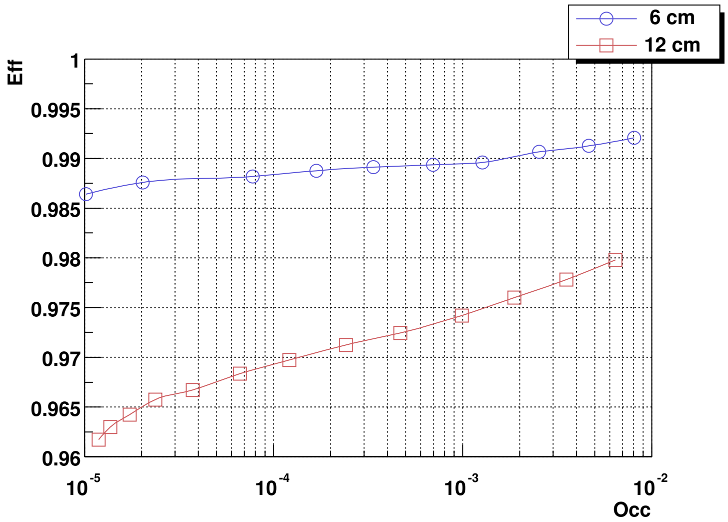

Figure 2.8: Efficiency versus noise occupancy for 6 and 12 cm strips ($\theta = 0°$).

requested. For a cluster to be considered efficient, the track intersection had to lie within the boundaries of the cluster. The minimum signal cut was also imposed on the matching cluster ($S^{min} = 50\,\mathrm{mV}$ for 6 cm strips and $S^{min} = 70\,\mathrm{mV}$ for 12 cm ones) so as to assure that the cluster was not due to a noise. See Fig:2.7 for the two plots. Then these two were combined to give the `efficiency versus occupancy` graph which is the standard representation. Fig:2.8 shows the results.

Now is the time to define the clustering cuts that will be used in the later analysis. The clustering cut Q^c and the seed cut Q^s are set to 3 and 4 respectively. This ensures that the noise occupancy stays below 5×10^{-4} (requirement for the ATLAS SCT) while still allowing the cluster to contain the boundary strips which receive only small quantities of charge. The minimal signal cut was $S^{min} = 50\,\mathrm{mV}$ for the 6 cm detectors and $S^{min} = 50\,\mathrm{mV}$ for the 12 cm detector. For the maximal signal cut the value of $S^{max} = 1000\,\mathrm{mV}$ proved to be adequate as there were some read-out errors which resulted in a signal readings above 1200 mV, while the highest signals collected at $\vartheta = 50°$ were not larger than 800 mV. $\mathcal{N}^{min}$ and $\mathcal{N}^{max}$ vary with the inclination of the detector so as to cover all expected cases (with a reasonable tolerance on each side).

2.5.2 Resolution

The beam telescope enables one to predict the track crossing position with a resolution of 2.5 μm. By comparing the measurements taken by the test detector (and using one of the position correction algorithms) to the predicted value one obtains its resolution. The distances are always calculated in the detector's plane. For $\theta = 0°, 10°$ there are mainly one–strip clusters present. For those only the `centre of gravity` method was used (which is equivalent to taking the strip's centre). For clusters of a larger size, the `eta` and `analogue head-tail` methods were also used.

Fig:2.9 compares the residual distributions for one strip clusters (where `centre of gravity` method was used) and for two strip clusters (`eta` method). The interesting thing to notice is that the single strip cluster resolution is improved at 10° as two-strip clusters are produced by the tracks close to the strip boundary.

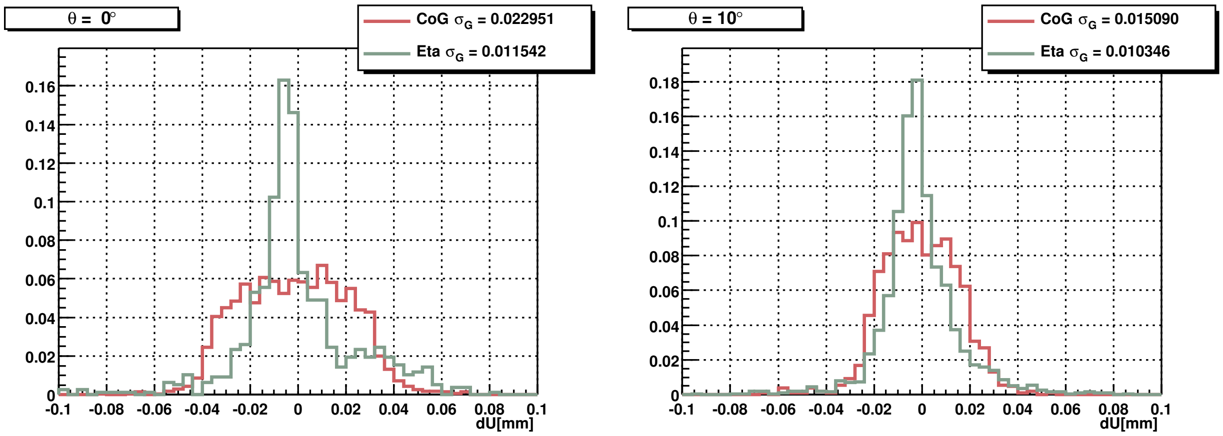

Figure 2.9: Comparison of residual distributions for one (red) and two-strip (green) clusters. Shown for 6 cm detector at $\theta = 0°$ (left), 10° (right).

Figure 2.10 shows the resolutions obtained with different methods as a function of the inclination of the detector. Single strip clusters have been omitted in this analysis. As expected, the `eta` method gives the best results for small inclinations (0° and 10°). The `analogue head-tail` method provides only a slight improvement compared to the `centre of gravity` method. For 6 cm and 12 cm detectors the best resolution can be obtained at 10°. For higher inclinations the resolutions degrade as the signal per strip gets smaller and its signal to noise ratio is reduced. This can also be observed by comparing the resolutions of the 6 cm detectors to those of the 12 cm ones for which the noise per strip is about 1.4 times larger.

2.5.3 Cluster size, signal and signal to noise

A particle passing through the detector creates electron–hole pairs in the semiconductor. Drifting charge then influences the voltage applied to the read out strips which are coupled capacitively to the electronics. Ideally one would expect that all the charge produced in the region covered by a single strip (that is the strip centre $\pm\frac{P}{2}$) gives rise to a signal on this strip only. But the finite collection time and charge diffusion cause the charge produced close to the two strip boundary to be distributed among both strips. Cluster size is the first measure of charge sharing, a detailed study of which is the subject of the next section.

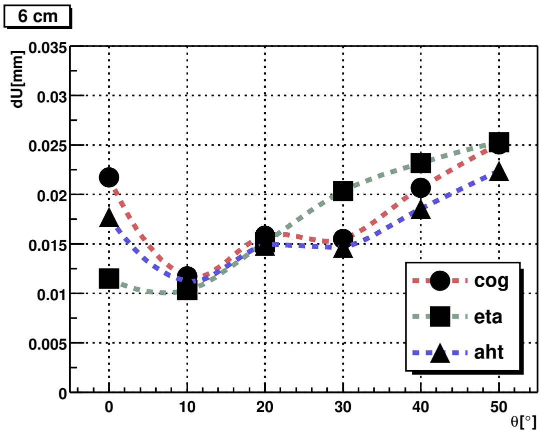

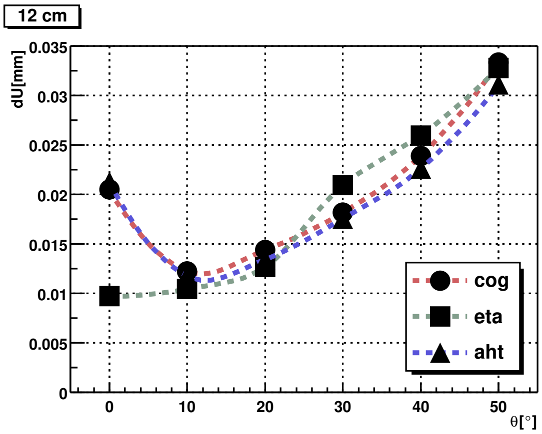

Figure 2.10: Sigma of Gaussian fit to residual distribution versus angle for different position correction methods. Clusters with at least two strips were used.

The cluster size is dependent on the inclination of the detector (see Fig:2.6 as a guideline). To estimate the cluster size, consider the projected track length on the detector plane in a direction perpendicular to the strips:

$$a = W \tan\theta. \tag{2.17}$$

Then there are two effects: the first one is rather artificial as it is introduced by the Q^c clustering cut. It truncates the effective length of tracks that cover a short distance under the region of the bordering strips. Effectively this reduces the thickness of the active region. The second effect is caused by charge diffusion which increases the cluster size and is independent of the inclination angle. All things considered, the average expected cluster size is:

$$\mathcal{N}_c = 1 + \frac{(W - w_c)\tan\theta + d}{P}, \tag{2.18}$$

where w_c is the effective width of the layer suppressed by the Q^c cut and d is the average charge diffusion length perpendicular to the strips. The dependence of the cluster size as a function of the inclination angle was then fitted with this function. The results obtained for the test detector are given in Fig:2.11. The loss of active area is larger for 12 cm detector as expected with the higher noise. The diffusion lengths are consistent.

Closely connected to cluster size is the distribution of the total signal collected in a cluster. Theoretically, for thin absorbers, given certain distance through the sensitive material, one finds that the signal follows the Landau distribution (see [18]):.

$$\Phi(\lambda) = \frac{1}{\pi}\int_0^\infty e^{s\log s - \lambda s}\sin \pi s \, ds, \tag{2.19}$$

$$\lambda = \frac{S^c - S^{\mathrm{MP}}}{\sigma_{\mathrm{L}}}. \tag{2.20}$$

The Landau distribution has two parameters: S^{MP} is the most probable signal (peak position) and σ_{L} is a width of its Gaussian core. Both increase with the thickness of the material. In practice, this distribution is effectively convoluted with a Gaussian of σ_{G}. Effectively this is the average signal fluctuation in a cluster due to a noise. Cluster signal S_C was histogrammed

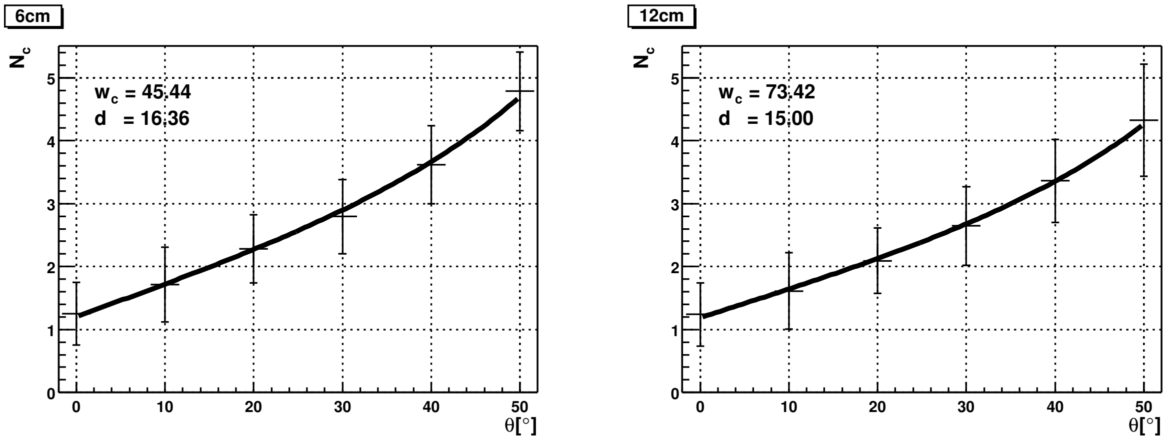

Figure 2.11: The cluster size for 6 cm (left) and 12 cm (right) detectors. The error bars show rms's of the distributions. The results of a fit to Eq:2.18 are superimposed on the plots.

for different angles and detector lengths and fitted to a convolution of Landau and Gaussian distributions. Figures 2.14 and 2.15 present the results (both figures can be found at the end of this chapter). As inclination increases a surplus of events in the high-signal tails of the distributions can be observed. These are caused by the δ-electrons.

For the most probable cluster signal, the relevant quantity is the track length through the sensitive material:

$$l = \frac{W}{\cos\theta}, \quad S_C^{\mathrm{MP}} \propto l. \tag{2.21}$$

To get a better estimation of the most probable signal per particle per distance travelled, the S^{MP} obtained from the Landau fits was plotted versus the angle and the points fitted with $S_0^{\mathrm{MP}}/\cos\theta$. Fig:2.12 shows the dependence of the most probable cluster signal $S^C(\vartheta)$ and results of the fit. Since 21 000 electron-hole pairs is the most probable yield for a minimum ionizing particle in 280 μm thick silicon layer and the signal amplification is linear, we can calculate the calibration constant to be 7.5 mV per 1 000 electron-hole pairs.

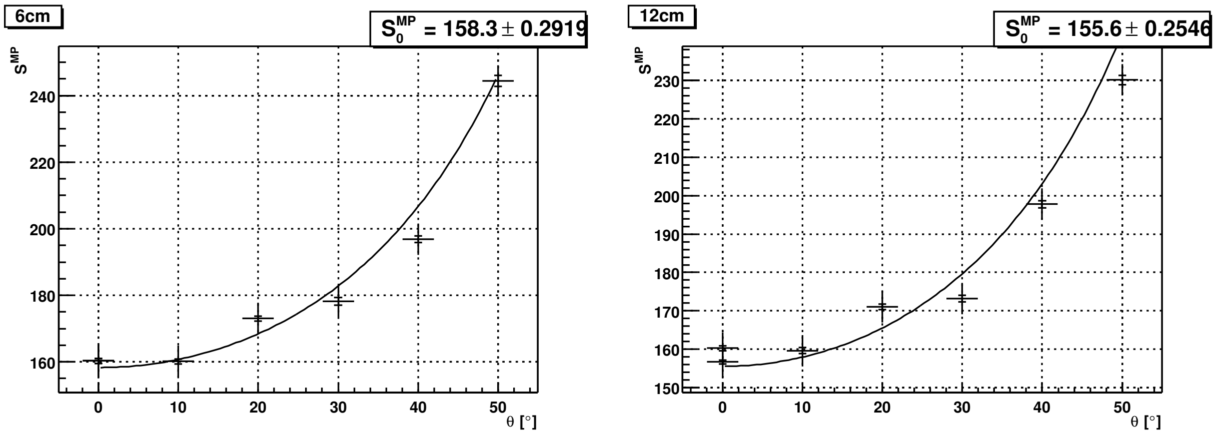

Figure 2.12: The most probable signal S^{MP} as a function of θ for 6 cm and 12 cm detectors. For both plots the fits to eq:2.21 are superimposed.

Another measure of a cluster's quality is its signal to noise ratio, defined in Eq:2.9. Fig:2.13 gives its dependence on the inclination of the detector. The average value of Q_C for the 6 cm detector is, on average, 1.3 times larger than that for the 12 cm one. By assuming that the noise of the electronics is constant and that the capacitive noise of the 12 cm detector is twice that of the 6 cm one, relative contributions from the electronics and detectors to the total noise can be estimated. The average number of electron-hole pairs produced (30 200) is also needed to extract the absolute values. The noise of the electronics 'measured' this way corresponds to the equivalent noise charge of $ENC_e \sim 730$ electron-hole pairs and that for the 6 cm detector to $ENC_{6\,\mathrm{cm}} \sim 390e^-$.

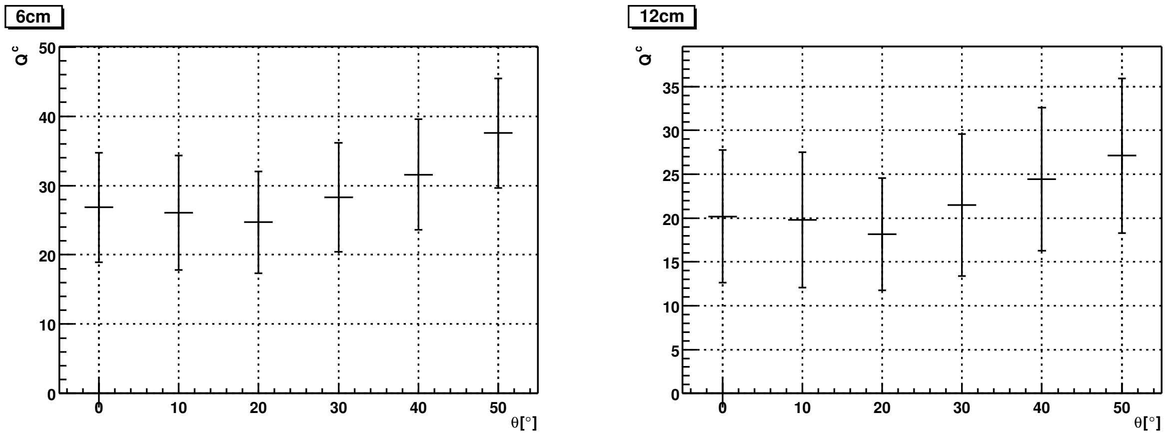

Figure 2.13: The mean value of cluster's signal to noise Q_C as a function of θ for 6 cm and 12 cm detectors. The error bars show rms's of the distributions.

2.5.4 Collected charge distribution

We are interested in how the charge gets distributed over the sensitive material. Having a cluster and knowing the intersection position, we can enter points representing each strip in two dimensional histogram. The charge fraction S_i/S_C was plotted versus the distance of the strip center from the intersection point in the detector plane (Figs. 2.16 and 2.18). A clearer picture but somewhat stripped of information can be obtained by profiling the histogram in the S_i/S_C axis and showing just the mean and rms versus distance (Figs. 2.17 and 2.19).

In these distributions one can notice a slight tendency for the strip signal increase, as we go toward higher strip indexes. This was introduced into the measurements by a malfunctioning ADC in the data acquisition system, which caused about 10% of a channel's signal to be sporadically added to its successor. This channel cross-talk has been reproduced afterwards but, unfortunately, no regular pattern has been observed that would enable it to be eliminated from the collected data.

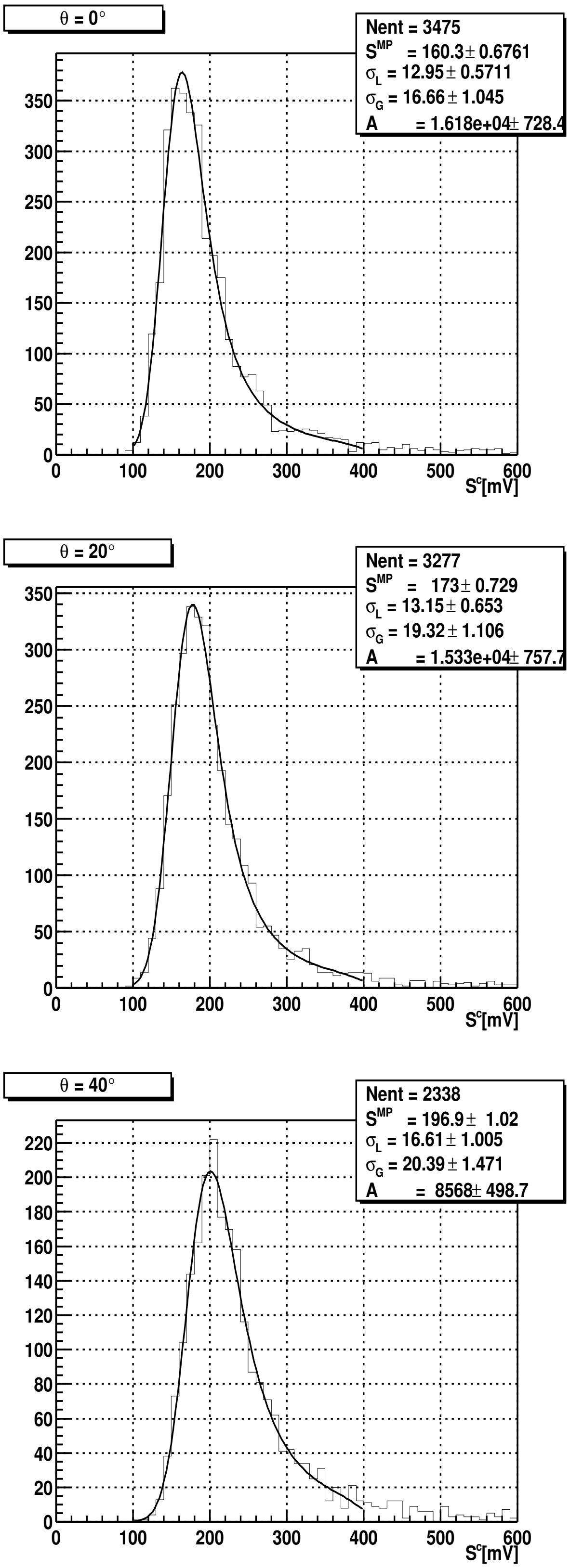

Figure 2.14: Distributions of the reconstructed signal with superimposed Landau fit in a range 100-400 mV for 6 cm detectors at different angles. Parameter A is the normalization constant.

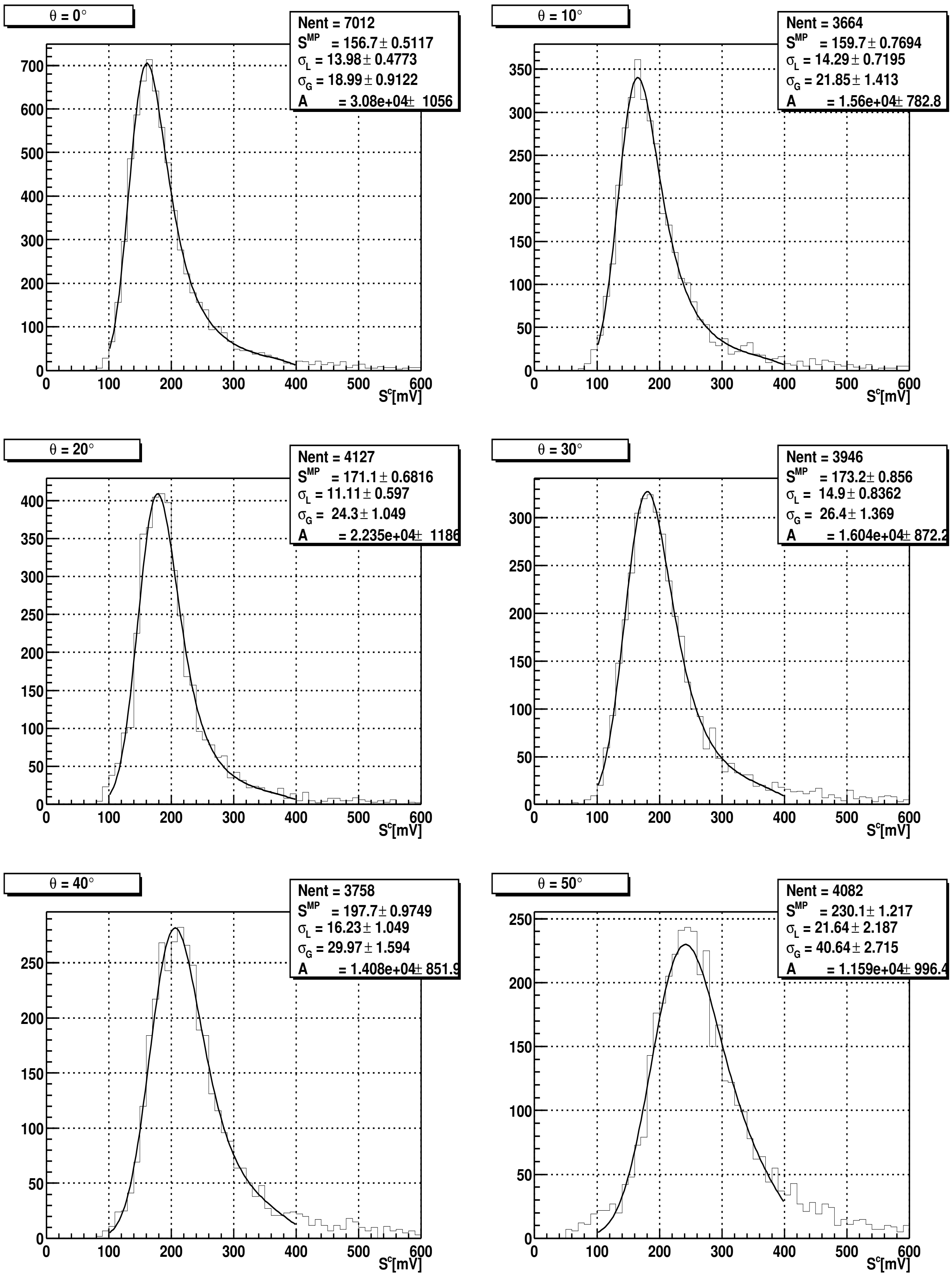

Figure 2.15: Distributions of the reconstructed signal with superimposed Landau fit in a range 100-400 mV for 12 cm detectors at different angles. Parameter A is the normalization constant.

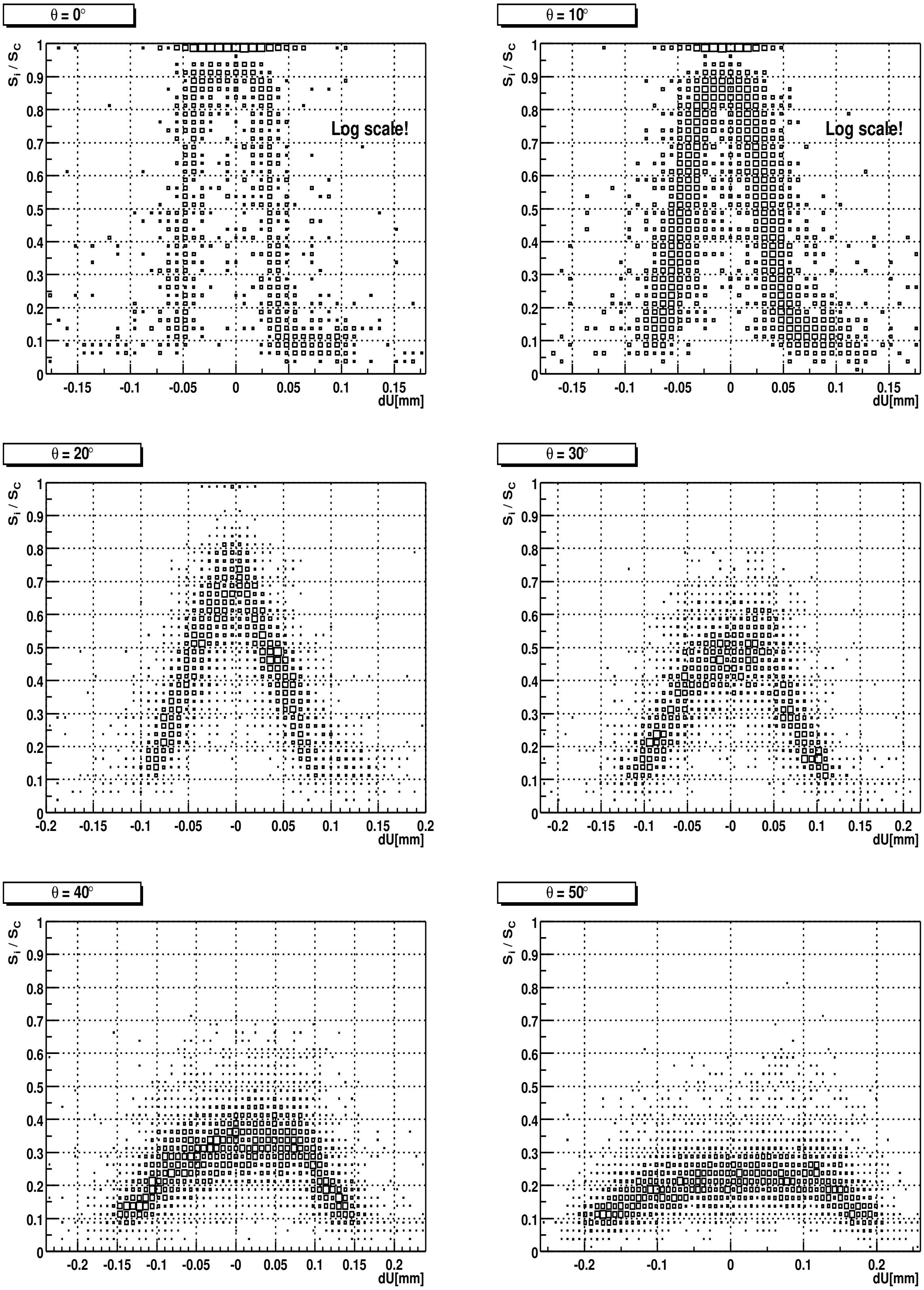

Figure 2.16: Collected charge distribution for 6 cm detectors at different angles. The z axis is logarithmic for $\theta = 0^\circ$, 10°.

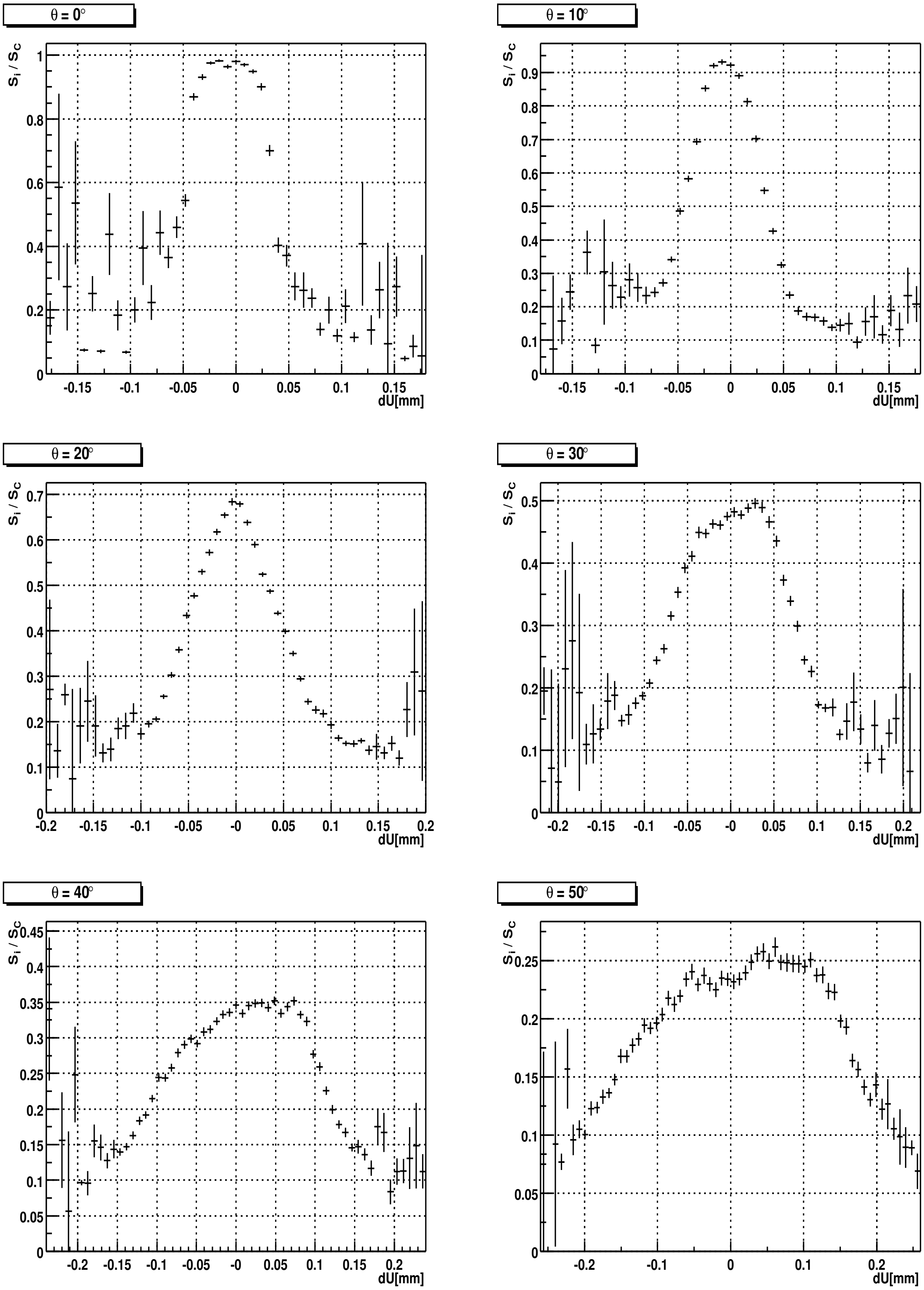

Figure 2.17: Collected charge distribution for 6 cm detectors at different angles shown as profiles.

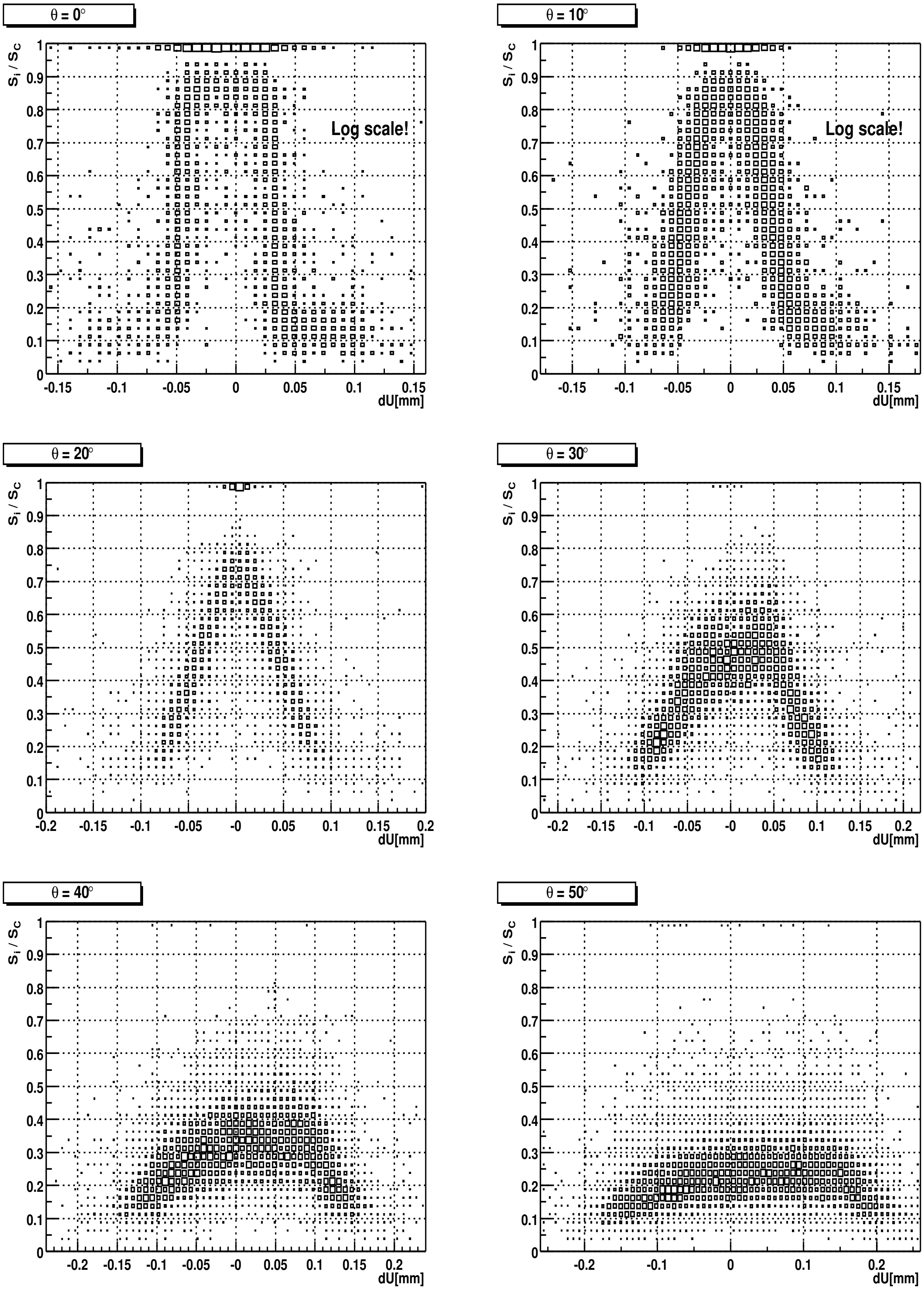

Figure 2.18: Collected charge distribution for 12 cm detectors at different angles. The z axis is logarithmic for $\theta = 0^\circ$, 10°.

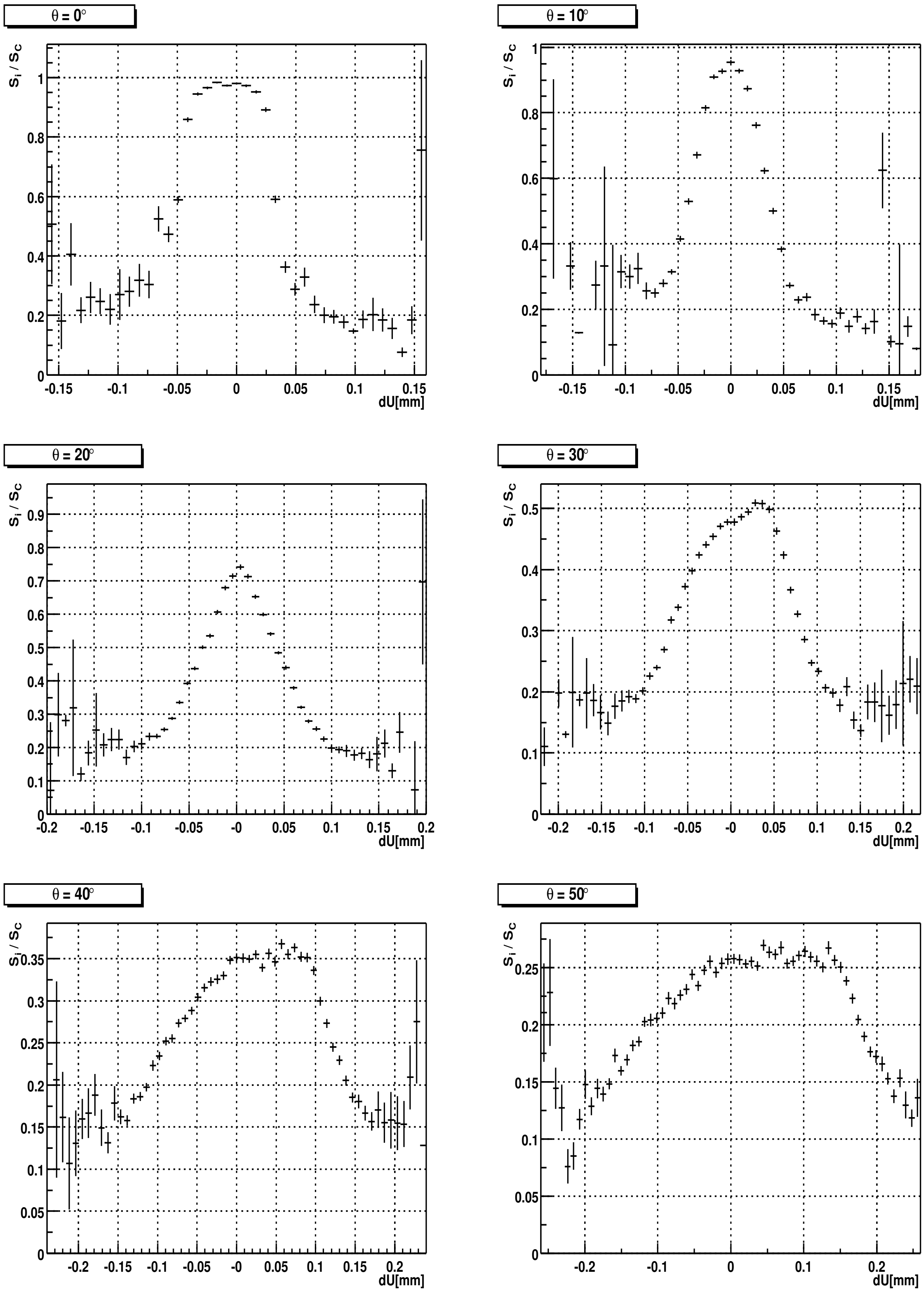

Figure 2.19: Collected charge distribution for 12 cm detectors at different angles shown as profiles.

Chapter 3

Electron track reconstruction

Electron's path through the ATLAS detector is marked by a track in the inner detector (ID) and a cluster in the EM calorimeter (ECAL). ATLAS's arsenal for electron identification consists of two independent weapons. The first one is matching the ID track to its associated ECAL cluster. Position matching is expected to be approximately independent of the energy, while E_T/p_T matching depends crucially on transverse energy, as the tracker resolution is degrading with increasing p_T and the accuracy of the energy measurement in the ECAL is improving. The second weapon is the transition radiation (TR) function of the TRT. As electrons are the lightest particles and transition radiation intensity depends linearly on the relativistic γ factor ($I_{\mathrm{TR}} \propto \gamma$), a higher signal is expected in the TRT from electrons than from other particles. On average, approximately 25% of the TRT hits are above the TR threshold for electrons (less than 10% for pions).

The first section of this chapter presents the electron reconstruction problems in full detail. In the following sections an appropriate algorithm for electron track reconstruction is presented and its efficiency and performance analysed.

3.1 Pitfalls in electron reconstruction

Electrons at the LHC energy scale are plagued by bremsstrahlung effects giving one trying to reconstruct them faithfully a most nightmarish time. The situation in general can be best summarized by the material distribution in the ATLAS inner detector (Fig:3.1) and the following points:

1. **the p_T resolution** is deteriorated due to radiation losses proportional to the amount of material traversed, but the curvature precision gets better with more measurements and improves quadratically with the track length. These two effects are of course in direct contradiction.

2. **The reconstruction efficiency** is sacrificed by the cuts required to retain resolution and to suppress fakes. Some well reconstructed tracks can get killed by blunt cuts even though their identity can be established unambiguously.

3. E_T/p_T **matching** for $e^{\pm}$ identification can be very misleading. In the case of a disastrous early bremsstrahlung, a method of the position matching of the track and EM cluster provides a better way of electron identification.

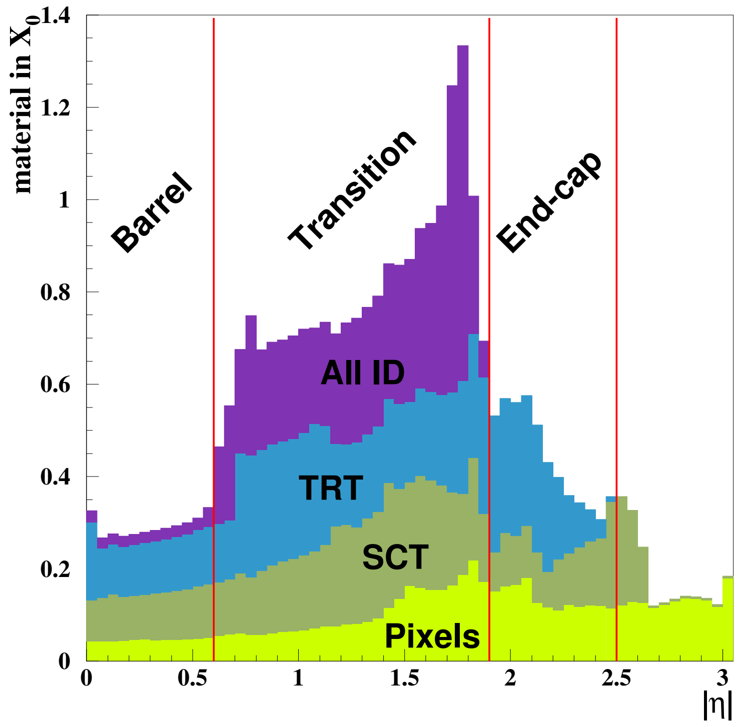

Figure 3.1: Distribution of the material in radiation length units versus $|\eta|$. Amount of material for each sub-detector is plotted in a cumulative way. Red lines separate the $|\eta|$ regions used in analysis.

The objective of this preliminary study was to find out what is the best one can do with the current detector layout in terms of the above quantities, to recognize the problematic cases and to prepare the guidelines for a later attack with appropriate reconstruction algorithms.

In the ID part of this initial study only information from the Monte-Carlo generated events was used. Hits belonging to electron tracks were picked from the structures describing the detector and then fitted with the standard offline track fitting package. No pattern recognition is thus needed and so the results really show the optimal outcome of any algorithm searching for tracks in the ID.

As this was a combined ID/ECAL study the data-sets were analysed in three $|\eta|$ ranges: $[0, 0.6]$, $[0.6, 1.9]$ and $[1.9, 2.5]$. The first one corresponds to a pure barrel section of the detector with the least traversed material. The second one is a barrel to end-cap transition with some of the worst materialistic horrors as most of the barrel services enter the ID in this region. The last one is a pure forward tracker (see Fig:1.4 for a schematic view of the inner tracker).

Technical note: The 5 and 20 GeV e^- datasets used for this analysis were produced with DICE 97_6 simulation chain. This is the same ID layout as was used for the Physics TDR, but the ECAL reconstruction code is slightly outdated. In the detector simulation phase a 1 MeV cut was applied to the secondary tracks, which means that bremsstrahlung photons with a lower energy were not stored in the output structures. The simulations were carried out with a constant solenoidal magnetic field $B = 2\,\mathrm{T}$ in the ID volume.

3.1.1 Bremsstrahlung in the ATLAS detector

High–energy (above a critical energy) electrons predominantly lose energy in matter through bremsstrahlung. The characteristic amount of matter traversed is called a *radiation length* ($X_0[\,\mathrm{m}]$, usually expressed as $\rho X_0[\,\mathrm{g\,cm^{-2}}]$) and is defined as the mean distance over which the electron's energy is reduced by a factor of $1/e$. The main dependence of X_0 is on the atomic properties of the material. An approximate formula [19], accurate to better than 2.5% (5% for He), is:

$$\rho X_0 = \frac{714.4 \;\; \mathrm{g\,cm^{-2}A}}{Z(Z+1)\ln(287/\sqrt{Z})}. \tag{3.1}$$

Consider again Fig:3.1: electrons on their way through the ID will have a rough ride before they make it to the ECAL. As bremsstrahlung is a pure QED process, given enough trials, anything can happen. But, how often? To answer this question we should study the energy distribution of the emitted photons. To overcome the immense amount of theoretical work on this topic, a brief survey of the problems encountered is made with references to the literature. In following discussion E denotes the initial energy of the electron and k the momentum of the emitted photon. The quantity $y = k/E$ denotes the fraction of energy carried away by the photon.

A first calculation of the bremsstrahlung process was made by Bethe and Heitler in 1934 [20]. For introductory purposes a slightly more modern (1954) review by Heitler is recommended [21]. The calculation of the differential cross-sections is followed by a discussion on the screening effect for high energies ($E \gg m_e$), which leads to a decrease in the cross-section. A technical review in a modern field theory language is given in [22]. Both references also discuss the cancellation of infrared divergences by including an amplitude for elastic scattering when evaluating the $k \to 0$ case.

The theory proposed by Landau and Pomeranchuk [23](calculation by Migdal [24]; theory addressed to as the *LPM effect*) goes one step further by considering the interference of scattering amplitudes from a larger area determined by the wavelength of a photon transferring momentum to the surrounding media ($\propto E^2/k$). The net effect is a significant suppression (order of 10% in 1 to 100GeV range) of the low k photon emission. Improved calculations were carried out by Baier and Katkov ([25], [26]) to better explain the results of a recent SLAC experiment [27].

A brief overview of bremsstrahlung properties can also be found in the Review of Particle Physics [19].

A good rule of thumb for the whole energy range of electron physics in ATLAS is still: $kd\sigma/dk \approx$ const. Deviations of up to 20% are present in the IR region $k/E < 0.1$.

In ATLAS detector simulation, bremsstrahlung photons are simulated with the `GEANT3` detector description and simulation package [28]. `GEANT3` uses functions fitted to a calculated data to generate random variables in the Monte-Carlo process and takes into account the Migdal corrections (refer to the manual for details, sections PHYS340 and PHYS341). In the following, a brief review of the simulated bremsstrahlung photon properties is given. The angular distribution and the k–spectrum are presented.

A favourable property of bremsstrahlung at ultra relativistic energies is that all photons are emitted parallel to the electron momentum. The angular distribution falls off exponentially: $dP/d(\Delta\varphi) \propto e^{-f(E)\Delta\varphi}$. $f(1\,\mathrm{GeV}) \approx 500$ which is already a factor 10 below the angular resolution of the ECAL. $f(E)$ increases with energy; e.g: $f(10\,\mathrm{GeV}) \approx 2700$ and $f(50\,\mathrm{GeV}) \approx 4300$. In practice this means that a bremsstrahlung photon emission results in a decrease of the electron momentum without a change in the momentum direction.

As transverse energy is more relevant to electron reconstruction, the event samples were generated at fixed transverse momenta (p_T). This corresponds to generating an electron with a flat energy distribution in the range $E = p_T$ to $E = p_T \cosh(\eta_{\max} = 2.5)$. Extraction of a clear event sample with a well defined E is therefore not possible. Instead an energy weighted photon distribution of the first photon emitted is shown for several energy ranges in Fig:3.2.

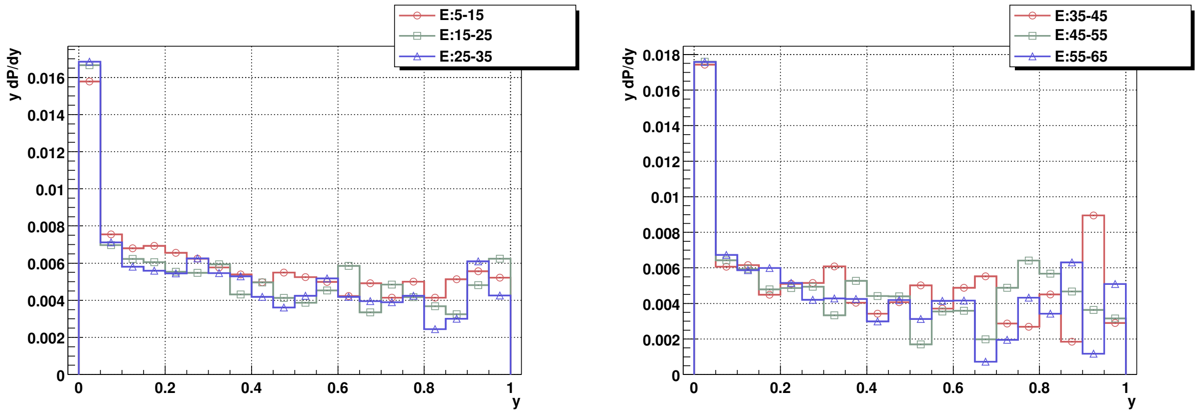

Figure 3.2: ydP/dy distributions of the first emitted photon for different energy ranges.

3.1.2 Electron energy losses in the ID

The first question asked is what fraction of $e^{\pm}$ lost more than a given percentage of their energy by a certain traversed distance in the ID. These losses are in direct correspondence with the systematic shift of a track's hits from its ideal (i.e., no bremsstrahlung) trajectory to its actual trajectory. Fig:3.3 shows the probability for an electron to lose 2%, 5%, 10%, 20% or 30% of its energy along its path for each of the three η regions. These losses are energy independent.

Here one should consider three points in more detail:

- 2% loss is to be compared to the statistical error from multiple scattering. After an electron loses more than 2% of its initial energy, systematic divergence from the fitted track can be observed.

- 10% loss is getting us into the tails of the calorimeter E_T measurement. These events should not be used for the ECAL calibration.

- 30% loss approximately corresponds to the $0.7 \leq E_T/p_T \leq 1.3$ cut used in the ID TDR for electron identification. In principle this cut should serve as a discriminator against the background while allowing for as high identification efficiency as possible. Often the choice between the two modes is specific to the analysis being performed.

  While this selects good electron candidates it also decreases the electron identification efficiency.

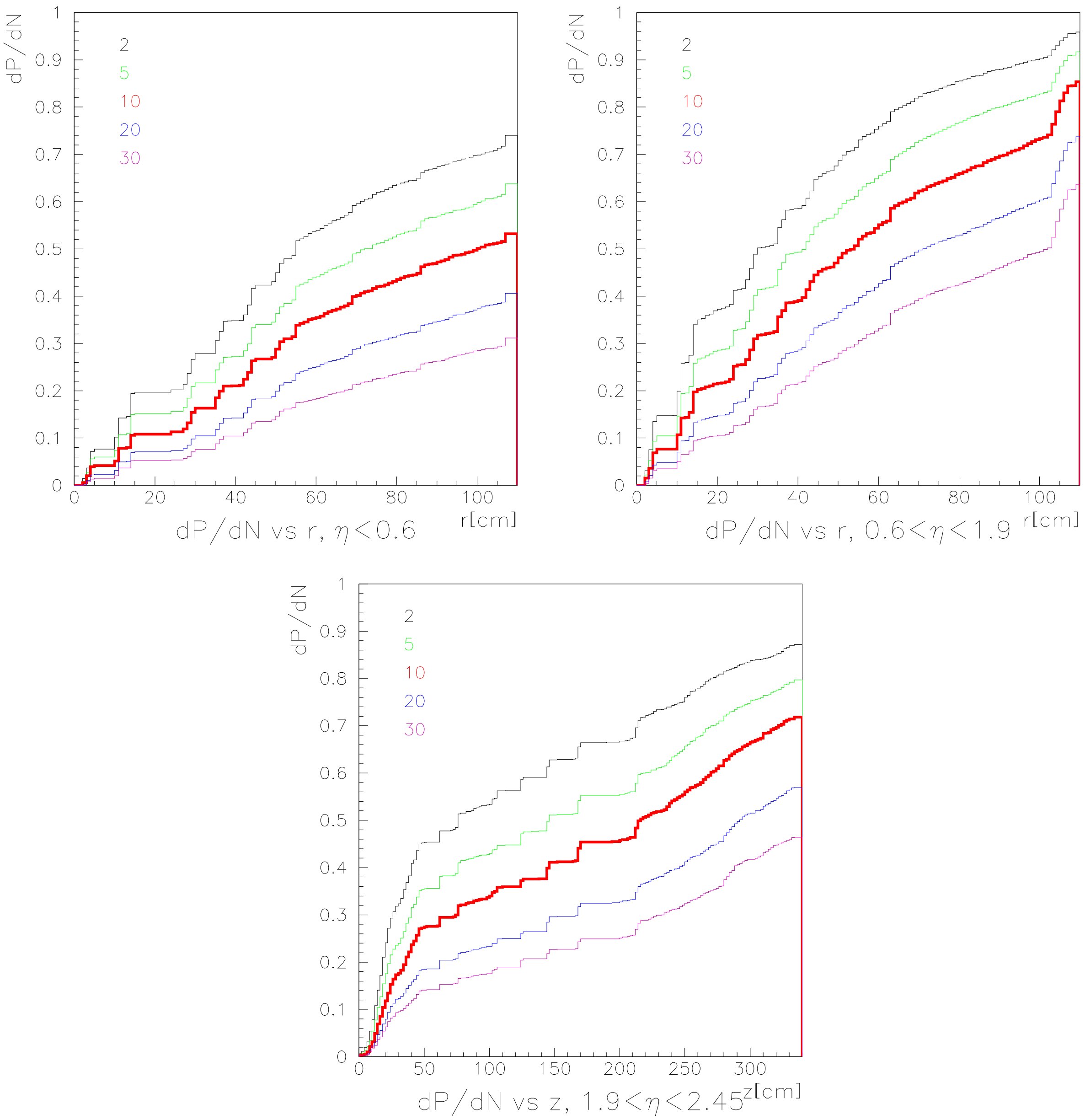

Figure 3.3: Fractions of electrons that lost more than certain percentage of their energy as a function of the distance traveled. Different colors correspond to the threshold of a different fractional loss. Each plot depicts one $|\eta|$ region.

Our goal, set at this point, was to improve the reconstruction of electrons losing more than 10% of their energy by the outer radius of the SCT. This would allow a harder cut on E_T/p_T and to better discriminate against the background as well as improve the identification efficiency. Tab:3.1 shows what fraction of the overall electron population are being addressed.

We need at least three points for a p_T measurement which corresponds to a track reconstruction in only the pixel detectors. Therefore the electrons losing more than 10% of their energy by the end of the pixels represent the irreducible background for which ID stand-alone reconstruction cannot make a good p_T measurement. All SCT measurements of these $e^{\pm}$ are plagued by a systematic shift.

η bins	$0-0.6$	$0.6-1.9$	$1.9-2.45$	weighted sum, all η
pixels	0.11	≈ 0.22	0.35	0.22
SCT	0.32	≈ 0.58	0.45	0.49
TRT	0.52	≈ 0.75	0.70	0.68

Table 3.1: The fraction of $e^{\pm}$ that have lost more than 10% of their energy by the end of each ID sub-detector. The three $|\eta|$ regions are shown together with the weighted average over the full ID η-coverage. The values in the table include the cases where the bremsstrahlung occurs close to the end of the sub-detector in question and are therefore a pessimistic estimation of the degradation of the reconstructed momentum.

In principle a vertex constrained fit could be used to improve the resolution. But this solution is not generally applicable because of the electron signal from displaced vertices such as B decays or early γ conversions (giving rise to over–corrected p_T). The application of this procedure is therefore limited to the reconstruction of narrow resonances selected according to an invariant mass cut.

3.1.3 Distributions of fitted p_T

The second question is how do the p_T distributions vary when we go along the track and keep adding in new measurements? We start with a pixel-only fit and then include SCT measurements, one layer (two measurements) at a time. To make the situation clearer, four samples were chosen according to the `GEANT3` tracking information:

- △ **Less** than 10% loss by the end of the SCT. This is the purest sample where we expect all subsequent measurements to improve the reconstructed p_T.

- ● All events; this provides a view of the overall situation and enables one to see individual influences on the big picture.

- ☆ **More** than 10% loss by the end of the pixels. These are catastrophic events where the tracker cannot make a good p_T measurement. By adding in new measurements the resolution should even deteriorate.

- ◇ **More** than 10% loss by the end of the SCT, excluding ☆. A good p_T measurement should be possible, but it is expected to give a poorer resolution through being too greedy in number of measurements.

Fig:3.4 shows the raw distributions for the best and the worst sample. The △ sample distribution becomes more Gaussian-like when adding in new measurements, while the ☆ one is running away from it by pulling in a longish low-p_T tail. A statistical view of the p_T distributions is shown in Fig:3.5. The mean values are systematically decreasing, going further and further away from the *true* value. The rms is around 0.3 for a pixel–only measurement, which is easily understood as the pixel measurements are lined up close together in r/z. The addition of a single SCT layer basically stabilizes the rms at a flat line.

We can also look at the problem from another angle and ask: What fraction of the reconstructed $e^{\pm}$ is outside a $0.9 \leq \frac{p_T}{p_T^{\mathrm{true}}} \leq 1.1$ selection? Fig:3.6 shows the results. There are two major points. Firstly, even in the best case (less than 10% bremsstrahlung), insisting

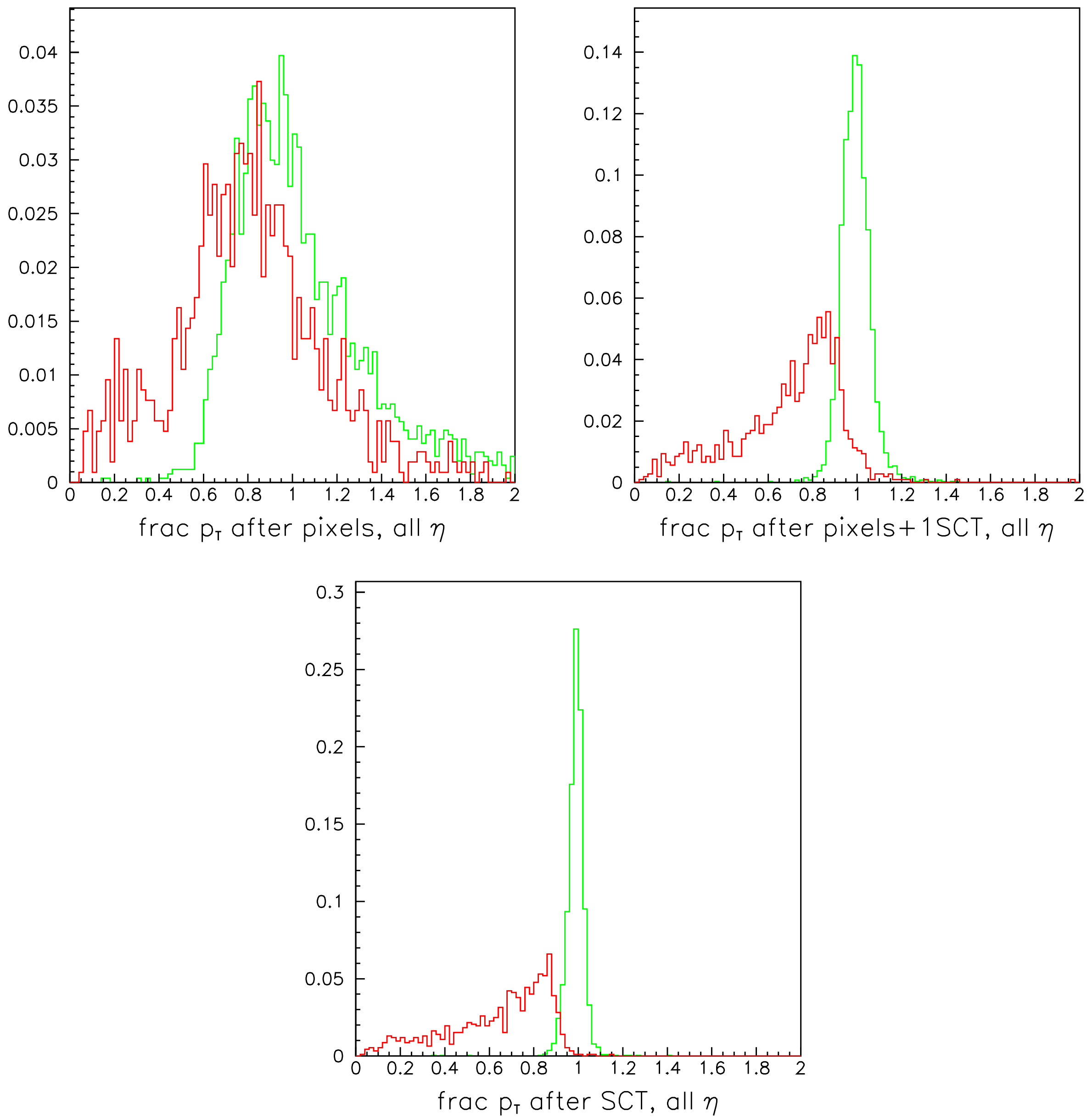

Figure 3.4: Raw p_T/p_T^{true} distributions for cases when 3, 4 or 7 measurements are included in the fit (see subtitles of plots). The red histogram in each plot corresponds to the ☆ sample and the green one to the △ one. Note that $1/p_T$ has a Gaussian distribution; p_T is shown as it better depicts the bremsstrahlung-tail.

on a full track length for the p_T measurement is futile. Secondly, reading from the minima of ● points, one finds the sad reality of electron reconstruction in ATLAS: bremsstrahlung recovery by cutting back on the number of measurements (or a two curvature fit, which allows for use of the full PR & TR info) will yield at best 15, 25, 35% of electrons outside the 10% limit (per η region). Still, one can compare this to an $\sim 50\%$ inefficiency obtained by requiring a full length track without any bremsstrahlung recovery (see Tab:3.1).

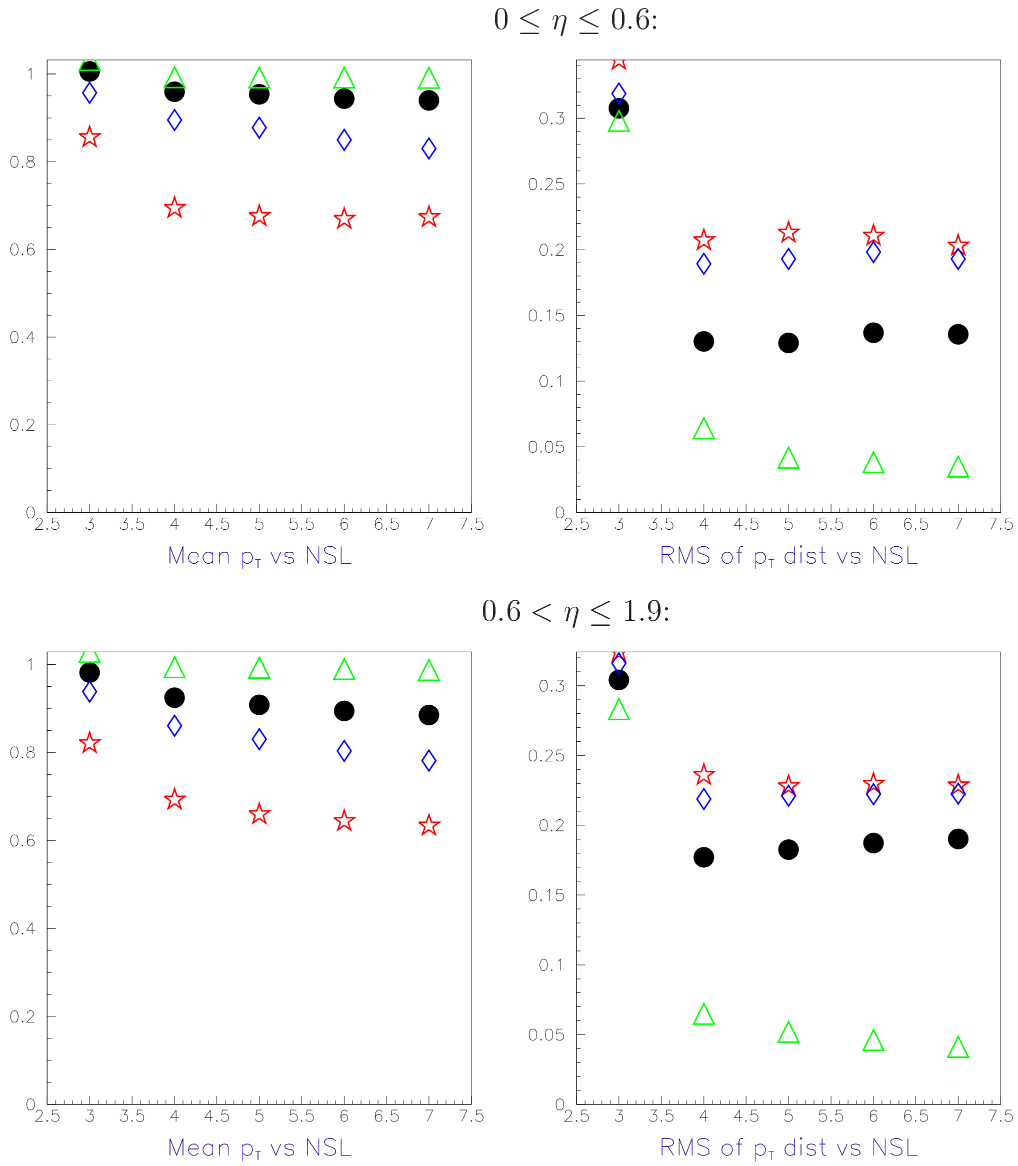

Figure 3.5: Mean & rms of the p_T/p_T^{true} distributions versus the number of layers (NSL) used in the fit. The barrel and transition regions are shown.

3.1.4 E_T/p_T matching

As already mentioned in the introduction, matching of the energy measured by the calorimeter to the momentum of the track reconstructed in the tracker is one of the primary means for electron identification. This and the following section address this topic.

Fig:3.7 shows the E_T/p_T match and Tab:3.2 gives the fraction of events that satisfy different cuts on this quantity. The p_T was chosen from the fit corresponding to the number of measurements giving the minimum fraction outside the 10% cut (4 for the 2$^{\text{nd}}$ bin; 5 for the other two), i.e., the fit with the best possible ID performance. The relevant observation is that blindly accepting a single value for E_T/p_T cut will reduce the electron identification efficiency at lower energies.

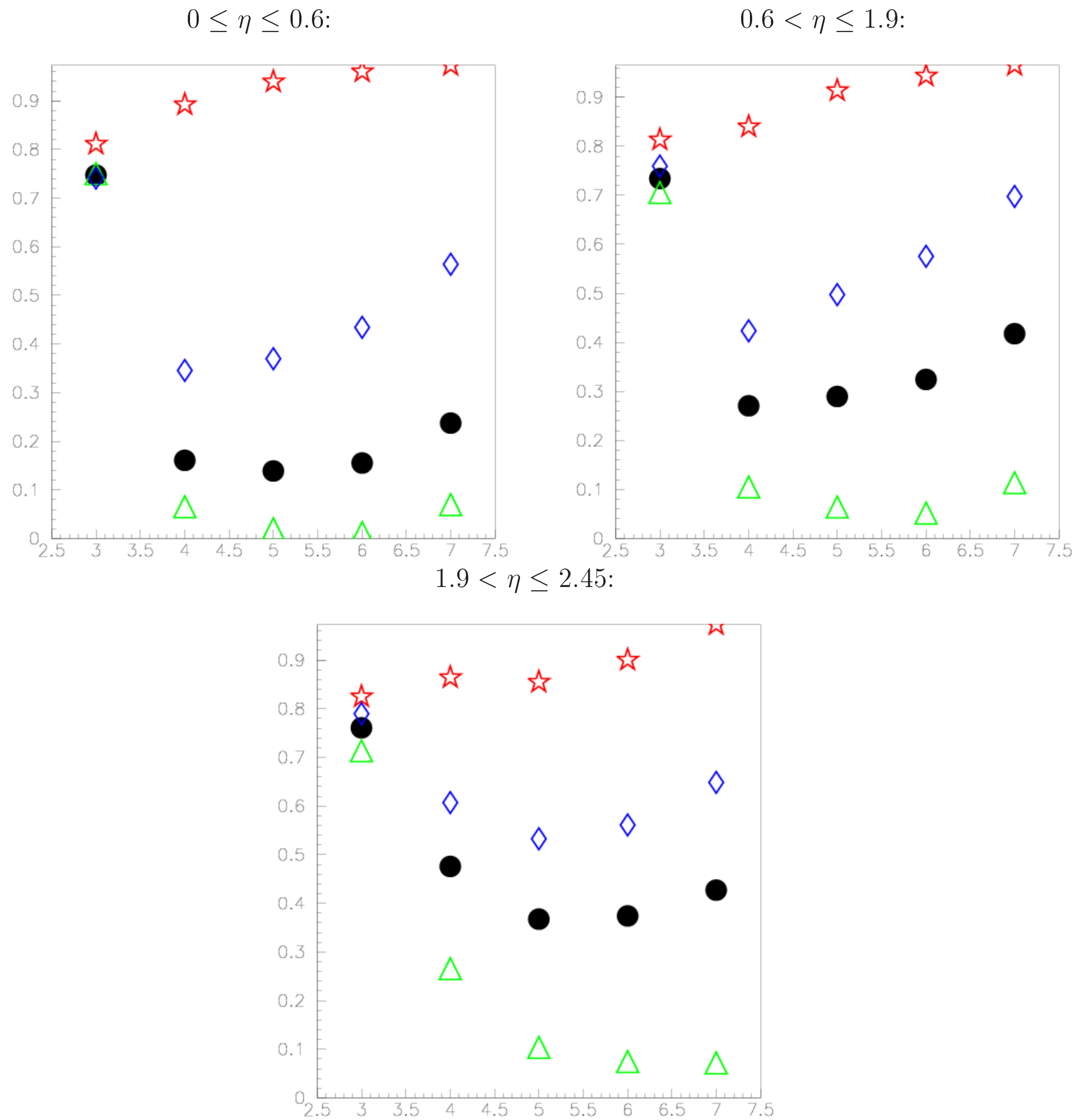

Figure 3.6: Fractions of electrons out of a 10% selection on p_T/p_T^{true} as a function of number of crossed layers. Fractions are shown for the three η regions and for four event samples.

frac within	20 GeV				5 GeV			
E_T/p_T cut	△	●	☆	◊	△	●	☆	◊
0.7-1.3	1.00	0.92	0.60	0.84	0.99	0.94	0.79	0.88
0.8-1.2	0.99	0.88	0.43	0.76	0.98	0.89	0.66	0.77
0.9-1.1	0.93	0.76	0.17	0.57	0.88	0.73	0.41	0.55

Table 3.2: Fractions of events that satisfy different E_T/p_T cuts, integrated over all η.

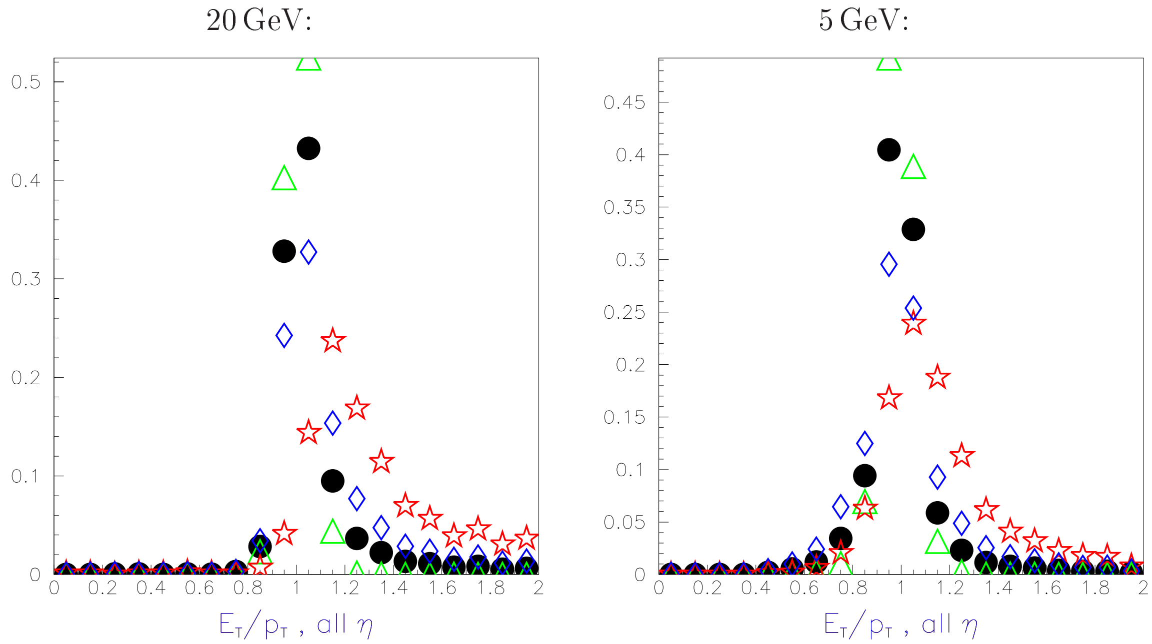

Figure 3.7: E_T/p_T distributions for four event samples over all η.

3.1.5 ECAL reconstruction

As the ID will not be used in the level 1 trigger(1.4.2), the first beast prowling for unfortunate electrons is the ECAL reconstruction inefficiency. To understand some of the peculiarities that we will meet in further discussion, a short description of the clustering algorithm is presented.

The ECAL clustering algorithm begins by collecting the contributions from all samplings (without the crack scintillators!) in a combined matrix with a grid size $(\Delta\eta \times \Delta\varphi) = (0.025 \times 0.025)$ corresponding to the cell size of the second sampling. Calibration corrections are applied in the process. The cluster search uses a sliding window algorithm with an adjustable window size. The algorithm centres the window such that the sum of the contained energy is maximized. For electrons a window size of 3×7 ($\eta \times \varphi$, in grid units) gives good results as it allows most of the bremsstrahlung photons to be included in the same cluster as the electron. A threshold of 1.1 GeV (clustering cut) is usually used to minimize the effects of electronic noise and contributions from minimum bias pile-up.

HCAL clustering uses the same philosophy, only the grid segmentation is four times coarser. The matrix is filled with the sum of the transverse energies in the EM (including the scintillator!) and hadronic sections, smeared according to the real cell size. The search for jet candidates uses a 3×3 window while kinematic variables (positions and spreads) are calculated using a 9×9 window centered around the found maximum. The typical clustering cut is 2 GeV.

As we are interested in performance of the calorimeter down to the lowest reasonable limit of $E_T \sim 1.5$ GeV, we used somewhat lower clustering cuts for single particle analyses: a threshold of 1 GeV was set on the E_T contained in an EM cluster for $E_T^{\mathrm{true}} > 10$ GeV and 0.7 GeV for $E_T \leq 5$ GeV. Still, there are two reasons causing some electrons with $p_T > 1$ GeV to fail this cut:

E_T		1.5	2	3	5
$E_T^{\text{cut}} = 0.7\,\text{GeV}$	all	70.9	89.1	97.1	99.3
	transition	52.6	80.4	94.5	98.6
$E_T^{\text{cut}} = 1.0\,\text{GeV}$	all	41.9	74.6	94.4	98.6
	transition	19.2	58.0	89.5	97.3

Table 3.3: Efficiency of the EM calorimeter at low transverse energies for clustering cut set to $E_T = 0.7\,\text{GeV}$ and $1\,\text{GeV}$. Values are quoted for all events integrated over η and for the transition region, where the efficiencies are at their worst.

	20 GeV		5 GeV	
ΔE_T	△	☆	△	☆
mean	0.01	0.03	0.07	0.17
rms	0.05	0.06	0.12	0.15

	20 GeV		5 GeV	
$\Delta R/Z$	△	☆	△	☆
mean	0.01	0.01	0.01	0.04
rms	0.25	0.26	0.56	0.60

	20 GeV		5 GeV	
$R\Delta\varphi$	△	☆	△	☆
mean	0.01	0.24	0.14	-0.47
rms	0.77	1.15	2.45	3.75

Table 3.4: Mean values and rms's of the residuals of calorimeter measurements for the △and ☆event samples (representing 51% and 22% of the event sample respectively).

1. For a very low p_T (up to 3 GeV) the bremsstrahlung can split the energy between two distinct clusters causing both of them to fail the E_T cut. This is most likely to happen in the regions with a large amount of material in front of the ECAL.

2. There is a crack at the join of the barrel and end-cap module ($|\eta| = 1.5$). An electron with p_T lower than $\sim$ 10 GeV can sneak through this crack with a minimal energy deposition and therefore miss the E_T threshold. Also, as the EM cluster searching algorithm does not include the crack scintillator measurement, some clusters can be lost even if a measurement has been made.

Tab:3.3 gives the ECAL reconstruction efficiencies at low energies for the two choices of the clustering cut. For 10 GeV and above the reconstruction is fully efficient.

E_T, η and $R\varphi$ matching

For electron identification the EM cluster is required to match the track in the ID. This section compares the ECAL measurements with the quantities projected from the true parameters at the vertex. Fig:3.8 shows the residual distributions and Tab:3.4 gives their statistical description in terms of a mean value and rms for the best and worst case (as seen by the amount of brem–losses).

The following conclusions can be made:

- In ΔE_T the bremsstrahlung effects can be seen as a missing energy. Usually this means that the electron didn't make it into the 3×7 window used for clustering.

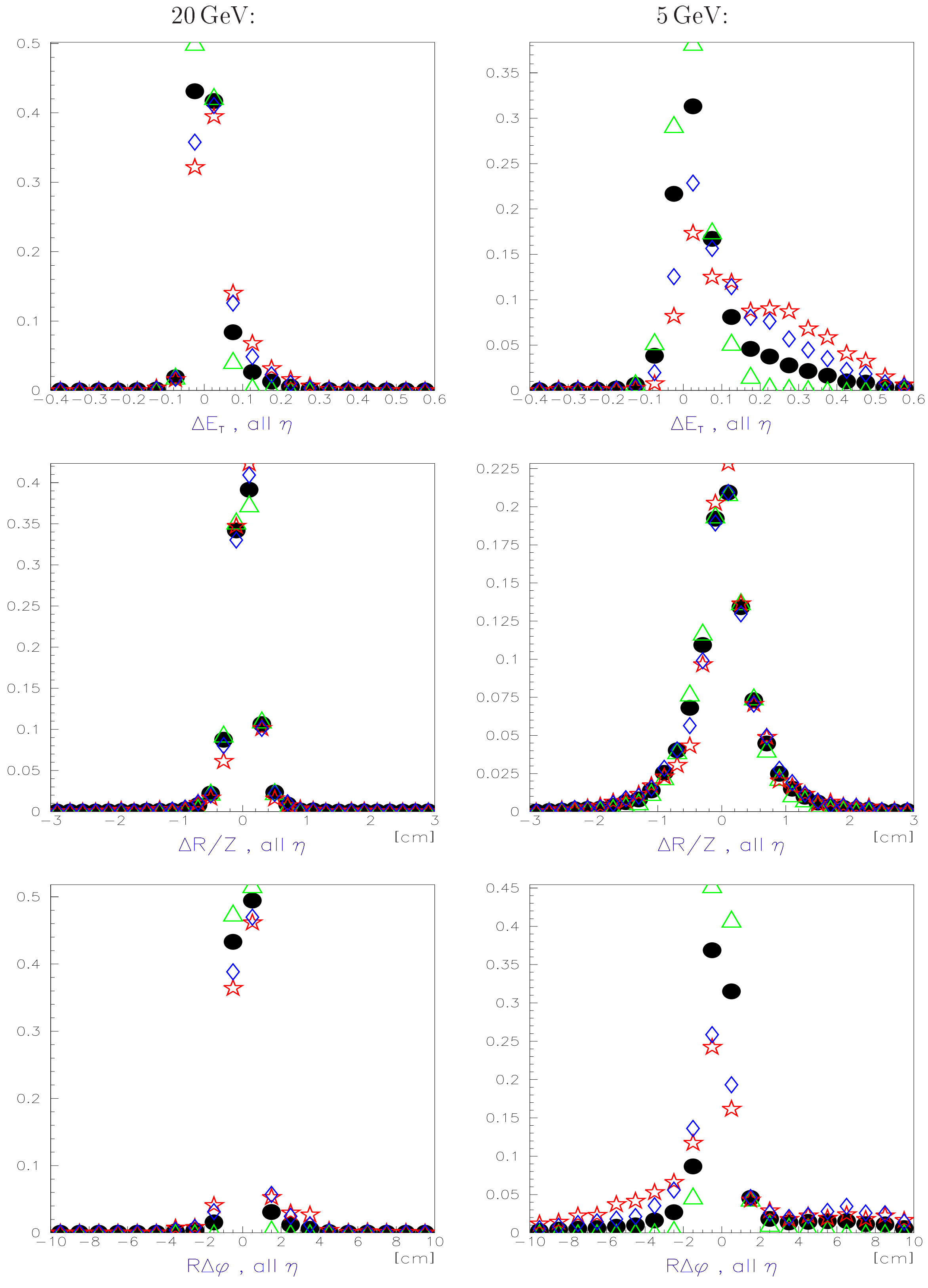

Figure 3.8: Residuals of the calorimeter energy and position measurements (expressed as difference $\frac{\text{true} - \text{reconstructed}}{\text{true}}$) for $E_T = 20\,\text{GeV}$ (left) and $5\,\text{GeV}$ (right). ΔR is used for the end-cap and ΔZ for barrel measurement.

- $R\Delta\varphi$ shows two effects: there can be a γ (a small bump on the positive side of the residual distribution) or an electron (longish tail on the negative side) falling out of the ECAL window.

- No bremsstrahlung effects can be observed in the longitudinal ($\Delta R/Z$) measurement.

This leads us to the conclusion: provided the energy is contained in the calorimeter window its position measurement is independent of bremsstrahlung. In the hard bremsstrahlung case, one can still use R/Z (or η) matching for $e^{\pm}$ confirmation.

To further investigate the correlation between ΔE_T and $R\Delta\varphi$, consider Fig:3.9. The systematic bumps from early hard brems that miss the 3×7 window can be seen for the 5 GeV sample. At 20 GeV one is basically saved from this kind of magnetic field induced loss.

20 GeV: 5 GeV:

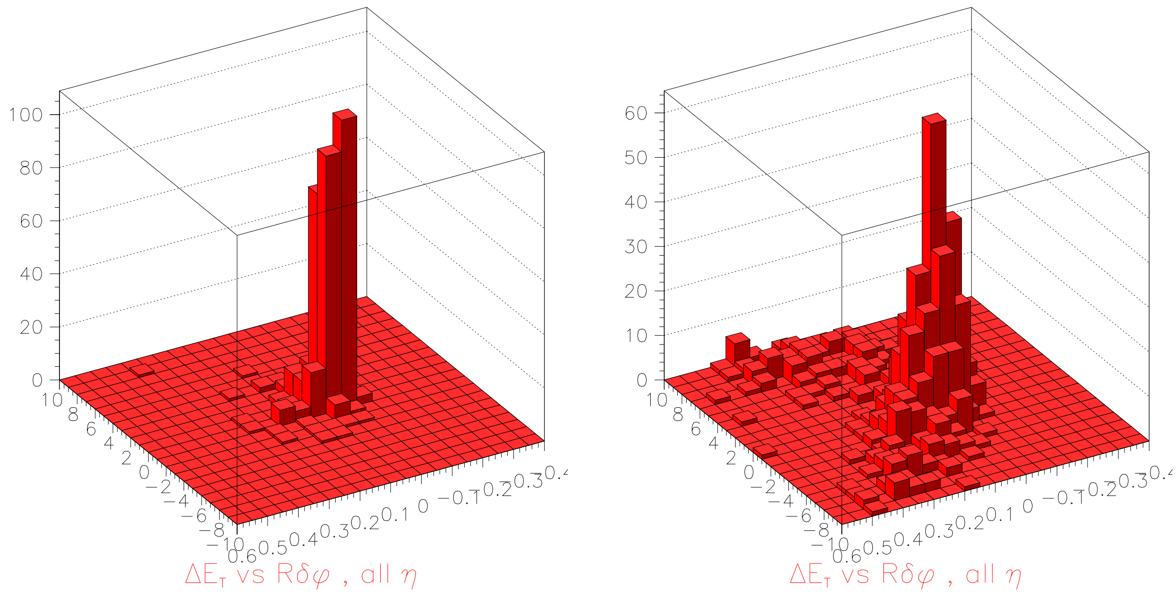

Figure 3.9: Distribution of the ☆ event sample over the $\Delta E_T(\swarrow) \times R\Delta\varphi(\nwarrow)$ plane.

The $E(\varphi)$ distribution and multiple EM clusters

As the electron and the emitted photon are separated by the magnetic field, one would expect this separation to reflect in the spread of the energy distribution in the EM cluster. At low energies (up to 10 GeV) this effect can indeed be observed but it is not very pronounced. A brief analysis showed that the ID measurements allow for a better bremsstrahlung tagging, thus the question will be revisited only when the ID pattern recognition is 'used up'.

Another problem occurs when the electron/photon separation produces two EM clusters. Due to the algorithm used in cluster reconstruction, these two clusters can partially overlap (see [29] for details of the algorithm). A simple method of resolving this ambiguity was developed and will also be discussed later.

3.1.6 Is a first order bremsstrahlung treatment sufficient?

Basically the question is: Is a bremsstrahlung treatment to the first order sufficient or is there a relevant fraction of events where two (or more) photons take away a significant amount of the energy? Higher order effects can be very tricky to reconstruct properly as each separate bremsstrahlung produces a kink on the track and introduces new unknowns to the pattern recognition process.

We proceed with a short overview of the properties of the hardest (primary) and the second hardest (secondary) emitted photon. First consider the distribution of the number of emitted photons (above the 1 MeVcut-off) versus η (Fig:3.10). As expected, it follows closely the material distribution. By taking into account the way the simulation of the bremsstrahlung is performed and the E_γ distribution (see Sec:3.1.1), we expect a first order treatment to be justifiable in the barrel and to some extent also in the end-cap region.

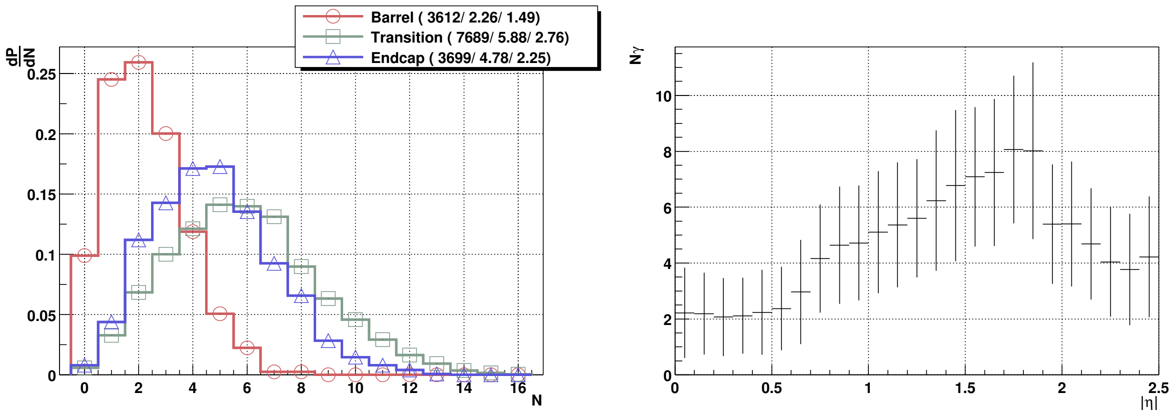

Figure 3.10: Left: The distribution of the number of emitted photons (above the 1 MeVcut-off) for the three η regions. Right: The mean number of photons versus $|\eta|$; the error bars represent the rms.

To get a qualitative measure of the effect the cumulative distribution of the probability for the photon in question to take away a certain fraction of all the emitted energy was plotted. (Fig:3.11). As these plots are a bit hard to read, Tab:3.5 summarizes the results. The conclusion is somewhat sad: a second order treatment is necessary in about half of the cases. The numbers are a bit overestimated as for two close photon emissions the pattern recognition can safely treat them as a single one. Also ... a bremsstrahlung close to the end of the TRT is harmless in view of the silicon oriented reconstruction. For completeness, the fractional amounts of bremsstrahlung loss by the end of the ID's sub-detectors are also given (Fig:3.12). This information can be combined with the above fractions to pinpoint the different cases for pattern recognition.

3.1.7 Expected cases

All these things considered, we can come up with different scenarios and probabilities for each of them to occur. We present three different methods of inspection. The first one is a cumulative tree with branchings occurring at the end of each of the sub-detectors (see Tab:3.6). This representation gives one a good feeling for the beginning of the track and where in the detector things start to go wrong.

	% bremmed energy	Barrel	Transition	Endcap
Primary	≥ 90	0.26	0.12	0.21
	≥ 80	0.47	0.27	0.38
	≥ 70	0.62	0.42	0.53
Primary + Secondary	≥ 90	0.69	0.40	0.56
	≥ 80	0.87	0.67	0.79
	≥ 70	0.95	0.84	0.91

Table 3.5: The fraction of events where the primary (primary + secondary) photon took more than 90,80,70% of all the energy radiated.

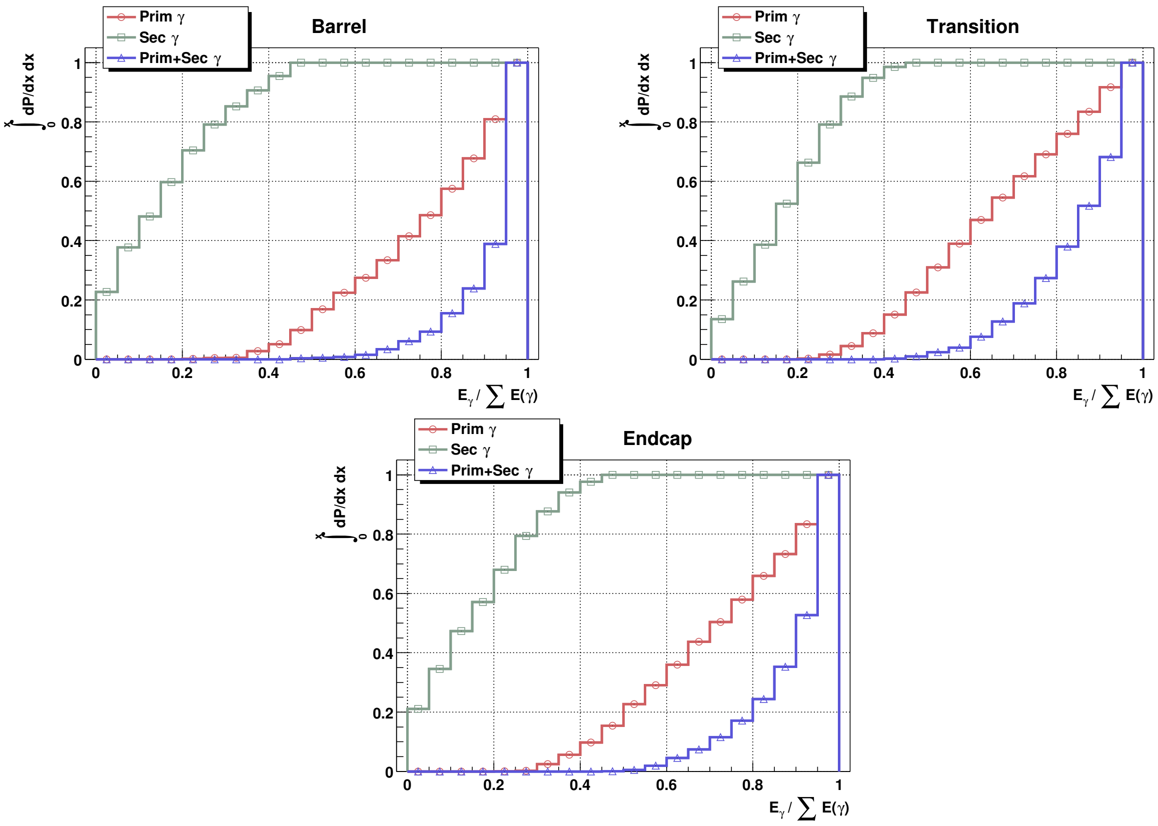

Figure 3.11: Cumulative probability distributions for the hardest(`Prim`) and second hardest(`Sec`) bremsstrahlung photon as well as their sum to take more then certain fraction of all emitted energy. The three η regions are separated.

The second representation is a bit more cumbersome as it treats each of the sub-detectors separately. We separate three cases for each sub-detector:

S (small) less than 2% loss in the sub-detector. No special treatment is necessary.

M (medium) loss between 2% and 10%. Some of the effect can be swept under the rug as a multiple scattering tail or by a degradation of the fit parameters. These events are basically hard to spot and reconstruct properly.

L (large) above 10% loss. The kink is more evident and can be found provided that enough measurements exist on both sides.

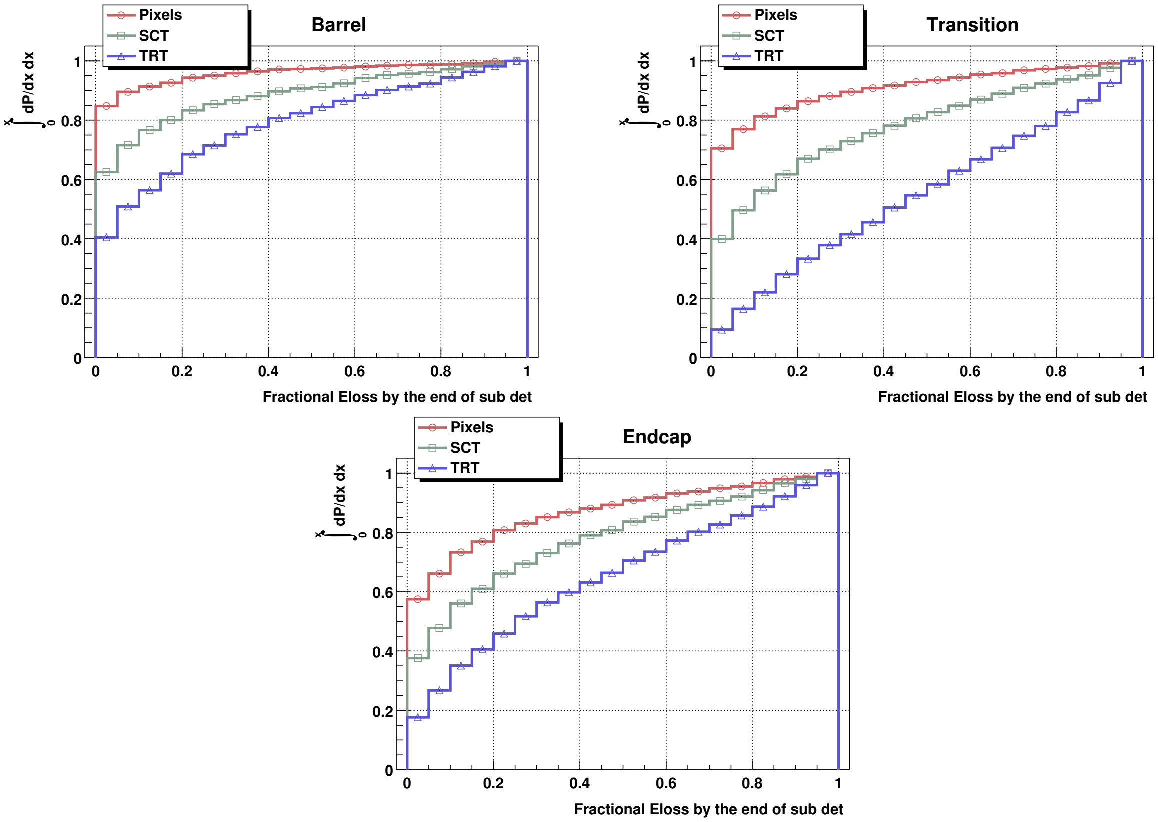

Figure 3.12: Cumulative probability distributions for an electron to lose certain fraction of all energy carried away by the bremsstrahlung by the end of the three sub-detectors.

This gives the 3^3 different cases presented in Tab:3.7. Here one can directly recognize different pattern recognition scenarios.

y_{Pix}	y_{SCT}	y_{TRT}	Barrel	Transition	Endcap
< 0.1	< 0.1	< 0.1	0.509	0.164	0.267
		> 0.1	0.207	0.332	0.210
	> 0.1	< 0.2	0.037	0.022	0.042
		> 0.2	0.143	0.251	0.142
> 0.1	< 0.2	< 0.2	0.012	0.011	0.035
		> 0.2	0.007	0.028	0.035
	> 0.2	< 0.3	0.017	0.009	0.036
		> 0.3	0.070	0.183	0.233

Table 3.6: Expected bremsstrahlung cases in electron reconstruction: cumulative view over the sub-detectors.

The third method is in fact a merge of the above two with an emphasis on silicon based reconstruction. The TRT is considered only as a bridge between the silicon tracker and the ECAL. By comparing the electron track to a non-electron track from the reconstruction's point of view we find the following bremsstrahlung scenarios:

Pix	SCT	TRT	Barrel	Transition	End-cap
S	S	S	0.304	0.054	0.119
S	S	M	0.090	0.063	0.052
S	S	L	0.141	0.190	0.105
S	M	S	0.063	0.021	0.029
S	M	M	0.020	0.021	0.011
S	M	L	0.033	0.073	0.026
S	L	S	0.089	0.050	0.063
S	L	M	0.027	0.049	0.024
S	L	L	0.039	0.101	0.026
Pix = S sum:			0.806	0.622	0.455
M	S	S	0.040	0.014	0.050
M	S	M	0.009	0.017	0.024
M	S	L	0.012	0.036	0.051
M	M	S	0.005	0.005	0.014
M	M	M	0.002	0.006	0.008
M	M	L	0.006	0.016	0.008
M	L	S	0.012	0.010	0.024
M	L	M	0.002	0.014	0.013
M	L	L	0.002	0.030	0.014
Pix = M sum:			0.090	0.148	0.206
L	S	S	0.043	0.033	0.127
L	S	M	0.016	0.031	0.042
L	S	L	0.007	0.059	0.062
L	M	S	0.012	0.010	0.028
L	M	M	0.002	0.015	0.010
L	M	L	0.002	0.021	0.008
L	L	S	0.016	0.021	0.033
L	L	M	0.002	0.019	0.014
L	L	L	0.003	0.021	0.014
Pix = L sum:			0.105	0.230	0.339

Table 3.7: Expected bremsstrahlung cases in the electron reconstruction: detailed view. See text for explanation of symbols.

1. **Negligible amount of bremsstrahlung (55% of events):** below 10% energy loss by the end of the SCT. This events can be handled with the usual fitting procedure.

2. **Single measurable bremsstrahlung photon emission (12%):** above 10% energy loss by the end of the SCT. The primary photon originates from the SCT and takes more than 80% of all the emitted energy. ID bremsstrahlung recovery can be applied.

3. **Early hard bremsstrahlung photon emission (10%):** as above with the hardest brem within the pixels. Can be reconstructed with a poorer p_T resolution. It remains to be seen how well these events can be tagged.

Case	Barrel	Transition	End-cap
1	0.716	0.496	0.477
2	0.122	0.122	0.116
3	0.066	0.080	0.190
4	0.096	0.302	0.217

Table 3.8: The expected bremsstrahlung cases encountered during electron reconstruction according to a silicon oriented classification. The four cases are defined in the text.

4. **Two (or more) hard bremsstrahlung photon emissions (23%)**, early ones not excluded. Recuperation of these events is questionable as it depends on several factors. Further investigation in the reconstruction environment is necessary to determine the possible outcomes.

The numbers in brackets give probabilities over the whole η coverage. The fractions for each of the sub-regions are given in Tab:3.8. The 80% cut on brem–hardness is somewhat arbitrary. By decreasing it to 70%, 5% of the events are 'transferred' from case 4 to cases 2 and 3.

3.2 Electron reconstruction algorithm

In the framework of ATLAS software three track reconstruction packages are being maintained:

- `iPatRec` is a pattern recognition package with a combinatorial search starting in the silicon layers. It is optimised to work in roads defined by the seeds from the calorimetry or muon system to avoid unnecessary processing in on-line and high-luminosity environments.

- `PIXLRec` puts its emphasis on exploiting the fine granularity of the pixel detector. Its aim is to test an alternate algorithm for track-finding, and thus obtain a more reliable understanding of the Inner Detector performance, especially in the b-tagging area. It is not meant to be a professional package and is not optimised for speed.

- `XKalman` starts its pattern recognition in the TRT using a histogramming method. Tracks are then projected into the precision layers using the Kalman filter–smoother formalism.

In short: `iPatRec` and `XKalman` are two track finding packages with very different basic algorithms. In an experiment of ATLAS's size it is vital to have several independent programs to allow for cross-checks regarding the reconstruction efficiency and execution speed.

All the work presented here was done in the framework of `iPatRec`. As `XKalman` already has a special electron treatment built into its guts, most of the algorithms developed can be seen as an extension of `iPatRec`, giving it electron identification and bremsstrahlung recuperation abilities. Historically, `iPatRec` had the option of a bremsstrahlung fit, which allowed for a kink on the track. Following the analysis presented in the previous section it was decided that this was inadequate as a first order treatment of bremsstrahlung is only appropriate for a limited fraction of events.

The fact that the developed algorithm is in a way an extension of `iPatRec` led to another design decision. As `XKalman` is seen more like a TRT based algorithm and `iPatRec` more as a SCT based algorithm, the TRT was intentionally not taken into account with its full design capacity. The TRT's tracking information, forming a base of the `XKalman`'s track searching logic, was only considered as a bridge between the silicon and the EM calorimeter and the TR information was extracted to play its part in the e/π separation. More emphasis was put on the EM calorimeter and its matching to the silicon reconstructed tracks. This introduces a higher level of redundancy in the electron identification should it turn out that the TRT does not function as well as anticipated.

As the understanding of the algorithm requires some references to the world surrounding it, a brief description of the reconstruction environment is made first. The algorithm itself is then explained together with its inner workings, and the rationale behind the imposed logic. But first let us briefly review the goals of the algorithm.

1. **Electron identification** is a prerequisite for the algorithm. The problematic aspects of identification are the separation of electrons from photons and pions, as well as identification in jets where the ECAL is polluted with depositions from hadrons.

2. **Bremsstrahlung tagging** is important to separate the wheat from the weeds. It is essentially linked to the electron identification because bremsstrahlung can lead to a degradation of the quantities used for identification.

3. **An improvement of p_T resolution** is important especially at energies below 20 GeV where the tracker precision is better than that of ECAL. As a kind of feedback it enables a better ECAL calibration.

4. **Improvement of perigee parameters** allows for smaller errors when fitting two electrons back to their common vertex. The impact parameter resolution is closely related to the p_T resolution.

Disclaimer: It has already been shown in Sec:3.1.7 that only about 50% of electrons can be reconstructed in their full vigor. The others are of a more or less questionable nature. A lot of effort has been put in being honest about what happened to the particular electron. Also no miracles were attempted as they turn out to cause more harm than good. In the case of an early bremsstrahlung photon emission no correction is applied to the track parameters to make the track fit the EM cluster better. Rather the best measurement available from the ID is chosen and the electron is tagged as a candidate for the occurrence of a disastrous bremsstrahlung. The dubious cases are left to a later stage of the analysis to decide how to deal with them. Thus a good systematic error assessment can be made and/or the best statistics out of the available event sample can be collected.

At this point it is appropriate to give a proper name to the electron reconstruction and identification package developed. In a way it has to be more than a mere algorithm as it has to talk to the outside world and be aware of special conditions that have nothing to do with anything else but the ATLAS detector.

`ieElRec`, Ego te baptizo in nomine Patris, et Filii, et Spiritus Sancti.

3.2.1 `ieElRec`'s habitat

It is not my intention to go into the depths of the geometry description of the detector, event structure and low–level detector reconstruction. Also I will not discuss how this information is carried over into the reconstruction environment and how it's kept there. Mentioning this topic and remarking that it is far from being trivial is sufficient for my purposes.

In essence, the whole business of pattern recognition is in transforming raw measured (or simulated) data into physical quantities. This is done in several stages:

1. In the ID the measurements are 'collected' into tracks and in the calorimeters they are grouped into clusters. Clusters are subjected to calibration and algorithmic corrections which render low level calorimeter measurements mostly useless for further analysis.

2. Special identification packages are run on top of that information. Results from them can be identified particles, reconstructed short–lived particles (decaying near the collision point) or just improvements to the measurements of certain quantities.

3. Later all this information is used in an analysis program serving some more physical goal, e.g., the spectroscopy of a new particle or the study of a special decay channel.

In terms of this enumeration `ieElRec` belongs to the 2nd step. Taking the tracks and EM clusters from the 1st step (`iPatRec` and ECAL reconstruction) it identifies electrons, determines what and where went wrong (i.e., bremsstrahlung identification), corrects what can be corrected (i.e., bremsstrahlung recuperation) and provides information used for background rejection.

Basics of `iPatRec`

As already mentioned above, `iPatRec` is optimised to run in roads defined by the calorimetry or muon system (with the general term `seed` used to describe any of the above). A road is a region of the detector obtained by projecting the η and φ coordinates of the seed to the vertex region. The algorithm can be made to work over all coverage of the ID by decomposing it into several roads with a small overlap in η and φ.

After initialization of the road `iPatRec` gathers all silicon hits within the road. The SCT hits from the same module are joined into *space-points* which are used in the search initiation phase only. The pixel hits form space-points directly. Then the combinatorial searches start. The result of the search is of course a list of tracks. Three types of tracks can make it to this final list:

- **Primary tracks** are full length tracks from the vertex region to the outer regions of the TRT.

- **Truncated tracks** have an association to the vertex region but fail the outward extrapolation.

- **Secondary tracks** fail the vertex association but succeed in outward extrapolation to at least some part of the TRT.

All of them are subjected to a quality control which assures a good efficiency and a low fake rate. The standard sample used for checking that the tracks have good quality are b-jet events with high luminosity pile-up which gives the highest detector occupancies expected in ATLAS.

A brief and crude description of the combinatorial search is given here as it is needed for an understanding of the track types produced by `iPatRec` and used by the electron reconstruction algorithm.

All in all there are ten combinatorial searches performed per road. Each of them is seeded from the combinatorials constructed from the space-points coming from a pair of layers designated as ‘outer’ and ‘inner’ layers. The choice of these search initiating layers is optimised with respect to execution speed and to give sufficient robustness against a realistic level of detector inefficiencies. Special patterns, targeted at short tracks (truncated and secondary) visible only in the inner or outer layers of the tracker are also included. For example the first search is performed by considering the combinatorials from the outermost and second SCT layer. The following is a more algorithmic transcription of the `iPatRec`’s search logic.

1. The first loop is made over all ‘outer’ points. For each of the outer points a reference to the best track is kept through the inner loops for each of the three kinds of tracks mentioned above. These are not their exact counterparts but rather candidates that are waiting to be promoted to this status. There is an implicit assumption that hits are unique – can only belong to one track – in the ‘outer’ layer.

2. The second loop is made over all ‘inner’ points. For each of the combinatorial *candidates* a loop is made over all points in ‘check’ layers until a first point compatible with the hypothesis of the track originating from the interaction point is found. Otherwise this combination is discarded.

3. A two point track is first constructed from the inner and outer point and interaction point constraint. Then interpolation is performed between these two points. If the interpolation succeeds we have at least three layers in the game and we're dealing with what is named a *track segment* and has all the track parameters defined by a fitting procedure. If the interpolation fails, we move on to consider the next inner point (2).

4. For each segment a list of compatible vertex points is created and for each of them interpolation from the 'outer' point to the vertex region is attempted. For the successful associations extrapolation to the outer SCT layers is performed and both tracks are offered as a replacement for the best track candidates (primary and secondary) found for the current outer point.

5. When all the combinations for a given outer point are exhausted the time comes to assess the new candidates (if any). The TRT association is attempted for the primary candidate and if it succeeds the truncated and secondary candidate are bluntly deleted and the new born primary is checked for ambiguities against the existing list of tracks upon insertion into the list of found tracks. Otherwise the truncated candidate (subjected to the same ambiguity check) is inserted into the track list and the secondary track is inserted into the list of pending secondaries.

At the end of the road processing the list of pending secondaries is scrutinized. Special care is taken to make the best possible TRT association for each group of the ambiguous secondary candidates.

As combinatorial searches can become very inefficient if they are taken too literally, the inner workings of `iPatRec` take special care not too replicate the effort i.e. duplicated tracks produced by the combinatorial search are suppressed in the moment their duplicity becomes obvious. This is essential if `iPatRec` is to be useful in the computationally intensive trigger environment.

Information available to `ieElRec`

`ieElRec` is entered at the end of each road processing. Its main input parameters are the road's center and width in η and φ together with the track list originating from the preceding track reconstruction package. `ieElRec` is independent of the seeding method used as it searches through the data produced by the ECAL and HCAL reconstruction for clusters lying within the road. Therefore the first level reconstruction entities used in `ieElRec` are:

- the list of tracks produced by `iPatRec`;
- access to the list of ECAL clusters and
- access to the list of HCAL clusters.

It is worth mentioning that the HCAL clusters include the energy deposited in the ECAL.

Another input to `ieElRec` is of a completely different nature. As already argued in several passages of Sec:3.1, matching the track parameters projected to the ECAL with the corresponding EM cluster provides valuable information. Another aspect of the EM clusters turned out to be of great importance in the pion rejection: namely the depth profile of the EM shower and leakage into the hadronic calorimeter. To get a good parameterization of these quantities a large sample of single electrons and positrons was produced in the $1.5\,\mathrm{GeV} \leq \mathrm{p_T} \leq 60\,\mathrm{GeV}$ energy range. The distribution of the generated events was flat within the range $-2.5 \leq \eta \leq 2.5$. Additionally, a smaller sample of single pions was also produced to measure the pion rejection efficiency. The produced data-sets with respective sample sizes are tabulated in Tab:3.9. All these productions were carried out with the "Physics TDR layout" and with the realistic magnetic field. Please note that all the data samples used for the "Physics TDR" were generated using a constant field approximation.

Energy [GeV]	No. $e^{\pm}$ [k]	No. $\pi^{\pm}$ [k]
1.5	60	12
2	60	12
3	60	12
5	40	2
10	30	2
20	30	2
30	20	2
40	20	2
50	12	2
60	10	2

Table 3.9: $e^{\pm}$ and $\pi^{\pm}$ single particle productions. All event samples are equally split into the particle/antiparticle halves.

For each of the $e^{\pm}$ event samples the following six quantities were histogrammed for all primary tracks found by `iPatRec`:

1. $\delta\varphi \sim -\mathrm{sgn}(\mathrm{p_T})(\varphi^{\mathrm{E}} - \varphi^{\mathrm{iPat}})$ the difference in φ of the EM cluster and track's projection to the ECAL. The sign of track's p_T was used to correct for differences between the electrons and positrons;

2. $\delta\eta \sim \eta^{E} - \eta^{\mathrm{iPat}}$ the difference in η of the EM cluster and track's projection to the ECAL;

3. $\delta p \sim 2(E_T^E - |p_T^{\mathrm{iPat}}|)/(E_T^E + |p_T^{\mathrm{iPat}}|)$ the difference between transverse energy measured by the ECAL and absolute value of the momentum measured in the tracker normalized by the mean energy of the EM cluster and the track;

4. $\delta E_1^2 \sim E^2/E^1$ the ratio of energies measured in the second and first sampling of the ECAL;

5. $\delta E_s^3 \sim E^3/E$ the ratio of energies measured in the third sampling of the ECAL and all the energy contained within the EM cluster;

6. $\delta E_e^h \sim E^H/E^E$ the ratio of energies measured in the HCAL and ECAL cluster.

All samples were divided into seven $|\eta|$ bins with the fences posted at the values 0, 0.3, 0.6, 1.0, 1.4, 1.8, 2.2 and 2.55. A look-up table was constructed out of the mean values and rms's of the distributions (quantities 2 and 3 were fitted with a Gaussian and the mean value and standard deviation used instead). The δX symbols will be used for the normalised residuals in later discussion. Fig:3.13 gives an example of these distributions.

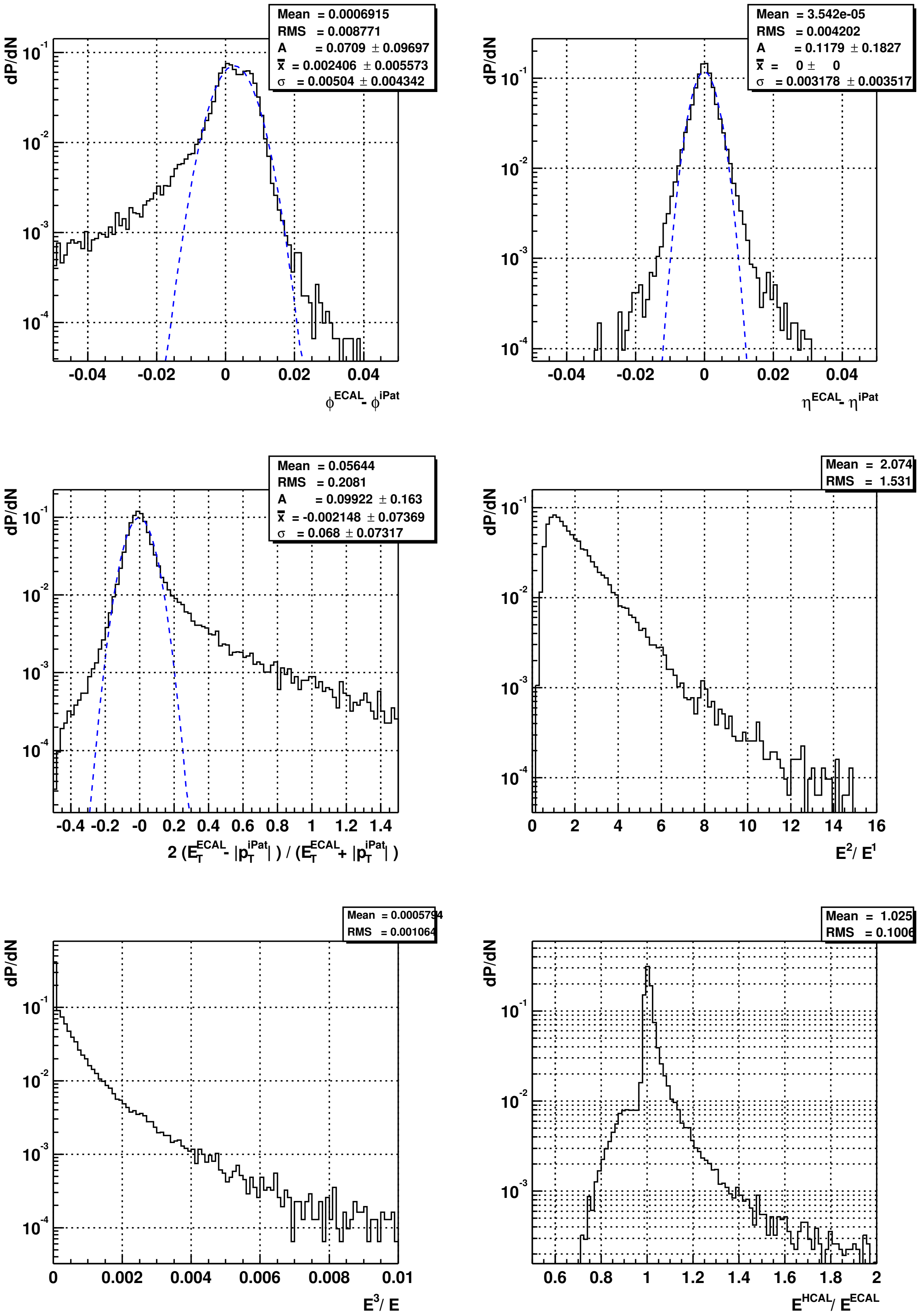

Figure 3.13: Examples of the distributions of quantities relevant for the electron reconstruction (see text for details). The sample used was $p_T = 5\,\mathrm{GeV}$ $e^{\pm}$s over all ID η. For the first three plots the Gaussian fit is superimposed.

3.2.2 Description of `ieElRec`

As already mentioned `ieElRec` itself is invoked for each of the roads analysed by `iPatRec`. But as the roads can be overlapping, the notion of an event is also known to `ieElRec`. In the same spirit as `iPatRec` produces list of tracks in road as its output, `ieElRec` outputs a list of electron candidates equipped with additional information. A detailed account of the information provided will be given by the end of the description.

Per event chores

Initialization of `ieElRec` is basically just re-initialization of the electron candidate container. It is then filled with the candidates coming from roads and a cross check is made if a candidate with the same ID track is already in it. If it is, the better one is kept. The meaning of *better* will become more obvious in later sections.

Road processing

First a list of ECAL clusters compatible with the current road is created and sorted by the cluster energy. This helps in resolving the ambiguities when several EM clusters are produced by a single electron with a hard bremsstrahlung. Then a loop over the clusters is entered. In it, three things happen.

1. The HCAL cluster that encompasses the ECAL cluster is searched. Especially at low energies there may be no HCAL association.
2. Pre-selection of tracks matching the cluster is made and the isolation is studied.
3. The detailed analysis is performed, followed by the selection and tagging of the tracks that made it through the needle's eye.

The details follow ...

Preselection is done in two steps. As we are selecting tracks from a road that can be much wider than reasonable for EM clusters, the first check excludes all tracks not satisfying the $|\eta^E - \eta^t| < 0.1$ cut. Passing this cut the normalized residuals for the track–cluster pair are produced from the look-up table (see the enumeration in Sec:3.2.1) and stored in a hash map for faster processing. At the same time χ^2 per degree of freedom is calculated for the first three variables (the ones with explicit dependence on the track parameters).[1] The tracks that are to pass are subjected to the following cuts:

- $|\delta\eta| < 50$ This cut is harmless to the electrons and is in some regions even looser than pre-pre-selection cut on the η matching. We need it to be rather large as isolation determination is based on the number of preselected tracks.
- $\chi^2 < 2500$ This one looks entirely out of proportion. Yet there are still some electrons that fail it miserably. These are the cases with more than 50% energy loss by the end of the pixels. Although there is not much hope for such deviant cases they're kept for their contribution to the electron identification.

[1] Its probability distribution is far from the χ^2 thingy known from the books about statistics as the original distributions are not Gaussian. It is used in the same sense however ... and also computed in the same way. Hence the name was kept.

Tracks of each kind (primary, truncated and secondary) are kept in separate containers. Each of the containers is sorted by $|\delta\eta|$ so that the more probable candidates will be processed first. Remember that matching in η is not spoiled by a bremsstrahlung.

Next the number of primary and truncated tracks is summed. If several tracks are found it means we're in a jet. This is important as different cuts are used for isolated and non-isolated tracks. Also ... if we're dealing with an isolated track we can afford a little more magick and recuperate the hard bremsstrahlung cases which produced two or more EM clusters. The procedure relies on the fact that in this case the HCAL cluster contains all of them properly weighted. (As mentioned before, the ECAL reconstruction applies per cluster corrections and merging them directly would lead to an even bigger error.) But there is still a chance of a neutral hadron making an invisible contribution to the HCAL cluster. Here is the collection of cuts that help us evade this possibility:

- $1 < E^H/E^E < 2.5$ Remember that EM clusters are sorted by energy and that we're targeting at merging two or at most three clusters.
- $\mathsf{rms}(\eta_H) < 0.06$: the spread of HCAL's cluster energy in η should be small. Both of these cuts are also targeted at the suppression of further processing of hadrons that left some of their energy in the ECAL. Their typical signature is a large $E^{\mathrm{HCAL}}/E^{\mathrm{ECAL}}$ and a width in η around 0.1.
- The EM clusters with their centers within $\eta_H \pm 2 \times \mathsf{rms}(\eta_H)$ and $\varphi_H \pm 2 \times \mathsf{rms}(\varphi_H)$ are searched for and their energy added to that of the current cluster. The sum of the EM energy should fulfill the requirement $1.1 \times \sum_{i\in\mathrm{cut}} E_i^E > E^H$.
- In case when no additional EM clusters are found and we have an electron candidate, the above cut is replaced by a requirement that matching to the HCAL cluster is better than to the ECAL one. This recovers catastrophic bremsstrahlung cases in the last layers of the SCT or in the TRT.

If all these happens to be true the current EM cluster is replaced by the content of the HCAL cluster and the rest of the EM clusters that were used up are wiped out of the road's list. As this procedure has certainly disrupted the residuals for our electron candidate, they are recalculated.

Primary cuts are applied to the preselected tracks before they enter the inner mechanism of `ieElRec`. For isolated tracks they are:

$$|\delta\eta| < 10 \quad \wedge \quad \chi^2 < 100 \qquad \text{or} \qquad |\delta\eta| < 4. \tag{3.2}$$

Of course, for the second variant the pre-selection χ^2 cut still applies. In jets we're a bit more picky as it is hard to estimate the authenticity of the EM cluster:

$$|\delta\eta| < 6 \quad \wedge \quad \chi^2 < 100. \tag{3.3}$$

These cuts are only applied to the primary and truncated tracks. Having a truncated track that passed the cuts, a matching secondary is searched for and attached onto its tail.

Candidate scrutinization is the core of `ieElRec`. Its logic is based on the results presented in Sec:3.1 and a later fine–tuning on the problematic events.

Pixel, Head and SCT fits of the track are built first. The pixel fit contains the first three measurements and the head fits are obtained by a successive addition of the layers up to the last SCT measurement. If the candidate is a truncated track, the head fits outside of candidate's original hits are suppressed (if a secondary is attached, its hits form a prolongation through the SCT into the TRT). The SCT fit is done for all hits belonging to the SCT. In case of a truncated track without an associated secondary it can happen that there isn't enough measurements available.

It was attempted to use the pixel $r\varphi$ residuals of the SCT fit for the early bremsstrahlung detection but mean values of the obtained distributions were negligible compared to their spread. Therefore no information could be extracted from them.

Selection of the best track fit is a bit trickier than anticipated due to the effects of multiple scattering. Three cases are considered in the following order:

1. **Pixel-only fit** is accepted if:

$$\chi^2_{\mathrm{pix}} < \chi^2_{\mathrm{i}} \quad \wedge \quad |p_T^{\mathrm{pix}}| > |p_T^{\mathrm{i}}|, \qquad \text{for all i},$$

   where index i applies to the head fits.

2. `iPatRec` **fit** (primary or truncated) is taken if multiple scattering effects are obvious. The SCT fit must exist for further consideration and its p_T measurement must yield a larger value than all the head fits:

$$|p_T^{\mathrm{sct}}|/|p_T^{\mathrm{i}}| > 1.015 \quad \wedge \quad \chi^2_{\mathrm{sct}} > \chi^2_{\mathtt{iPatRec}}, \qquad \text{for all i}.$$

   Index i iterates over head fits.

3. **Head fit** with the smallest χ^2 is selected otherwise.

Candidate labeling provides the tracks with information about the detected bremsstrahlung, quality of matching with the ECAL cluster and pion ambiguity level. In most of the cases the goodness of match and bremsstrahlung type are closely correlated. The information available is scarce and heavily hidden under the rug of multiple scattering so it is hard to provide but the most general information. Regarding the bremsstrahlung `ieElRec` separates four cases: no relevant bremsstrahlung (`B1`), a hard bremsstrahlung photon emission in the pixels(`B2`) or in the SCT(`B3`). The last case is a possible catastrophe(`B-1`), a very hard bremsstrahlung occurring in the beam-pipe or b-layer which results in a failure of extrapolation of the track into the b-layer.

ECAL/ID matching is based on the cuts in the δp-$\delta\varphi$ plane. Again one cannot do much magick without producing spurious artefacts. The following enumeration presents the possible cases and their respective cuts. The first matching case is accepted.

M1 **Good match** corresponds to the cuts $|\delta p| < 3 \wedge |\delta\varphi| < 3$. There exists a subset of these events that does not associate to the b-layer and members of which are candidates for an early catastrophic bremsstrahlung. To differentiate between the two cases, we label the events with the b association as **M1b** and bremsstrahlung type `B1`, while those without the b association get a bremsstrahlung type `B-1`.

It is possible to get a sample with a 'cleaner' p_T signature by further narrowing of the residual cuts. As these are the *representative* sets of events, the b-layer association is required. Later we will study two subsets in further detail:

M1b$^+$ with cuts $\delta p < 1 \ \wedge \ \delta\varphi > -1$ and

M1b^{++} with cuts $\delta p < 0 \ \wedge \ \delta\varphi > 0$.

M2 **Imprecise ECAL**. Especially at low energies, where the tracker is still precise, it is quite frequent to get a good p_T measurement but not too good match with the EM cluster. These cases are obtained by applying the cut $-3 < \delta p < 1 \ \wedge \ -10 < \delta\varphi < -3$. Bremsstrahlung type remains undetermined.

M3 **Poor ID** corresponds to an early bremsstrahlung in pixels where only a poor p_T measurement can be made. The applied cuts are: $\delta p > 1 \ \wedge \ \delta\varphi < 3$. Quite obviously, this corresponds to the `B2` brem-type.

M4 **Poor ECAL** is a variation on the theme of **M2**, enhanced by a post p_T measurement hard bremsstrahlung which causes the electron to spiral way to far in φ. The cut is $\delta p < -3$. No cut is applied to φ as it can become basically anything. Many pions sneak through this classification but are later identified by the longitudinal profile of the EM cluster. Bremsstrahlung wise, these are labeled as `B3`

M0 **Unknown** ... which simply means that the event has failed all the above options.

Pion ambiguity (A_π) is expressed as a signed integer obtained by summing together the *pion/anti-pion signals*. They are extracted from the track's behaviour, the TR information and EM cluster properties.

1. A weight of $|\delta p|/3$ is assigned to candidates originating from a primary track with $\delta p < -3 \ \wedge \ \delta\varphi > -3$. This signals a "missing" energy in the ECAL without a brem correlation which would suggest $\delta\varphi < 0$.
2. Selection of the pixel fit is considered an anti-π signal with a weight -1.
3. The TR information contributes a weight in the range from 2 to -2 and is based on percentage of the TR hits. Inner fences are posted at 5%, 10%, 16% and 26%; e.g., tracks with 10 to 16% of the TR hits are assinged a weight of 0.
4. Each of the longitudinal EM residuals (δE_1^2 and δE_s^3) contributes a weight of $+1$ if $\delta E > 3$ and a weight of $+2$ if $\delta E > 6$.

This served mostly as an introduction as the relevance of these categories can only be proven in action. Also ... it introduced the nomenclature and notation.

3.3 Results for single electrons

`A notational convenience:` throughout this section p_T and E_T are shamelessly used as shorthands for "p_T (or E_T) measurement provided by `ieElRec`". Please note that these symbols are also used as "the true transverse energy". In dubious cases they are set as $E_T^{\rm true}$ or $p_T^{\rm true}$.

For all results presented in this section, the reduced ECAL clustering cut of $E_T^{\rm EM} = 0.7\,{\rm GeV}$ was used for $E_T^{\rm true} \leq 5\,{\rm GeV}$ (see Sec:3.1.5).

3.3.1 Efficiency

As already mentioned the electron reconstruction inefficiency at low energies is dominated by the EM reconstruction (see Tab:3.3). In all following discussion the efficiencies are quoted for the events that produce an EM cluster. In more than 99% of cases an inefficiency of `ieElRec` is in fact an inefficiency of `iPatRec`. And again ... most of these can be attributed to a disastrous bremsstrahlung.

The first thing of interest is *Electron identification efficiency.* It should be interpreted as: if we have an isolated ECAL cluster produced by an electron, what is the probability of finding and assigning an ID track to it. The dependence of efficiency on transverse energy and $|\eta|$ is shown in Fig:3.14. The efficiency is increasing with E_T as there is less and less probability for a catastrophic bremsstrahlung to cause the electron to spiral along the magnetic field before obtaining the minimum number of position measurements. The $|\eta|$ dependence follows the material distribution. In the very last bin we can observe a drop in the efficiency as we are approaching the limit of the ID coverage.

Another thing is how well these electrons are reconstructed. For an analysis that needs electron tracks reconstructed with a high precision the electron reconstruction efficiency is only the first step toward obtaining a good electron sample. Fractional decomposition into the types of track matching can now be enumerated. For its true meaning one should combine these fractions with resolutions that accompany them, and that will be discussed in later sections.

The table showing the efficiencies/probabilities (Tbl:3.10) grew quite large. It is not my intention to overwhelm the reader but rather to provide the detailed information for cross-checks and comparison with other reconstruction programs.

3.3.2 p_T resolution and E/p

Overview of match types

For warm-up, let us begin with some raw $p_T^{\rm true}/p_T$ distributions. The intention is to make an overview of the different ID/ECAL matching types and to further classify the events that failed to make a good association (aka **M1**).

Comparison of all the reconstructed tracks to those that make a good match (**M1** and **M1b**$^{++}$ classes) is shown in Fig:3.15. The important thing is that the bremsstrahlung tails are effectively suppressed by the application of the cuts. Purity of the **M1** samples is better at higher energies where the effects of the multiple scattering are negligible. Further analysis of the mean values, resolutions and tail content will be made later when studying the E_T/p_T distribution.

E_T	η	ECAL	`ieElRec`	M1	M1b	M1b$^+$	M1b^{++}	M2	M3	M4	M0
1.5	all	70.91	93.31	81.91	76.87	66.75	28.12	2.69	1.43	4.05	3.24
	barrel	84.89	96.67	82.17	78.89	66.57	27.81	2.19	0.34	5.80	6.17
	transition	52.62	93.07	79.70	74.01	64.02	28.67	4.69	0.42	4.85	3.40
	endcap	97.02	90.62	84.30	78.50	70.15	27.73	0.74	3.60	1.54	0.44
2	all	89.12	94.23	79.20	74.04	64.03	27.46	3.36	2.70	6.15	2.81
	barrel	97.72	97.01	79.54	76.07	64.70	26.11	3.11	0.86	8.86	4.64
	transition	80.35	93.60	77.49	71.95	61.41	25.93	5.15	0.72	7.33	2.92
	endcap	99.66	92.60	81.88	75.72	67.96	31.46	0.47	7.98	1.43	0.84
3	all	97.08	95.30	78.93	74.35	64.56	29.00	3.24	4.75	6.20	2.17
	barrel	99.98	97.65	80.34	77.95	66.81	26.07	2.26	1.37	10.25	3.44
	transition	94.45	94.55	77.35	72.19	62.33	27.31	5.25	2.64	6.81	2.50
	endcap	99.87	94.46	80.78	75.17	66.89	35.45	0.09	12.53	0.86	0.20
5	all	99.30	96.28	82.16	78.71	69.90	35.45	2.27	6.98	4.03	0.84
	barrel	100.00	98.30	85.49	83.72	74.35	32.65	2.35	3.09	6.21	1.17
	transition	98.65	95.90	82.13	77.88	68.90	34.38	3.30	4.86	4.56	1.05
	endcap	99.97	95.05	78.86	75.39	67.50	40.55	0.02	15.40	0.71	0.07
10	all	99.86	97.08	85.20	83.02	74.13	41.67	0.68	9.27	1.77	0.17
	barrel	99.99	98.56	88.62	87.21	78.65	39.53	1.23	5.53	2.96	0.21
	transition	99.82	97.02	86.53	83.78	74.88	42.41	0.74	7.67	1.85	0.22
	endcap	99.83	95.75	78.95	77.28	68.06	42.19	0.01	16.37	0.41	0.00
20	all	99.99	97.88	86.20	84.87	75.79	44.43	0.04	10.47	1.14	0.03
	barrel	99.99	99.34	90.65	89.49	80.37	42.93	0.08	6.78	1.80	0.03
	transition	100.00	97.74	87.29	85.67	77.12	46.82	0.04	9.32	1.05	0.04
	endcap	99.96	96.68	79.25	78.39	68.16	40.70	0.00	16.79	0.65	0.00
30	all	100.00	98.34	86.35	85.31	75.72	44.99	0.00	10.85	1.12	0.02
	barrel	100.00	99.05	89.68	88.57	78.76	43.24	0.00	7.50	1.83	0.04
	transition	100.00	98.58	88.00	86.79	77.74	48.16	0.00	9.65	0.92	0.01
	endcap	99.98	97.08	79.31	78.72	68.14	39.81	0.00	16.95	0.83	0.00
40	all	99.98	98.54	86.50	85.58	75.93	44.91	0.00	10.80	1.25	0.00
	barrel	100.00	99.42	88.64	87.40	77.82	44.38	0.00	8.69	2.09	0.00
	transition	100.00	98.69	87.71	86.74	77.57	47.54	0.00	9.90	1.07	0.00
	endcap	99.94	97.33	81.64	81.17	70.37	39.62	0.00	14.93	0.76	0.00
50	all	99.98	98.77	86.56	85.66	76.56	44.68	0.00	10.99	1.23	0.00
	barrel	100.00	99.39	87.93	86.50	76.23	41.55	0.00	9.32	2.14	0.00
	transition	100.00	99.01	87.71	86.83	78.43	49.08	0.00	10.23	1.07	0.00
	endcap	99.93	97.57	82.53	82.14	72.73	38.12	0.00	14.42	0.61	0.00
60	all	100.00	98.89	86.83	86.02	76.43	45.85	0.01	10.86	1.19	0.00
	barrel	100.00	99.68	89.45	88.54	77.31	44.84	0.05	8.29	1.90	0.00
	transition	100.00	99.01	87.86	86.94	77.64	47.75	0.00	10.13	1.01	0.00
	endcap	100.00	97.85	81.95	81.49	72.88	42.74	0.00	15.03	0.87	0.00

Table 3.10: Efficiencies relevant for `ieElRec` (all given in %). For completeness the ECAL reconstruction efficiency and electron indentification efficiencies are also presented. Types of matching (**Mx**) are explained in Sec:3.2.2. Please note that cases under **M1x** are subsets of **M1**. η regions used are the same as throughout Sec:3.1: barrel $\sim\ |\eta| \leq 0.6$, transition $\sim\ 0.6 < |\eta| \leq 1.9$ and end-cap $\sim\ |\eta| > 1.9$.

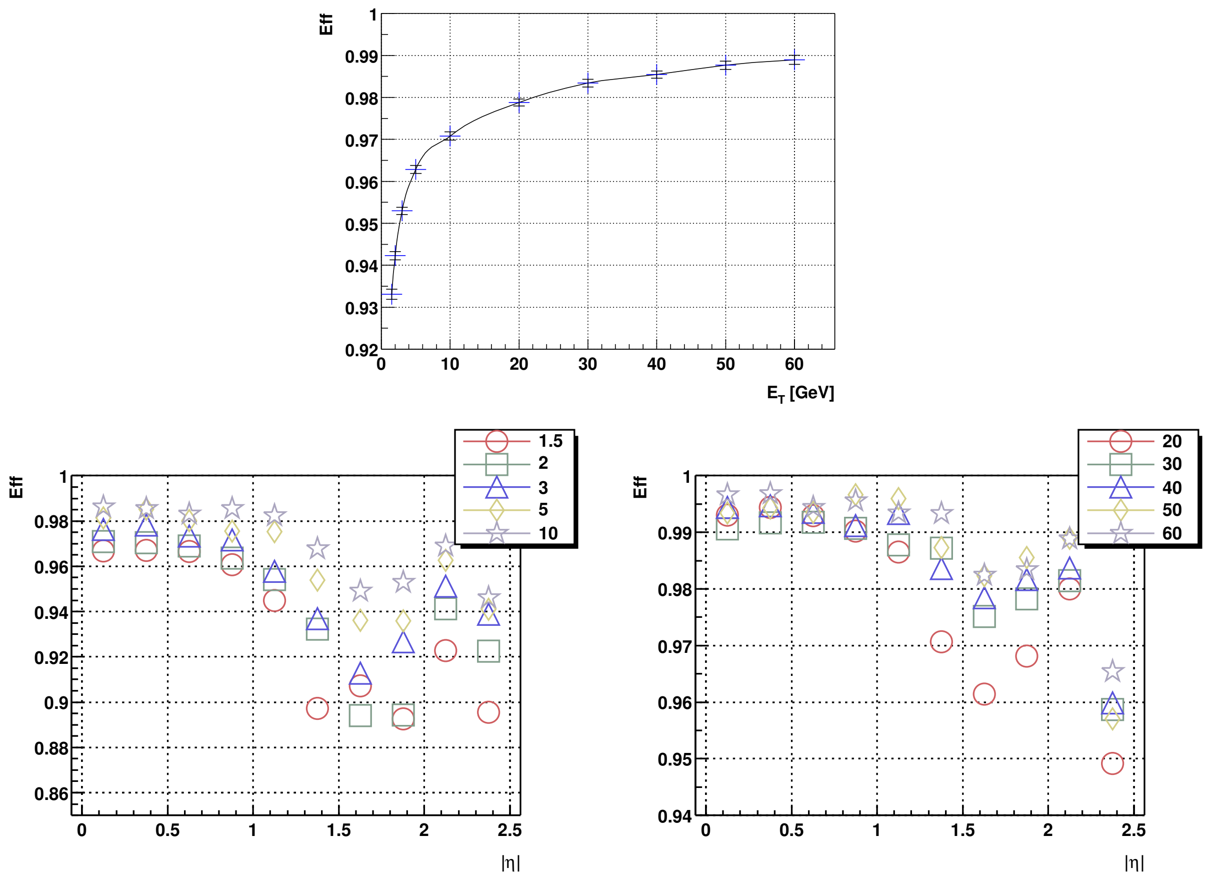

Figure 3.14: Electron identification efficiency of `ieElRec` versus transverse energy over all ID coverage (top). Efficiencies versus $|\eta|$ for different transverse energies (left: E_T from 1.5 to 10 GeV, right: 20 to 60 GeV).

Next we consider match types **M2** and **M4** which are supposedly only relevant at lower energies. Raw p_T^{true}/p_T distributions for low energies are presented in Fig:3.16. To give a more quantitative description one should combine the fractional probabilities (Tab:3.10) with Fig:3.17, which shows mean values and rms's of both p_T^{true}/p_T and E_T/E_T^{true}.

M2 is occurring only up to $E_T \sim 20\,\text{GeV}$ with a fractional probability of about 2%. We see that both p_T and E_T are underestimated on average and that the p_T measurement *is* better over all region of validity. At $E_T = 20\,\text{GeV}$ this match type becomes very unlikely so the statistics for these entries in Fig:3.17 is insufficient ($\sim$ 12 events).

M4 is suppressed by the ECAL clustering cut at very low energies (up to 2 GeV) where one would expect it to flourish. So it peaks at 5% for $E_T \sim 3\,\text{GeV}$ and then falls to slightly above 1% for transverse energies above 10 GeV. Note that the p_T measurement is satisfactory up to 20 GeV and that the E_T measurement is quite bad. Also note that the E_T measurement is of approximately the same quality as p_T at 30 GeV which implies that the **M4** match type should only be considered seriously up to this energy.

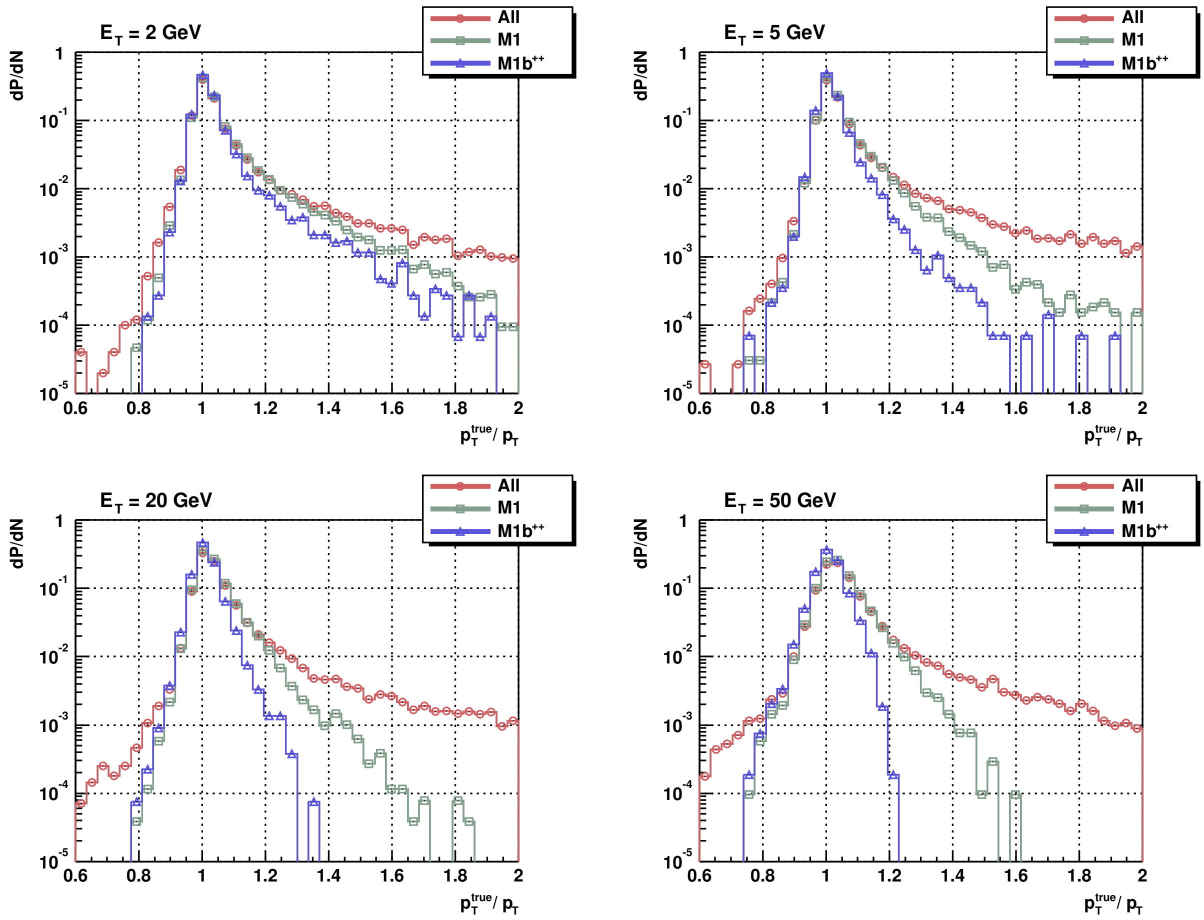

Figure 3.15: $p_T^{\rm true}/p_T$ distributions of all electron tracks and match types **M1** and $\mathbf{M1b}^{++}$ for transverse energies 2, 5, 20 and 50 GeV.

M0 has a certain relevance up to $E_T \sim 10\,\mathrm{GeV}$ with a fractional probability at the 1% level. Both the p_T and E_T are underestimated. The p_T is better up to $E_T \sim 2.5\,\mathrm{GeV}$ where the E_T measurement takes over with an under-estimation of the energy of about 15%.

M3 corresponds to a poor p_T measurement. Its fractional probability starts low ($\sim$ 1%) at $E_T = 1.5\,\mathrm{GeV}$ and increases steadily to $\sim$ 10% at 20 GeV where it takes over the event classes belonging to **M2** or **M0** at lower energies. For higher energies it remains constant at the same level. Consider Fig:3.18 which presents the details of the p_T and E_T measurements. p_T is indeed poor over all energy range. By considering also all the events and **M1** (Fig:3.15) one can observe that a large fraction of the bremsstrahlung tails is slurped into the **M3** category. As we're dealing with the early bremsstrahlung cases it is no surprise that the E_T measurement is also spoiled at lower transverse energies where bending power of the solenoidal field is sufficient to split the electron–photon pair. This effect becomes negligible at $E_T \sim 30\,\mathrm{GeV}$.

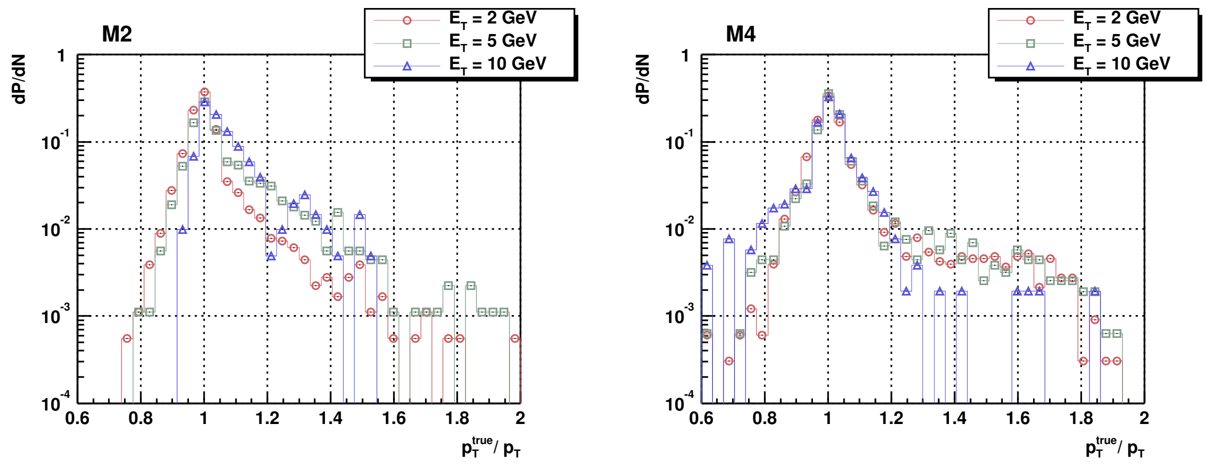

Figure 3.16: p_T^{true}/p_T distributions of match types **M2** and **M4** for transverse energies 2, 5 and 10 GeV.

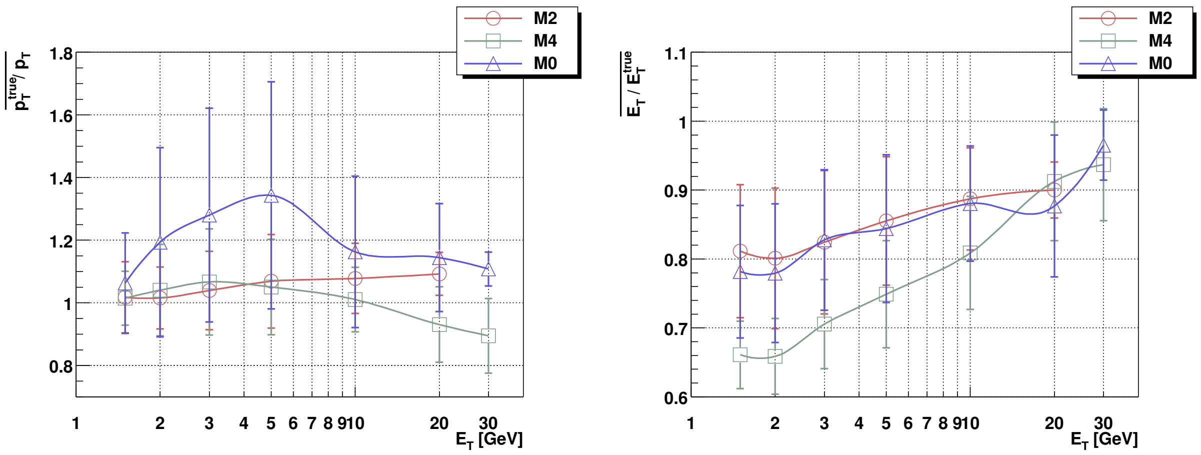

Figure 3.17: The mean values and rms's (error bars) of the p_T^{true}/p_T (left) and E_T/E_T^{true} (right) distributions versus transverse energy. The match types shown are **M2**, **M4** and **M0**.

Improvement of the p_T measurement by `ieElRec`

As `iPatRec` is desperately trying to make the tracks as long as possible it is not infrequent for it to overshoot beyond reasonable limits. The method of accepting one of the head-fits (see Sec:3.2.2) is trying to correct this feature as it is a bug in case of electrons. To estimate if it is doing any good, the following quantity was studied:

$$\Delta_{p_T}^{\texttt{ieElRec}} = \frac{|p_T^{\text{true}} - p_T^{\texttt{iPatRec}}| - |p_T^{\text{true}} - p_T^{\texttt{ieElRec}}|}{|p_T^{\text{true}}|}. \tag{3.4}$$

This quantity measures the difference of the p_T mismatch for the track candidate obtained from `iPatRec` and for the final electron fit chosen by `ieElRec`. Positive values mean improvement of the p_T measurement and the negative ones a degradation. Fig:3.19 shows the behaviour of $\Delta_{p_T}^{\texttt{ieElRec}}$. There is a strong η dependence (following the material distribution) and the average improvement of the p_T is increasing from about 1% at $E_T = 1.5\,\text{GeV}$ to 4% at 60 GeV. The **M3** case gives a better correction but it shouldn't be taken too seriously

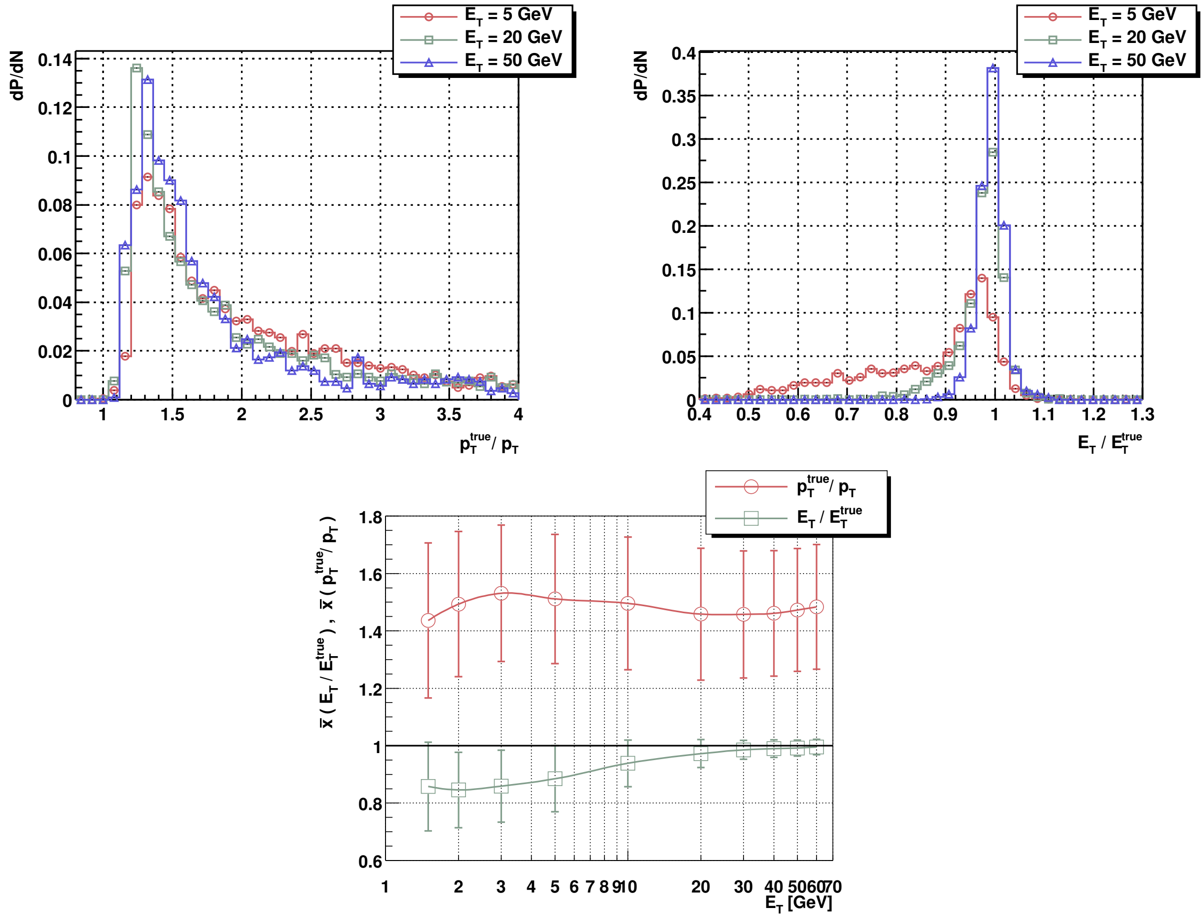

Figure 3.18: Scrutinization of **M3**. Top two plots show raw p_T^{true}/p_T and E_T/E_T^{true} distributions for typical energies. Note that x-axis scales are radically different. The bottom one presents mean values and rms's of the two distributions versus E_T.

as the p_T measurement is screwed in this case anyway and can't be resurrected but with a divine intervention.

Resolutions, E/p and tailers

Let us give some further consideration to the p_T^{true}/p_T and E_T/E_T^{true} distributions for good match types. To arrive to the statistical description, the distributions were fitted with a Gaussian curve in a $\pm 2 \times$ rms range around the center. The mean values and resolutions obtained in this way are shown in Fig:3.20. As far as the p_T measurement is concerned, improved matching types (**M1b**$^+$ and **M1b**$^{++}$) provide a progressively better mean value and resolution. For the E_T measurement the mean value of **M1b**$^{++}$ is slightly less good at low energies (up to $E_T \sim 10\,\text{GeV}$). The p_T resolutions for **M1b**$^+$ and **M1b**$^{++}$ are better in this energy range and **M1b**$^+$ provides a good compromise between the E_T and p_T accuracy.

For those searching the best energy measurement available, we can summarize the results in the following points. For $E_T \leq 10\,\text{GeV}$ the p_T measurement is better, regardless of the type of matching. In the intermediate energy range ($10\,\text{GeV} < \text{E}_\text{T} \leq 30\,\text{GeV}$) the p_T measurement is better for events belonging into **M1b**$^{++}$. Otherwise the E_T measurement is better. At higher energies ($E_T > 30\,\text{GeV}$) the E_T measurement is always better.

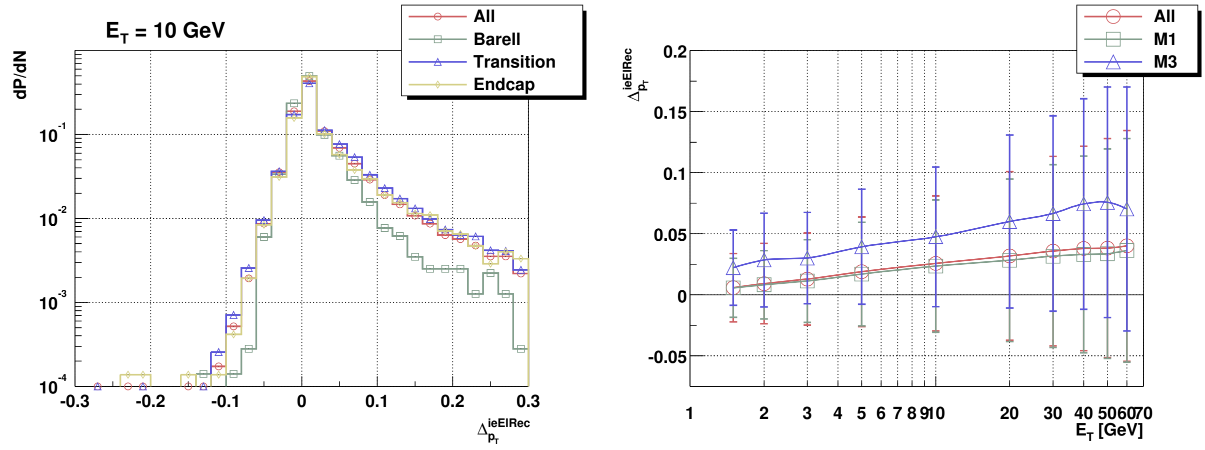

Figure 3.19: Behaviour of the $\Delta_{p_T}^{\mathtt{ieElRec}}$ parameter. Raw distributions for all events and for the three $|\eta|$ regions are shown for $E_T = 10\,\mathrm{GeV}$ (left). Dependence of the mean value and rms on the transverse energy is given in the right plot.

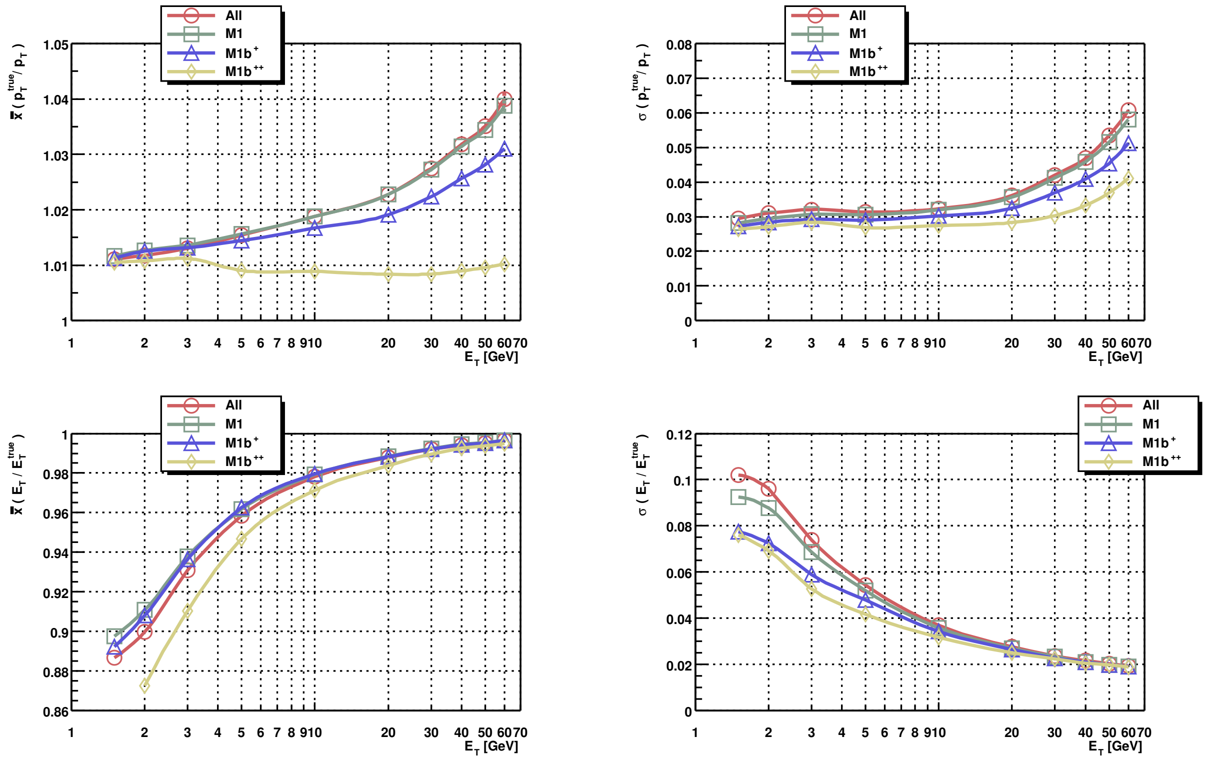

Figure 3.20: The mean values (left) and resolutions (right) of the p_T^{true}/p_T (top) and E_T/E_T^{true} (bottom) versus the transverse energy.

The $|\eta|$ dependence of the parameters of Gaussian fits to the p_T^{true}/p_T and E_T/E_T^{true} distributions is shown in Fig:3.21. Plots for $E_T = 5, 40\,\mathrm{GeV}$ are chosen as the representatives for the two energy regions. Basically what we're looking at is the material distribution which is in the case of $\bar{x}(E_T)$ modulated by all the bremsstrahlung misfortunes mentioned before.

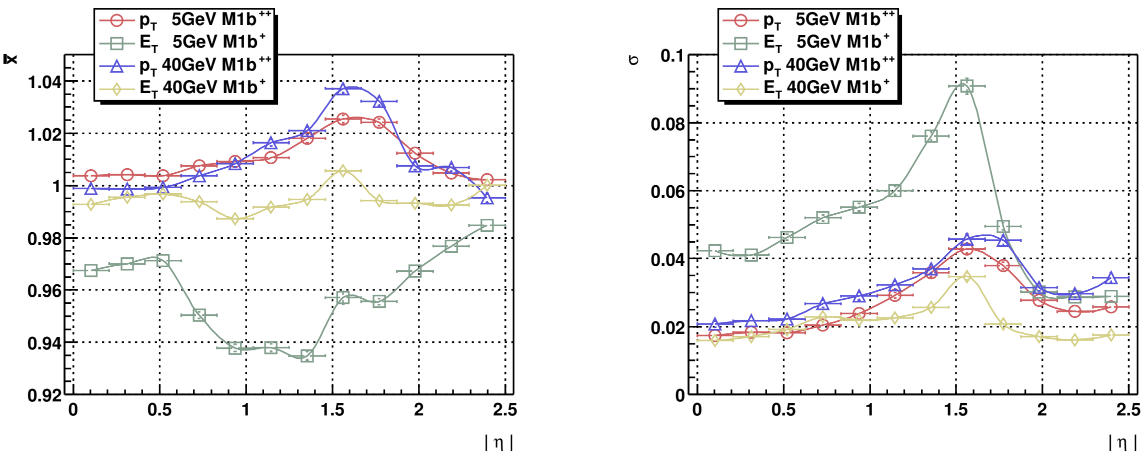

Figure 3.21: $|\eta|$ dependence of the mean values (left) and resolutions (right) of the$p_T^{\rm true}/p_T$ and $E_T/E_T^{\rm true}$ distributions for $E_T = 5$, $40\,$GeV. $\mathbf{M1b}^{++}$ and $\mathbf{M1b}^{+}$ samples were used for obtaining values for the p_T and E_T respectively (as labeled).

The E_T/p_T distribution is considered the fruit of all the foregoing work. First it is valuable in identifying the electrons. This fact has been used in `ieElRec` by use of the δp variable. Second, it serves as an important source for the calibration of the ECAL. Events from the $\mathrm{Z}^0 \to ee$ decays will be used for this purpose. While it can be a source of a stand-alone ECAL calibration, it also enables the calibration by the ID. As bremsstrahlung is standing in our way, we need a good detector description and bremsstrahlung simulation. The precise peak positions, as well as the resolutions, and their dependence on E_T and η must be known. (See [2], Sec:7.2.2.) With this weapon in our hands, we can also use the $\mathrm{W}^\pm \to e\nu$ events.

To obtain these values the cores of the E_T/p_T distributions were fitted with a Gaussian. Fig:3.22 shows the E_T dependence of the parameters. At low transverse energies (up to $10\,$GeV) the mean value behaviour is dominated by a too low E_T measurement caused by the 3×7 cluster window size. At higher energies the mean value is following the shift of the p_T distribution due to bremsstrahlung. The resolution of the E/p is of course a merging of the two underlying distributions (as in $\sigma^2_{E/p} = \sigma^2_E + \sigma^2_p$) and is again dominated by the ECAL at low energies and tracker at higher energies. The seemingly unnatural improvement of the resolution at $E_T = 1.5\,$GeV is due to the suppression of the hard bremsstrahlung events by the ECAL clustering cut.

The $|\eta|$ dependence is shown in Fig:3.23. As it was the case for the E_T and p_T distributions, the material effects are the most important. At lower energies the offset from unity is ECAL dominated (therefore decreasing the mean value of the E/p), while the tracker takes the responsibility at higher energies (increasing the mean value).

Fractions of events in the tails is another big concern. It is `ieElRec`'s responsibility to filter them out and to prove that it is doing a good job we plotted the contour lines of the E_T/p_T distributions (cumulated along each $|\eta|$ bin) in Fig:3.24.

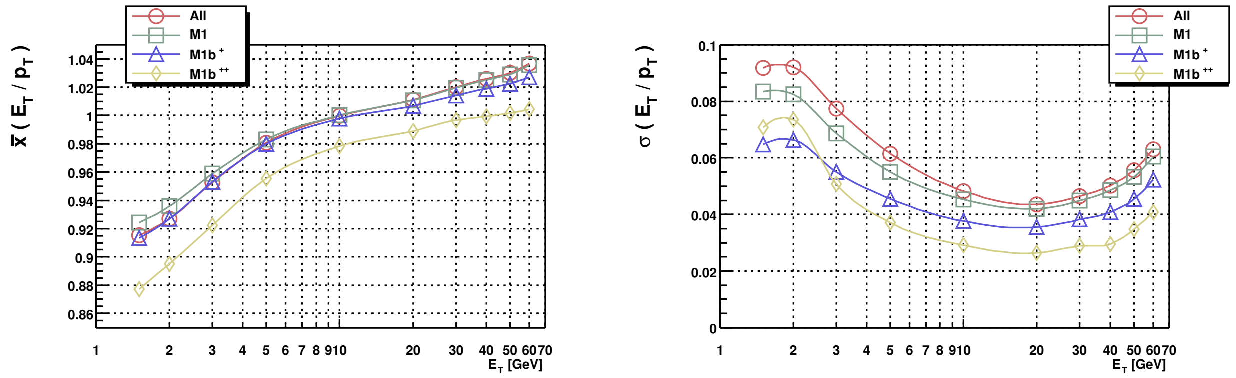

Figure 3.22: Mean values (left) and resolutions (right) of the E_T/p_T distribution versus transverse energy.

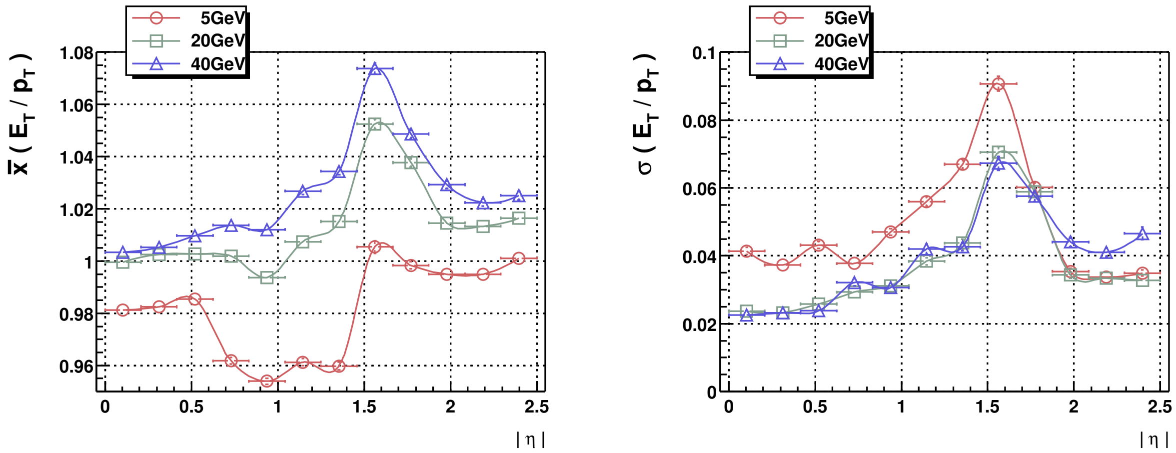

Figure 3.23: $|\eta|$ dependence of the mean values (left) and resolutions (right) of the E_T/p_T distribution. Transverse energies 5, 20 and 40 GeVare shown for the match type **M1b**$^+$.

3.3.3 Impact parameter resolution

Determination of the impact parameter is important for secondary vertex reconstruction (e.g., B decays), heavy flavour tagging, lifetime measurements and association of the track to the correct primary vertex at high luminosity. The measurement of impact parameter is dominated by the first few layers i.e. the pixel detector. Since the pixel pad size is 6 times larger in z than in r-φ direction, the resolution in the transverse direction is much better. At lower energies multiple scattering contributes most uncertainty to the measurement. It can be approximated by a const/$\mathrm{p_T}$ power law. For a further discussion and comparison see [5], Sec:4.4.

Transverse impact parameter (a_0) resolutions as functions of the transverse energy and $|\eta|$ are shown in Fig:3.25. The variation of the resolution with the match type is minimal and is improving with increasing transverse energy. As the first few layers are dominating the resolution and unnatural prolongation of tracks in the transverse direction leads to a degradation of measurement, one expects an improvement of the resolution by the usage of the truncated tracks. To quantify and prove this assertion resolutions for original tracks are

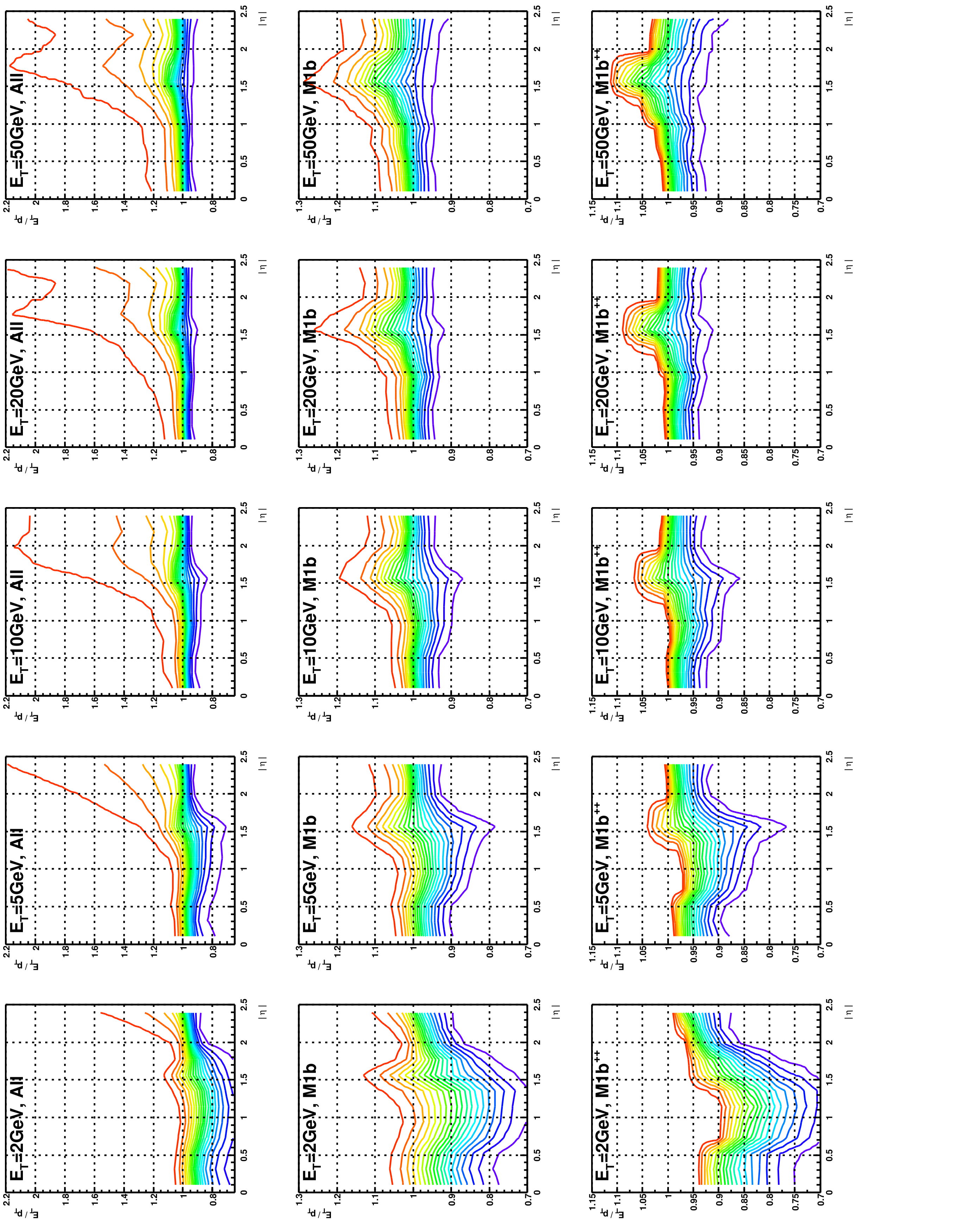

Figure 3.24: 5% contour lines of the E_T/p_T distributions for different transverse energies (row-wise). Curves are shown for all the events and for the match types **M1b** and **M1b**$^{++}$ (column-wise). y axis scales are different for each event selection!

also plotted versus $|\eta|$. The effect is of course most pronounced in the regions with highest amount of material where it improves the resolution by about 15%.

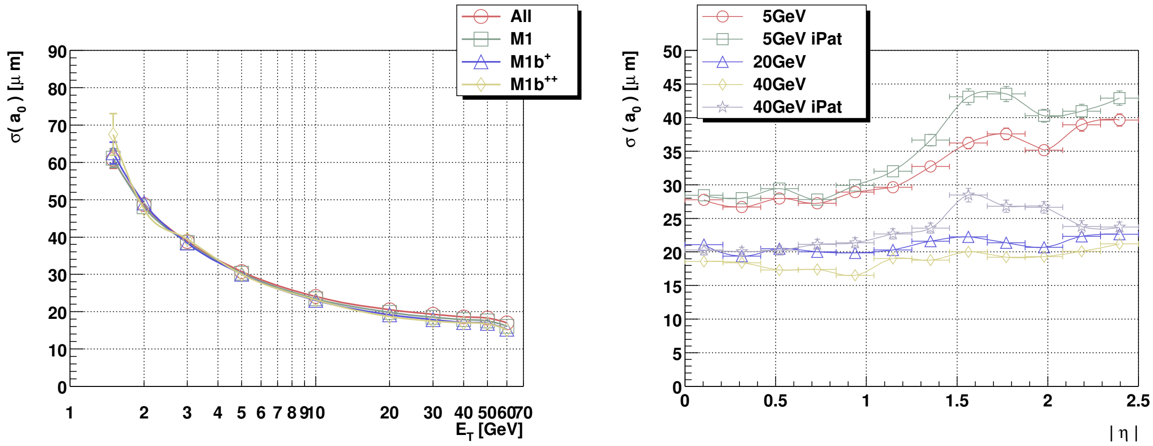

Figure 3.25: Resolution of the transverse impact parameter a_0. E_T (left) and $|\eta|$ (right, match type **M1b**$^+$) dependencies are shown. The curves labeled by iPat correspond to the resolutions obtained from seed tracks coming from `iPatRec` (before possible truncation).

Logitudinal impact parameter (z_0) should, on the other hand, in principle benefit from longer tracks as track's direction in r-z plane is not influenced by the bremsstrahlung. By observing the same kind of plot as for a_0 (Fig:3.26) we must discard this hypothesis as the resolutions are basically unaffected. Again there is no dependence on the match type.

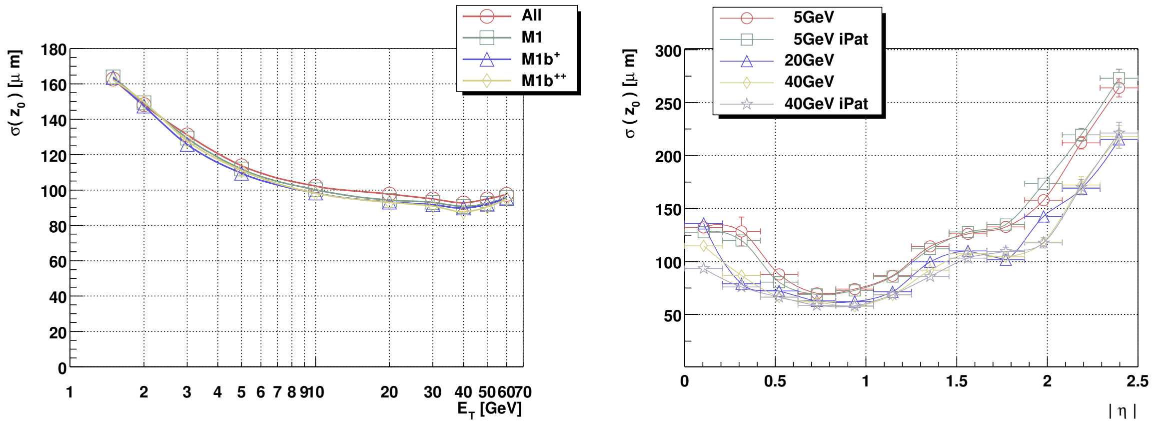

Figure 3.26: Resolution of the longitudinal impact parameter z_0. E_T (left) and $|\eta|$ (right, match type **M1b**$^+$) dependencies are shown. The curves labeled by iPat correspond to resolutions obtained from seed tracks coming from `iPatRec` (before possible truncation).

3.3.4 Angular resolution

The direction of the track at the vertex point plays a crucial role in the measurement of an invariant mass. It is expressed by two angles: φ is measured in the transverse plane (x-y) and θ in the r-z plane. It is more practical to consider the $\cot\theta$ as this equals p_z/p_T. The transverse energy dependence can again be parameterized by $A + B/p_T$. As the φ measurement is sensitive to bremsstrahlung, its η dependence follows the material distribution and is improved by the usage of the truncated tracks (Fig:3.27).

For the $\cot\theta$ measurement the resolution is constant in the barrel and then degrades with η when we shift into the end-cap region where r is measured with a fixed resolution. No significant worsening of the resolution by the track truncation can be observed (Fig:3.28).

For comparison with the muon tracks see [5]:Sec:4.3.

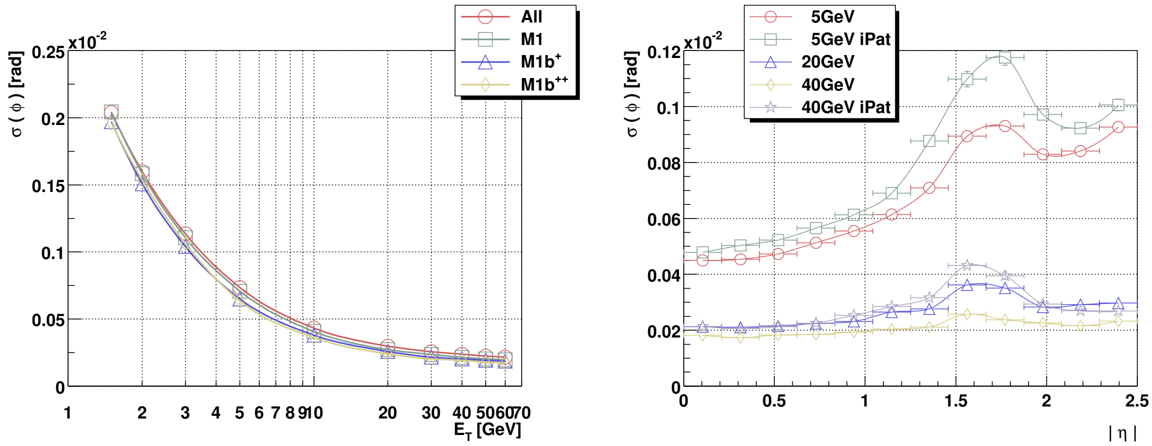

Figure 3.27: Resolution of ϕ. E_T (left) and $|\eta|$ (right, match type **M1b**$^+$) dependencies are shown. The curves labeled by iPat correspond to the resolutions obtained from the seed tracks coming from `iPatRec` (before possible truncation).

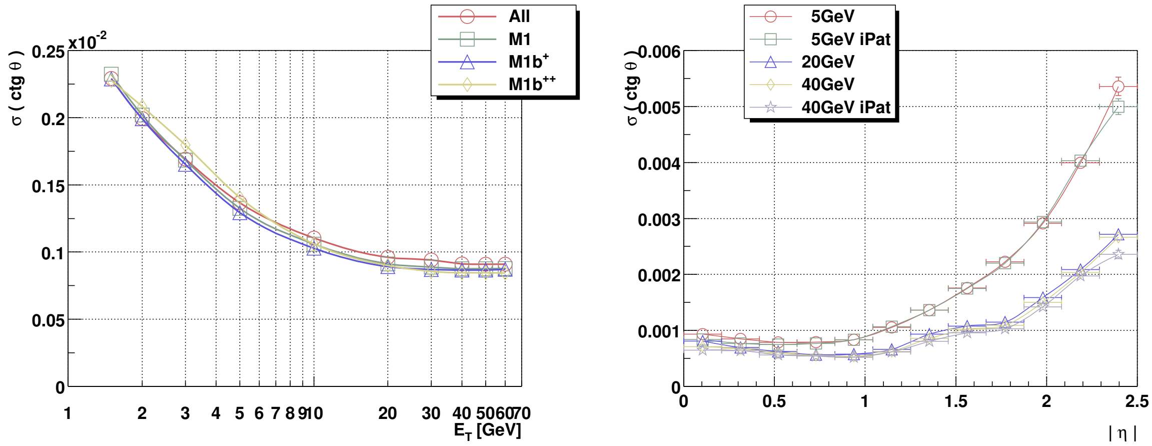

Figure 3.28: Resolution of $\cot\theta$. E_T (left) and $|\eta|$ (right, match type **M1b**$^+$) dependencies are shown. The curves labeled by iPat correspond to the resolutions obtained from the seed tracks coming from `iPatRec` (before possible truncation).

3.4 Pion rejection

For all the results presented in this section, the reduced ECAL clustering cut of $E_T^{\mathrm{EM}} = 0.7\,\mathrm{GeV}$ was used for $E_T^{\mathrm{true}} \leq 5\,\mathrm{GeV}$ (see Sec:3.1.5).

Charged pions can produce a large energy deposit in the ECAL via the formation of the Δ resonance which has a plentiful spectrum of excited states ($\pi^+ n \rightarrow \Delta \rightarrow \pi^0 p$ and $\pi^- p \rightarrow \Delta \rightarrow \pi^0 n$) in 1.2 to 3 GeVrange. The π^0 promptly decays into two photons and the misfortune occurs. The cross-section for this process is decreasing with energy and above 10 GeV sporadic low energy EM interactions prevail. These cases are then easy to spot by a large E_T-p_T mismatch. A more complete study of the electron/pion separation with emphasis on the trigger level application can be found in [2]:Sec:7.3.1. The basic difference is that while trigger's goal is assuring as high pion rejection as possible, `ieElRec` is trying to obtain very good electron efficiency at about 1% pion acceptance.

The variables used for obtaining the pion ambiguity A_π are discussed in Sec:3.2.2. But before we plunge into the rejections and efficiencies, some thought must again be given to the ECAL reconstruction efficiency. We saw that the ECAL is not fully efficient for electrons at low energies. And luckily it is not fully efficient for pions, either. Fig:3.29 shows fractions of pions and electrons that make it all the way through the `ieElRec` without applying any pion rejection cuts yet. As pion efficiencies are already lower, some part of the rejection has already been done. By futher requiring the electron candidate to be of the **M1** class, the π rejection factor is above 30 for 10 GeV and higher transverse enrgies. In what follows we will consider the electron efficiency to be 100% if all the electrons passing the `ieElRec` processing also pass the rejection cuts. In the same spirit we will not count the pions that fail `ieElRec` (mostly by not producing the EM cluster) to be successfully rejected. Therefore we will be studying the internal `ieElRec` rejection. To come to the absolute values one should combine this information with the values extracted from Fig:3.29.

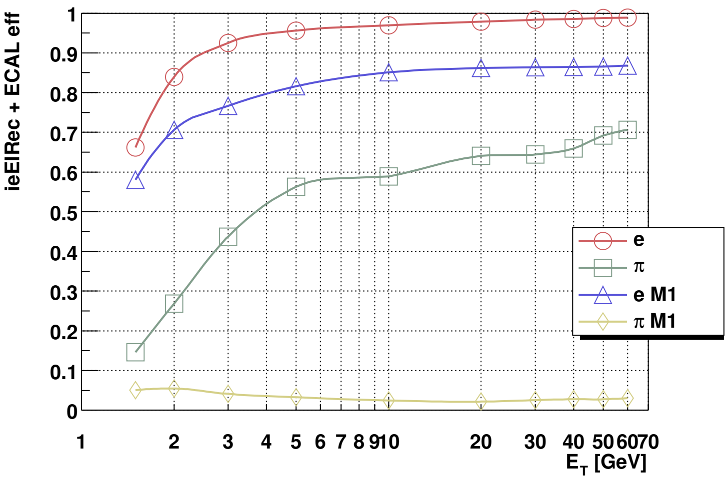

Figure 3.29: Efficiencies for electrons and pions to pass the `ieElRec`'s processing and making it into the electron candidate class.

The most interesting things happen in the range $A_\pi : -2 \nearrow 2$. The electron reconstruction and pion rejection efficiencies for these cases are shown in Tab:3.11. Note that a rather small number of the generated pion events (Tab:3.9) casts some shadows on the statistical value of the rejection factors. This is especially true for the pion rejection versus the electron inefficiency plot presented in Fig:3.30. The last point (with the highest rejection) for each curve was obtained by substituting the last entry with 100% pion rejection with the number of events that passed the pre-`ieElRec` cuts (therefore assuming that the next generated pion would be identified as an electron).

E_T [GeV]	e_{eff}	-2 π_{rej}	e_{eff}	-1 π_{rej}	e_{eff}	0 π_{rej}	e_{eff}	1 π_{rej}	e_{eff}	2 π_{rej}
1.5	0.405	1.000	0.803	0.998	0.938	0.987	0.986	0.970	0.997	0.899
2	0.428	1.000	0.826	0.998	0.946	0.987	0.987	0.975	0.997	0.925
3	0.456	1.000	0.839	0.998	0.951	0.983	0.988	0.975	0.997	0.946
5	0.471	1.000	0.850	1.000	0.957	0.996	0.990	0.988	0.997	0.959
10	0.491	1.000	0.854	1.000	0.961	0.984	0.992	0.980	0.998	0.959
20	0.487	1.000	0.843	1.000	0.958	0.984	0.991	0.975	0.998	0.955
30	0.495	1.000	0.846	1.000	0.958	0.990	0.991	0.981	0.998	0.954
40	0.481	1.000	0.831	1.000	0.952	0.987	0.989	0.979	0.997	0.956
50	0.474	1.000	0.827	1.000	0.951	0.985	0.989	0.974	0.997	0.947
60	0.471	1.000	0.826	0.999	0.954	0.987	0.990	0.975	0.998	0.938

Table 3.11: Electron reconstruction and pion rejection efficiency for the relevant values of A_π.

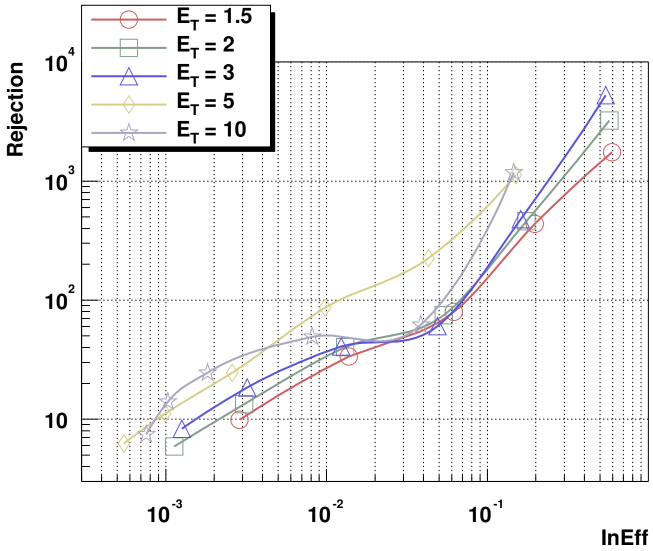

Figure 3.30: Pion rejection versus electron reconstruction inefficiency for different values of E_T.

3.5 Reconstruction in jets

So far we have been only considering isolated electrons. In this section we review the relevant quantities for electrons in jets. To cover a wide range of track multiplicities, we used the $B^0 \to J/\Psi \to ee$ event sample. The same event sample was used for the analysis presented in 4.1, where it is discussed in more detail. The important details are that the p_T of e's was forced to be above 2 GeV and the $|\eta|$ cutoff was 2.5. The distributions are shown in Fig:3.31. Total number of $e^{\pm}$'s was 62700. For this study the ECAL clustering cut (explained in 3.1.5) was set to $E_T = 1\,\mathrm{GeV}$ for all transverse energies.

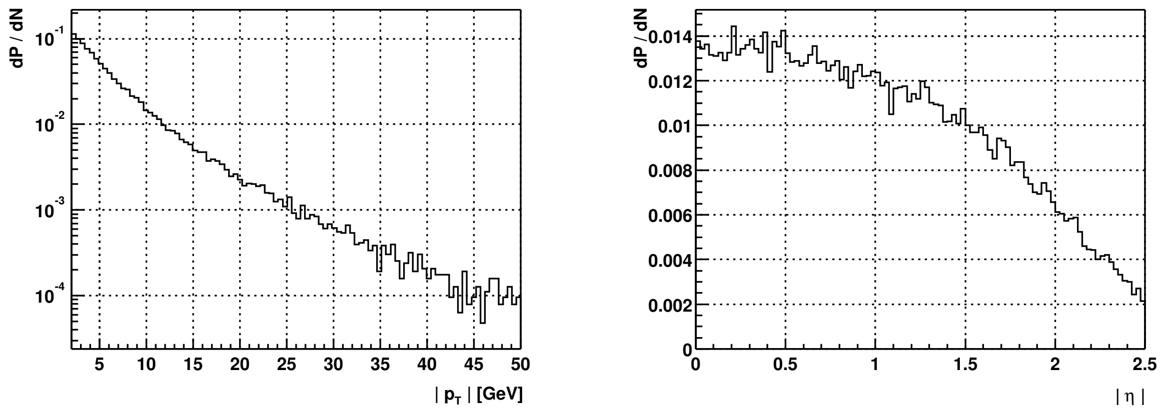

Figure 3.31: Distributions of generated $|p_T|$ and $|\eta|$.

Some deteriorations in `ieElRec`'s performance are expected to occur. They can be attributed to a degradation of `iPatRec`'s reconstruction efficiency and higher occupancy of the ECAL, which results in poorer resolutions of all its measurements. Also, more stringent selection cuts are applied inside `ieElRec` when it suspects to be running inside a jet (Sec:3.2.2). It is also true that most of the lost electrons are of poor match type, i.e., we cut them out as the ECAL information is possibly polluted. As we're interested in how well we can find and tag good electrons, we study the `ieElRec`'s efficiency and ECAL's purity for different track multiplicities. Plan of attack would be slightly different if we were interested in the electron/jet separation. This topic is covered in the 'Physics TDR' ([2]:Sec:7.4).

To determine the track multiplicity (N_T) information from the event generation record was used. Given an electron track, we first searched for the matching HCAL cluster. Then all the charged particles with $p_T > 1\,\mathrm{GeV}$ that projected into that cluster within $\eta^{\mathrm{HCAL}} \pm 2 \times \mathsf{rms}_\eta^{\mathrm{HCAL}} \;\wedge\; \varphi^{\mathrm{HCAL}} \pm 2 \times \mathsf{rms}_\varphi^{\mathrm{HCAL}}$ were counted. Fig:3.32 shows the distribution of multiplicities 'measured' this way. To retain statistical plausibility, we individually considered multiplicities up to $N_T = 7$. The rest were analysed in one bunch (marked as 8^{++}). The second plot on the same figure shows the mean value and rms of the distribution obtained by histogramming the sum of p_T of neighbouring tracks divided by the true p_T of the electron versus the multiplicity of the event.

To further differentiate the event sample we separately studied the three $|\eta|$ regions: barrel (32.1% of events), transition (56.6%) and end-cap (11.3%). As the ECAL's efficiency is varying significantly within the p_T range covered by the generated electrons, we also studied three p_T regions: $|p_T| < 4\,\mathrm{GeV}$ (39.0%), $4\,\mathrm{GeV} \le |\mathrm{p_T}| < 10\,\mathrm{GeV}$ (43.6%) and $|p_T| \ge 10\,\mathrm{GeV}$ (17.4%).

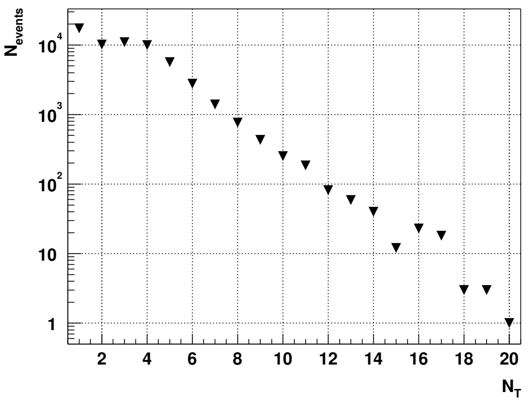

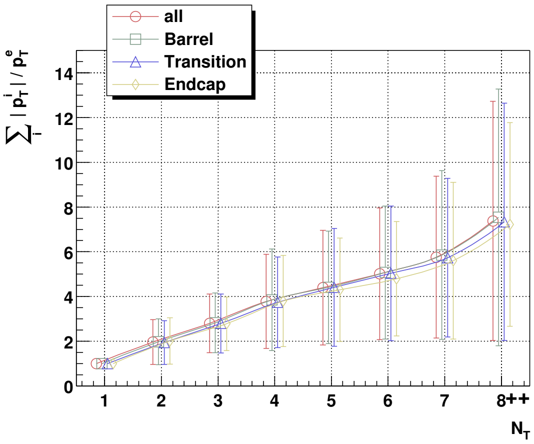

Figure 3.32: Left: number of available events for a given value of track multiplicity. Right: Average $p_T^{\rm jet}$ of a jet normalized to the electron p_T. The error bars show the rms's of the distributions.

3.5.1 ieElRec's efficiency

As ECAL's efficiency is studied separately, here we only consider events for which the EM cluster was successfully reconstructed. ieElRec's efficiency as a function of the track multiplicity is shown in Fig:3.33. Compared to resultus for single particles, about 4% drop in efficiency can be observed over the available N_T range, without much deviations for different $|\eta|$ and p_T regions.

The iPatRecreconstruction efficiency (added to the right plot of Fig:3.33) in jets could be affected by a higher occupancy of the silicon detectors and possible shared hits. But, as can be seen, there is no observable effect. Tracks reconstructed by iPatRec were required to be either primary or truncated with majority of hits belonging to the *true* track in question. No cuts on ECAL association were applied.

The decrease of efficiency due to the *jet cuts* inside ieElRec can be determined by comparing the presented results to the efficiencies obtained for single particles (Sec:3.3.1). No change can be observed.

Another thing of interest is how the different match types partake in the multi-pie. Fractional contributions for all match types are shown in Fig:3.34. The most noticeable variation is the raise of the **M3** match type (i.e., poor p_T measurement by the tracker) for about 10% over the studied region. To a smaller extent ($\sim 2\%$) **M0** is also raising. On the other hand, to compensate for this raise, fractions of **M1** ($\sim 8\%$), **M2** ($\sim 1.5\%$) and **M4** ($\sim 2.5\%$) decline accordingly.

As there is no reason for the electrons to behave differently in jets and there is no observable change in iPatRec's efficiency, we are led to the conclusion that the efficiency loss of ieElRec is caused by the more stringent cuts and ECAL pollution. On the other hand, migration of events into more dubious categories is entirely due to the degradation of ECAL performance.

3.5.2 ECAL pollution

First we study the efficiency of the EM cluster reconstruction. It is a bit problematic to define it for the non-isolated tracks as the cluster searching algorithm is looking for local

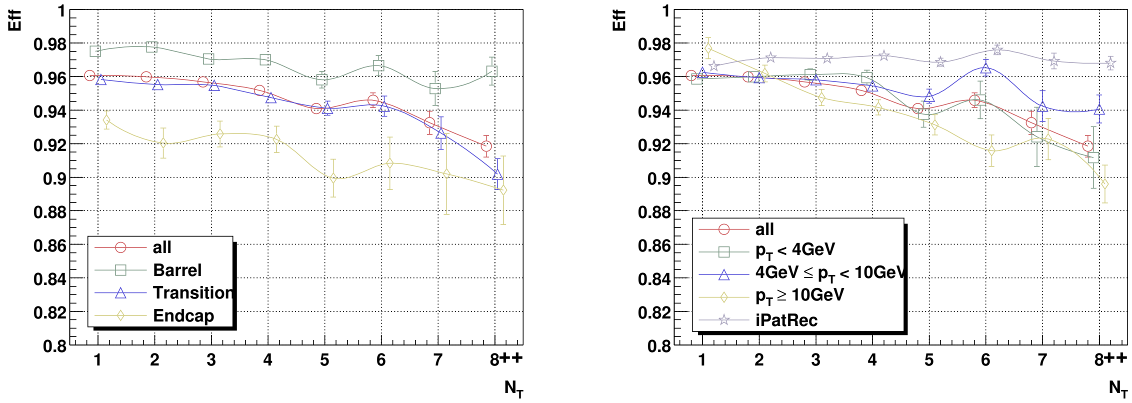

Figure 3.33: `ieElRec`'s efficiency as a function of the track multiplicity. $|\eta|$ regions are shown on the left plot. The right plot shows efficiencies for the p_T regions and also efficiency for `iPatRec` to find a primary or truncated track (no additional quality cuts applied).

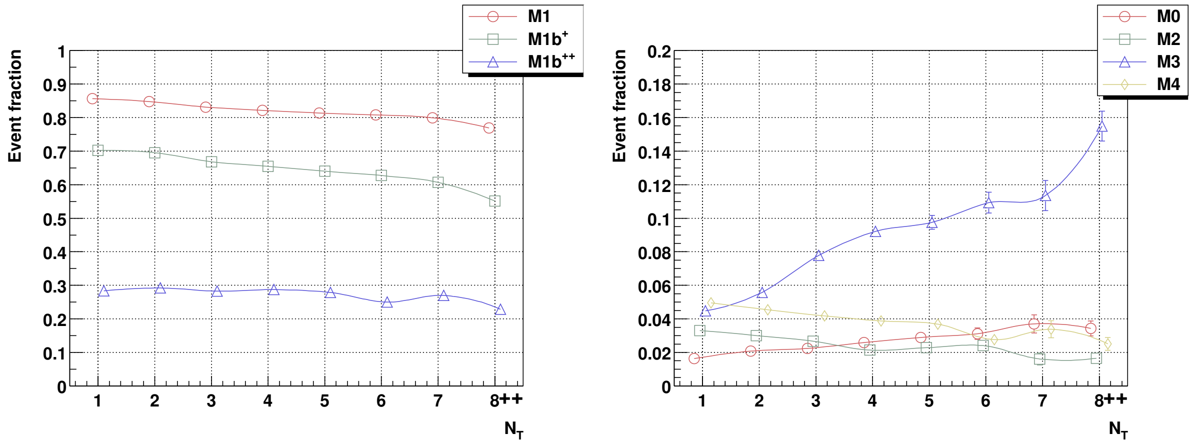

Figure 3.34: Fractions of events belonging to the different match-types as a function of track multiplicity. Good match types are shown on the left and the others on the right plot. y-axis scales are different.

maxima on the cell grid and can therefore fail to separate two closely lying tracks. Since we're only interested in cases where electron assignment can be made unambiguously (with reasonable tolerances), we consider the ECAL to be efficient in the following two cases.

1. `ieElRec` succeeds in finding the electron (EM clusters are used as seeds for `ieElRec`).
2. An EM cluster is found around the spot in ECAL to which the generated track projects to. The cut applied was (see Fig:3.13 for residual distributions):

$$4 \times \Delta\eta + \Delta\varphi \leq 0.15.$$

The results are presented in Fig:3.35. For transverse energies above 4GeV, where the ECAL is almost fully efficient, higher multiplicities only degrade the reconstruction efficiency. At lower energies additional depositions made by neighboring tracks first help the EM cluster to climb over the clustering threshold and only at multiplicities above $N_T > 4$ the efficiency begins its decline. Basically the same situation can be seen for the transition region ($0.6 < |\eta| < 1.9$), where the huge amount of material causes the ECAL to be more inefficient.

Another measure of the alien track conspiracy can be obtained by inspecting the behaviour of the mean value and spread of the E_T/E_T^{true} distribution as a function of the track multiplicity (Fig:3.36). While no specific η or p_T dependence can be observed, we can still estimate the average contribution of the neighboring tracks to the E_T measurement.

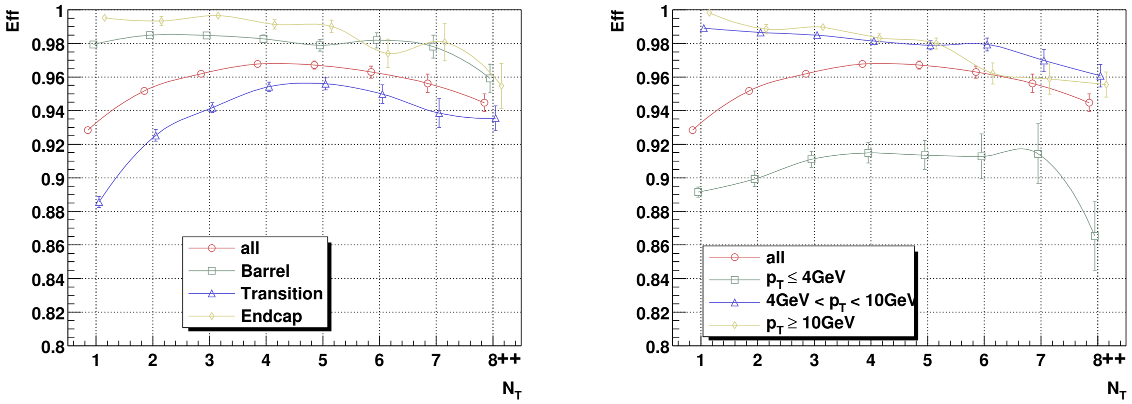

Figure 3.35: ECAL's efficiency as a function of track multiplicity. $|\eta|$ regions left, p_T right.

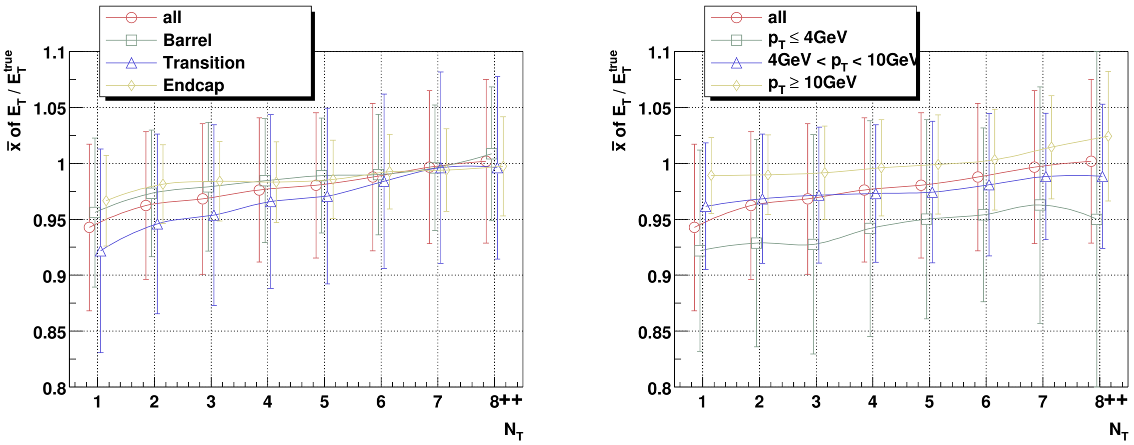

Figure 3.36: The mean values and resolutions (represented by error bars) of the EM clusters as a function of track multiplicity. $|\eta|$ regions left, p_T right.

3.6 Effects of pile-up

In contrast to the clean environment of lepton-antilepton colliders (such as LEP) the rich structure of colliding protons gives birth to many soft collisions for which the cross-section is many orders of magnitude larger than for the processes of interest ($\sim$ 100 mb to be compared to, say, H production with a cross-section of $\sim$ 5 pb for $m_H = 500\,\mathrm{GeV}$). One of the design decisions for the LHC was to choose higher luminosity instead of higher energy and a multitude of minimum-bias events (as soft hadronic interactions are called) is the price that the LHC experiments must pay in terms of their operational environment. During the high-luminosity operation there will occur, on average (Poisson distributed), 23 such interactions in each bunch crossing. Luckily, many of the interaction products (and deflected protons) are emitted at low angles to the beam axis. As a rule of thumb, the number of particles is constant in each η interval up to $\eta \sim 6$. The average number is 7.5 charged particles (0.64 for a $p_T > 1\,\mathrm{GeV}$ cut) and 9 neutral particles (90% of them are photons with the mean $E_T = 235\,\mathrm{MeV}$) per unit of pseudo-rapidity for one minimum-bias event. Another saviour comes in the flesh of the magnetic field which effectively curls up particles with $p_T < 0.5\,\mathrm{GeV}$ so that they never make it to the outer parts of the detector. However, the tracker material produces a significant number of secondary interactions and conversions in front of the calorimeter.

Besides being a generic nuisance as a source of radiation damage and higher detector occupancy, minimum-bias events have a special pinch for sub-detectors with signal collection times longer than the time between consecutive collisions. Signals from several bunch crossings begin to overlap, both in space and time; this is called *pile-up*. From this perspective, the TRT and ECAL are the most heavily exposed parts of the ATLAS detector. Silicon vertex detectors have a $\sim$ 20 ns shaping time and each of the electronic channels covers a very small area of the detector. In contrast, straws of the TRT are much longer and wider and, which is more important at the moment, the electron charge collection time in gas is about 60 ns, not to mention the ten times longer ion contribution, which has to be canceled out by the front end electronics. Even so, the expected TRT occupancy during the high-luminosity operation ranges from 15% to above 40%.

Things are even worse for the ECAL, where charge collection times can be as long as 500 ns (20 bunch crossings). Therefore, to correctly account for the effects of pile-up in the calorimeter, one has to superimpose about 500 minimum-bias events. Again, electronics is used to bypass the long collection time and to give a uniform 40 ns peaking time of the signal. While shaping can solve the problem of bunch crossing identification, a large contribution to the overall noise of the calorimeter is here to stay. For electrons, the most important piece of information is that pile-up contribution to the noise in the 3×7 window is $\sim$ 300 MeV. Pile-up effects in the calorimeter are studied in detail in *Calorimeter Performance TDR* [8]:Sec:1.4.

There are other traps for electrons in the presence of pile-up than just the increase in noise. To stay with the ECAL associated problems, there will be random contributions to the reconstructed energy in the EM cluster belonging to an electron. This will inevitably lead to migration of some otherwise well reconstructed electrons to the **M3** match type or, even worse, to **M0** or even to fail the ID/ECAL association completely. Furthermore, some pattern recognition problems may be expected from the higher number of combinatorials. But things are far less tragic in this respect than generally believed. To quantify this statement note that while there are about the same number of tracks that pass the pre-selection cuts within `ieElRec` for the jet and pile-up data samples, the track multiplicity count, where a $p_T > 1\,\text{GeV}$ cut is applied, yields about 50% of events with a track multiplicity greater than one for the jet sample and only about 1% of events for the high-luminosity pile-up.

To study the effects of pile-up in detail, 2 000 events from the generated $e^{\pm}$ samples (1 000 e^{-}'s and 1 000 e^{+}'s) were merged with a high-luminosity pile-up using the standard procedures described in [2]:Sec:2.3. Electron samples with p_T up to 20 GeV were considered as no degradation in performance is expected above this energy.

More or less the same steps were taken as for the analysis of reconstruction in jets. Instead of studying the reconstruction efficiency and ECAL degradation as a function of track multiplicity, the dependency of both effects on the generated single electron p_T were be considered.

3.6.1 Efficiencies

As all along this chapter, EM clusters were used to define roads and initiate the ID reconstruction. The ECAL clustering cut was set to $E_T^{\text{EM}} \geq 1\,\text{GeV}$ for all event samples under study.

The first thing to note is that the ECAL reconstruction efficiency (as defined in Sec:3.5.2) increases at low p_T. The increase is 32% at $p_T = 1.5\,\text{GeV}$, 10% at 2 GeV and a bit more than 1% at 3 GeV. At 5 GeV the efficiency reaches the value obtained without pile-up. This can be partially understood by additional contribution of pile-up to an otherwise inefficient EM cluster which helps it crawl over the mark set by the clustering cut and therefore increases the ECAL reconstruction efficiency. The left plot of Fig:3.37 shows its dependence on p_T together with the electron identification efficiency of `ieElRec` and the reconstruction efficiency of `iPatRec`. Since EM clusters are used to seed the reconstruction, more is learned by studying efficiencies relative to the ECAL. Their E_T dependence is presented in the right plot of the same figure. The `iPatRec` curve starts above one at $p_T = 1.5\,\text{GeV}$, which means that the track gets reconstructed by virtue of a closely lying EM cluster produced by a track from a minimum-bias event or noise (a road half-width of $\Delta\varphi \times \eta = 45° \times 0.1$ around the seed coordinate was used in ID reconstruction). This awakes further suspicion on the quality of reconstructed electrons at very low p_T, as can be seen from the efficiencies plotted for sub-selections of good (**M1**) and reasonably good (**M1**, **M2** or **M4** which all yield a good p_T measurement) electrons. Looking at the absolute scale, pile-up introduces a 5% drop in reconstruction efficiency for the **M1** match type at $p_T \leq 5\,\text{GeV}$, about a 2% drop at $p_T = 10\,\text{GeV}$ and above that the results are consistent with the data without pile-up.

To further investigate the effects of pile-up, the relative fractions of all match types were plotted versus E_T (Fig:3.38). The **M1** match type has already been discussed, it was observed that its relative fraction is below the one obtained without pile-up. The largest increase in fractional frequency is seen for the **M0** and **M3** match types. The first case corresponds to an ECAL cluster that can't be attached to an ID track in a reasonable way and therefore signifies EM clusters that have nothing to do with the electron. In contrast to those, the **M3** match type signals a lousy p_T measurement and in this case the transition is induced by an additional deposition of energy in the direct vicinity of the triggering EM cluster. The **M2** and **M4** match types are basically unaffected by pile-up.

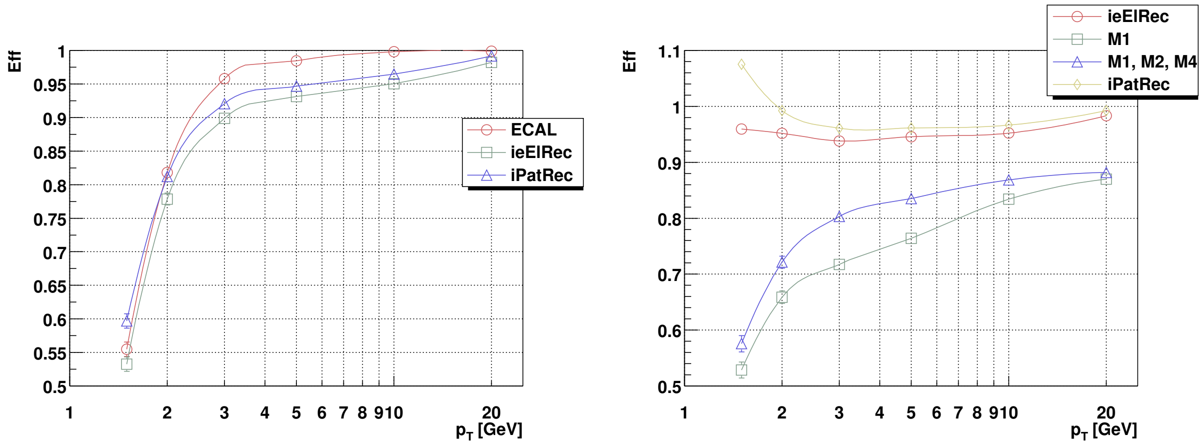

Figure 3.37: *Left:* absolute efficiencies of ECAL, `ieElRec` and `iPatRec` as a function of electron transverse momentum. *Right:* efficiencies, *relative* to the ECAL reconstruction efficiency, of `ieElRec`(irrespective of match type, for **M1** and for a union of **M1/2/4** match types) and `iPatRec`.

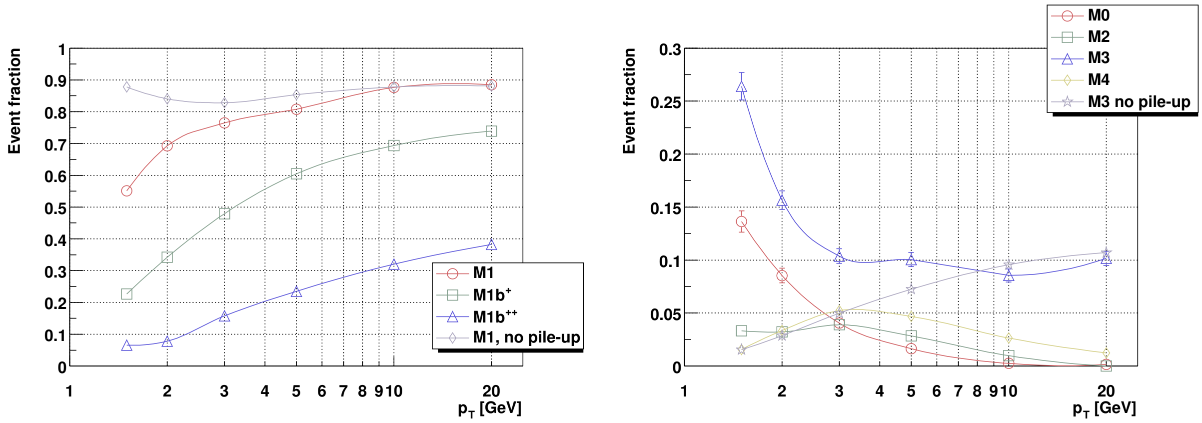

Figure 3.38: Relative fractions of ID/ECAL match types. Good matches are presented in the left plot (for comparison, **M1** *without* pile-up is also plotted) and poor ones in the right plot (with **M3** *without* pile-up added).

3.6.2 ECAL's E_T measurement

So far only event fractions and efficiencies have been considered without any concern for the underlying distributions of reconstructed p_T. The p_T distributions of tracks reconstructed in the ID differ from the ones without pile-up by migration of some well reconstructed electrons into poorer match types. This means that the p_T^{true}/p_T distributions of the **M0** and **M3** match types have more events in the central region and therefore a better mean value.

The normalised E_T/E_T^{true} distributions of the ECAL E_T measurement are presented in Fig:3.39. The distributions for the previously distinguished ID/ECAL match types support the statements made above about the inflow of energy into the area of ECAL to which an electron track projects to, and gives a more qualitative measure of the two effects. A statistical description of these distributions, in terms of mean values and rms's versus transverse energy, is presented in Fig:3.40. Returning to the **M1** match type, one can observe that its mean value is fixed at $E_T/E_T^{\rm true} = 1$ which is basically just a cursor of the ECAL calibration that has been performed to account for the effects of high-luminosity pile-up. More interesting is the increase of noise, which manifests itself in a broadening of the distributions by 100 MeV.

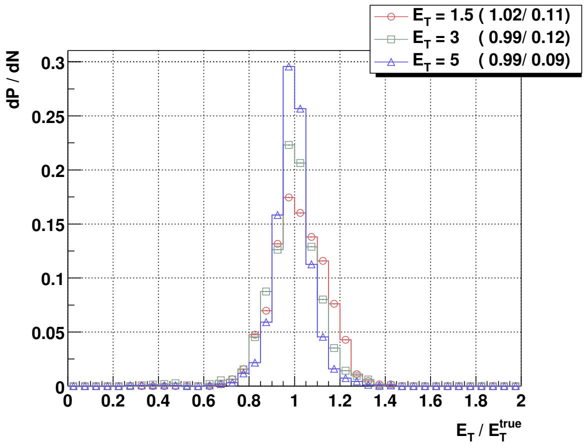

Figure 3.39: *Left:* normalised $E_T/E_T^{\rm true}$ distributions of **M1** ID/ECAL match type for $E_T =$ 1.5, 3 and 5 GeV. *Right:* normalised $E_T/E_T^{\rm true}$ distributions of poor match types for $E_T =$ 2 GeV. Both plots are labeled by mean values and rms's of distributions.

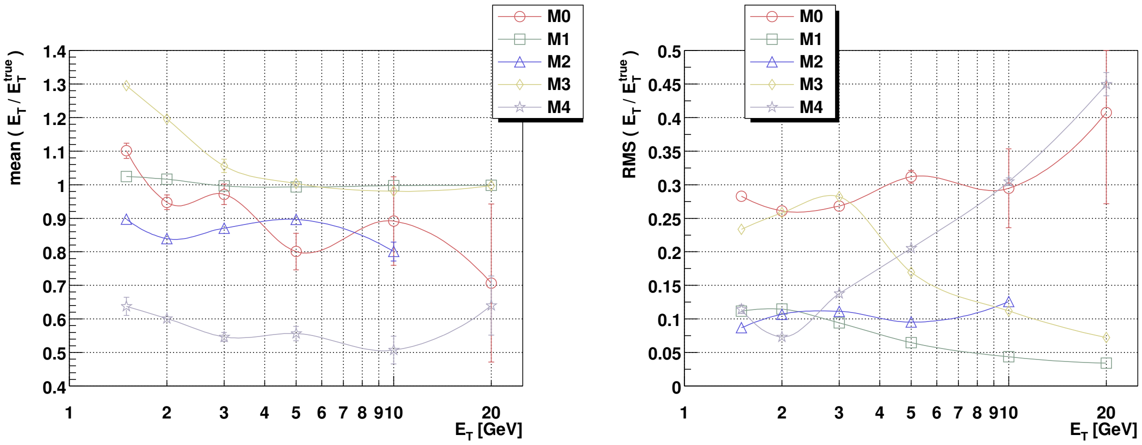

Figure 3.40: Mean values (left) and rms's (right) of $E_T/E_T^{\rm true}$ distributions. All ID/ECAL match types are presented. For **M1** the plotted value was obtained from a Gaussian fit in a range of $\pm 2 \times$ rms around the mean.

Chapter 4

Applications of the electron reconstruction algorithm

This chapter presents the behaviour of `ieElRec` in some channels for which a good electron reconstruction is of prime importance for ATLAS. One should understand that the primary goal of the analyses presented here is the study and benchmarking of `ieElRec` and `iPatRec` for relevant physics events. The results are compared to the corresponding sections of the ATLAS *Physics Performance TDR* [3] when the comparison is possible.

All event samples have been generated using PYTHIA 5.7 & JETSET 7.4 event generators [30]. Final state radiation for decays involving the Z^0 boson (which is known to be inadequate in PYTHIA 5.7) was simulated by the PHOTOS package [31]. The same set-up was used for the production of events as that used for the *Physics TDR*: a single photon emission with the IR cutoff set at 1% of the total Z^0 energy.

The detector simulation was performed using the TDR layout and the corresponding DICE [32] production version (CVS tag 1.0.1). The only change was the introduction of the realistic magnetic field (TDR productions were done with a constant solenoidal field in the ID).

4.1 $B^0 \to J/\Psi \to ee$

Beauty production in a high energy hadron collision is not yet well understood theoretically as proven by the Tevatron measurements. Calculations to a higher order (NNLO) in α_S need to be carried out as their correction is of the same order as that of the NLO. Reference [3]:Sec:15.8.3 gives an overview of the situation, while a detailed study aimed at assuring a consistent Monte-Carlo production for the LHC conditions can be found in [33]. More technical aspects and details of the event generator settings are presented in [34].

As already mentioned in Sec:1.5.2, the level 1 trigger for the B-physics is selected by a muon with $p_T > 6\,\mathrm{GeV}$. Therefore one of the b hadrons was required to decay into $\mu^{\pm}X$, with $|\eta_\mu| < 2.5$. The charge of this muon will also be used for tagging the particle/anti-particle state of the decaying b quark. The other hadron (B^0 or $\bar{B}^0$) is forced to decay into $K^0 J/\Psi$ and further $J/\Psi \to e^+e^-$. The cuts imposed upon the electron and positron in this study are $p_T > 2\,\mathrm{GeV}$ and $|\eta| < 2.5$. In total 32 700 events have been generated.

4.1.1 Sub-selections and efficiencies

The relatively large data sample allows us to make further sub-selections for a detailed study. Some properties of the $e^{\pm}$'s, irrespective of the particle type, were already presented in the introduction to Sec:3.5. Further, the efficiencies of `ieElRec` and ECAL reconstruction have already been scrutinized. Here this separation will not be redone. One should keep in mind though, that inefficiencies of the electron reconstruction for $p_T < 5\,\mathrm{GeV}$ are dominated by the ECAL cluster reconstruction.

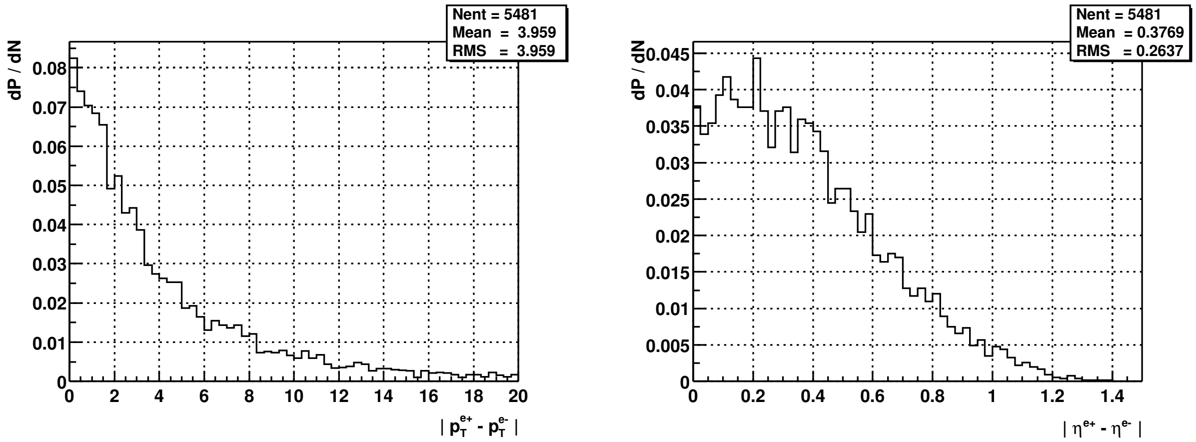

Figure 4.1: Distributions of difference in p_T (left) and η (right) between the $e^{\pm}$ originating from the decay of J/Ψ.

Basically all reconstructed quantities show a strong p_T dependence. While the average p_T of the electron and positron are used for most of the plots, it is still useful to define three sub-selections for results presented in the tables and to unveil the fractions of events belonging to each set of cuts.

Label	Cuts	Fraction
P_L	$p_T < 5\,\mathrm{GeV}$ for both $e^{\pm}$	30%
P_H	$p_T > 5\,\mathrm{GeV}$ for both $e^{\pm}$	25%
P_I	the rest of events	45%

One should combine the left plot of Fig:3.31 (showing a joint distribution of the p_T) with the left plot of Fig:4.1, which shows the distribution of the difference of p_T between electron and positron, to get a firm grip of the situation.

The η dependence due to the geometry of the tracker and its material distribution is also well pronounced. The barrel/transition/end-cap separation is retained, but since now there are two particles covered, five categories have been defined.

Label	Cuts	Fraction
BB	$\lvert\eta\rvert \leq 0.6$ for both $e^{\pm}$	22%
BT	$\lvert\eta\rvert \leq 0.6$ for one of $e^{\pm}$ and larger for the other one	20%
TE	$\lvert\eta\rvert \geq 1.9$ for one of $e^{\pm}$ and smaller for the other one	12%
EE	$\lvert\eta\rvert \geq 1.9$ for both $e^{\pm}$	6%
TT	$0.6 < \lvert\eta\rvert < 1.9$ for both $e^{\pm}$	40%

Again, Figs:3.31 and 4.1 (right plots on both figures) provide a touch of the relevant distributions.

J/Ψ reconstruction efficiency

For each of the aforementioned sub-selections there are further cuts applied to the sum of *pion ambiguities* of both particles ($A_\pi^{ep} = A_\pi^e + A_\pi^p$) and to the invariant mass of the reconstructed J/Ψ ($m_{J/\Psi}$). The behaviour of A_π for single electrons has been studied in Sec:3.4. Values of A_π^{ep} are presented in the range from -2 to 0. The resolution of the $m_{J/\Psi}$ measurement will be discussed in more detail later (Sec:4.1.3); here cuts of ±5, 10 and 20 percent are considered along with the efficiency in the absence of this cut. The results are summarized in Tab:4.1.

$m_{J/\Psi}$ cut	5%			10%			20%			none		
A_π^{ep} cut	-2	-1	0	-2	-1	0	-2	-1	0	-2	-1	0
All	40.22	49.28	53.39	49.60	59.89	64.53	55.64	66.66	71.62	61.44	73.18	78.46
BB	39.48	56.93	66.25	44.55	63.82	74.00	47.32	67.81	78.52	50.02	71.39	82.58
BT	46.21	59.02	64.47	52.72	66.91	72.91	56.01	70.97	77.40	59.70	75.52	82.31
TT	39.88	45.13	46.95	51.15	57.43	59.71	58.49	65.24	67.72	64.92	72.28	74.98
TE	33.75	36.40	37.70	47.98	51.36	52.92	58.20	62.21	63.91	68.30	72.95	74.97
EE	37.26	40.64	41.81	50.28	54.54	55.98	61.07	66.00	67.66	73.31	78.90	80.90
PL	39.23	48.20	52.17	47.68	57.82	62.35	52.63	63.61	68.39	57.53	69.19	74.24
PI	40.67	49.77	54.08	50.01	60.36	65.20	56.53	67.48	72.64	62.18	73.85	79.39
PH	40.57	49.67	53.60	51.08	61.45	65.88	57.52	68.73	73.54	64.61	76.58	81.68

Table 4.1: J/Ψ reconstruction efficiencies for different sub-selections. For each of them different cuts are applied to the A_π^{ep} and reconstructed invariant mass.

4.1.2 Secondary vertex reconstruction

As we are primarily interested in the performance of `ieElRec` no corrections of the track parameters were made (vertex fitting). At this stage it is more important to show what performance can be expected from a *raw* reconstruction as it will serve as an input to any more specialized algorithm.

One should take into account that the resolutions of the perigee parameters improve with the increasing p_T. This is a study at the low-end of the transverse energies that will be used in the ATLAS physics. So it is no surprise that the resolutions of the secondary vertex parameters are rather poor.

To differentiate from the perigee parameters, the quantities describing the secondary vertex are marked by capital letters:

R_0 distance from the origin in the r-φ plane;

Z_0 distance from the origin along the z axis;

P_T, P_L transverse and longitudinal momentum of the decaying particle;

Φ, Θ directional angles of the momentum of the decaying particle.

The search for the secondary vertex was performed in the r-φ plane, by calculating the intersection points of the two circles. The point with a smaller r was selected and the path lengths from the perigee calculated. The Z_0 coordinate was determined by calculating the mean value of the z coordinates predicted by both tracks. This gave better results than using the z coordinate predicted by the track with a higher p_T, although resolutions of z_0 and $\cot\vartheta$ improve with increasing p_T.

P_T and P_L were obtained by transporting the track parameters from the perigee to the intersection point and summing the momenta.

R_0 and Z_0 resolutions

The residual distributions of both quantities have a well pronounced Gaussian center and a rich tail content with about 10% of the events floating outside three standard deviations from the core resolution. Fig:4.2 shows the two residual distributions as a function of the average $|\eta|$ of the $e^{\pm}$ pair. In subsequent discussions the resolutions are obtained by fitting the residual distribution with a Gaussian in the range mean $\pm\, 2 \times$ rms.

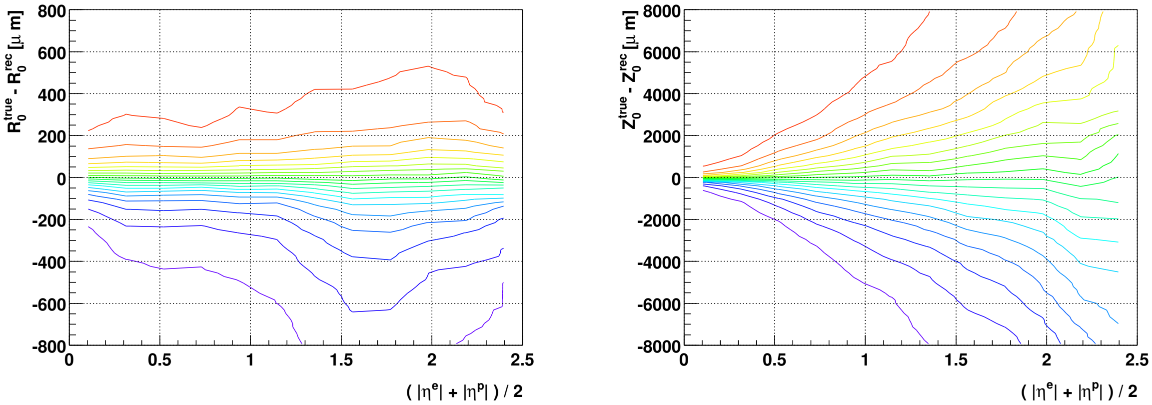

Figure 4.2: Residual distributions of the R_0 (left) and Z_0 (right) measurement. 5% contours are shown (between any two consecutive lines and outside the outer lines, lays 5% of events per x-axis bin).

The distribution of R_0 is exponential with a mean length of 1.75 mm. Resolution of the R_0 measurement as a function of the average $|\eta|$ and p_T is shown in Fig:4.3. It is about a factor of 2 worse than the single track a_0 resolution (taking $p_T = 3\,\text{GeV}$ as a reference value), but one should bear in mind the procedure that leads to the secondary vertex determination and know that the comparison is not exactly fair. The resolution is constant in the barrel region (up to $|\eta| \approx 1$) and then worsens by a factor of approximately 1.5 through the transition region. As a function of the average p_T the resolution deteriorates linearly, degrading by a factor of two in the range from $p_T = 2\,\text{GeV}$ to $10\,\text{GeV}$. Note that the p_T resolution is constant in this energy range and that the a_0 resolution is improving with increasing p_T. Nevertheless, the intersection position is defined poorer and poorer as the tracks get stiffer. Improvement of the order of a few percent can be observed by applying the cuts on the reconstructed invariant mass. Requiring that both particles belong to the **M1b**$^+$ class also improves the resolution. The overall resolution, without applying any cuts, is $\sigma(R_0) = 110\,\mu\text{m}$.

The Z_0 resolution is about ten times worse than the transverse one. Its average value is $\sigma(Z_0) \approx 1.2\,\text{mm}$, which is to be compared to the width of the true Z_0 distribution (Gaussian with $\sigma = 55.6\,\text{mm}$). The dependencies of the resolution on $|\eta|$ and p_T are shown in Fig:4.4. A degradation of the resolution by a factor of ten can be observed over the ID η coverage and by a factor of two over the available p_T range ($2 \nearrow 10\,\text{GeV}$). Basically the same comments

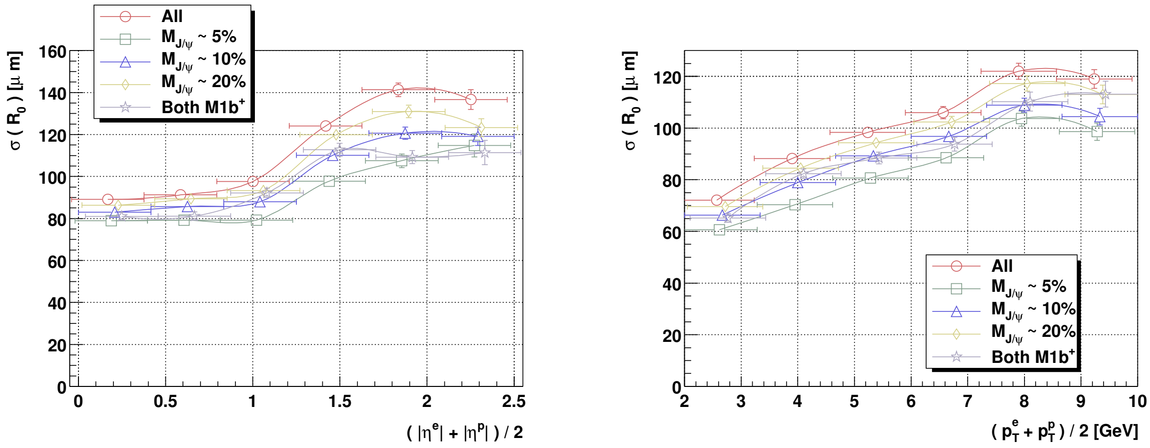

Figure 4.3: $|\eta|$ (left) and p_T (right) dependence of the R_0 resolution. Curves are shown for all events, for three different cuts on reconstructed $m_{J/\Psi}$ ($|\delta m_{J/\Psi}|/m_{J/\Psi}^{\rm true} < 5,\ 10,\ 20\%$) and for the case when both the electron and positron belong to the **M1b**$^+$ class.

apply as for the R_0 resolution dependence as the intersection position is sought for in the transverse plane. Application of cuts on the reconstructed invariant mass brings only a minor improvement to the resolution.

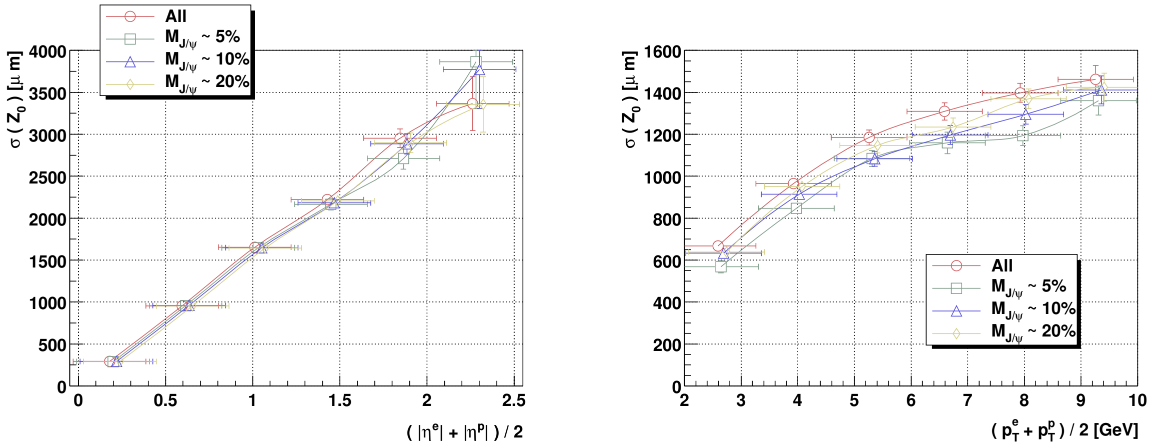

Figure 4.4: $|\eta|$ (left) and p_T (right) dependence of the Z_0 resolution. Curves are shown for all events and for three different cuts on reconstructed $m_{J/\Psi}$ ($|\delta m_{J/\Psi}|/m_{J/\Psi}^{\rm true} < 5,\ 10,\ 20\%$).

P_T and P_L resolutions

The normalised residual distributions of the P_T and P_L versus the average $|\eta|$ are presented in Fig:4.5. Both quantities exhibit a rather long tail on the 'missing reconstructed momentum' side. There is no dependence on the average transverse energy of the $e^{\pm}$ pair.

The $|\eta|$ dependence of the resolutions of the normalised residuals are shown in Fig:4.6. As expected, the application of cuts on the reconstructed invariant mass improves the resolutions. The 5% cut effectively cancels out the degradation outside the barrel region.

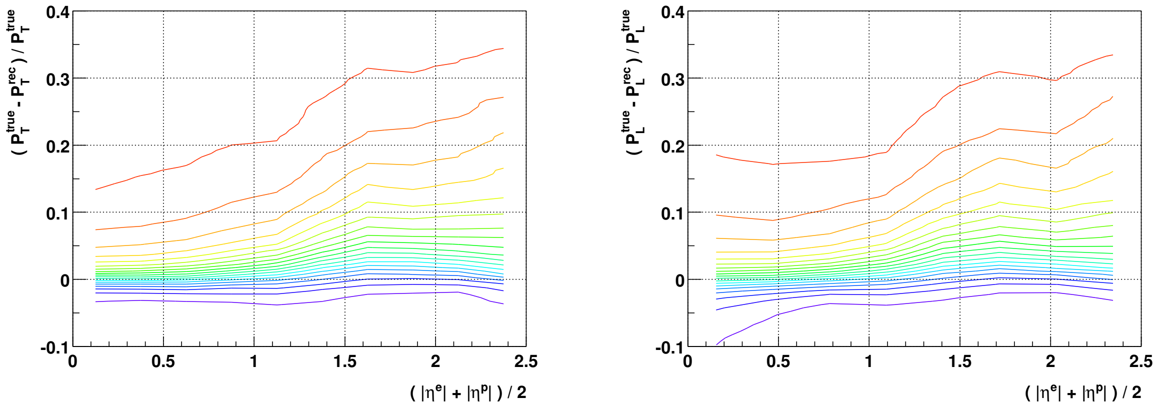

Figure 4.5: Normalised residual distributions of the P_T (left) and P_L (right) measurement as a function of the average $|\eta|$ of the $e^{\pm}$ pair. 5% contours are shown.

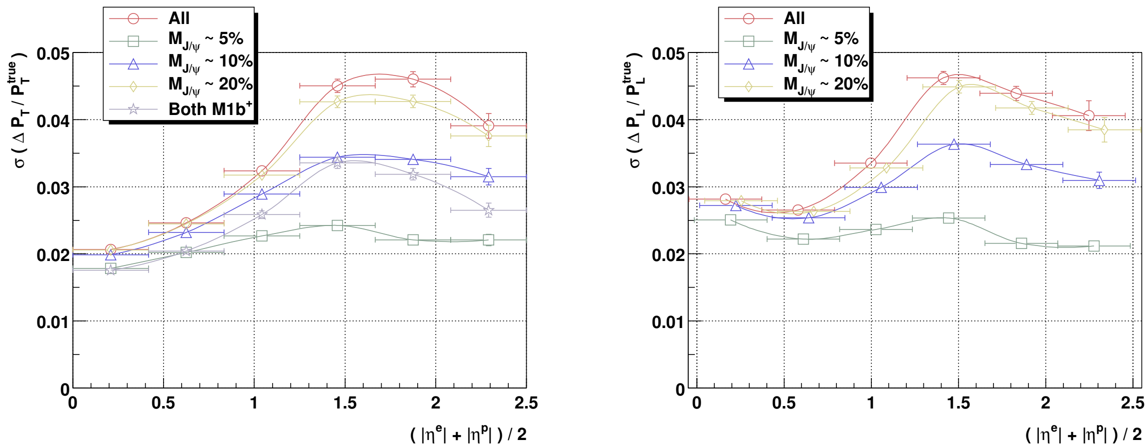

Figure 4.6: Resolutions of the normalised residual distributions of the P_T (left) and P_L (right) as a function of the average $|\eta|$ of the $e^{\pm}$ pair. Curves are shown for all events and for the three different cuts on the reconstructed $m_{\mathrm{J}/\Psi}$ ($|\delta m_{\mathrm{J}/\Psi}|/m_{\mathrm{J}/\Psi}^{\mathrm{true}} < 5, 10, 20\%$). For the P_T case the resolution for the sub-sample when both tracks belong to the **M1b**$^+$ class is also shown.

Angular resolution

The resolutions of the measurements of the direction angles in the transverse (Φ) and r–z planes (Θ, expressed as $\cot\Theta$) are shown in Fig:4.7. Compared to the resolutions of single particles (see Sec:3.3.4) the Φ resolution is about five times worse and the $\cot\Theta$ one is degraded by a factor of two. Again, the comparison is not exactly fair, as the angular parameters of the secondary vertex are obtained by transporting the perigee parameters to the reconstructed vertex and in the process we pick up every possible experimental error. The cut on the reconstructed $m_{\mathrm{J}/\Psi}$ improves the resolutions in the transition and end-cap regions.

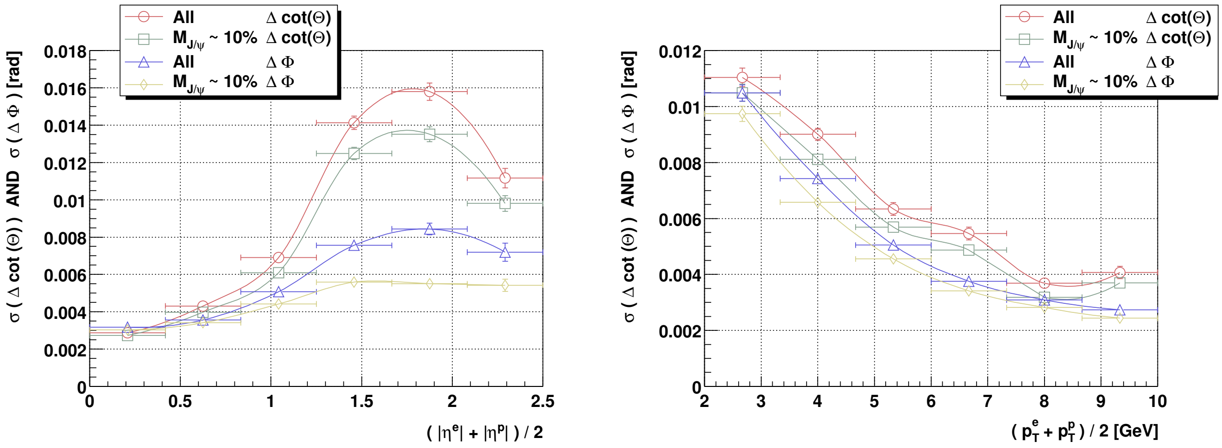

Figure 4.7: Resolutions of Φ (blue and yellow curves) and $\cot\Theta$ (red and green) as a function of the average $|\eta|$ (left) and p_T (right).

4.1.3 $m_{J/\Psi}$ resolution

Finally, we arrive to the gem stone of this analysis, to the reconstruction of the invariant mass of the J/Ψ resonance. To begin with, the distributions of the reconstructed $m_{J/\Psi}$ are presented in Fig:4.8. As the $|\eta|$ dependence is the most pronounced effect, we will further study the position of the peak value and the width of the distribution as a function of pseudo-rapidity.

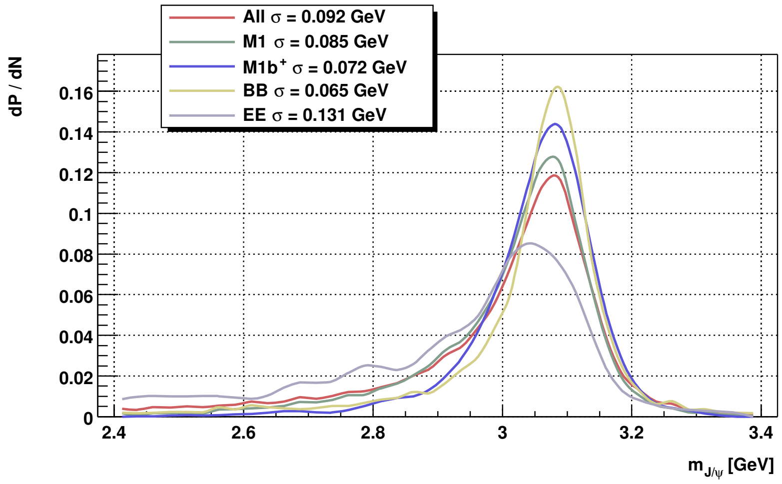

Figure 4.8: The distributions of the reconstructed $m_{J/\Psi}$ for all events and for two different kinds of sub-selections: a) for the cases when both the electron and positron belong to the **M1** or **M1b**$^+$ class; b) for the pure barrel (BB) and pure end-cap (EE) regions. The resolutions obtained by fitting them with a Gaussian in the range mean $\pm 2 \times \mathsf{rms}$ are appended to the legend.

But before we plunge into the gaussological description, some attention must be paid to events that populate the tails of the distributions as they will be neglected when their cores are studied. Fig:4.9 presents the raw distributions of the reconstructed $m_{J/\Psi}$. By requiring both particles to belong to the **M1** class, the tail extension is reduced by a factor of two in the barrel region. This factor increases through the transition region and reaches a value of three in the end-cap.

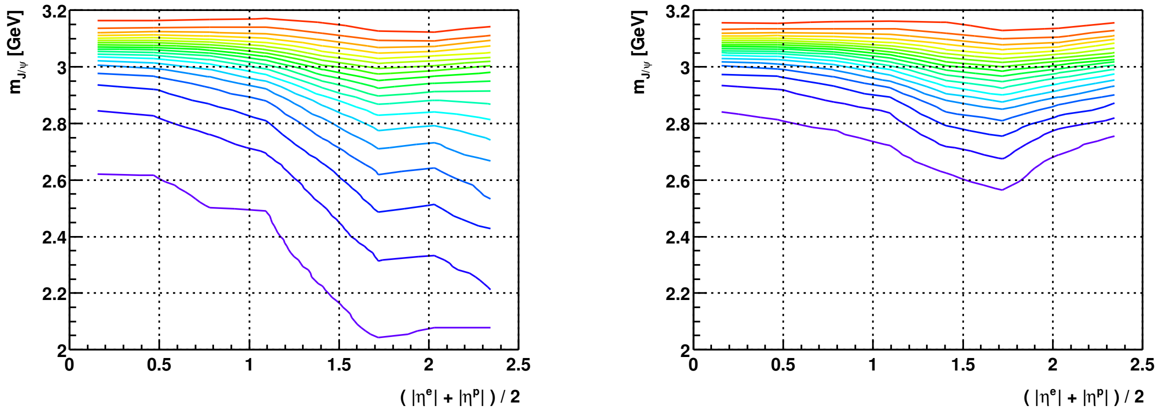

Figure 4.9: 5% contours of the reconstructed $m_{J/\Psi}$ versus the average $|\eta|$. Left: all events, right: both $e^{\pm}$ belong to the **M1** class.

The mean values and resolutions obtained by fitting the cores (mean $\pm 2 \times \mathsf{rms}$) with a Gaussian are shown in Fig:4.10. Both quantities show a direct dependence on the thickness of the tracker. By choosing the **M1** (**M1b**$^+$) sample, a substantial improvement in the resolution and mean value can be observed, especially in the end-cap region where the improvement is of the order of 10% (25%).

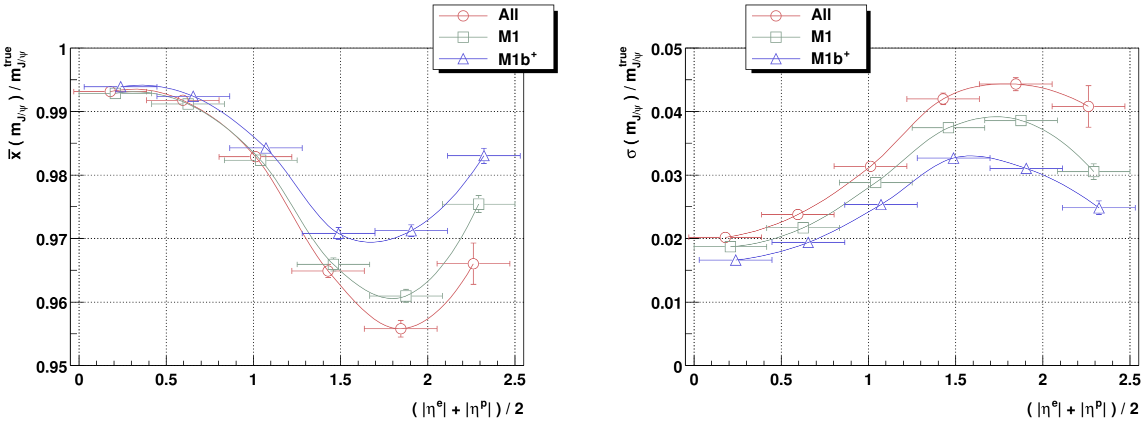

Figure 4.10: The mean values (left) and the resolutions (right) of the Gaussian fit to the reconstructed $m_{J/\Psi}$ as a function of the average $|\eta|$. All events and the sub-samples with both particles belonging to **M1** and **M1b**$^+$ are shown.

Here we can compare the obtained $m_{J/\Psi}$ shape to the one presented in the B-physics chapter of the Physics TDR ([3]:Sec:17.2.2). As the resolution quoted in the TDR was obtained by fitting the Gaussian curve over the symmetric core and tail-less side only, it is better to compare FWHMs. `ieElRec` wins with 150 MeV (for all reconstructed events) against 190 MeV presented in the TDR. Tail content is also reduced by a factor of two.

4.2 $Z \to ee$

The $Z \to ee$ events will form the basis of stand-alone ECAL calibration on the electro-weak scale. The results of a calorimeter-only study are presented in [2]:Sec:4.6 and [3]:Sec:12.3.1. There are some concerns expressed about the impact of the *final state radiation* (FSR) and hard ID bremsstrahlung on the uncertainty of the absolute electron energy scale. Here we present a complementary study, arguing how the ID measurements can contribute to the overall performance of the ATLAS detector for this specific process.

A total of 30 000 events have been simulated using the generator and detector simulation settings described in the introduction to this chapter. Furthermore, both the electron and positron were required to have $|\eta| < 2.5$ and $p_T > 5\,\text{GeV}$. As reconstruction of electrons depends crucially on p_T and $|\eta|$, the relevant distributions are presented in Fig:4.11.

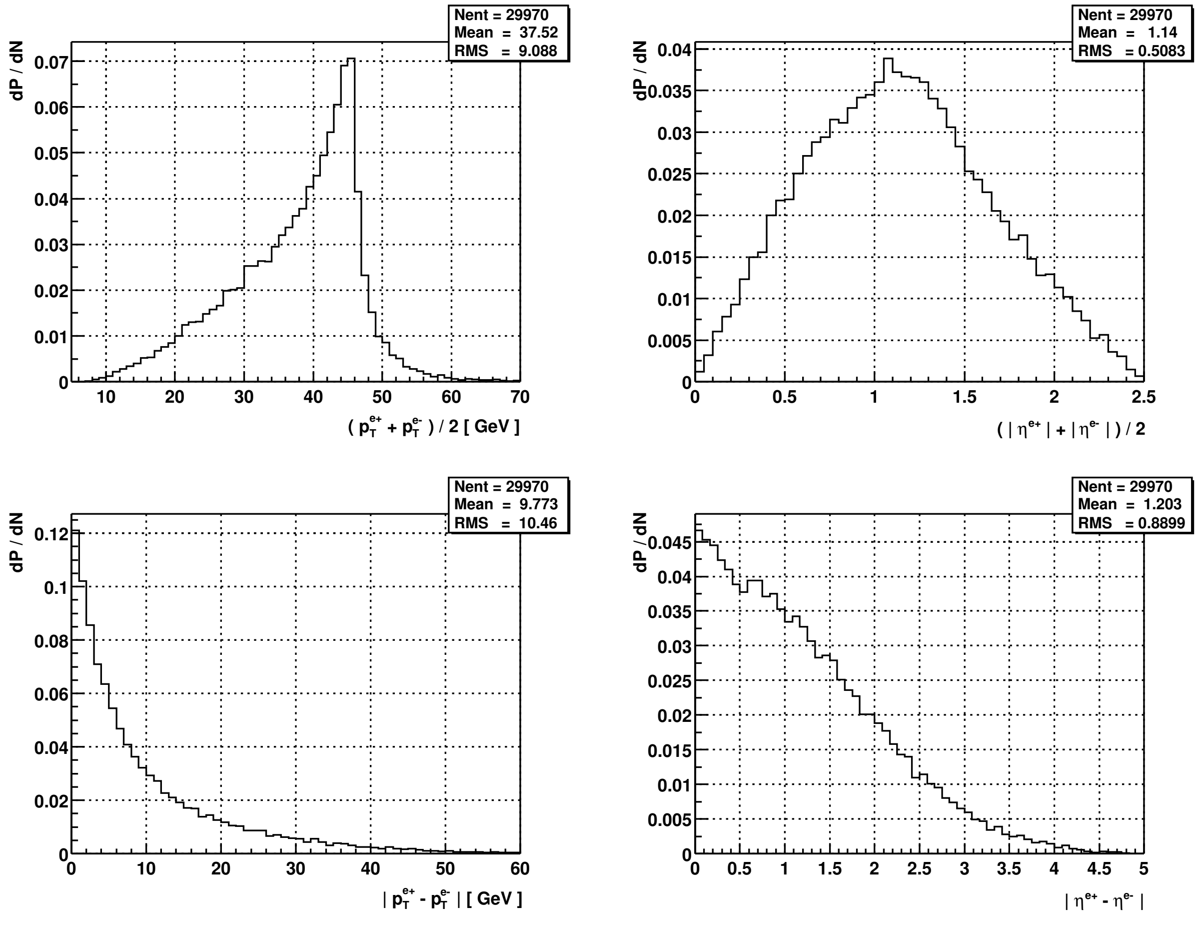

Figure 4.11: Distributions of average values of p_T and $|\eta|$ for the $e^{\pm}$ pair (top). Distributions of absolute values of differences in p_T and η (bottom). All plots show the generated quantities with FSR photons already 'emitted'.

Since the problems connected with FSR and bremsstrahlung are a major issue, the overall effects of both misfortunes will first be compared. Fig:4.12 makes a comparison of the reconstructed m_Z using different sources. The ECAL reconstruction should in principle manage to collect most of the radiated photons. Next, the reconstruction from the KINE banks is already plagued by the missing FSR photons. Both previous cases should be compared to the 'corrected KINE' case (labeled as wFSR) where FSR photons were excavated and their momenta added to the $e^{\pm}$ ones (this should in principle show PYTHIA's idea of the Z^0 shape). Reconstruction in the ID is a victim of both FSR and early bremsstrahlung and is also compromised by a poorer p_T resolution of about 5% (the energy resolution of the ECAL is about 2% in the relevant region).

The reconstruction efficiencies are the next matter of general concern. A division into barrel, transition and end-cap regions (as defined in Sec:4.1.1) is adopted again, with the addition of a new category named **BE** to cover the cases with one e in the barrel and the other one in the end-cap region. As the invariant mass cut will be used to pinpoint the Z^0 events, three invariant mass cuts are studied (5, 10 and 15%). The details of the invariant mass reconstruction are described in later sections. Efficiencies for good ID–ECAL match types are also presented. Tab:4.2 provides the numbers. For readers not too keen on tabular material, the results can be summarized by saying that the efficiency varies from about 50% (with a 5% cut on the reconstructed m_{Z^0} and requiring a good ID–ECAL match for both electrons) to 94.7% (with both electrons reconstructed in the ID but without applying any cuts).

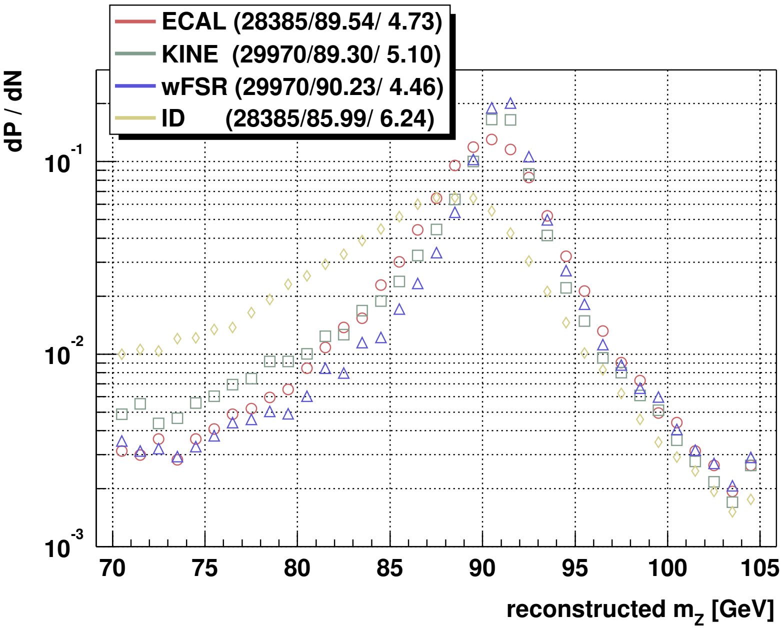

Figure 4.12: Comparison of distributions of the reconstructed m_Z using different available information. The ECAL plot was obtained by using E_T measurement of the calorimeter and direction measurements from the tracker. For the KINE plot information from the generation banks for the $e^{\pm}$ pair was used; for the wFSR plot the FSR photon momenta are included. The ID plot is what `ieElRec` manages to reconstruct without applying any quality cuts. All plots are labeled with their number of entries, mean values and rms's of the distributions.

4.2.1 Reconstruction of vertex parameters

While the EM calorimeter has a better E_T resolution, the tracker outperforms it in measurement of the z vertex position (a factor of 300 in resolution) and directional parameter $\cot\vartheta$ of the tracks in the r-z plane (an improvement in resolution by a factor of about 20). The

m_{Z^0} cut		5%			10%			15%			none		
Match type		All	M1	M1b$^+$	All	M1	M1b$^+$	All	M1	M1b$^+$	All	M1	M1b$^+$
All	100.0	68.87	51.90	38.61	82.81	61.84	45.93	87.32	65.09	48.31	94.71	69.98	51.91
BB	8.0	72.80	55.69	41.67	84.94	64.35	48.08	88.95	67.41	50.29	96.65	72.30	53.77
BT	30.7	70.80	54.80	40.50	84.22	64.61	47.52	88.83	67.99	49.87	96.09	72.79	53.47
TT	28.0	67.97	52.71	39.90	83.14	63.74	48.05	87.54	66.99	50.54	95.23	72.32	54.41
TE	19.5	66.04	47.67	34.97	81.10	58.06	42.98	85.88	61.46	45.66	92.88	66.11	49.13
EE	4.1	66.83	44.55	32.84	77.97	51.68	37.76	81.65	53.97	39.15	89.35	58.39	42.10
BE	9.8	68.63	48.88	36.10	81.10	57.38	42.42	85.86	60.57	44.56	93.20	65.16	48.03

Table 4.2: Z^0 reconstruction efficiencies for different $|\eta|$ sub-selections. For each of them different cuts are applied to the $e^{\pm}$'s match type and reconstructed invariant mass.

radial distance of the Z^0 vertex is much better constrained by the beam width (20 μm at low luminosity and 15 μm at high luminosity operation) and there is not much more one can do.

Again, capital letters are used to denote vertex parameters in order to differentiate them from track parameters.

A precise reconstruction of the Z_0 coordinate of a vertex is important for resolving the ambiguities in the assignment of tracks to different vertices. As Z^0 decays will be the bread and butter of LHC physics, it is important to know the precision which can be expected from ID reconstruction. Fig:4.13 shows the $|\eta|$ dependence of the Z_0 coordinate of the vertex. The overall Z_0 resolution is $\sigma(Z_0) = 75\,\mu$m.

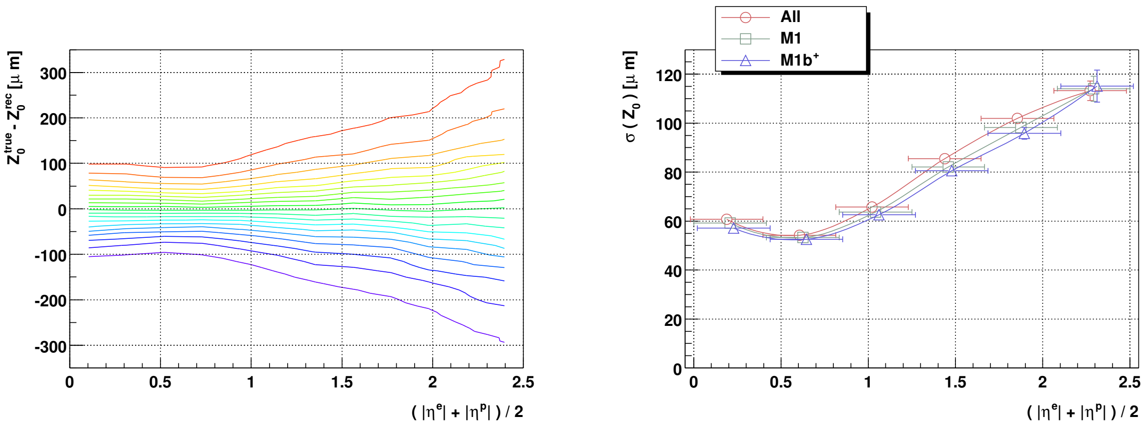

Figure 4.13: The $|\eta|$ dependence of the Z_0 measurement. The residual distribution with 5% contour lines is shown in the left plot and resolutions in the right one.

The main contribution to the error on the reconstructed invariant mass comes from the p_T (or E_T) resolution. Nevertheless, a good reconstruction of the tracks' direction at the vertex is still important. Also, one must know its resolution to correctly account for the experimental error. Although the resolution of the $\cot\vartheta$ measurement has already been studied in Sec:3.3.4, it is presented again for the electron/positron sample provided from Z^0 decays. Fig:4.14 presents its dependence on the average $|\eta|$ of the $e^{\pm}$ pair. The overall resolution is $\sigma(\cot\vartheta) = 0.089 \cdot 10^{-2}$.

The directional parameter φ of the $e^{\pm}$ tracks is measured by the tracker to a higher precision ($\sigma_{\mathrm{ID}}(\varphi) \sim 0.2 \cdot 10^{-3}$ rad in the relevant p_T region, see Sec:3.3.4) but one must be careful to check if a hard FSR or a hard early bremsstrahlung is lurking behind the curtain.

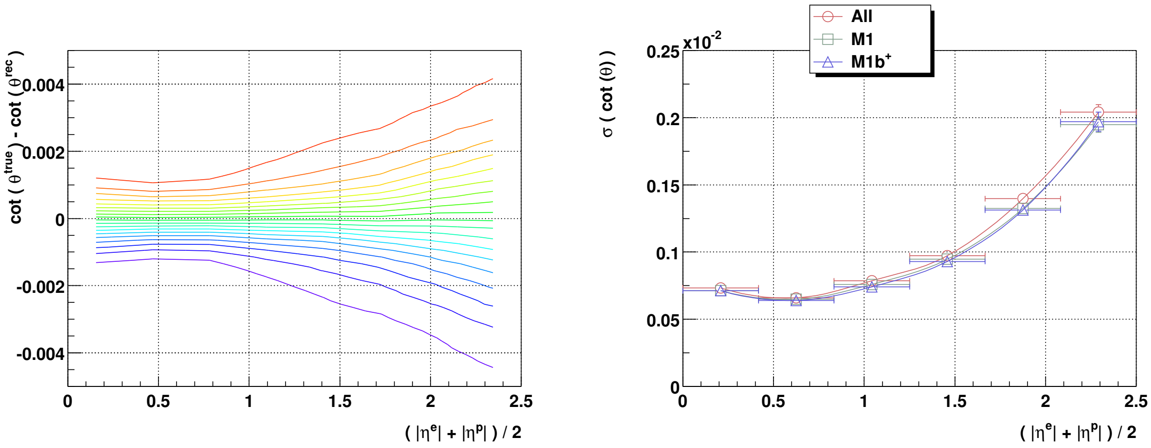

Figure 4.14: The $|\eta|$ dependence of the electron's and positron's $\cot\vartheta$ measurement. Residual distribution is shown in the left and resolutions in the right plot.

A correction based on ECAL φ measurement was attempted for cases when an electron track was not of the **M1b** match type, but the obtained resolution was worse than without applying any correction.

Warning: For the following results the directional parameters of the $e^{\pm}$ tracks used for the vertex reconstruction were always obtained from the ID. The p_T measurement was taken from the ECAL, unless explicitly stated otherwise.

Z^0 momentum reconstruction

A good Z^0 momentum reconstruction is of prime importance for the reconstruction of the invariant mass of particles decaying to Z^0. The $H \to ZZ^{(\star)} \to 4e$ decay, presented in the next section, is one of its most prominent clients.

The residual distributions of the directional angles $\cot\Theta$ and Φ as well as dependence of their resolution on average $|\eta|$ of the $e^{\pm}$ pair are presented in Fig:4.15. Both distributions are exhibiting tails that would make any peacock die of envy. The central resolution (obtained by fitting the residual distribution with a Gaussian curve in the range $\pm$ 2 $\times$ rms) of the $\cot\Theta$ measurement is $\sigma(\cot\Theta) = 0.218$ and $\sigma(\Phi) = 0.052\,\mathrm{rad}$ for the Φ measurement. The resolution of $\cot\Theta$ shows a strong dependence on average $|\eta|$. A seemingly unnatural goodness of the resolution at low $|\eta|$ can be explained by the fact that only the Z^0's produced with a low longitudinal momentum in the detector's reference frame can decay so that both the electron and positron have low $|\eta|$.

Distributions of transverse (P_T) and longitudinal (P_L) momentum of generated Z^0's are both approximately exponential with mean values of $\tau(P_T) \sim 16\,\mathrm{GeV}$ and $\tau(P_L) \sim 137\,\mathrm{GeV}$. Normalized residual distributions of both quantities are shown in Fig:4.16. As expected, the ECAL measurement (using directional parameters as reconstructed by the tracker) is more precise and almost unbiased by the early photon emission. On the other hand, the ID stand-alone reconstruction is plagued by a systematic shift and an asymmetric tail toward the missing momentum side. Sub-selections with good match classes give better results, but can't really do much to remedy the situation. For the case when p_T is taken from the ECAL these sub-selections provide only a minor improvement. The resolution of the P_T

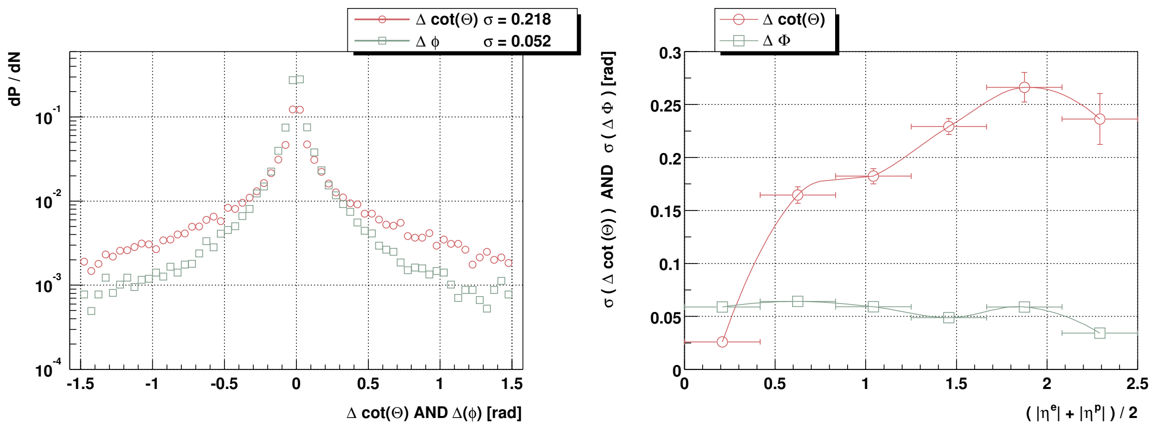

Figure 4.15: The angular parameters of the Z^0's momentum. Overall residuals of the $\cot\Theta$ and Φ measurements are presented in the left plot. The right plot show the dependence of their resolutions on the average $|\eta|$ of the $e^{\pm}$ pair.

measurement using ECAL's p_T measurement is $\sigma(P_T) = 5.2\%$ and $\sigma(P_L) = 2.5\%$ for the P_L measurement.

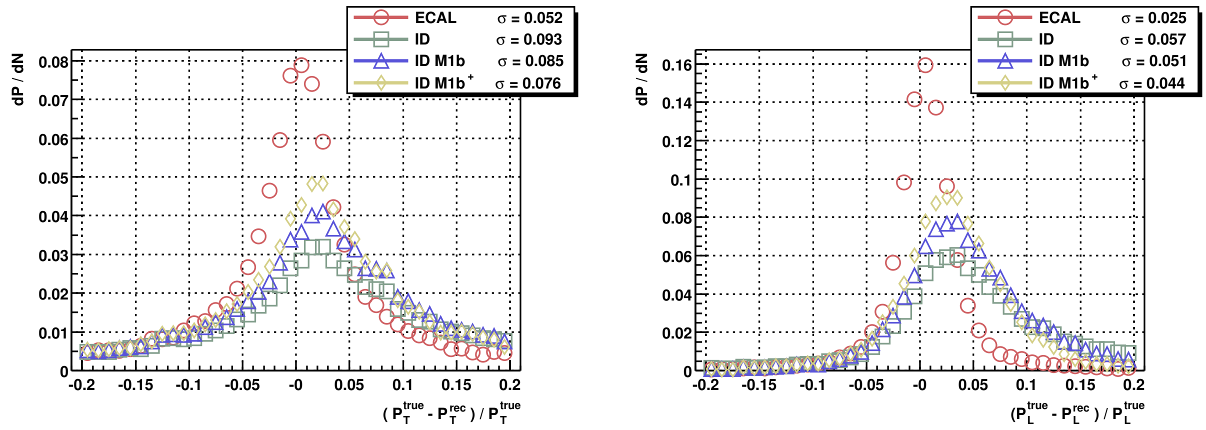

Figure 4.16: The normalized residual distributions of transverse (P_T, left) and longitudinal (P_L, right) momentum of the Z^0 vertex. Labels ECAL and ID denote the origin of the p_T measurement only. For the ID all events and cases when both $e^{\pm}$ belong to match type **M1b** and **M1b**$^+$ are shown.

4.2.2 m_{Z^0} resolution

As the width of the Z^0 resonance is comparable to the expected resolution of the m_{Z^0} measurement, it is more instructive to study the resolution of the reconstructed m_{Z^0} with respect to the generated $m_{Z^0}^{gen}$. Distributions of the generated and reconstructed m_{Z^0} were already presented in the introduction (see Fig:4.12).

It has been shown in the previous sections that due to FSR we can't hope for a good m_{Z^0} measurement relying on the ID alone. The adopted procedure has been explained in the previous section (see the warning). The left plot of Fig:4.17 shows the distribution of the reconstructed m_{Z^0} as a function of the average $|\eta|$ of the $e^{\pm}$ pair. There is no dependence on $|\eta|$ and the tails are well behaved over all the ID coverage. The right plot shows the normalized residual distribution of the same quantity, produced by using the generated $m_{Z^0}^{gen}$ on a per event basis. It serves to estimate the expected tail content. Mean values and resolutions, obtained by fitting $|\eta|$ slices with a Gaussian in the range mean $\pm 2 \times$ rms, are presented in Fig:4.18. While the behaviour of the mean value is a question of calibration in the used version of ECAL reconstruction code, the dependence of the resolution gives a measure of the effective broadening of the reconstructed Z^0 shape ($\Gamma_{Z^0} = 2.49\,\mathrm{GeV}$). In the barrel section the natural width and the experimental resolution are approximately the same, while in the transition region of the ID the experimental resolution is worse by 60%.

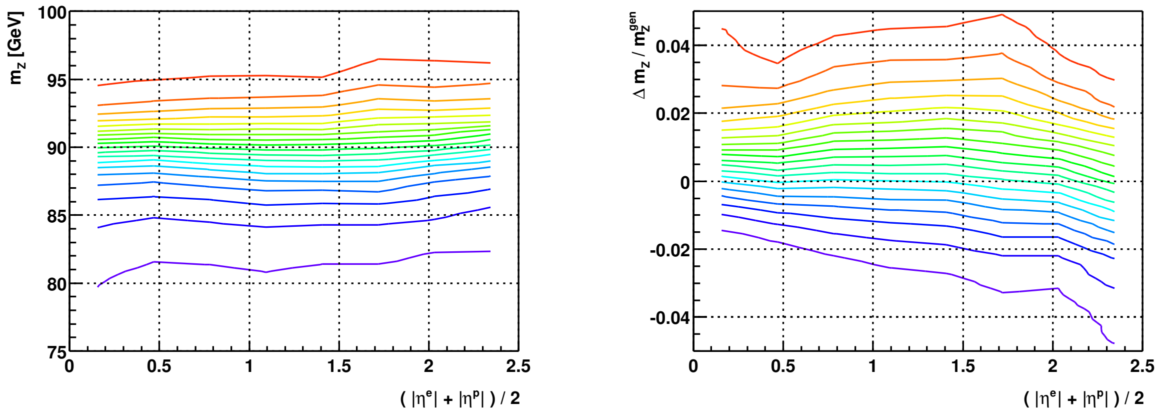

Figure 4.17: Left: 5% contour lines of the reconstructed m_{Z^0}. Right: 5% contour lines of the normalized residual distribution of the reconstructed m_{Z^0} with respect to the generated m_{Z^0}. Both quantities are plotted versus the average $|\eta|$ of the $e^{\pm}$ pair.

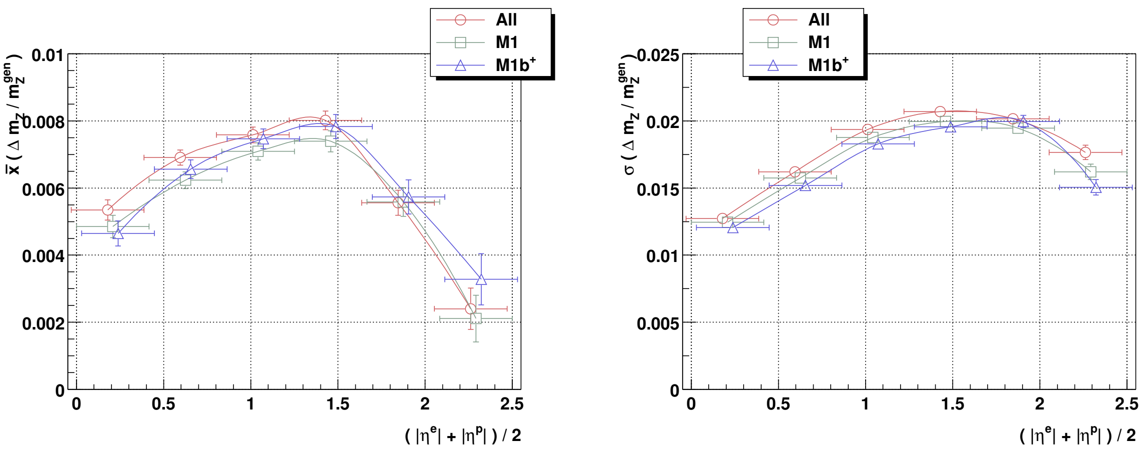

Figure 4.18: Mean values (left) and resolutions (right) of the normalized residual distribution of reconstructed m_{Z^0} versus the average $|\eta|$ of the $e^{\pm}$ pair. Curves are shown for all events passing the `ieElRec` reconstruction and for those with both electron and positron belonging to the **M1b** and **M1b**$^+$ class.

To compare the results to those presented in the TDR section "Calorimeter performance and calibration with $Z^0 \to ee$ events" ([2]:Sec:4.6) additional event selections must be done.

Firstly, events containing a hard FSR photon were omitted from their analysis. Since this separation can only be done using the information from the generation banks, some shadows of doubt are cast on the realism of the TDR results. And secondly, the events containing electrons in the ECAL's crack region ($1.37 < |\eta| < 1.52$) were not considered. Following the same steps the obtained resolution is $11.7\%/\sqrt{E}$ (see Fig:4.19) while the one quoted in the TDR is $11.4\%/\sqrt{E}$. However, the tail content outside the Gaussian tail is reduced by a factor of 3.

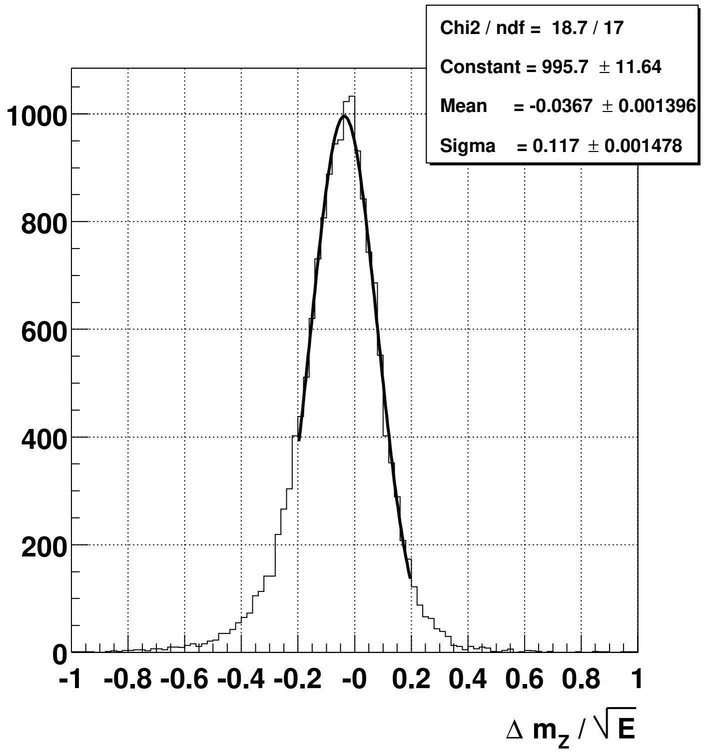

Figure 4.19: Difference between the reconstructed energy in the calorimeter and the true energy, divided by the square root of the true energy, as obtained for electrons from Z^0 decays.

4.3 $\mathbf{H \to ZZ^{(\star)} \to 4}e$

As a discovery of the Higgs boson in any form (even its absence) is one of the primary goals of the LHC project, it seems rather unnecessary to make much further introduction. The following study of the SM Higgs decay to four electrons complements the results presented in the *Physics TDR* by putting more emphasis on the ID reconstruction ([3]:Sec:19.2.5 ($H \to ZZ^\star \to 4l$) and [3]:Sec:19.2.9 ($H \to ZZ \to 4l$)). Detailed electron p_T distributions are presented and the role of the ID in their reconstruction is discussed together with its impact on the reconstruction of the Higgs boson mass.

10 000 events for each of $m_{\rm H}$=(130, 150, 180, 200 GeV) were simulated using the generator and detector simulation settings described in the introduction to this chapter. Associated W and Z productions were not included in the event generation (their cross-section is about 50 times smaller). The production is dominated by gluon fusion ($\sim 70\%$) and WW fusion ($\sim 20\%$). The H boson was forced to decay into $Z^{(\star)}Z^{(\star)}$. Both Z's were allowed to be off-shell, mainly out of curiosity, since this effect is below 1% even with the lowest value of $m_{\rm H}$ (also, standard ATLAS analysis cuts require one Z to be close to m_{Z^0}). Furthermore, rather obviously, both Z's were forced to decay into two electrons. All electrons were required to have $p_T > 5$ GeV (before FSR corrections were applied) and $|\eta| < 2.5$.

The full width and branching ratios of the SM Higgs boson vary rapidly through the studied region. Their behaviour, as obtained by the HDECAY package ([35]), is shown in Fig:4.20. When considering branching ratios remember that the LHC environment is 'full of jets' and that the $b\bar{b}$ decay channel is only considered with an associated W or Z production and a leptonic decay of the accompanying gauge boson. Decays into gg and $\tau\bar{\tau}$ are not considered at all by ATLAS. For $m_H \sim 200$ GeV the natural width and experimental resolution are getting comparable and it becomes possible to measure Γ_H provided our knowledge of the detector's resolution is sufficient. This measurement provides a direct test for physics beyond the SM as the SM predictions of Γ_H as a function of m_H are firm and unambiguous.

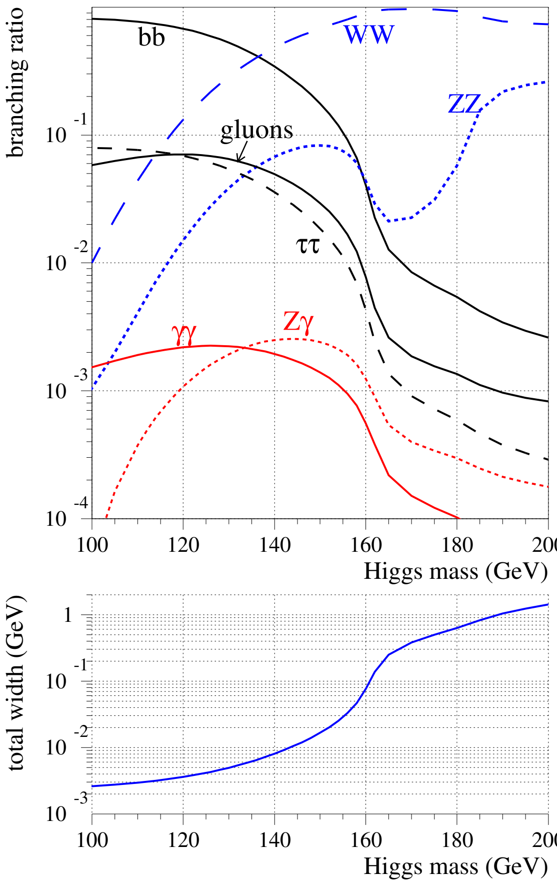

Figure 4.20: Branching ratios and full width of the SM Higgs boson as obtained from the HDECAY package.

4.3.1 Some peculiarities

This section is a brief survey of some kinematic properties of the system under study. It is meant as a reference for those who will delve in the lower parts of the analysis and will, on occasion, have to think in the context of these distributions.

Kinematics of H

H production mechanisms at the LHC are far from trivial and they result in Higgs bosons produced at different angles toward the beam axis and with a wide range of boosts. Fig:4.21 presents $|\eta|$ distributions and the correlation between this angle and the relativistic γ factor. In general, due to the proton's structure functions, it's hard (or at least very rare) to squeeze more than 1 TeV of energy out of two protons colliding at 14 TeV cms energy. When the Higgs boson is produced at low $|\eta| \lesssim 1.5$, its momentum is generally small. Higher boosts are available at higher $|\eta|$. One should keep in mind though, that this distribution is sliced heavily by the requirement of all electrons having $|\eta| < 2.5$.

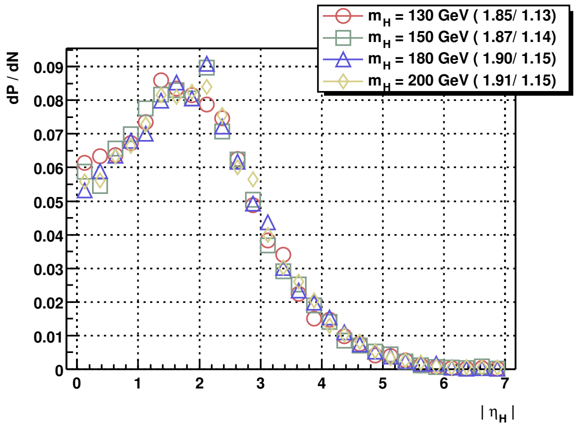

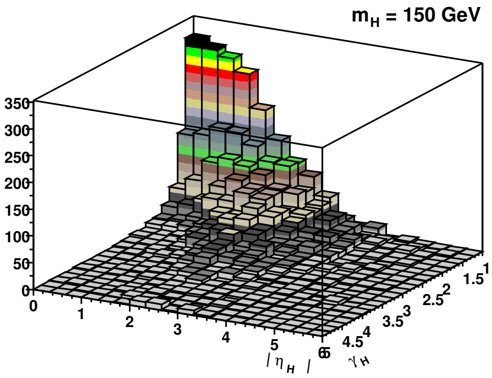

Figure 4.21: Left: $|\eta|$ distributions of the momentum of the generated Higgs bosons. Mean values and rms's are appended on the label. Right: correlation of boost with $|\eta|$ for $m_{\mathrm{H}} =$ 150 GeV.

Role of Z*'s

The electron spectrum from singly produced Z's (presented in Fig:4.11) is rather different than the one emanating from H decays. The difference is even more striking in the case of Z* and it implies that a different electron reconstruction approach might be more fruitful for a low mass H.

The first messenger of the fact, that some low-p_T electrons ($p_T < 20$ GeV, where the ID is more precise than the ECAL) show up in the final state can be seen in the invariant mass distribution of the off-shell Z* (Fig:4.22). There are basically no surprises, one should perhaps note that there is a substantial fraction of Z*'s produced at the lower end of the available phase space.

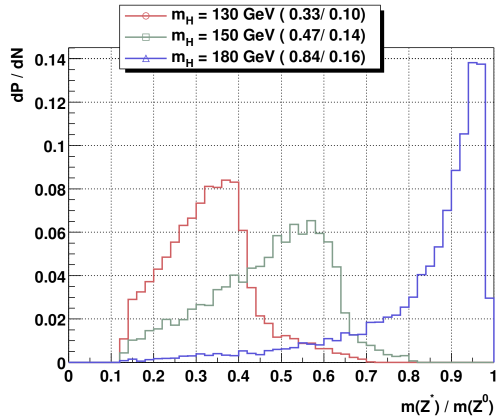

Figure 4.22: Off-shellness of the Z*'s originating from H decays for different m_H.

Fig:4.23 presents the electron p_T and $|\eta|$ distributions from the decays of the lighter of the two Z's. The curve for $m_{\mathrm{H}} = 200$ GeV can safely be taken as a representative of the

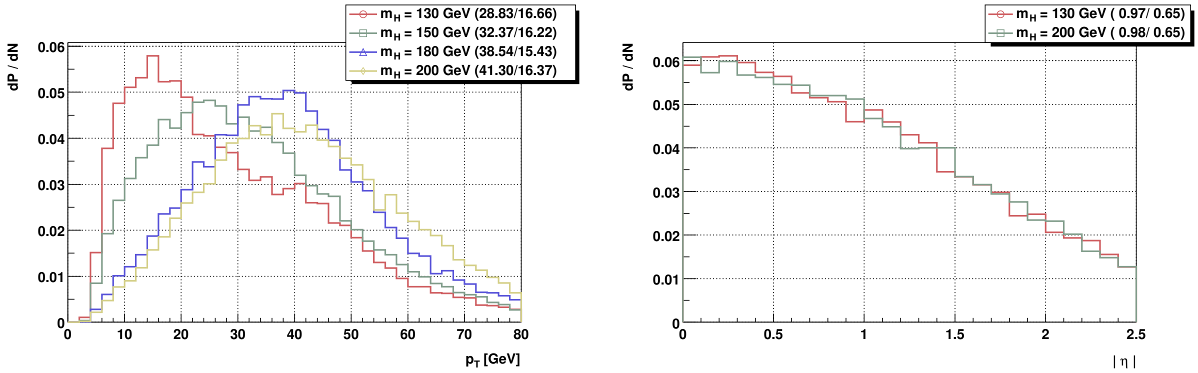

Figure 4.23: p_T (left) and $|\eta|$ (right) distributions of electrons from the Z* decays.

decaying on-shell Z. As far as the p_T distributions are concerned, the most important aspect is the percentage of electrons with $p_T < 20\,\text{GeV}$:

m_H	[GeV]	130	150	180	200
$p_T < 20\,\text{GeV}$	[%]	39	27	13	10

This corresponds to fractional usefulness of the tracker for a p_T measurement used for H reconstruction. One should in principle be careful to check for a hard FSR. In the following analysis the p_T measurement of an electron was taken from the tracker if p_T measured by the ECAL was below 20 GeV and its ECAL/ID match was of the **M1** type with $p_T^{\mathrm{ID}} > p_T^{\mathrm{ECAL}}$. The improvement obtained for the reconstructed $m_{Z^\star}$ is shown in Fig:4.24. The correction is at 1% level and is getting smaller with increasing average $m_{Z^\star}$. Fraction of events, to which the correction is applied, is also falling from about 33% for the Z* sample from $m_{\mathrm{H}} = 130\,\text{GeV}$ to about 9% of cases for on-shell Z's. $|\eta|$ distributions are not influenced by m_{H} or off-shellness of the Z boson.

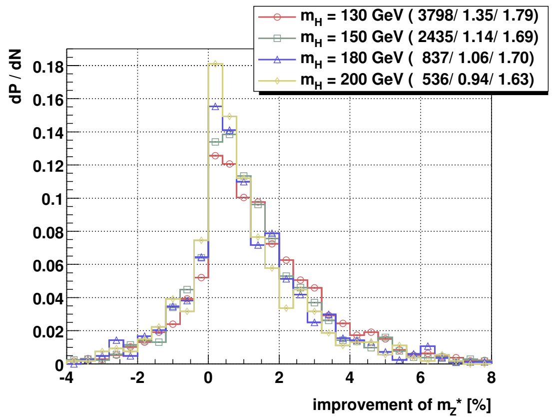

Figure 4.24: Relative improvement (positive values) of the reconstructed $m_{Z^\star}$ by use of tracker's p_T measurement. Distributions are labeled by number of entries, their mean values and rms's.

4.3.2 Reconstruction efficiency

As it is slightly omisive to study efficiency of reconstruction of a yet undiscovered physical system without an accompanying study of background processes, an overview of the situation is provided in the following. The first event pre-selection is done by application of simple kinematical cuts on the p_T of electrons (some already by the trigger) and mass of reconstructed Z$^{(\star)}$'s. For the decay channel under study the reducible background comes from $t\bar{t}$ and $Zb\bar{b}$ productions. Details are studied in [36] and reviewed also in the 'Physics TDR' ([3]:Sec:19.2.5.3). Further rejection of this background is based on calorimeter isolation and cuts on the impact parameter of reconstructed electrons. For the irreducible background, the continuum ZZ* production, some additional separation can be obtained by using the sum of four-lepton transverse momenta and the opening angle between the Z–Z* pair[37].

More technically, as it is hard to apply cuts on non-existent electrons, the use of `ieElRec` provides a 4% improvement of electron reconstruction efficiency which results in a $\sim 10\%$ increase of raw reconstruction efficiency of the H boson. Mainly this increase can be attributed to a better understanding of the electron behaviour in the detector and re-inclusion of some well reconstructed electrons that would fail a more stringent set of requirements. Nevertheless, one should still be concerned about the quality of reconstructed electrons. For an event to be considered efficient, it was required that all electrons belong to **M1** or **M3** ECAL/ID match type. By inclusion of the **M3** match type (ECAL provides a better measurement) it is in part accounted for cases of a hard FSR and early bremsstrahlung. This, of course, must have some impact on the derived reconstructed quantities. To observe this effect, windows of different size were set upon mass of the reconstructed H. Obtained reconstruction efficiencies are dumped in Tab:4.3. For the reconstruction efficiency improvement of 10% quoted above, a 10% cut on m_H was used. As will be seen later, inclusion of the events with **M3** electrons worsens the $m_{\rm H}$ resolution by about 3%. Nothing is for free ...

$m_{\rm H}$ cut	2%			5%			10%			none		
Match type	All	M1/3	M1	All	M1/3	M1	All	M1/3	M1	All	M1/3	M1
m : 130 GeV	60.15	57.71	36.26	83.28	78.47	47.89	87.32	81.32	49.39	89.11	82.11	49.86
m : 150 GeV	62.23	59.61	37.16	83.89	79.29	47.79	87.43	81.91	49.14	89.23	82.87	49.63
m : 180 GeV	61.35	58.74	34.58	81.27	77.25	44.51	85.49	80.88	46.49	88.90	83.09	47.74
m : 200 GeV	63.47	60.51	35.53	82.39	77.87	45.08	86.64	81.45	47.15	89.64	83.49	48.30

Table 4.3: H reconstruction efficiencies for different values of generated $m_{\rm H}$. For each of them different cuts are applied to the $e^\pm$'s match type and reconstructed invariant mass.

In further analysis the same kinematic cuts were applied as enumerated in the 'Physics TDR' ([3]:Sec:19.2.5.1). All electrons were required to have $p_T > 7\,\mathrm{GeV}$ and at least two must have had $p_T > 20\,\mathrm{GeV}$ (level 1 trigger). One of the $e^\pm$ pairs was further required to have its invariant mass within an energy dependent window around $m_{\rm Z^0}$ (from 15 down to 6 GeV) and the invariant mass of the second pair had to be above a certain threshold (from 20 to 60 GeV).

4.3.3 Vertex parameters

Cuts imposed upon impact parameters of all electrons in the final state can serve for rejection of the reducible backgrounds. Since the $pp \rightarrow {\rm Z}^0 b\bar{b}$ process was included in Pythia 5.7 as a preliminary feature that was not intended for use in physical analyses, the results presented in the TDR can well happen to be widely off the track with respect to its cross-section and final state kinematics. This particular study will therefore have to be redone with an improved Monte-Carlo generator. Here the results obtained with `ieElRec` are presented with emphasis on their application to the background rejection.

Both longitudinal (z_0) and transverse (a_0) impact parameters of individual e's can be used for secondary b-vertex detection. Displaced b-vertices will occur for ${\rm Z}^0 b\bar{b}$ and $t\bar{t} \rightarrow b\bar{b}{\rm W}^+{\rm W}^-$ processes, as both b-quarks must decay into electrons to actually provide the $4e$ signature. Fig:4.25 shows the relevant distributions for $m_{\rm H} = 150\,\mathrm{GeV}$. Statistical values obtained for other event samples deviate from the one presented below 1% level. For the a_0 measurement, the minimum, average and maximal values of its absolute value are shown. While cuts can be applied directly upon the a_0 measurements by using the beam constraint, the Z_0 coordinate of the vertex has first to be determined by using the four independent measurements. The right plot of the figure is a collage of the z vertex coordinate related distributions:

δZ_0 is a residual distribution of the Z_0 measurement obtained by averaging individual z_0 measurements (a resolution of 50 μm is consistent with the results for single particles);

$Z_A - Z_B$ is a distribution of difference between the reconstructed Z_0 coordinates of the two Z^0's;

$\max(\Delta Z_0)$ is a distribution of distance between the two most separated electrons.

For the actual rejection one would of course try to use both variables, possibly simultaneously. The exact form of the cuts can only be determined by inspection of the other (back-ground) side of the coin.

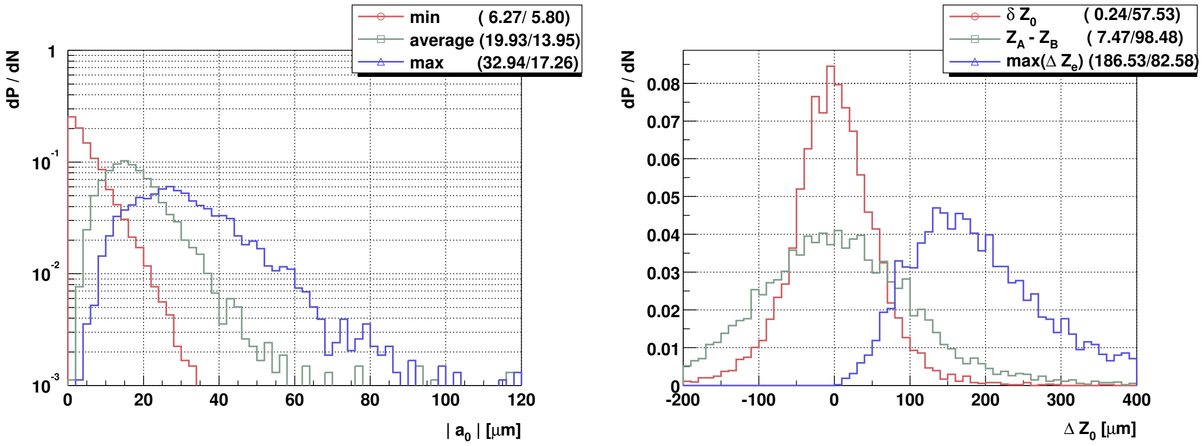

Figure 4.25: Various distributions portraying the reconstruction of single-electron perigee parameters a_0 (left) and z_0 (right) for H $\rightarrow$ ZZ* $\rightarrow$ $4e$ at $m_H = 150$ GeV. All plots are labeled by mean values and rms's. Detailed description is interwoven with the text.

4.3.4 α_Z: the Z^0–$Z^{0(\star)}$ opening angle

As already mentioned, the angle between the reconstructed Z^0 bosons can be used for rejection against the ZZ* background. In the studied range of H's masses there is a chronic shortage of invariant mass and the momentum 'given' to the H's decay products is on average substantially smaller than the original boost of the H boson. This results in a small opening angle α_Z between the two Z^0 bosons as shown in the left plot of Fig:4.26. The residuals of this measurement are presented in the partner-figure. Their distributions are more exponential than Gaussian with a characteristic angular difference of 0.01 rad.

4.3.5 Reconstruction of m_H

The improvement of the $m_{Z^\star}$ measurement by usage of the tracker's p_T measurement has already been presented and now it's time to assess its impact on the m_H resolution. Another improvement is expected from application of the m_{Z^0} constraint as the experimental invariant mass resolution at the Z^0 resonance is smaller than its width. This constraint is, following the TDR, applied if the mass of the electron pair is within a ± 6 GeV window around m_{Z^0}. Both

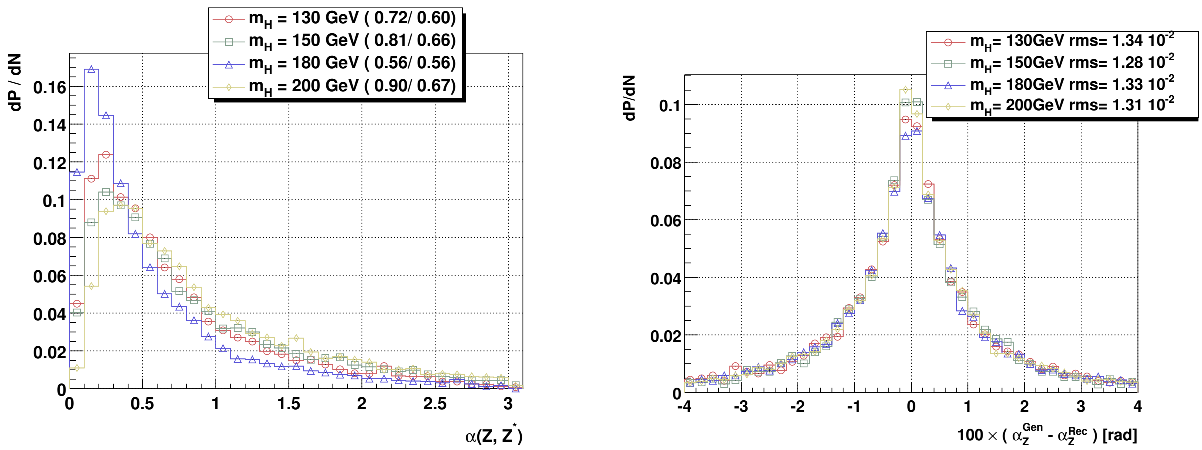

Figure 4.26: Left: distributions of the $\alpha_{\rm Z}$ angle. Right: corresponding residual distributions labeled by their rms's.

corrections are compared in Fig:4.27, which shows raw $m_{\rm H}$ distributions for $m_{\rm H} = 130\,{\rm GeV}$ and $180\,{\rm GeV}$. ID contributions are important for low $m_{\rm H}$, where there are still many clients for the p_T correction, and the overall effect is a $\sim 4\%$ improvement of the mass resolution. The impact of the $m_{\rm Z}$ constraint has a well pronounced effect on the peak position and also introduces a mass resolution correction, most pronounced at $m_{\rm H} = 180\,{\rm GeV}$, where the improvement reaches 15%.

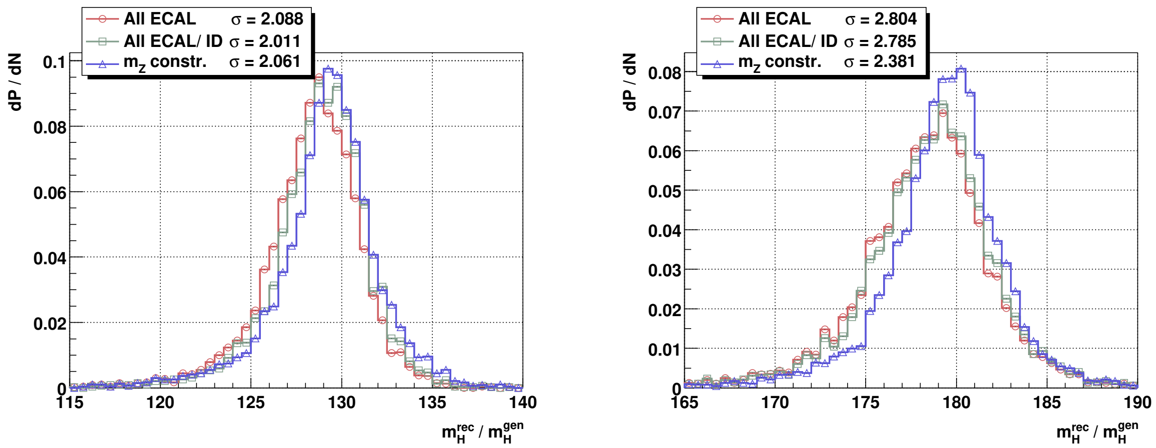

Figure 4.27: Reconstructed $m_{\rm H}$ shapes for $m_{\rm H} = 130\,{\rm GeV}$ (left) and $180\,{\rm GeV}$ (right). The plots are labeled by their resolutions. ID corrections were applied for the 'green' sample only.

A more statistical presentation of the results, expressed in statistical terms, is given in Fig:4.28. For comparison, the results obtained without using the $m_{\rm Z^0}$ constraint and ID corrections are also presented. The `no FSR` curve was obtained by discarding all the events for which a FSR photon was detected in the generation banks. The overall effect of the FSR is an increase of the width by about 3%, accompanied by a slender tail on the low-mass-side.

Compared to the *Phyisics Performance TDR* results, the resolutions obtained from **M1/3** event sample are worse by 25% for $m_{\rm H} = 130, 150\,{\rm GeV}$ and by 10% for $m_{\rm H} = 180\,{\rm GeV}$. However, another H $\rightarrow$ ZZ$^{(\star)}$ $\rightarrow 4e$ study (at $m_{\rm H} = 130\,{\rm GeV}$), presented in the *Calorimeter*

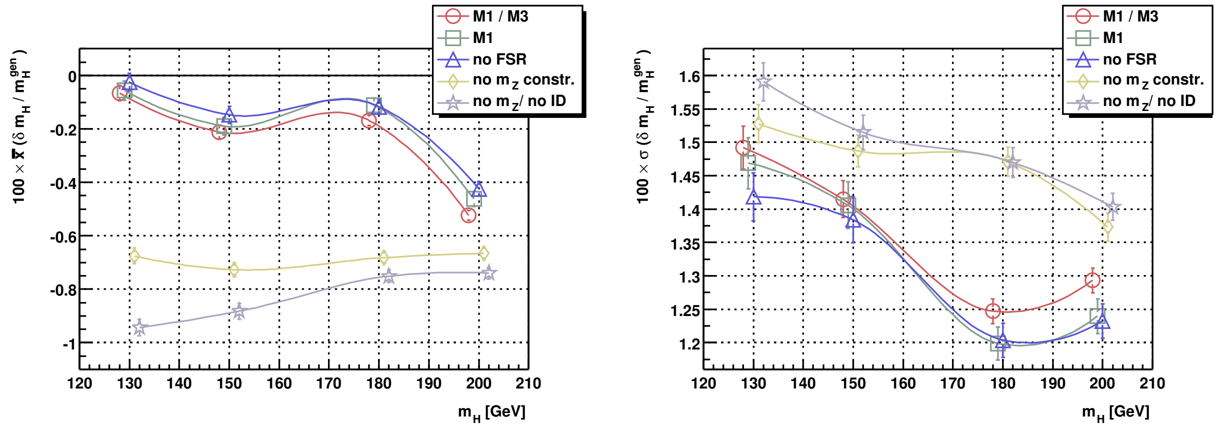

Figure 4.28: Mean value (left) and width (right) of the normalized m_{H} residual distribution as a function of m_{H}. The values were obtained from a Gaussian fit in a range from -1.5σ to 2.5σ around the mean. Warning: suppressed zero.

Performance TDR [8], advertises tighter cuts on the mass of the on-shell Z^0 ($\pm 6\,\mathrm{GeV}$). By applying tighter cuts, the results can be brought in accordance with the ones presented in the TDR. An improvement of about the same size is also achieved by further application of track isolation cuts (no charged tracks with $p_T > 1\,\mathrm{GeV}$ in a $d\eta \times d\varphi = 0.1 \times 0.1$ window) at the expense of $\sim 30\%$ loss in efficiency.

Conclusion

As each chapter forms a well defined whole, the conclusions can be made for each of them independently. The observations and results are recapitulated with a strong emphasis on the original work performed.

Beam test of a prototype SCT module

The analysis of data gathered in a beam test of a prototype silicon-strip half-module equipped with analogue read-out chip SCTA128HC is presented in detail. The module was constructed in such a way to allow for a simultaneous measurements of 6 cm and 12 cm long detectors. While the detectors in ATLAS will operate at a constant tilt angle of 10°, in this beam test inclinations from 0° to 50° (in steps of 10°) were studied. The beam test set-up is described and the resolution of the beam telescope, at the point where the device under test was inserted into the beam, is found to be $2.5\,\mu$m. Extraction of clusters of hits from the raw data is performed and the efficiency versus noise occupancy for the detectors of both lengths is studied. The efficiency at an occupancy of $5 \cdot 10^{-4}$ is found to be 98.8% for the 6 cm detector and 97.2% for the 12 cm detector.

The resolution of the 12 cm detector at 10° was found to be $\sigma(dU) = 12.2\,\mu$m. There are 40% of single strip hits ($\sigma_1(dU) = 15.1\,\mu$m) and the remainder of them are two-strip hits for which the *eta* reconstruction method can be used ($\sigma_2(dU) = 10.3\,\mu$m). The average signal-to-noise ratio is 26 for the 6 cm detector and 20 for the 12 cm detector. Based on the difference between the detectors of different lengths, relative contributions to the noise from the electronics and the detector were estimated: the noise of the electronics is $\mathrm{ENC}_{\mathrm{el}} = 730\mathrm{e}^-$ and the noise of a single, 6 cm strip is $\mathrm{ENC}_{6\,\mathrm{cm}} = 390\mathrm{e}^-$. The net noise of the 12 cm detector is therefore $\mathrm{ENC}_{12\,\mathrm{cm}} = 1510\mathrm{e}^-$.

The tested module fully conforms to the ATLAS specifications. Given the 10-year operational time in a high radiation environment with limited planned service access to the modules, the analogue read-out solution would provide a better control over detector noise and common-mode variations resulting in a more robust quality control that is essential for achievement of ATLAS's physics goals. The collaboration may, now that the feasibility of the analogue read-out has been proven, seriously reconsider its baseline solution for the SCT read-out electronics.

Electron reconstruction algorithm

The analysis of bremsstrahlung effects. Electron reconstruction in the ATLAS detector is compromised by the large amount of material in the tracking volume, which leads to frequent emissions of hard bremsstrahlung photons. As a consequence, the affected electrons curl away from their previous trajectory in a magnetic field and make the p_T measurement (based on measurement of a track's curvature) prone to errors. Especially at lower electron transverse energies (up to $p_T = 20\,\mathrm{GeV}$) an electron and the emitted photon can separate in their φ coordinate so much that the *electro-magnetic calorimeter* (ECAL) clustering algorithm, which operates with a fixed-size window, can not unambiguously make them fit into the same cluster. In this manner, the ECAL measurements of E_T and φ can also be affected.

It is demonstrated that by using position measurements close to the interaction point only (the first 5 space-points in the barrel and end-cap regions and the first 4 space points in the transition region), the mean value and rms of distribution of the measured p_T can be improved significantly. But even using the optimal track-length for each event, there are still 15%(barrel), 25%(transition) or 35%(end-cap) of events further than 10% away from the true value. As far as the ECAL is concerned, matching in η is shown to be unaffected by a bremsstrahlung while both E_T and φ residual distributions exhibit correlated tails that can be attributed to an electron or photon missing the EM cluster. The effect is well pronounced at $p_T = 5\,\mathrm{GeV}$ while at $p_T = 20\,\mathrm{GeV}$ the reconstructed EM cluster quantities are hardly changed even for electrons that lose more than 10% of their energy by the end of the pixel sub-detector.

Next, the question of second-order bremsstrahlung effects is addressed and it is shown that only about 50% of events with an appreciable energy loss can be handled by allowing for a single kink on the track (standard bremsstrahlung recuperation method). Then the coin is flipped and the fraction of events that can be handled by different pattern recognition methods is presented: 55% of events can be handled using the standard fitting procedure (less than 10% energy loss by the end of the SCT); 12% of events have a single measurable bremsstrahlung occurrence which can be reconstructed by allowing for a kink; 10% of the events have a hard bremsstrahlung before the end of the pixel detector and so the electron can only be reconstructed with a poorer p_T resolution; the rest (23%) undergo two or more hard bremsstrahlung-photon emissions and their recuperation is not covered properly by the existing algorithms.

The electron reconstruction algorithm was developed taking into account the results of the above analysis (christened `ieElRec`). Instead of trying to instantiate a full-length track in the track searching phase, the `iPatRec` pattern recognition package was modified to provide a list of secondary tracks (those that don't extrapolate to the vertex region). A special method for the extrapolation of those tracks through the TRT was also developed. By de-weighting silicon hits it tries to extend a track as far as possible into the TRT. Special attention was paid to obtain the best possible results with respect to electron identification, bremsstrahlung tagging and improvement of p_T resolution as well as perigee parameters of tracks reconstructed in the inner detector. The inputs for `ieElRec` are clusters reconstructed in the ECAL and tracks found by `iPatRec` (secondary tracks included). `ieElRec` then finds close matches of the tracks to ECAL clusters (if any) and proceeds with further scrutinization of the pair. If the matching track failed the TRT association, a matching secondary track is searched for and, if found, attached onto its tail. Surroundings of the ECAL cluster are scanned for any neighbouring energy depositions to determine track isolation and to recover some cases of hard bremsstrahlung. Detector hits, constituting the ID track (and its possible prolongation in a case of a hard bremsstrahlung in the mid-SCT, when two shorter tracks are reconstructed), are fitted using an increasing number of hits from the beginning of the track as well as from its end. By using pre-built look-up tables and heuristic rules, it then selects the fit that best realizes the ID/ECAL matching (the original fit from `iPatRec` is also considered). The selected rule characterizes the type of bremsstrahlung that occurred and can form a useful criterion in later analyses. Therefore: `ieElRec` doesn't attempt to build a long track (for purposes other than TRT association), but de-constructs the input track and takes the segment that best matches the ECAL cluster as a base for p_T and impact parameter measurement. Based on ID/ECAL matching, the *transition radiation* information and the properties of the EM cluster, the level of difference from a charged pion signal is estimated (*pion ambiguity*).

Single electrons in the transverse energy range from $p_T = 1.5$ to 60 GeV were analysed with respect to `ieElRec`'s performance and the quality of obtained track parameters. The reconstruction efficiency for good ID/ECAL matches ranges from 80% for low p_T to 86% for $p_T > 10$ GeV. The electron identification efficiency is about 12% higher over all energy range. At low p_T these events are tagged either as poor p_T measurements by the ECAL or as an unknown match type. As transverse energy increases, the fraction of events that are recognized to have undergone an early hard bremsstrahlung increases and above 10 GeV they represent all the events not classified as good matches. This fraction corresponds directly to the fractional probability of a hard early bremsstrahlung before the end of the pixel sub-detector. At lower energies precision of the ECAL is lower and splitting of an electron and its accompanying photon in the magnetic field can cause part of the original electron's energy to be irrecoverably lost, while at higher energies ECAL accounts correctly for all cases of hard bremsstrahlung.

The measurement of a track's p_T is improved by 1% at 1.5 GeV and this correction increases to 4% for $p_T > 20$ GeV. The correction is strongly η dependent, directly following the material distribution. The transverse impact parameter and the directional angle in the x-y plane are likewise improved by track truncation. On the other hand, the longitudinal impact parameter and the directional angle in the r-z plane are not degraded by this procedure.

The pion rejection based on the pion ambiguity and ID/ECAL match type as determined by `ieElRec` is studied. As a smaller fraction of pions than electrons pass the `ieElRec` cuts and provide a good ID/ECAL match, a rejection factor of 30 for $p_T \geq 10$ GeV was obtained (decreases with p_T, e.g., 15 for $p_T = 2$ GeV) before considering the pion ambiguity variable. Additional rejection, enforced by imposing a cut on pion ambiguity, can be obtained at a sacrifice of electron efficiency: for $p_T = 2$ GeV the rejection factor is 150 (2000) at a 90% (50%) electron efficiency.

Reconstruction in jets was studied on a $\mathrm{B}^0 \rightarrow \mathrm{J}/\Psi \rightarrow ee$ sample, where different track multiplicities ($1 \leq N_T \leq 8$ charged tracks with $p_T > 1$ GeV) could be compared on a uniform data sample and also at transverse energies where the expected effects will be most pronounced (from 2 to 10 GeV). No change in the overall `ieElRec` efficiency can be observed. The most noticeable effect is that a fraction of events, tagged as 'poor ID measurement' increases linearly with track multiplicity and gets to 10% above the isolated electron level at N_T=8. This can be attributed to additional energy deposited into the EM cluster which tricks the algorithm into believing that a hard bremsstrahlung has occurred.

Pile-up effects are most pronounced in the ECAL where they manifest as noise as well as additional clusters due to minimum-bias events. Pattern recognition is burdened by the higher number of combinatorials but the charged track multiplicity (with $p_T > 1\,\mathrm{GeV}$) in a cone around the triggering EM cluster is 25 times lower than for the jet sample discussed above. The observed drop in reconstruction efficiency for good ID/ECAL match types was found to be 5% for $p_T \leq 5\,\mathrm{GeV}$, 2% for $p_T = 10\,\mathrm{GeV}$ and no change was observed for higher transverse energies. ECAL reconstruction efficiency, compared to the no pile-up sample with the same ECAL clustering cut $E_T > 1\,\mathrm{GeV}$, is increased, but this is a consequence of additional energy being deposited in the ECAL. `ieElRec` classifies these events into two categories: first, about 70% of these events are marked to have a poor p_T measurement, which is symptomatic of the addition of energy into an otherwise existing EM cluster. The rest of the events are tagged to be of unknown ID/ECAL match type which signifies that the track and ECAL cluster are not correlated.

It has been shown that use of an electron reconstruction algorithm that takes into account the fact that ATLAS's inner tracker *is* thick results in an approximate 5% increase in reconstruction efficiency and can be made almost insensitive to the effects of high-luminosity pile-up and the presence of jets. Also, all but the most catastrophic occurrences of an early bremsstrahlung can be tagged and at higher p_T's recuperated using the ECAL measurement. However, problems related to bremsstrahlung are here to stay and a further increase in the ID material,[1] especially in the pixel sub-detector, could result in the electron identification efficiency dropping below the limit needed for the attainment of the ATLAS physics goals. It should also be seriously noted, that it is the pixel sub-detector and the inner layers of the SCT that are crucial to a reliable electron reconstruction and identification. ATLAS should therefore make every effort to keep these layers operational during the whole data-taking period.

Applications of the electron reconstruction algorithm

To test the algorithm's performance on physical events of the type that will be observed (or searched for) and studied by the ATLAS collaboration, three physics channels were studied. The emphasis was put on quantities related to electron reconstruction. An important difference from the *Physics Performance TDR* productions was the inclusion of the realistic magnetic field.

The $\mathbf{B^0 \to J/\Psi \to} \boldsymbol{ee}$ process was as analysed in detail with respect to $J/\Psi \to ee$ reconstruction. The J/Ψ reconstruction efficiency was studied as a function of invariant mass cut and pion ambiguity. The efficiency varies from 40% to 78%; for a 10% cut on the reconstructed invariant mass the efficiency is 65%. Then the J/Ψ vertex reconstruction was addressed with respect to transverse (R_0) and longitudinal (Z_0) position. The overall R_0 resolution is $\sigma(R_0) = 110\,\mu\mathrm{m}$ with a variation by a factor of 2 over the η coverage and it degrades by the same factor over the available range of average transverse momentum of the final state electrons (getting worse with increasing momentum). The Z_0 resolution is strongly η dependent, deteriorating linearly from $250\,\mu\mathrm{m}$ at $|\eta| \sim 0.2$ to $3500\,\mu\mathrm{m}$ at $|\eta| \sim 2.3$.

[1] Recent changes in the ID layout will increase the amount of material in the beam-pipe, pixel detector services and supports by roughly 50% in the sensitive tracking volume. The exact values haven't yet been estimated.

The average value is $\sigma(Z_0) = 1200\,\mu$m. J/Ψ momentum reconstruction was also studied. The transverse (P_T) and longitudinal (P_L) momentum resolutions are both improved by application of an invariant mass cut on the reconstructed $m_{J/\Psi}$. For a 10% cut, Gaussian widths of the normalised residual distributions are about 3%. The $m_{J/\Psi}$ reconstruction greatly benefits from the improved electron treatment. Even by using all ID/ECAL match types, an improvement of 20% is achieved on FWHM of the $m_{J/\Psi}$ distribution as well as a reduction of the tails by a factor of two. By further requiring a good ID/ECAL match, the resolution is improved by additional 10%.

The $\mathbf{Z} \to \boldsymbol{ee}$ process is of prime importance for calibration of the ECAL. The role of ID electron track reconstruction is to provide the z vertex coordinate and directional angles as well as to tag events that have undergone a hard FSR or an early hard bremsstrahlung photon emission. The reconstruction efficiency as a function of invariant mass cut and ID/ECAL matching was studied and found to vary from 51%, with a 5% invariant mass cut and the requirement of a good ID/ECAL match, to 95% when no cuts were applied. The resolution of the z vertex position is $\sigma(z) \sim 55\,\mu$m in the barrel ($|\eta| < 1$) and then rises linearly to $115\,\mu$m towards the end of the η coverage.

The reconstruction of m_{Z^0} was studied with respect to its $|\eta|$ dependence. In the central barrel region the experimental resolution and the natural width are approximately the same while in the transition region the experimental resolution is worse by 60%. The tail content outside 2σ is well behaved over all the η coverage and only a minor asymmetry can be observed on the low-energy side of the residual distribution.

$\mathbf{H} \to \mathbf{ZZ}^{(\star)} \to \mathbf{4}\boldsymbol{e}$ was studied as an example of how `ieElRec` can be used in a real physics analysis. The process was considered for m_{H}=(130, 150, 180, 200 GeV), the main differences being in distributions of invariant mass of the off-shell Z^0. This has a direct consequence in the electron transverse momentum distribution with a lower mean value for lower m_{H}, in which case the ID track reconstruction has more clients for improvement of transverse momentum measurement. For $m_{\mathrm{H}} = 130$ GeV there are 39% of events with $m_{\mathrm{Z}^\star}$ calculated using at least one ID measurement and the average correction is 1.3% of the invariant mass. For on-shell Z^0's the event fraction drops to 10% and the correction to 0.75%.

The reconstruction efficiency was again studied in a view of a cut on the reconstructed m_{H} and ID/ECAL matching. By using a 10% cut on the invariant mass and selecting good matches as well as those for which the ID p_T measurement shows on an early bremsstrahlung or FSR (the track directional parameters are not spoiled) a 10% improvement of reconstruction efficiency is obtained compared to the *Physics Performance TDR* ($\sim$ 81%). In a view of the reducible $t\bar{t}$ and $\mathrm{Z}^0 b\bar{b}$ background rejection, impact parameter and z-vertex reconstruction was addressed. In the same spirit the Z^0–$\mathrm{Z}^{0(\star)}$ opening angle was analysed.

The impact of usage of the ID p_T measurement and m_{Z^0} constraint on the mean value and resolution of the m_{H} measurement was studied. The ID p_T measurement improves the resolution by 4% for $m_{\mathrm{H}} = 130$ and to a smaller extent ($\sim$ 2%) also for $m_{\mathrm{H}} = 150$ and 200 GeV. The mean value is improved for $\sim$ 400 MeV. The m_{Z^0} constraint improves the resolution for $\sim$ 5% at $m_{\mathrm{H}} = 150$ and 200 GeV while at $m_{\mathrm{H}} = 180$ GeV the correction is 15%. The mean value improvement is $\sim$ 750 MeV.

It has been demonstrated that the electron reconstruction algorithm can be used in the physical analysis. In particular, the processes crucial for EM calorimeter calibration

($B^0 \rightarrow J/\Psi \rightarrow ee$ and $Z \rightarrow ee$), have been addressed and the usefulness of the algorithm for improving the track parameters of the low and intermediate p_T electrons as well as for the detection of a hard FSR or an early bremsstrahlung photon emission, has been established. Furthermore, in order to study a realistic physics process, the $H \rightarrow ZZ^{(\star)} \rightarrow 4e$ decay channel has been used and a 10% increase of the H reconstruction efficiency has been observed.

Appendix A

Tracking Magick, Resolution of Beam Telescope and More

This appendix explains track finding and track fitting methods used in analysis of beam test data. Beam telescope properties are studied in greater detail and methods used to extract them are discussed. Alignment procedure for inclined detector is described.

Please note that the term *detector* is used as an abbreviation for silicon strip detector.

1.1 Tracking

Method used for fitting the tracks is a bit of an overkill as detector orientation is allowed to be any member of vector space generated by O(3) operators. But since such representation was needed to fully explore the inclined detector the choice seemed quite natural. What follows is a description of path leading from clusters to space points and then on to tracks.

1.1.1 Representation of marks and points

After doing archaeological excavations on raw data one usually ends up with a set of clusters. For silicon–strip detectors these are just intervals of strips with signal above certain cuts (clustering procedure is discussed in Sec:2.3). Given this information one proceeds using one or the other algorithm for position prediction and comes up with a single number. Making an agreement with oneself as to where the origin of the *local coordinate system* (LCS) is (say, on the middle strip) and knowing the pitch of the detector one gets a measurement of track crossing point u in LCS. For convenience let us define perpendicular coordinate in detector plane as v and coordinate in direction normal to detector plane as w. With a strip detector we can't really say much about v coordinate (but that it is somewhere within the size of the detector) and the best one can do is to set it to value corresponding to the middle of the detector. w coordinate of the measurement is undoubtedly zero.

Trying to get this measurement useful for track fitting, measurements from all detectors must be transformed to *tracker's coordinate system* (TCS). This means that we must know positions and rotation angles of each detector. Which, with certain uncertainty, we do. Let us return to LCS and discuss errors. Error on u can be measured for given position prediction algorithm and is typically some fraction of detector's pitch. Error on v can not be defined reasonably in terms of a Gaussian error as distribution of residuals in this direction is basically flat (following track position distribution). It is best to leave it infinite and let detectors with different orientation of strips pinpoint track position in this direction. Error on w is the trickiest one as one is tempted to set it to zero. But since measurement vector will be transformed to TCS the wisest choice is to set it to precision with which detector position in w direction is determined. Here is formalistic compression of all the talking, giving definition of measured quantities in LCS:

$$\vec{R} = (u, 0, 0) \tag{A.1}$$

$$\vec{S} = (\sigma_u, \infty, \sigma_w). \tag{A.2}$$

These will be refered to as *marks* as opposed to their representation in TCS where they will be called *points*.

Transforming a mark into a point one first notices that vector representation for errors is inappropriate. It has to be a matrix as errors get correlated when subjected to rotations. For later convenience we define it as:

$$W_{\mathrm{LCS}} = \begin{pmatrix} \frac{1}{\sigma_u^2} & 0 & 0 \\ 0 & 0 & 0 \\ 0 & 0 & \frac{1}{\sigma_w^2} \end{pmatrix}. \tag{A.3}$$

I won't bother myself by writing down transformation rules ... perhaps it is only worth mentioning that I used `homogeneous coordinates` where position vector is extended by one dimension (called scale) and it enables one to write translation and rotation in LCS using a 4×4 matrix. This 'trick' is usually used in computer graphics and interested parties are kindly invited to consult the literature ([38] or just search the www).

1.1.2 Track fitting formulas

Fitting a straight line is to fitting as `hello world` example is to programming, so this little expose serves more for documentation purposes. Besides ... I want to argue how three degrees of freedom from 3D representation of a point are squished into a single one.

I will present formulas defining least squares fitting procedure with Gaussian errors. See one of the classics (e.g., [39]) or excellent series on applied fitting theory by Paul Avery ([40]) for details. This just wants to put some context to further manipulations.

Problem definition can be split into few points:

1. For start ... we have n measured values denoted by y_l.

2. We would like to 'summarize' this data in terms of a mathematical model with m parameters α_i, $m < n$. At each of the data points l our model makes a prediction $f_l(\alpha)$ (dropping an index implies a vector).

3. With this, we can define difference between measured data and model prediction at given values of parameters α:

$$\chi^2 = \sum_l \frac{\left(y_l - f_l(\alpha)\right)^2}{\sigma_l^2}, \tag{A.4}$$

where σ_l is the error (expected to be Gaussian and uncorrelated) of measurement l. Of course ... we want the best set of parameters, that is parameters that minimize χ^2:

$$\frac{\partial \chi^2}{\partial \alpha} = 0. \tag{A.5}$$

4. One expects to have certain clue about initial values of parameters $\widetilde{\alpha}$ ('seed' parameters) and that expansion to first order in $\alpha - \widetilde{\alpha}$ will take us on a way to the minimum. That is ... we approximate $f_l(\alpha)$ by:

$$f_l(\alpha) = f_l(\widetilde{\alpha}) + \sum_i (\alpha_i - \widetilde{\alpha}_i) \frac{\partial f_l(\alpha)}{\partial \alpha_i}\bigg|_{\widetilde{\alpha}} \equiv f_l(\widetilde{\alpha}) + \sum_i A_{li}\eta_i \tag{A.6}$$

$$f(\alpha) = f(\widetilde{\alpha}) + \mathbf{A}\eta. \tag{A.7}$$

First we defined derivatives of model function with respect to parameters evaluated at their initial values ($\mathbf{A}_{n\times m}$) and distance in parameter space (η_n) from seed to improved values. Then we introduced matrix notation.

5. Rewriting χ^2 with this expansion yields:

$$\chi^2 = \sum_l \frac{\left(y_l - f_l(\widetilde{\alpha}) - \sum_i A_{li}\eta_i\right)^2}{\sigma_l^2}. \tag{A.8}$$

Let me define $\Delta\mathbf{y} = y_l - f_l(\widetilde{\alpha})$ which is difference between measurements and values predicted by seed parameters. More interesting quantity is a residual vector $\varepsilon = \Delta\mathbf{y} - \mathbf{A}\eta$ which is difference of measurements and final predicted values. To put χ^2 expression to matrix form, we need to define the weight matrix (this is just fitological term for inverse of correlation matrix) ... remember, we are still talking uncorrelated errors ... so this is really simple: $\mathbf{W}_{n\times n} = \mathrm{diag}(1/\sigma_1^2 \ldots\ 1/\sigma_{\mathrm{i}}^2 \ldots\ 1/\sigma_{\mathrm{n}}^2)$. This brings us to:

$$\chi^2 = (\Delta\mathbf{y} - \mathbf{A}\eta)^T \mathbf{W}\,(\Delta\mathbf{y} - \mathbf{A}\eta) = \varepsilon^T \mathbf{W}\,\varepsilon. \tag{A.9}$$

6. Doing the partial derivations with respect to α_m, we get m equations:

$$\mathbf{A}^T \mathbf{W}\,(\Delta\mathbf{y} - \mathbf{A}\eta) = 0. \tag{A.10}$$

Defining $\mathbf{V_A} = \left(\mathbf{A}^T\mathbf{W}\,\mathbf{A}\right)^{-1}$, we get solution for η:

$$\eta = \mathbf{V_A}\mathbf{A}^T\mathbf{W}\,\Delta\mathbf{y} \tag{A.11}$$

By using $\alpha = \widetilde{\alpha} + \eta$, we get the improved set of parameters. As we only made the linear approximation, several iterations of the above procedure are needed when model function is non-linear with respect to model parameters..

Not to be too verbose ... we're still interested in errors on fitted parameters and their correlation. One of the surprises of the least square method is that it always yields correlation matrix of the form : $\mathbf{V}_\alpha = \mathbf{V}_\eta = \mathbf{V}_A$.

7. Fitting with correlated errors basically means inverting the covariance matrix $\mathbf{V_y} = \langle \delta y^T \delta y \rangle$. This can get messy, especially with near–singular correlation matrices. There are ways around it, though not a general one.

1.1.3 Application to beam telescope track reconstruction

Since the beam energy is 300 GeV (90% pions, 10% muons) and longitudinal dimension of the telescope is 20 cm, track is modeled as a straight line without accounting for multiple scattering. Four parameters were used:

- x and y coordinate of track intersection with $z = 0$ plane, packed in a vector $\vec{p}$:

$$\vec{p} = \begin{pmatrix} x & y & 0 \end{pmatrix}$$

- directions q_x and q_y of track with q_z fixed to 1:

$$\vec{q} = \begin{pmatrix} q_x & q_y & 1 \end{pmatrix}.$$

This yields parametrization of a straight line $\vec{p} + t\vec{q} = \vec{x}(t)$ and n measurements $\vec{r_i}$ on i-th detector plane defined by a normal $\vec{z_i}$ (i going from 0 to $N_{\text{det}} - 1$). In order to calculate the distance from measured intersection to predicted one ($\vec{\varepsilon_i}$), we require for it to lie in the detector plane: $\vec{z_i} \cdot (\vec{r_i} - \vec{x}(t)) = 0$, giving:

$$t_i = \frac{\vec{z_i} \cdot (\vec{r_i} - \vec{p})}{\vec{z_i} \cdot \vec{q}} \tag{A.12}$$

$$\vec{\varepsilon_i} = \vec{r_i} - \vec{p} - t_i\vec{q}. \tag{A.13}$$

Or in language of model function $\vec{f_i}(\alpha)$:

$$\vec{f_i}(\vec{p}, \vec{q}) = \vec{p} + t_i\vec{q}. \tag{A.14}$$

Index i is counting the detector planes. So far nothing was said about direction in which actual measurement was done. Let's keep it this way a bit longer. Introducing a new index $j \in \{1, 2, 3\}$ to subscript x, y and z components of vectors and defining the overall index as $k = 3i + j$, we get close to 'linear' structure required by fitting procedure. For example $z_{1,2}$ stands for y component of normal of second detector. With this, we can calculate partial derivatives needed to form matrix $\mathbf{A}$:

$$\frac{\partial}{\partial p_m}\varepsilon_{i,j} = -\delta_{jm} + \frac{z_{i,m}}{\vec{z_i} \cdot \vec{q}}\, q_j, \tag{A.15}$$

$$\frac{\partial}{\partial q_m}\varepsilon_{i,j} = -\vec{z_i} \cdot (\vec{r_i} - \vec{p})\, \frac{\delta_{jm}(\vec{z_i} \cdot \vec{q}) - q_j z_{i,m}}{(\vec{z_i} \cdot \vec{q})^2}. \tag{A.16}$$

Index m is taking values 1 and 2 (as third components of $\vec{p}$ and $\vec{q}$ are held fixed) and δ_{jm} is the Kronecker delta symbol.

Now we have to build the weight matrix. This is done by simply transforming $\mathbf{W}_{\text{LCS}}$ with the transformation matrix $\mathbf{T}$ from LCS to TCS: $\mathbf{W}_{\text{TCS}} = \mathbf{T}\,\mathbf{W}_{\text{LCS}}\,\mathbf{T}^{-1}$ and building a block–diagonal matrix out of these transforms. Two points are crucial. First, the v direction 'measurement', which is in fact just detector position, does not contribute anything to χ^2 because its error is set to be infinite. Second, error on w is projected out by requiring the track intersection to lie in plane of the detector. General treatment was necessary to be able to cope with detectors under arbitrary orientations.

1.2 Resolution of beam telescope

Basic description of beam telescope is given in Sec:2.2.1. Material shown there is just about enough to convince a careless reader that error on predicted track position at $z = 0\,\mu$m is $\delta u_t = 2.5\,\mu$m. Here you can find the full story.

1.2.1 Alignment

Alignment of telescope detectors was carried out in $z =$ const plane. This amounts to moving the detector in direction perpendicular to strips and rotating it around the z axis. See [41]:Ch:4 for more details. In our case *eta* method was used all along for determination of hit positions.

Additionally, whole tracker was moved and rotated so that its z axis coincided with average track direction and that average x and y of reconstructed tracks were zero.

Results of alignment are implicitly visible on plots showing residual distributions of telescope planes.

1.2.2 Estimation of resolution of telescope detectors

It is a bit of a wrong idea to use residual distributions of detectors used in track fitting as a measure of their resolution. The proper thing to do is to exclude them, one by one, from the track fit. Fig:A.1 compares both cases. So we take resolution from non–fitted planes as basic input. One is tempted to forget that this is in fact a convolution of errors given by the detector and intrinsic error of the tracker:

$$\sigma^2_{i\ m} = \sigma^2_i + \sigma^2_t(z_i). \tag{A.17}$$

i is index of the plane, m stands for 'measured' and t for 'tracker'. The dependence of tracker's resolution on z coordinate is implied by functional notation. Resolution is better for planes 1-4 than for planes 5-8. This is explained by different number of interpolation strips (see Tab:2.1).

Assuming that planes with the same number of interpolation strips have the same resolution, one can argue that when one of the planes is not used in the fit, resolution of the other one (on its 'side' of the tracker) dominates the tracker's resolution. That is, e.g.,

$$\sigma^2_{5\ m} = \sigma^2_5 + \sigma^2_8 = 2\sigma^2_5 \tag{A.18}$$

and all other combinations. From this follows

$$\sigma_i = \frac{\sigma_{i\ m}}{\sqrt{2}}. \tag{A.19}$$

Using this prescription we come up with values $\sigma_{1-4} = 2.28\,\mu$m and $\sigma_{5-8} = 5.48\,\mu$m.

These were used as first guesses for monte carlo simulation in which marks in detectors were smeared by this amount from values obtained by calculating the track intersection. The same resolution was used to calculate χ^2 contribution of point in question. Residuals obtained from MC runs were in agreement with the true ones but distribution of χ^2 per degree of freedom for real data had mean at 0.72. Honestly ... and quite obviously ... resolutions obtained in this way are worse than actual ones.

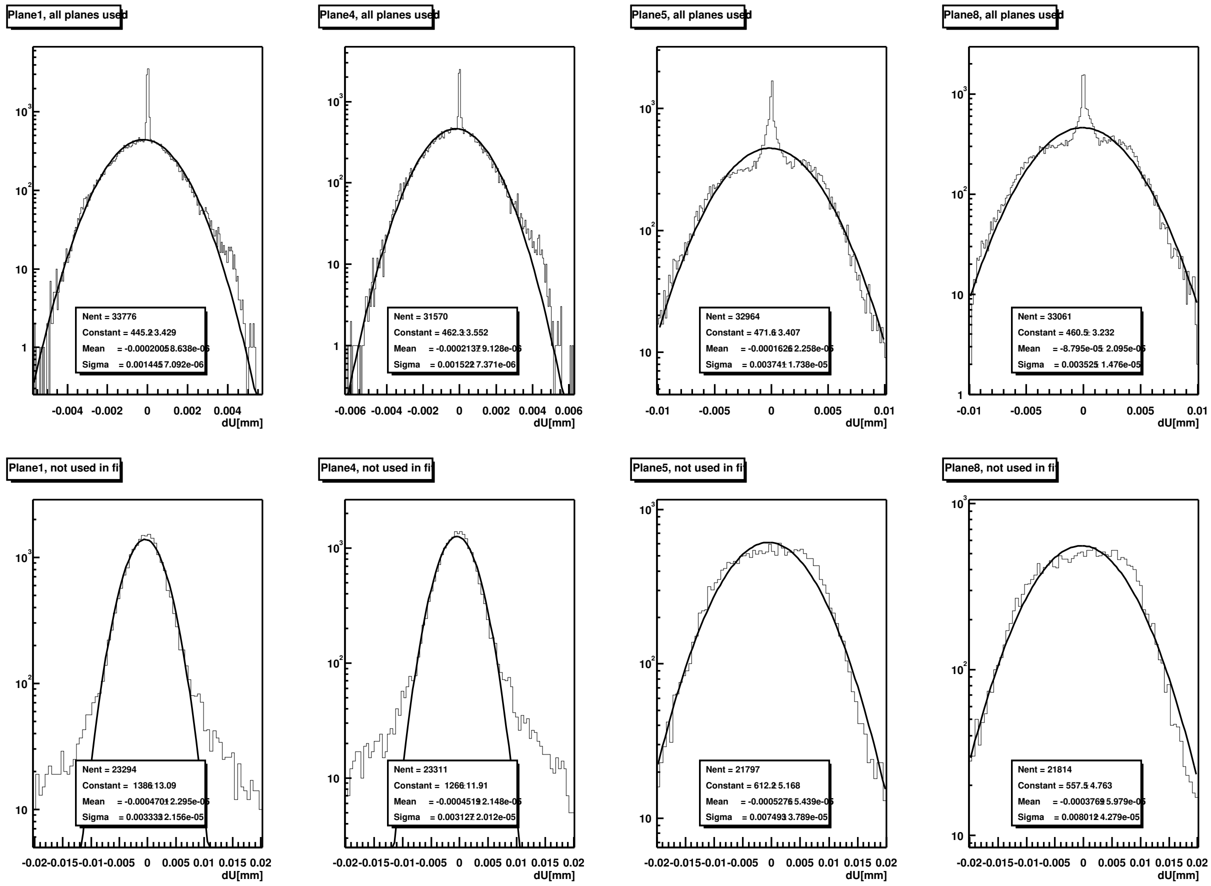

Figure A.1: Residuals for Planes 1, 4, 5 and 8 when they have been all used in the fit (top line) and when they were omitted (one at the time) from the fit (botom line). Note that scales of x-axes are different.

This leads us to the conclusion that we swallowed the tracker's resolution into the resolution of the detector plane. This excess can be attributed to telescope misalignment in directions where explicit alignment hasn't been performed. But we have another cross-check. When both planes are used in the fit, we are in fact looking at the distribution of $u = x_5 - (x_5 + x_8)/2 = (x_5 - x_8)/2$, where x_i is the position measurement of i-th plane. Resolution of this quantity, let's name it $\sigma_{i\,u}$, can be written:

$$\sigma_{i\,u}^2 = \frac{\sigma_i^2}{2}. \tag{A.20}$$

This way we obtain resolutions $\sigma_{1-4} = 2.1\,\mu$m and $\sigma_{5-8} = 5.15\,\mu$m. These were then used for calculation of the χ^2 of the track fit. Residuals obtained by MC simulation are shown in Fig:A.2 and basic parameters of fit quality on real data in Fig:A.3. Additionally, distributions of fitted track parameters (position and direction of track) is given in Fig:A.4.

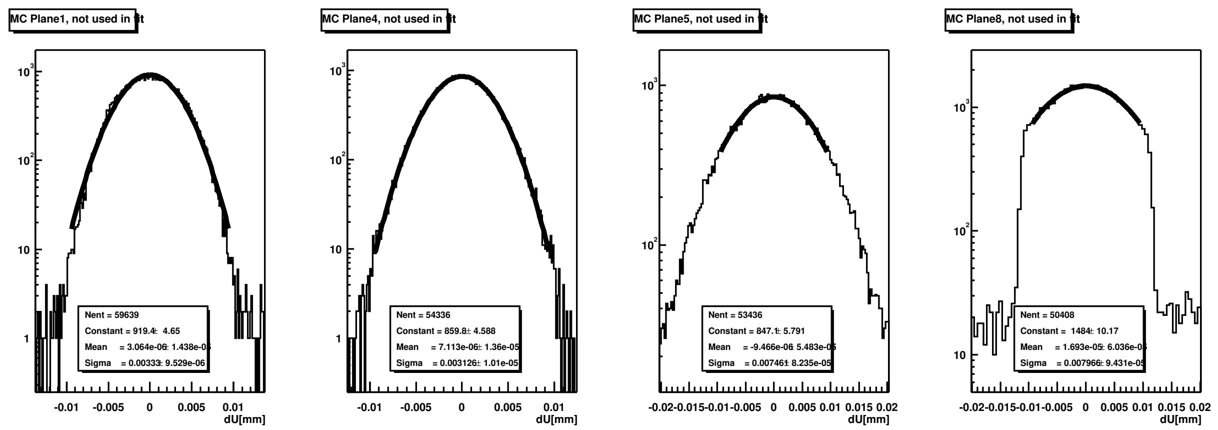

Figure A.2: Residuals for Planes 1, 4, 5 and 8 with monte-carlo generated tracks, where plane in question was not used in track fit.

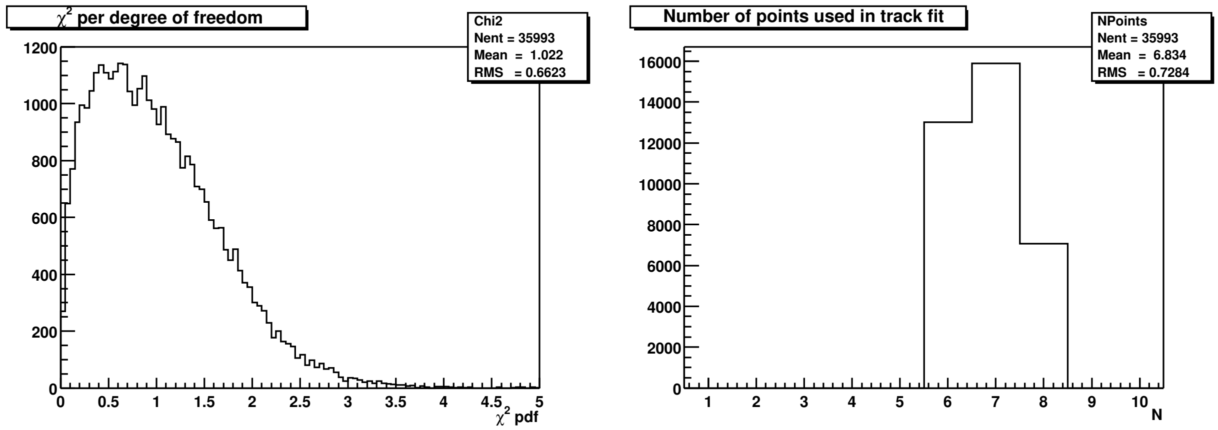

Figure A.3: Track fit quality for real data. Note that fitologically we expect $<\chi^2/\text{pdf}>= 1$ and $\mathsf{rms}(\chi^2/\text{pdf}) = 1/\sqrt{2} \approx 0.71$.

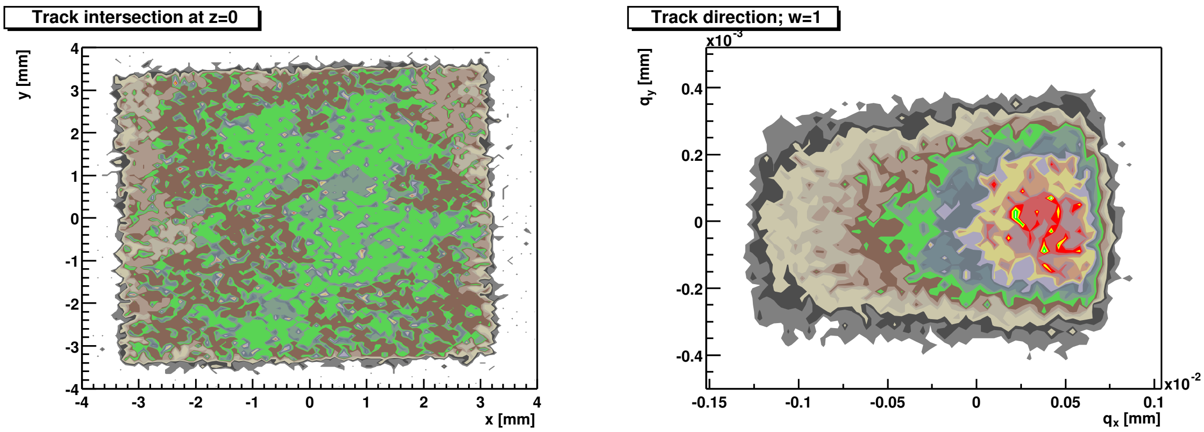

Figure A.4: Distributions of fitted parameters.

1.3 Alignment of the inclined detector

For detector under test a special alignment procedure was adapted as it had to be aligned with respect to six degrees of freedom. Positioning of the detector was described by position vector of center of the detector and three cardanian angles giving its orientation in local reference frame (beware ... different set of cardanian angles can represent the same physical orientation). Problem of alignment is basically equivalent to minimization of chi–square function for the detector for a set of events. Due to finite sample of events and its statistical fluctuations the problem is somewhat ill–defined and using traditional gradient methods tends not to converge but on a narrow area around the true minimum.

To find the way through the scattered landscape of the chi–square function a cross between simplex minimization and Metropolis algorithm was used (see [39], chapter 10) leading to the following algorithm:

1. Position detector 'by hand' to provide solid starting conditions. Especially bad choice of angular variables can lead to unnecessary long minimization.

2. Iterate through the available events. Choose events where there is no ambiguity (single track, single cluster in the detector) and cluster position reconstruction is good (i.e., for low inclinations use only two–strip clusters). Number of good events will be refered to as N_e.

3. For sizes of inital simplex use mean values of residual distributions for u, v coordinates, width of the detector for w coordinate and hard–coded value of 1° for angular variables.

4. Enter the minimization loop with inital value of temperature set to one tenth of inital χ^2. Set fractional convergence to $1/\sqrt{N_e}$. It is enough to set maximum number of iterations per given temperature to $\sqrt{N_e}$. Decrease the temperature in N_s steps (50 to 100 steps showed adequate for $N_e \approx 3000$) with annealing scheme $T_i = T_0(1 - i/N_s)^{1.2}$.

One has to admit that the method used was a bit of an overkill. But it is always like this with numerics: one either uses the most optimal algorithm and spends an eternity tuning it to work well in given case or chooses to use a more general one that safely bypasses the obstacles. Size of the problem and amount of data that has to be processed are the guidelines for deciding which path to take in a particular case. We only had to perform alignment six times (once for each run) and getting to the bottom of all pitfalls hidden in alignment was not our intention in presented work.

Bibliography

[1] G. Jarlskog and D. Rein, editors. *Large Hadron Collider Workshop*, volume 1–3, 1990. CERN 90-10.

[2] Atlas detector and physics performance technical design report, 1999. CERN/LHCC/99-14.

[3] Atlas detector and physics performance technical design report, 1999. CERN/LHCC/99-15.

[4] Atlas technical proposal, 1994. CERN/LHCC/94-63.

[5] Atlas inner detector technical design report, 1997. CERN/LHCC/97-16.

[6] Atlas pixel detector technical design report, 1998. CERN/LHCC/98-13.

[7] Atlas inner detector technical design report, 1997. CERN/LHCC/97-17.

[8] Atlas calorimeter performance, 1996. CERN/LHCC/96-40.

[9] Atlas liquid argon calorimeter technical design report, 1996. CERN/LHCC/96-41.

[10] Atlas tile calorimeter technical design report, 1996. CERN/LHCC/96-42.

[11] Atlas muon spectrometer technical design report, 1997. CERN/LHCC/97-22.

[12] Atlas level–1 trigger technical design report, 1998. CERN/LHCC/98-14.

[13] Atlas computing technical proposal, 1996. CERN/LHCC/96-43.

[14] M. Dittmar and H. Dreiner. How to find a higgs boson with a mass between 155-gev to 180-gev at the lhc. *Phys. Rev.*, D55:167–172, 1997.

[15] J. Kaplon et al. Dmill implementation of the analogue readout architecture for position sensitive detectors at lhc experiments. Given at 4th Workshop on Electronics for LHC Experiments (LEB 98), Rome, Italy, 21-25 Sep 1998.

[16] Lau Gatignon (liason physicist). *Secondary Beamlines at the SPS.* `http://sl.web.cern.ch/SL/eagroup/beams.html`, 1998.

[17] R. Turchetta. Spatial resolution of silicon microstrip detectors. *Nucl. Instrum. Meth.*, A335:44, 1993.

[18] William R. Leo. *Techniques for Nuclear and Particle Physics Experiments.* Springer–Verlag, 2^{nd} edition, 1994.

[19] D. E. Groom et al. Review of particle physics. *Eur. Phys. J.*, C15:1, 2000.

[20] H. Bethe and W. Heitler. On the stopping of fast particles and on the creation of positive electrons. *Proc. Roy. Soc. Lond.*, A146:83–112, 1934.

[21] W. Heitler. *The Quantum Theory of Radiation.* Oxford University Press, 3$^{\text{rd}}$ edition, 1954.

[22] Claude Itzykson and Jean–Bernard Zuber. *Quantum Field Theory.* McGraw–Hill Inc., 1980.

[23] L.D. Landau and I.Ya. Pomeranchuk. *Dokl. Akad. Nauk SSSR*, 92, 1953. English translation in *The Collectd Paper of L.D. Landau*, Pergamon Press, New York 1965.

[24] A.B. Migdal. *Phys. Rev.*, 103:1811, 1956.

[25] V. N. Baier and V. M. Katkov. The theory of the landau-pomeranchuk-migdal effect. *Phys. Rev.*, D57:3146–3162, 1998.

[26] V. N. Baier and V. M. Katkov. Integral characteristics of bremsstrahlung and pair photoproduction in a medium. 2000.

[27] P. L. Anthony et al. Bremsstrahlung suppression due to the lpm and dielectric effects in a variety of materials. *Phys. Rev.*, D56:1373–1390, 1997.

[28] Application Software Group. *GEANT3 – Detector Description and Simulation Tool.* CERN Program Library Long Writeup W5013, 1993.

[29] J. Schwindling. The reconstruction code for the electromagnetic calorimeter in `ATRECON`, 1997. Version 97/3.

[30] Torbjorn Sjostrand. High-energy physics event generation with pythia 5.7 and jetset 7.4. *Comput. Phys. Commun.*, 82:74–90, 1994.

[31] Elisabetta Barberio and Zbigniew Was. Photos: A universal monte carlo for qed radiative corrections. version 2.0. *Comput. Phys. Commun.*, 79:291–308, 1994.

[32] A Artamonov, A Dell'Acqua, D Froidevaux, M Nessi, P Nevski, and G Poulard. Dice–95, 1995. ATLAS Internal Note ATL-SOFT-95-014.

[33] S. P. Baranov and M. Smizanska. Beauty production overview from tevatron to lhc, 1998. ATLAS Internal Note ATL-PHYS-98-133.

[34] M. Smizanska et al. Overview of monte-carlo simulations for atlas b-physics in the period 1996-1999, 1999. ATLAS Internal Note ATL-COM-PHYS-99-042.

[35] A. Djouadi, J. Kalinowski, and M. Spira. *HDECAY: a Program for Higgs Boson Decays in the Standard Model and its Supersymmetric Extension.* hep-ph/9704448, 1997.

[36] O. Linossier and L. Poggioli. h to zz^* to 4 leptons channel in atlas. signal reconstruction and reducible backgrounds rejection., 1997. ATLAS Internal Note ATL-PHYS97-101.

[37] O. Linossier and R. Ztoun. h to zz^* to 4 leptons channel in atlas. a complementary study of the zz^* irreducible background., 1996. ATLAS Internal Note ATL-PHYS96-096.

[38] James D. Foley, Andries van Dam, Steven K.Feiner, and John F. Hughes. *Computer Graphics, principles and practice*. Addison-Wesley Publishing Company, 2^{nd} edition, 1990.

[39] William H. Press, Saul A. Teukolsky, William T. Vetterling, and Brian P. Flannery. *Numerical Recipes in C*. Cambridge University Press, 2^{nd} edition, 1992.

[40] Paul Avery. *Fitting Magick*. `http://www.phys.ufl.edu/~avery/fitting.html`, 1996–1998.

[41] Dirk Meier. *Diamond Detectors for Particle Detection and Tracking*. PhD thesis, University of Heidelberg, January 1999. Carried out at RD42 in ATLAS/SCT group at CERN.